Fine-scale, Multidimensional Spatial Patterns of Forest Canopy Structure
Derived from Remotely Sensed and Simulated Datasets

by

Gordon Wilson Frazer
B.A., University of Western Ontario, 1982
M.Sc., University of Western Ontario, 1986

A Dissertation Submitted in Partial Fulfillment of the
Requirements for the Degree of

DOCTOR OF PHILOSOPHY

in the Department of Geography

Fine-scale, Multidimensional Spatial Patterns of Forest Canopy Structure
Derived from Remotely Sensed and Simulated Datasets

by

Gordon Wilson Frazer
B.A., University of Western Ontario, 1982
M.Sc., University of Western Ontario, 1986

Supervisory Committee

Dr. K. Olaf Niemann, Supervisor
(Department of Geography)

Dr. Mike A. Wulder, Co-Supervisor
(Canadian Forest Service, Pacific Forestry Centre)

Dr. Mark S. Flaherty, Departmental Member
(Department of Geography)

Dr. Barbara J. Hawkins, Outside Member
(Department of Biology)

Dr. Kenneth P. Lertzman, Additional Member
(School of Resource and Environmental Management, Simon Fraser University)

Dr. Geoffrey G. Parker, External Examiner
(Smithsonian Environmental Research Center, Maryland, U.S.A.)

Supervisory Committee

Dr. K. Olaf Niemann, Supervisor
(Department of Geography)

Dr. Mike A. Wulder, Co-Supervisor
(Canadian Forest Service, Pacific Forestry Centre)

Dr. Mark S. Flaherty, Departmental Member
(Department of Geography)

Dr. Barbara J. Hawkins, Outside Member
(Department of Biology)

Dr. Kenneth P. Lertzman, Additional Member
(School of Resource and Environmental Management, Simon Fraser University)

Dr. Geoffrey G. Parker, External Examiner
(Smithsonian Environmental Research Center, Maryland, U.S.A.)

ABSTRACT

Forests are not simply storehouses of timber or wood fibre for human consumption and economic development. They represent structurally and ecologically rich habitat for an estimated 40 percent of the earth's extant species, and form the functional interface between the biosphere and atmosphere for some 27 percent of the earth's terrestrial surface. Forests, therefore, play a vital role in the maintenance of biodiversity and the regulation of local to global scale ecosystem processes and functions. Present strategies for conserving biodiversity in managed forests are based on the notion that maintaining the full range of structural conditions historically present in natural forests is the best approach for assuring the long-term persistence of a broad range of native species.

The overarching goal of this dissertation is to contribute to the development of novel forest measurements that are relevant to organisms and ecosystems, and much needed by forest scientists and managers to recognize and retain the key elements and patterns of forest structure that are crucial for the conservation of forest biodiversity. This study focuses explicitly on fine-spatial-scale, multidimensional patterns of forest canopy

structure based on the assumption that the 'canopy' is the primary focal site of complex interactions between vegetation and the physical environment. Two disparate remote sensing technologies—ground-based hemispherical (fisheye) canopy photography and airborne discrete-return LiDAR—are employed to characterize angular, vertical, and horizontal patterns of forest canopy structure.

A quantitative technique is developed for precise measurements of gap fraction (P), element clumping (Ω), mean projection coefficient (G), and leaf area index (L) from sequences (sets) of black and white pixels extracted at specific view angles in digital fisheye photos. Results are compared with three other leading techniques and validated using well-documented simulated and real fisheye photosets. Variables P, Ω, G, and L control light capture and penetration in forest canopies, and are key input parameters for process-based models of stand productivity, stand dynamics, and material (CO_2 and H_2O) and energy fluxes between the canopy and atmosphere. Findings show that this new technique consistently produced the best estimates of stand LAI in each of the three experimental forest sites. However, further validation work is required to determine the adequacy of these methods in other closed and discontinuous canopies.

Finally, a methodological framework is devised for quantifying, classifying, and comparing fine-spatial-scale vertical and horizontal patterns of canopy structure derived from airborne LiDAR data. This methodology is tested with simulated forest canopies and ultimately demonstrated using an airborne LiDAR dataset collected over very young to old, coastal Douglas-fir/western hemlock forests on Vancouver Island, British Columbia. A pseudo 'space-for-time substitution' sampling approach is used to investigate age-related developmental changes in canopy structure at decadal and century time scales. Discrete classes of vertical and horizontal canopy structure are identified by k-means partitioning. The structural differences found among age-classes were consistent with the characteristics, patterns, and dynamics predicted by generalized models of stand development for similar coastal Douglas-fir/western hemlock forests of northwestern North America.

Table of Contents

Supervisory Committee..... ii
Abstract..... iii
Table of Contents..... v
List of Tables..... viii
List of Figures..... ix
Acknowledgements..... xii
Dedication..... xiii

CHAPTER 1: Introduction..... 1
1.1. Background and Problem Statement..... 1
1.2. Research Objectives and Questions..... 4
1.3. Scope and Format of the Dissertation..... 5
1.4. References..... 7

CHAPTER 2: Characterization of Angle-Dependent Element Clumping and Leaf Area Index in Spatially Heterogeneous Forest Canopies Using Hemispherical Canopy Photography and Lacunarity Analysis..... 11
2.0 Abstract..... 11
2.1. Introduction..... 12
2.2. Lacunarity as a Scale-Dependent Measure of Spatial Nonrandomness..... 17
2.2.1. Definition and measurement of lacunarity..... 17
2.2.2. The scale-dependency and interpretation of $\Lambda(r)$..... 18
2.2.3. A lacunarity-based clumping index $\Omega_{LAC}(\theta)$..... 21
2.3. Materials and Methods..... 25
2.3.1. Description of hemispherical canopy photosets..... 25
2.3.2. Image pre-processing and extraction of binary sets..... 31
2.3.3. Estimation of LAI and canopy openness..... 31
2.3.4. Photo-based estimates of $\Omega(\theta)$..... 34
2.3.5. Statistical analysis..... 38
2.4. Results and Discussion..... 38
2.4.1. Estimates of L_e, CO, and L from simulated canopies..... 38
2.4.2. Estimates of L_e, CO, L_t, and L from real forest canopies..... 41
2.4.3. Angular dependence of optical LAI measurements..... 46
2.4.4. Impact of image resolution on $\Omega(\theta)$ and L..... 53
2.5. Conclusions..... 56
2.6. References..... 59

CHAPTER 3: Simulation and Quantification of the Fine-Scale Heterogeneity of Forest Canopy Structure: A Lacunarity-Based Method for Analysis of Continuous Canopy Heights..... 66
3.0 Abstract..... 66
3.1. Introduction..... 67
3.2. Spatial Pattern Analysis..... 71
3.2.1. Lacunarity as a scale-dependent measure of spatial heterogeneity in forest canopies..... 71
3.2.2. Lacunarity analysis using the 'gliding-box' algorithm and 2-D quantitative data..... 73
3.2.3. Five examples illustrating the application of lacunarity analysis to forest CHMs..... 74
3.3. Forest Canopy Simulation and Pattern Ordination..... 82
3.3.1. Development of simulated CHMs..... 82
3.3.2. Attributes of forest canopy structure and spatial pattern..... 84
3.3.3. Statistical analyses..... 86
3.4. Results..... 88
3.4.1. Structural characteristics of the simulated 3-D stand models and derived CHMs..... 88
3.4.2. Scale-dependent estimates of the lacunarity statistic..... 88
3.4.3. Ordination of lacunarity statistics using PCA..... 92
3.4.4. Correlations between principal components, lacunarity, and attributes of forest stand and canopy structure..... 94
3.5. Discussion and Conclusions..... 98
3.6. References..... 104
Appendix 3..... 112

CHAPTER 4: Use of Airborne LiDAR to Characterize Fine-Scale Vertical and Horizontal Patterns of Canopy Structure in *Pseudostuga-Tsuga* Forests of Varying Stand Age and Structural Complexity..... 123
4.0 Abstract..... 123
4.1. Introduction..... 124
4.2. Materials and Methods..... 127
4.2.1. Study area description..... 127
4.2.2. Sampling design and plot selection..... 129
4.2.3. Ground-reference plots and field measurements..... 131
4.2.4. LiDAR data processing..... 134
4.2.5. LiDAR-based measures of vertical structure..... 135
4.2.6. LiDAR-based measures of horizontal structure..... 139
4.2.7. Canopy density, surface, and volumetric indices..... 142
4.2.8. Exploratory data analysis..... 142
4.3. Results..... 146
4.3.1. Relationship between inventory and LiDAR-derived metrics..... 146
4.3.2. Interpretation of lacunarity statistics..... 151
4.3.3. Vertical and horizontal patterns of canopy structure..... 153

4.4. Discussion and Conclusions..... 174
4.4.1. LiDAR-derived measurements of forest canopy structure..... 174
4.4.2. Structural differences among forest age classes..... 181
4.4.3. Developmental aspects of *Pseudotsuga-Tsuga* canopies..... 183
4.4.4. Structure-based classification of forest canopies..... 186
4.5. References..... 190
Appendix 4A..... 203
Appendix 4B..... 223

CHAPTER 5: Conclusions and Future Directions..... 226
5.1. References..... 235

List of Tables

Table 2.1. Description of selected stand and fisheye-photo characteristics for three experimental forest sites..... 30

Table 2.2. Summary of canopy openness, element clumping, and LAI calculations for the 12 simulated fish-eye photos..... 39

Table 2.3. Summary of Ω, L_t, and L for CC, LAC, LX, and PCS clumping methods..... 44

Table 2.4 Summary of L estimated by Miller's theorem and at 57.5°..... 53

Table 2.5. Summary of L_e, Ω, and L for different image resolutions..... 55

Table 3.1. Stand attributes and spatial characteristics of five simulated forest canopies..... 78

Table 3.2. Formulae for plot-level attributes used to describe canopy structure..... 85

Table 3.3. Principal component loadings and Pearson correlations between principal components and lacunarity statistics..... 93

Table 3.4. Pearson correlations between principal components and attributes of stand structure..... 96

Table 4.1. Summary of LiDAR flight and instrument settings..... 129

Table 4.2. Summary of live-tree (≥2 m tall) stand attributes for 16 ground-reference plots established in Sooke Lake watershed, Vancouver Island, BC..... 134

Table 4.3. Summary of linear discriminant models, canonical loadings, and univariate and multivariate test statistics..... 157

Table 4.4. Chance-corrected classification matrices..... 158

Table 4.5 Two-way contingency table summarizing the frequency of observations for all combinations of vertical (row) and horizontal (column) k-means classes..... 167

List of Figures

Figure 1.1. A hemispherical optical sensor (radiation or camera) indirectly measures the angular distribution of canopy elements within a hemispherical (180°) object region..... 3

Figure 2.1. Simulated binary sets displaying six unique scale-dependent patterns of foliage (black) and gap (white) dispersions..... 19

Figure 2.2. Log-log lacunarity plot..... 20

Figure 2.3. Equiangular projection of circular sample transects placed every 1° of θ between $10° \leq \theta \leq 90°$..... 22

Figure 2.4. Normalized lacunarity curves identifying the position of the mean 'observed' curve relative to CSR and maximal clumping..... 24

Figure 2.5. Simulated hemispherical canopy photos with known values of LAI = 2, 4, and 6 and Fc = 0.0, 0.2, 0.4, and 0.6..... 26

Figure 2.6. Examples of hemispherical canopy photos representing each of the three experimental forest sites..... 27

Figure 2.7. A single simulated 5 m (width) × 5 m (length) × 10 m (height) canopy volume V displaying increasing amounts of spatial aggregation (Fc = 0.0, 0.2, 0.4, 0.6)..... 28

Figure 2.8. Angular variation of the canopy gap fraction, gap frequency, mean gap size, and coefficient of variation (COV) of gap size data derived from the simulated fisheye photoset..... 47

Figure 2.9. Scatterplots displaying the angular response of $\Omega(\theta)$ estimated by four different clumping methods (CC, LAC, LX, PCS) applied to the simulated photoset..... 49

Figure 2.10. Nonlinear relationship between $\Omega(\theta)$ and mean gap size..... 50

Figure 2.11. Line and scatterplots showing the strong angular variation in mean $P(\theta)$, $\Omega(\theta)$, $G(\theta)$, $L_e(\theta)$ and $L_t(\theta)$ retrieved from the three experimental forest sites..... 52

Figure 3.1. Five examples of simulated 3-D stand models and canopy height models developed for Random, Aggregated, and Uniform distributions of tree locations..... 75

Figure 3.2. Line and scatterplots showing the natural logarithm of the lacunarity statistic plotted against the natural logarithm of box size r..... 80

Figure 3.3. Boxplots summarizing the frequency distributions of 12 different attributes of stand and canopy stratified by stand class..... 89

Figure 3.4. Boxplots showing the frequency distributions of the lacunarity statistic $\Lambda(r)$ stratified by linear box size r and stand class..... 91

Figure 3.5. Ordination diagram showing the distribution of sample points in reduced ordination space..... 94

Figure 3.6. Overlay plot summarizing the relationship between attributes of stand and canopy structure and the first (PC1) and second (PC2) principal components..... 95

Figure 3.7. Selected examples of the 187 simulated CHMs..... 97

Figure 4.1. Site map showing the location of 152 square (0.25 ha) sample plots within the Sooke Lake watershed..... 128

Figure 4.2. Dimensions and layout of 0.25 ha (50 m × 50 m) ground-reference plots used for inventory sampling and other indirect canopy measurements..... 132

Figure 4.3. Geometry of the five silicon detector rings of the LAI-2000 PCA projected onto a hemispherical canopy photograph..... 134

Figure 4.4. Examples of one-sample quantile plots and histograms of LiDAR canopy height frequencies and field-measured basal areas per tree height class constructed for young, mature, and old-growth plots..... 137

Figure 4.5. Multiscale (0.5 m to 50 m) lacunarity statistics $\Lambda(r)$ and curves derived for three separate 50 m × 50 m (0.25 ha), 0.5 m spatial resolution LiDAR-derived CHMs..... 141

Figure 4.6. Pattern of pairwise correlations (R2) between log-transformed quantiles of laser canopy height Lhq ($0 \leq q \leq 1$) and log-transformed attributes of stand structure..... 147

Figure 4.7. Pattern of pairwise linear correlations between CC_{PCA} and CC_f at all possible height fractions f..... 149

Figure 4.8. Scatterplot of canopy height diversity (CHD) computed from LiDAR canopy height frequencies versus field-based measurements of tree height diversity (H'_h)..... 150

Figure 4.9. Patterns of pairwise linear correlations between log-transformed lacunarity statistics $\Lambda(r)$ and untransformed CC_f at all relative canopy heights f..... 151

Figure 4.10. Scatterplot and best-fit nonlinear regression line of $Lh_{0.85}$ versus Λ_{Scale}..... 153

Figure 4.11. NMS biplots summarizing the distribution of sample units, age classes, and k-means clusters in reduced ordination space..... 155

Figure 4.12. Univariate box-and-whisker plots (boxplots) summarizing the nonparametric distributional characteristics of 18 separate attributes of vertical and horizontal canopy structure..... 159

Figure 4.13. Examples of nine statistically unique classes of vertical canopy structures identified using k-means partitioning..... 161

Figure 4.14. NMS biplots summarizing the distribution of sample units, age classes, and k-means clusters in two-axis ordination space..... 163

Figure 4.15. Examples of nine statistically unique classes of horizontal canopy structure identified using k-means partitioning..... 166

Figure 4.16. NMS biplots summarizing the distribution of sample units, age classes, and k means clusters in two-axis ordination space..... 170

Figure 4.17. Illustrative examples of k-means classes derived from pooled attributes of vertical and horizontal canopy structure..... 171

Figure 4.18. Median and interquartile ranges (IQR) of canopy density (CC_f) computed by age class for all relative canopy heights f..... 172

Figure 4.19. Scatterplot of log-transformed $\Lambda(r = 1$ in grid cell units) against canopy cover..... 179

Figure 4B.1. Results of a non-hierarchical cluster analysis by k-means partitioning ($k = 8$)..... 224

Figure 4B.2. k-means classes were assigned by order of ascending LiDAR canopy height ($Lh_{0.85}$)..... 225

Acknowledgements

Many people contributed to the successful completion of this dissertation. I sincerely thank my supervisor, Olaf Niemann, for his tremendous generosity of time, intellectual encouragement, and material support that made all of this work possible; Mike Wulder for his introduction to the unlimited possibilities LiDAR; Ken Lertzman for opening my eyes to the real value of forests, and inspiring me to work towards his high standard of academic scholarship; and the rest of my supervisory committee, Mark Flaherty and Barbara Hawkins, for their valuable time and expertise over the course of the research and in the completion of the dissertation. I expressly thank my colleague and good friend Richard Fournier, who freely contributed hours of editorial review, discussion, and fieldwork in support of this research. I also gratefully acknowledge the external examiner, Geoffrey Parker, who provided a thorough and helpful review of this dissertation, and whose publications have been instrumental in my thinking about forest canopies.

The following individuals generously contributed in some unique way to the development and production of this dissertation: Charles Canham, Jing Chen, Jean-François Côté, Nandakumar Divakarannair, Glen Dunsworth, Fangliang He, Ole Heggen, Sylvain Leblanc, Don Leckie, Rafael Loos, Dimitri Marinakis, Roy Plotnick, Rick Quinn, Pamela Sallaway, Kamel Soudani, Nick Smith, Andrés Valle-Doménech, and Jean-Michel Walter. Funding for this research was provided by the British Columbia Advanced Systems Institute, British Columbia Forest Science Program, Canadian Forest Service (Pacific Forestry Centre, Graduate Student Award), Science Council of British Columbia (Graduate Research, Engineering, And Technology Scholarship), Terra Remote Sensing Inc., and Weyerhaeuser.

Last, I thank my family, especially Andrea, Niamh, Keitha, and Bill, for keeping the ship afloat through so many years of study.

To my parents, Marg and Don,
in love and gratitude

CHAPTER 1

Introduction

1.1. Background and Problem Statement

Forests are not simply storehouses of timber or wood fibre for human consumption and economic development. They represent structurally and ecologically rich habitat for an estimated 40 percent of the earth's extant species[1], and form the functional interface between the biosphere and atmosphere for some 27 percent of the earth's terrestrial surface (Ozanne et al., 2003). Forests, therefore, play a vital role in the maintenance of biological diversity (biodiversity) and the regulation of local to global scale ecosystem processes and functions (i.e., plant production, biogeochemical cycles, and biosphere–atmosphere interactions) (Parker, 1995; Perry, 1994; Chapin et al., 2002). Loss of ecologically rich old forests; simplification of forest stand and landscape structures; truncation of stand development; fragmentation of continuous forest cover; modification of natural disturbance regimes; development of extensive road networks; invasion by exotic species; pollution, and global warming are regarded as some of the most significant and immediate threats to forest biodiversity and ecosystem function, today (Voller and Harrison, 1998; Noss, 1999; Hayes et al., 2005).

Abiotic (climate, topography, soils, and disturbance), biotic (species life histories, activities, and interactions), and stochastic (random) processes, which operate continuously over a broad range of spatiotemporal scales, interact to produce forest stands and landscapes that are structurally, functionally, and biologically diverse (Spies and Turner, 1999; White and Jentsch, 2001). Current theoretical and empirical research suggests that compositional, structural, and functional heterogeneity are critical components of forests that must be maintained in order to preserve the long-term health, productivity, resilience, and biodiversity of forest ecosystems (Perry and Amaranthus, 1997; Pickett et al., 1997; Hooper et al., 2005). Present strategies for conserving

[1] The total number of recognized, living species (plants, animals, and microbes) is estimated to be around 1.5 million, with 13,000 new species identified each year. The true number of living species is expected to be closer to 10 million (Wilson, 1999).

biodiversity in managed forests are based on the notion that maintaining the full range of structural types and conditions historically present in natural forest landscapes is the best approach for assuring the long-term persistence of a broad range of native species (Franklin, 1993; Landres et al., 1999; Odion and Sarr, 2007). Implementation of silvicultural systems that retain critical habitat elements (e.g., snags, large live trees, downed wood, etc.), structures (e.g., vertical foliage diversity, horizontal patchiness, gaps, etc.), and landscape features (e.g., interior forest, habitat connectivity, etc.); establishment of riparian, old growth, and other ecosystem reserves; and the structural restoration of managed second-growth forests have all been identified as possible ways to conserve biodiversity in forest landscapes (Lindenmayer and Franklin, 2002; Cary, 2003; Kremsater et al. 2003; Schulte et al., 2006).

Forest structure is widely regarded as a unifying variable and key ecological indicator in conservation biology, ecosystem science, and sustainable forest management, because of its direct link to habitat (biodiversity), ecosystem function, and timber production (O'Hara, 1998; Spies, 1998; Noss, 1999; Lindenmayer et al., 2000; Franklin et al., 2002). At the plot level, structure is defined by the size, shape, number, and variety of all aboveground, living or dead vegetation components (e.g., foliage, branches, boles, shrubs, snags, logs, etc.) and their organizational properties in space and time (Spies, 1998). 'Stand structure' is the term most often used to describe plot-level tree diameter and height distributions, while 'canopy structure' refers more specifically to the finer-scale details contributed by foliage, twigs, and branches, and their three-dimensional (3-D) spatial distributions (Parker, 1995). At the landscape level, structure is alternatively characterized by the number, size, shape, arrangement, and dynamics of forest patches (i.e., areas of forest cover that are relatively homogeneous in composition, soils, productivity, age, and disturbance history), and the contrast and connectivity between them (Turner et al., 2001).

Airborne and satellite optical remote sensing (including aerial photography) have played an important role in stand- and landscape-level descriptions of forest structure in the horizontal domain (Wulder and Franklin, 2003); however, even at very high spatial (<1 metre in horizontal ground units) resolutions, these instruments are limited in their ability to characterize the internal structure of forests. The internal organization of forest

stands, particularly their vertical canopy structure, is closely associated with gradients of microclimates (e.g., light, temperature, humidity, moisture, etc.), materials (e.g., phytomass, nutrients, gases, water, pollutants, etc.), processes (e.g., light capture, photosynthesis, throughfall, evapotranspiration, etc.), and organisms (e.g., epiphytes, birds, insects, etc.), and therefore a strong determinant and correlate of biodiversity and ecosystem function (Brokaw and Lent, 1999; Parker et al., 2004a; Winchester, 2006).

Recent advances in ground-based (in situ) remote sensing (i.e., hemispherical optical sensors [Fig. 1.1], range-finding lasers, and 3-D imaging lasers) and airborne discrete-return and full-waveform LiDAR (Light Detection and Ranging) technologies have made it possible to study the fine-spatial-scale, multidimensional structure of forest canopies within plots and over relatively broad areas at extremely high spatial resolutions (Lefsky et al., 2002; Fournier et al., 2003; Parker et al., 2004b; Leblanc et al., 2005; Omasa et al., 2007). These technologies show strong potential to measure the kinds of structure (habitat) variables that are relevant to organisms, ecosystems, and resource managers (Vierling et al., in press); however, further methodological and application development are required before they can be readily deployed in an operational setting.

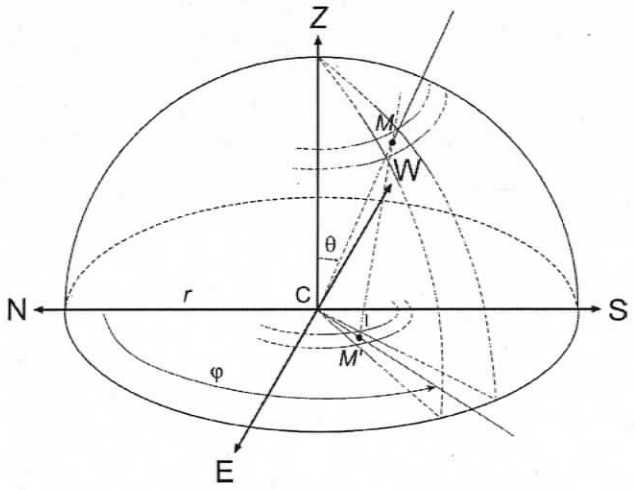

FIGURE 1.1. A hemispherical optical sensor (radiation or camera) indirectly measures the angular distribution of canopy elements within a hemispherical (180°) object region. The locations of discrete objects in the hemisphere (*M*) are defined by angular distances in the vertical plane (zenith angle θ) and horizontal plane (azimuth angle φ). A fisheye camera projects these objects onto a 2-D image plane (*M'*) using a lens-specific geometric distortion model. (Graphic courtesy of Dr. Jean-Michel Walter, Université Louis Pasteur).

1.2. Research Objectives and Questions

The most significant challenge facing forest managers today is no longer deciding what part of the forest to remove, but rather deciding what should remain. The primary and overarching goal of this dissertation research is to contribute to the development of novel remotely sensed forest measurements that are relevant to organisms and ecosystems, and much needed by forest scientists and managers to recognize and retain the key elements and patterns of forest structure that are crucial for the conservation of forest biodiversity. In this dissertation, I ask and attempt to answer the following research questions:

- How can we capitalize on the rich spatial information captured by hemispherical canopy photographs? Can spatial statistics adequately describe the scale-dependent spatial heterogeneity inherent in natural forest canopies? Do these spatial indices help to improve the prediction of other conventional structural descriptors?
- How do we apply the lessons learned with hemispherical canopy photographs to simulated 3-D forest canopies viewed from above? How can we conceptualize and quantify the scale-dependent heterogeneity of forest canopy structure using spatially continuous measurements of canopy surface height? Can the same spatial statistics used to describe scale-dependent heterogeneity in binary sets be applied to continuous random fields? How might these techniques be applied in a real world setting?
- How can an airborne discrete-return LiDAR be used to characterize fine-scale vertical and horizontal patterns of canopy structure in coastal *Pseudotsuga-Tsuga* (Douglas-fir/western hemlock) forests? What are the key attributes of canopy structure that separate and define young, mature, and old-growth *Pseudotsuga-Tsuga* forests? Are these age-class differences consistent with the structural characteristics, patterns, and dynamics predicted by generalized, process-based models of forest stand development for Pacific Coast *Pseudotsuga-Tsuga* forests of western North America? Is it possible to partition sample units and landscapes into other ecologically relevant classes based entirely on the fine-spatial-scale measurements of canopy structure derived from an airborne LiDAR?

1.3. Scope and Format of the Dissertation

I limit my research focus to fine-spatial-scale measurements of forest canopy structure based on two main assumptions: (1) that the 'canopy' is important habitat for many known and unknown species (Winchester, 2006), and the primary focal site of complex interactions between plants and the physical environment (Parker, 1995); (2) that conventional airborne and satellite optical remote sensing techniques are already well suited to coarser-scale characterizations of stand and landscape structure (Wulder et al., 2004). I make use of two separate perspective views to quantify forest canopy structure in this research. First, I employ skyward-looking, hemispherical canopy photography from within the forest stand to describe the view-angle-dependent dispersion of foliage, branches, boles, and gaps. This perspective view has a long history of use in the study of understory light environments, microclimate, stand dynamics, and canopy structure (Canham et al., 1994; Parker et al., 2002; Leblanc et al., 2005). Second, I apply the more familiar remote sensing view from above to characterize the vertical and horizontal patterns of canopy structure found in simulated and real forest canopies. I do not, however, attempt to integrate above- and below-canopy perspectives, except when dealing with vertically projected estimates of canopy cover.

This dissertation is composed of five chapters that describe three related, standalone research projects. Chapter 1 provides a broad overview and introduction to the research, including a formal statement of the problem, research objectives and questions, and scope and format of the thesis. Chapters 2, 3, and 4 present three separate, self-contained research studies each with their own sets of objectives, methods, findings, and conclusions. Last, Chapter 5 summarizes the key findings and future research directions.

In the first of these three studies (Chapter 2), I demonstrate how lacunarity analysis can be used to derive estimates of element clumping from sequences of black (canopy) and white (gap) pixels extracted at specific view angles in hemispherical (fisheye) canopy photographs. Element clumping is a spatially integrated measure of the spatial nonrandomness or heterogeneity found at various organizational levels (i.e., foliage, branch, bole, and crown) in forest canopies. This parameter is strongly view-angle and scale dependent, and plays an important role in controlling light capture and

penetration in forest canopies. I further show how estimates of element clumping can be used to improve optical measurements of leaf area index.

In the second study (Chapter 3), I borrow and extend the lacunarity approach presented in Chapter 2 to measure the scale-dependent spatial heterogeneity embedded in 2-D arrays (models) of simulated canopy heights. I use simulated canopies rather than real ones as a quick way to generate a large, well-documented dataset covering a broad range of canopy surface patterns. I also illustrate and explain the statistical behaviour of lacunarity as a potentially useful descriptor of spatial heterogeneity in forest canopy research. Finally, I suggest practical applications of this technique in the area of sustainable forest management.

In the final study (Chapter 4), I apply the techniques and lessons learned in the previous two studies to develop a conceptual and methodological framework for quantifying, classifying, and comparing fine-scale vertical and horizontal patterns of forest canopy structure. I demonstrate this methodology using a discrete-return LiDAR dataset collected over managed and natural, very young to old-growth *Pseudotsuga-Tsuga* forests on Vancouver Island, British Columbia. I also examine age-related developmental changes in canopy structure at decadal and century time scales using a pseudo 'space-for-time substitution' sampling approach. Finally, I show how non-hierarchical cluster analysis by *k*-means partitioning can be used to generate an unsupervised structure-based classification of these diverse multivariate descriptors of forest canopy structure.

1.4. References

Brokaw, N.V.L., Lent, R.A., 1999. Vertical structure. In: Hunter, M.L. (Ed.), Maintaining Biodiversity in Forest Ecosystems. Cambridge University Press, New York, NY, pp. 373–399.

Canham, C.D., Finzi, A.C., Pacala, S.W., Burbank, D.H., 1994. Causes and consequences of resource heterogeneity in forests: interspecific variation in light transmission by canopy trees. Canadian Journal of Forest Research 24, 337–349.

Carey, A.B., 2003. Biocomplexity and restoration of biodiversity in temperate coniferous forests: inducing spatial heterogeneity with variable-density thinning. Forestry 76, 127–136.

Chapin, III, F.S., Matson, P.A., Mooney, H.A., 2002. Principles of terrestrial ecosystem ecology. Springer-Verlag, New York, NY.

Fournier, R.A., Mailly, D., Walter, J-M. N., Soudani, K., 2003. Indirect measurement of forest canopy structure from *in situ* optical sensors. In: Wulder, M.A., Franklin, S.E. (Eds.), Remote Sensing of Forest Environments: Concepts and Case Studies. Kluwer Academic Press, Norwell, MA, pp. 77–114.

Franklin, J.F., 1993. Preserving biodiversity: species, ecosystems or landscapes? Ecological Applications 3, 202–205.

Franklin, J.F., Spies, T.A., Van Pelt, R., Carey, A.B., Thornburgh, D.A., Berg, D.R., Lindenmayer, D.B., Harmon, M.E., Keeton, W.S., Shaw, D.C., Bible, K., Chen, J., 2002. Disturbances and structural development of natural forest ecosystems with silvicultural implications, using Douglas-fir forests as an example. Forest Ecoology and Management 155, 399–423.

Hayes, J.P., Schoenholtz, S.H., Hartley, M.J., Murphy, G., Powers, R.F., Berg, D., Radosevich, S.R., 2005. Environmental consequences of intensively managed forest plantations in the Pacific Northwest. Journal of Forestry 103, 83–87.

Hooper, D.U., Chapin, III, F.S., Ewel, J.J., Hector, A., Inchausti, P., Lavorel, S., Lawton, J.H., Lodge, D.M., Loreau, M., Naeem, S., Schmid, B., Setälä, H., Symstad, A.J., Vandermeer, J., Wardle, D.A., 2005. Effect of biodiversity on ecosystem functioning: a consensus of current knowledge. Ecological Monographs 75, 3–35.

Kremsater, L., Bunnell, F., Huggard, D., and Dunsworth, G. 2003. Indicators to assess biodiversity: Weyerhaeuser's coastal British Columbia forest project. Forestry Chronicle 79, 590–601.

Landres, P.B., Morgan, P., Swanson, F.J., 1999. Overview of the use of natural variability concepts in managing ecological systems. Ecological Applications 9, 1179–1188.

Leblanc, S.G., Chen, J.M., Fernandes, R., Deering, D.W., Conley, A., 2005. Methodology comparison for canopy structure parameter extraction from digital hemispherical photography in boreal forests. Agricultural and Forest Meteorology 129, 187–207.

Lefsky, M.A., Cohen, W.B., Parker, G.G., Harding, D.J., 2002. Lidar remote sensing for ecosystem studies. BioScience 52, 19–30.

Lindenmayer, D.B., Franklin, J.F., 2002. Conserving forest biodiversity: a comprehensive multiscaled approach. Island Press, Washington, DC.

Lindenmayer, D.B., Margules, C.R., Botkin, D.B., 2000. Indicators of biodiversity for ecologically sustainable forest management. Conservation Biology 14, 941–950.

Noss, R.F., 1999. Assessing and monitoring forest biodiversity: A suggested framework and indicators. Forest Ecology and Management 115, 135–146.

Odion, D.C., Sarr, D.A., 2007. Managing disturbance regimes to maintain biological diversity in forested ecosystems of the Pacific Northwest. Forest Ecology and Management 246, 57–65.

O'Hara, K.L., 1998. Silvicultural for structural diversity: a new look at multiaged systems. Journal of Forestry 96, 4–10.

Omasa, K., Hosoi, F., Konishi, A., 2007. 3-D lidar imaging for detecting and understanding plant responses and canopy structure. Journal of Experimental Botany 58, 881–898.

Ozanne, C.M.P., Anhuf, D., Boulter, S.L., Keller, M., Kitching, R.L., Korner, C., Meinzer, F.C., Mitchell, A.W., Nakashizuda, T., Silva Das, P.L., Stork, N.E., Wright, S.J., Yoshimura, M., 2003. Biodiversity meets the atmosphere: a global view of forest canopies. Science 301, 183–186.

Parker, G.G., 1995. Structure and microclimate of forest canopies. In: Lowman, M.D., Nadkarni, N.M. (Eds.) Forest Canopies. Academic Press, Orlando, FL, pp. 73–98.

Parker, G.G., Davis, M.M., Chapotin, S.M., 2002. Canopy light transmittance in Douglas-fir/western hemlock stands. Tree Physiology 22, 147–157.

Parker, G.G., Harding, D.J., Berger, M.L., 2004b. A portable lidar system for rapid determination of forest canopy structure. Journal of Applied Ecology 41, 755–767.

Parker, G.G., Harmon, M.E., Lefsky, M.A., Chen, J., Van Pelt, R., Weiss, S.B., Thomas, S.C., Franklin, J.F., 2004a. Three-dimensional structure of an old-growth *Pseudotsuga-tsuga* canopy and its implications for radiation balance, microclimate, and gas exchange. Ecosystems 7, 440–453.

Perry, D.A., 1994. Forest ecosystems. The John Hopkins University Press, Baltimore, MD.

Perry, D.A., Amaranthus, M.P., 1997. Disturbance, recovery, and stability. In: Kohm, K.A. and Franklin, J.F. (Eds.), Creating a forestry for the 21st century. Island Press, Washington D.C., pp. 31–56.

Pickett, S.T.A., Ostfield, R.S., Shachak, M., Likens, G.E., (Editors), 1997. The ecological basis of conservation. Chapman & Hall, New York, NY.

Riaño, D., Valladares, F., Condés, S., Chuvieco, E., 2004. Estimation of leaf area index and covered ground from airborne laser scanner (Lidar) in two contrasting forests. Agricultural and Forest Meteorology 124, 269–275.

Schulte, L.A., Mitchell, R.J., Hunter, Jr., M.L., Franklin, J.F., McIntyre, R.K., Palik, B.J., 2006. Evaluating the conceptual tools for forest biodiversity conservation and their implementation in the U.S. Forest Ecology and Management 232, 1–11.

Spies, T.A., 1998. Forest structure: A key to the ecosystems. In: Trofymow, J.A., MacKinnon, A. (Eds.), Structure, Process, and Diversity in Successional Forests of Coastal British Columbia. Northwest Science 72 (Special Issue No. 2), 34–39.

Spies, T.A., Turner, M.G., 1999. Dynamic forest mosaics. In: Hunter Jr., M.L. (Ed.), Maintaining Biodiversity in Forest Ecosystems. Cambridge University Press, New York, NY, pp. 95–160.

Turner, M.G., Gardner, R.H., O'Neill, R.V., 2001. Landscape ecology in theory and practice. Springer-Verlag, New York, NY

Vierling, K.T., Vierling, L.A., Gould, W.A., Martinuzzi, S., Clawges, R.M., 2007. Lidar: shedding new light on habitat characterizations and modeling. Frontiers in Ecology and Environment, in press.

Voller, J., Harrison, S., (Editors), 1998. Conservation Biology Principles for Forested Landscapes. UBC Press, Vancouver, B.C.

White, P.S., Jentsch, A., 2001. The search for generality in studies of disturbance and ecosystem dynamics. Progress in Botany 62, 399–450.

Wilson, E.O., 1999. The diversity of life. W.W. Norton & Company, New York, NY.

Winchester, N.N., 2006. Ancient temperate rain forest research in British Columbia. The Canadian Entomologist 138, 72–83.

Wulder, M.A., Franklin, S.E., (Editors), 2003. Remote Sensing of Forest Environments: Concepts and Case Studies. Kluwer Academic Press, Norwell, MA.

Wulder, M.A., Hall, R.J., Coops, N.C., Franklin, S.E., 2004. High spatial resolution remotely sensed data for ecosystem classification. Bioscience 54, 511–521.

CHAPTER 2

Characterization of Angle-Dependent Element Clumping and Leaf Area Index in Spatially Heterogeneous Forest Canopies Using Hemispherical Photography and Lacunarity Analysis

2.0 Abstract

Optical measurements of leaf area index (LAI) obtained by gap fraction analysis using the Beer-Lambert (Poisson) model are well known to underestimate stand LAI when vegetative canopies display distinct patterns of aggregation at one or more spatial scales. Past studies show that the amount of this underestimation may be substantially reduced or even eliminated by incorporating a zenith-angle-dependent clumping index $\Omega(\theta)$ into the Beer-Lambert equation. Here we present a new, lacunarity-based clumping method that can be used to derive estimates of $\Omega(\theta)$ directly from sequences (sets) of black (canopy) and white (gap) pixels extracted at specific view angles θ in hemispherical (fisheye) canopy photographs. We compare the performance of this new technique with three other published clumping indices using well-documented simulated and real fisheye canopy photosets as validation. Our results show that the lacunarity-based method consistently produced the best estimates of stand LAI in each of the three experimental forest sites: 4.89 m^2/m^2 (LAI = 6.80 m^2/m^2; black spruce), 3.95 m^2/m^2 (LAI = 4.08 m^2/m^2; Scots pine), and 3.94 m^2/m^2 (LAI = 6.06 m^2/m^2; sugar maple). We suggest two reasons why photo-based estimates of $\Omega(\theta)$ were unable to completely eliminate the disparity between optical LAI and the LAI measured by allometrics or litterfall collection. First, the aggregation of foliage into coarser-scale spatial entities (i.e., branches, whorls, crowns, and stands) produces areas within the photo that are entirely opaque and thus devoid of the canopy gaps needed to predict LAI. When this occurs, optical methods only measure the 'imaginary' surface area of foliage clumps and not the LAI found within them. Second, estimates of $\Omega(\theta)$ derived from 1-D binary sets are

unlikely to fully describe the complex, multiscale patterns of spatial clumping that exist within the original three dimensions of canopy space. Integration of optical LAI between the limits $0° \leq \theta \leq 90°$ following Miller's theorem is often prescribed when the projection coefficient $G(\theta)$ is unknown. However, we found that strict adherence to Miller's theorem was never possible due to the short length of sample transects at $\theta < 10°$ and lack of canopy gaps at $\theta > 70°$. We alternatively chose to estimate LAI at 57.5°, but found this approach to be biased when the vertical distribution of foliage and clump angles deviated from spherical (random). Further validation work is required to determine the adequacy of photo-based clumping and LAI measurement techniques in other closed and discontinuous canopies.

2.1. Introduction

Leaf area is considered a key attribute of forest canopy structure, because of its direct link to light interception, photosynthesis, and forest productivity; energy and material cycles; thermal cover and habitat, and as the primary surface of reflectance and absorptance in many terrestrial remote sensing applications (Bonan, 1993; Spanner et al., 1994; Parker, 1995; Gower et al., 1999; Asner et al., 2003). Leaf area is most often quantified by a dimensionless index (LAI) that describes the amount of leaf area per unit of underlying ground surface area. The precise definition of LAI varies widely in the literature (Barclay and Goodman, 2000); however, 'one-half the total leaf surface area (m^2) per unit of horizontal ground surface area (m^2)' has been demonstrated theoretically to be the most practical and ecologically relevant definition used to describe forest canopies composed of either flat or non-flat leaves (Lang, 1991; Chen and Black, 1992; Fassnacht et al., 1994; Stenberg et al., 1994).

Numerous direct (i.e., destructive sampling and litterfall collection), semi-direct (i.e., vertical- and inclined-point-quadrat sampling), and indirect (i.e., optical sensors) techniques have been developed to measure LAI in forest canopies (Gower et al., 1999; Bréda, 2003; Jonckheere et al., 2004). Indirect methods employ linear or hemispherical optical instruments (i.e., quantum sensors, pyranometers, and hemispherical canopy photography) to measure solar radiation transmittance or gap frequency data at single or

multiple view angles beneath the canopy, and have been a popular choice for rapid LAI estimation due to their relative accuracy, non-destructive nature, and ease of use (Welles and Cohen, 1996; Fournier et al., 2003). Optically derived estimates of solar radiation transmittance or gap frequency are generally referred to as the canopy 'gap fraction' (Welles and Norman, 1991).

The theoretical relationship between the canopy gap fraction and LAI has been widely described for homogenous and heterogeneous forest canopies using a specialized formulation of the Beer-Lambert equation known also as the 'Markov' model (Nilson, 1971; Chen et al., 1997; Kucharik et al., 1999; Weiss et al., 2004):

$$P(\theta) = \exp[-G(\theta)\Omega(\theta)L_t/\cos(\theta)] \qquad (2.1)$$

where $P(\theta)$ is the gap fraction, or more formally the statistical probability of an infinitely narrow beam of light successfully penetrating the canopy at view (zenith) angle θ (Welles and Norman, 1991); $G(\theta)$ is the mean projection coefficient of unit leaf area (i.e., the ratio of projected needle area to one-half the total needle surface area) on the plane oriented perpendicular to θ (Chen and Cihlar, 1995; Stenberg, 2006); $\Omega(\theta)$ is a clumping index that defines the spatial dispersion of canopy elements (foliage and woody structures) at all spatial scales within the optical sensor's field of view (FOV) at θ (Chen et al., 1997; Kucharik et al., 1999); L_t is one-half the total plant (including foliage, branches, and boles) surface area per unit ground surface area (Chen and Black, 1992), and $1/\cos(\theta)$ is the relative pathlength of a ray of light passing through the canopy at θ.

The Beer-Lambert equation (also commonly known as the 'Poisson' model) is most often parameterized under the assumption that foliage and other support structures (i.e., twigs, branches, and boles) are spatially dispersed both randomly and independently of each other within the optical sensor's FOV (Nilson, 1999). When this assumption is violated, the canopy gap fraction will always appear larger or smaller than what would theoretically be expected under the condition of complete spatial randomness (Lang and Xiang, 1986). Forest canopies, especially those of temperate and boreal conifer forests, naturally exhibit distinct patterns of spatial aggregation or clumping at many organizational levels (Oker-Blom et al., 1991; Cescatti, 1998). At the lowest level of organization or finest spatial scale of observation, individual needles are clumped within

shoots (twigs) of varying size, shape, and density (Smolander et al., 1994; Stenberg, 1996). In turn, shoots are spatially arranged into progressively coarser-scale structures, such as branches, whorls, crowns, and ultimately into neighbourhoods of individual crowns (Cooper, 1961; Parker, 1995; Fournier et al., 1997). Canopies that display marked clumping at one or more of these spatial scales will allow substantially more light to penetrate at a given LAI than spatially random canopies (Baldocchi et al., 1985; Law et al., 2001). As a result, optical sensors routinely underestimate LAI in conifer forests (Gower et al., 1999). The full magnitude of this underestimation, however, is tempered to some extent by the added shading contributed by branches and boles. It is also theoretically possible that optical methods may overestimate stand LAI when canopy elements are spatially over-dispersed (i.e., uniformly or regularly distributed), although such occurrences are rarely reported in the literature (e.g., Whitford et al., 1995).

Five different techniques have been proposed to improve the accuracy of optically derived estimates of LAI collected in spatially heterogeneous forest canopies. First, alternative gap-probability models such as the negative and positive binomial models have been used in place of the Poisson model to improve LAI estimates in clumped and uniform canopies, respectively (Nilson, 1971; Baldocchi et al., 1985; Neumann et al., 1989; Chason et al., 1991). Second, Lang and Xiang (1986) recommended averaging the logarithm of gap fractions sampled at finer spatial scales where canopy elements are considered more likely to be randomly dispersed (e.g., Fassnacht et al., 1994; Planchais and Pontailler, 1999; van Gardingen et al., 1999). Third, additional attributes of stand structure such as canopy cover, tree height, crown depth, stand density, relative density, and indices of tree dispersion have been incorporated into the Beer-Lambert model to explicitly account for influences of crown size, crown porosity, stem density, and inter-crown spacing on the canopy gap fraction and LAI (Smith, 1993; Nilson, 1999; Stenberg et al., 2003; Nilson and Kuusk, 2004). Fourth, a single correction factor or linear regression equation derived from the empirical relationship between direct (destructive sampling and allometrics) and optical LAI measurements has been applied to optical LAI data to compensate for measurement biases related to spatial clumping and inclusion of the woody area fraction (Gower and Norman, 1991; Smith et al., 1993; Deblonde et al., 1994; Fassnacht et al., 1994; Barclay and Trofymow, 2000). Last, specialized sensors

(e.g., Tracing Radiation and Architecture of Canopies (TRAC) and Multiband Vegetation Imager (MVI)) and supporting analytical theory have been devised to estimate $\Omega(\theta)$ for insertion in the Beer-Lambert model (Chen and Cihlar, 1995; Chen et al., 1997; Kucharik et al., 1997).

Although each of these methods has generally proven helpful in past studies, some appear more beneficial, practical, and easily replicated than others. The negative binomial model, for instance, is rarely applied because the required clumping parameter (ΔL) has been difficult to estimate without existing empirical data (Nilson, 1971; Baldocchi et al., 1985; Neumann et al., 1989). The 'finite-length averaging' technique proposed by Lang and Xiang (1986) is known to be sensitive to the segment length (or scale) over which gap fractions are integrated (van Gardingen et al., 1999; Walter et al., 2003; Leblanc et al., 2005); however, there are still no dependable, objective criteria that exist to help determine an optimal sampling scale. Recent modifications to the Beer-Lambert model by Nilson (1999), Stenberg et al. (2003), and Nilson and Kuusk (2004) show substantial future promise, but also require a large number of additional, more difficult-to-measure attributes of stand structure, as well as more intensive gap fraction sampling to parameterize the model. Application of a single correction factor or linear equation has generally been considered the least reliable solution because of the presumed linearity between direct and optical LAI measurements (Fassnacht et al., 1994; Smolander and Stenberg, 1996; Stenberg et al., 2003). Finally, the derivation and inclusion of $\Omega(\theta)$ in the Beer-Lambert model has received significant research attention over the past decade, and is now widely accepted as common practice and currently the best way to correct optical LAI data (Gower et al., 1999; Bréda, 2003; Jonckheere et al., 2004; Chen et al., 2006).

Recent advances in optical LAI measurement theory and methods (van Gardingen et al., 1999; Walter et al., 2003; Leblanc et al., 2005) suggest that hemispherical (fisheye) canopy photography may offer several advantages over traditional light-sensor-based technologies (e.g., TRAC) for indirect LAI estimation. First, fisheye photos provide a permanent, two-dimensional (2-D) spatial record of the size, shape, and distribution of all canopy components (i.e., leaves, woody structures, and gaps). Second, the ability to detect small canopy gaps in fisheye photos is constrained only by image quality and

resolution, and not by the penumbral effect that can seriously limit the retrieval of small gaps from sunfleck data (Chen and Cihlar, 1995). Third, because light-sensor-based technologies such as TRAC depend on the solar beam as a probe, sunfleck measurements are often spatially restricted to only a very limited portion of the canopy. Fisheye photos, on the other hand, allow analysts to extract gap-size, $P(\theta)$, and $\Omega(\theta)$ at any θ or azimuth angle within a 180° hemispherical FOV. This distinction is important because these attributes are well known to be strongly angle- (zenith and azimuth) and scale-dependent in spatially heterogeneous forest canopies (Black et al., 1991; Chen and Black, 1991; Kucharik et al., 1999; Walter et al., 2003). Last, fisheye photos can be readily used to model a broad range of canopy attributes (e.g., gap-light transmittance, sunfleck-frequency distribution, gap fraction, and canopy openness; Frazer et al., 2000; Walter, 2002), thereby eliminating the need for multiple instruments, field conditions, sampling designs, and site visits.

The main purpose of this article is to present a new lacunarity-based method that we developed for the retrieval of $\Omega(\theta)$ directly from fisheye canopy photos. Lacunarity, as a concept and metric, finds its earliest roots in fractal mathematics (Mandelbrot, 1983); however, it is now widely employed in many other applied sciences as a general measure of spatial heterogeneity to describe the scale-dependent texture of fractal, multifractal, and nonfractal geometric patterns (Kirkpatrick and Weishampel, 2005; Frazer et al., 2005; Saunders et al., 2005). Here, we show how lacunarity analysis can be used to quantify the scale-dependent spatial nonrandomness present in binary sets of black (canopy) and white (gap) pixels extracted from fisheye canopy photos at known view angles. We have four specific objectives in this paper:

(1) To briefly illustrate and describe the application of lacunarity analysis using six simulated binary sets with different scale-dependent spatial patterns.

(2) To outline the derivation of a new angle-dependent clumping index $\Omega_{LAC}(\theta)$ that can be used directly in the Beer-Lambert model (Eq. 2.1) to compensate for the nonrandom spatial distribution of canopy elements.

(3) To compare lacunarity-based estimates of $\Omega(\theta)$ and LAI retrieved from simulated and real photosets with results obtained using three other published

clumping indices by Chen and Cihlar (1995), Walter et al. (2003), and Leblanc et al. (2005).

(4) To illustrate and discuss the angular-dependence of optical LAI measurements.

2.2. Lacunarity as a Scale-dependent Measure of Spatial Nonrandomness

2.2.1. Definition and measurement of lacunarity

Lacunarity is formally defined as the scale-dependent deviation of a geometrical object or pattern from translational invariance or homogeneity (Gefen et al., 1983; Cheng, 1997). Spatial patterns that exhibit 'low lacunarity' generally have small gaps, appear fine-grained, and are homogeneous with respect to the size-frequency and spatial distributions of gaps. In contrast, spatial patterns that have large gaps, look coarse-grained, and display substantial heterogeneity in the size-frequency and spatial distributions of gaps are described as being 'highly lacunar' (Plotnick et al., 1996; Blumenfeld and Mandelbrot, 1997). Lacunarity analysis is explicitly a multiscale technique, because pattern is well known to be strongly dependent on the spatial scale (grain and extent) of observation (Plotnick et al., 1996; Dale, 1999). Lacunarity has been estimated in several ways; however, many use the 'gliding-box' algorithm because of its simplicity and computational efficiency (Allain and Cloitre, 1991).

The gliding-box algorithm requires five main steps to compute the lacunarity of binary sets composed of 1s (occupied) and 0s (unoccupied) (Plotnick et al., 1993, 1996; Cheng, 1997; Dale, 2000). First, a gliding or moving window of box size r (in gridcell units) is shifted one position at a time along the entire length n (in gridcell units) of the set. At each gridcell position i along the set, the sum or box mass s of gridcell values x_j contained within the box of size r is computed until all positions i along the set have sampled. The result is a frequency distribution of box masses $n(s,r)$ sampled at r. Second, each box mass s of the frequency distribution $n(s,r)$ sampled at box size r is divided by the total number of sampled boxes of size r to generate a probability distribution $Q(s,r)$.

Third, the first and second statistical moments of the probability distribution $Q(s,r)$ are computed (Cheng, 1997; Dale, 1999):

$$Z_Q^{(1)}(r) = \frac{1}{(n+1-r)} \sum_{i=1}^{n+1-r} \sum_{j=1}^{i+1-r} x_j \tag{2.2}$$

$$Z_Q^{(2)}(r) = \frac{1}{(n+1-r)} \sum_{i=1}^{n+1-r} \left(\sum_{j=1}^{i+r-1} x_j \right)^2 \tag{2.3}$$

Fourth, lacunarity at r is estimated by dividing the second moment of the probability distribution $Q(s,r)$ by the square of the first moment (Plotnick et al., 1996):

$$\Lambda(r) = \frac{Z_Q^{(2)}(r)}{\left[Z_Q^{(1)}\right]^2} = 1 + \frac{\sigma_Q^2(r)}{\left[Z_Q^{(1)}\right]^2} \tag{2.4}$$

where $\sigma_Q^2(r)$ and $Z_Q^{(1)}$ are, respectively, the sample variance and mean of the probability function $Q(s,r)$. Last, repeating the lacunarity calculations at box sizes $1 \leq r \leq n$ reveals a distinct pattern of variation in the logarithm of $\Lambda(r)$ when plotted against logarithm of r.

2.2.2. The scale-dependency and interpretation of $\Lambda(r)$

Three general patterns of spatial dispersion are recognized in binary sets composed of occupied (black = 1) and unoccupied (white = 0) sites: random, uniform, and aggregated (Dale, 1999). Random patterns arise when occupied sites occur randomly and independently of one another along the length of a set (e.g., set A, Fig. 2.1). Uniform and aggregated patterns, in contrast, are neither random nor independent and exhibit characteristics of spatial dependence or interaction. For example, uniform patterns form a 'regular' spacing of occupied sites, where the presence of one occupied site reduces the probability that another will be found in close proximity to it (e.g., set B, Fig. 2.1). Aggregated patterns, on the other hand, appear 'clumped', and the presence of an occupied site increases the probability that another will be found close by (e.g., sets C-F, Fig. 2.1). Spatial pattern, however, is strongly scale-dependent and those that appear random, uniform, or aggregated at one measurement scale may be different at finer or coarser scales (Plotnick et al., 1996; Dale, 2000).

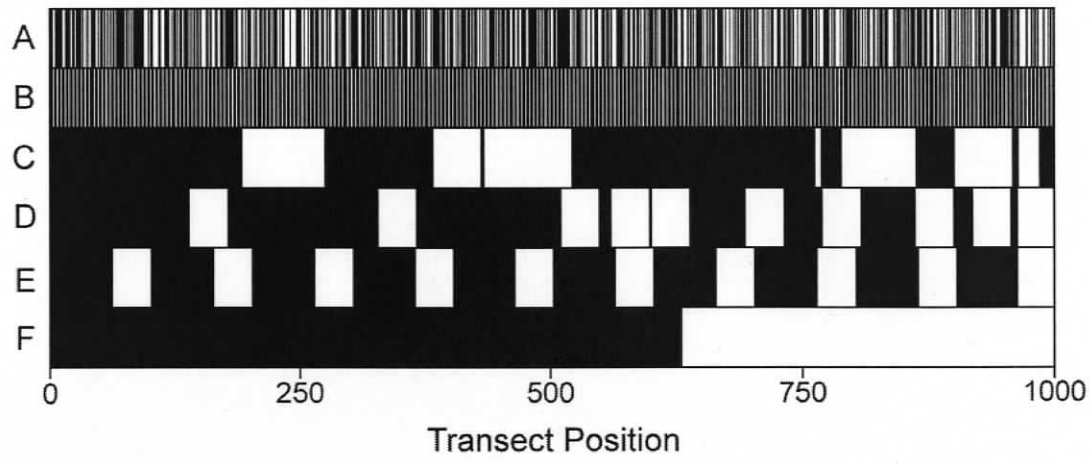

FIGURE 2.1. Simulated binary sets displaying six unique scale-dependent patterns of foliage (black) and gap (white) dispersion: (A) random, (B) uniform, (C) randomly distributed gaps of random width, (D) randomly distributed gaps of equal width, (E) uniformly distributed gaps of equal width, and (F) single gap. Each set has the same number of occupied sites (a = 630), total length (n = 1000), and density p (a/n = 0.63).

Scatterplots of the logarithm of $\Lambda(r)$ against the logarithm of r reveal the scale-dependent spatial structure, heterogeneity, and nonrandomness associated with each of the binary sets described below (Fig. 2.2). The magnitude of $\Lambda(r)$ is a measure of the spatial heterogeneity found in the set at scale r (Plotnick et al., 1996). For example, values of $\Lambda(r)$ that are equal or close to 1 indicate translational invariance or spatial homogeneity at r, and increasingly larger values of $\Lambda(r)$ denote increasing spatial heterogeneity. Lacunarity curves A to F show an overall decline in $\Lambda(r)$ with increasing r; however, the rate and pattern of this decline differ according to the set's scale-dependent spatial structure or geometry. All six curves share the same X and Y intercepts, because each set has the same number of occupied sites ($a = 630$), total length ($n = 1000$), and pattern density ($p = a/n = 0.63$). The magnitude of $\Lambda(r)$ at $r = 1$ will vary inversely with p, since $\Lambda(1)$ is equal to $1/p$ (Plotnick et al., 1996).

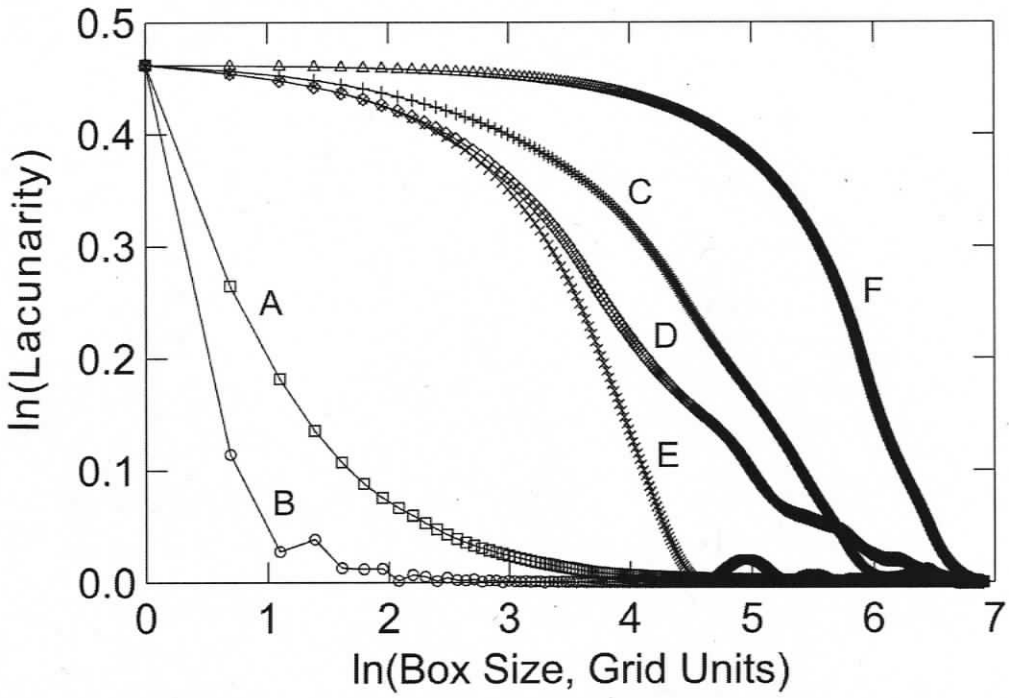

FIGURE 2.2. Natural logarithm of $\Lambda(r)$ plotted against the natural logarithm of box size r. Lacunarity curves A to F correspond directly to binary sets A to F in Fig 2.1. Lacunarity curves that lie above or fall below $\Lambda(r)$ expected under CSR (curve A) indicate the kind, magnitude, and scale of nonrandomness. For example, curve B falls substantially below CSR and thus indicates spatial uniformity across all measurement scales. Curves E, D, C, and F, on the other hand, all lie above CSR and display, in ascending order, increasing quantities and scales of spatial aggregation or clumping.

Lacunarity curves generated for sets A and B approach translational invariance ($\Lambda(r) = 1$) more rapidly than curves representing the coarser-grained sets C to F. The steepest decline in $\Lambda(r)$ with increasing r occurs when discrete occupied sites are regularly spaced (set B). When occupied sites are dispersed randomly and independently of one another, as in set A, the decline in $\Lambda(r)$ occurs at a rate predicted by the Binomial Theorem (Dale, 2000):

$$\Lambda_{CSR}(r) = 1 + 1/rp - 1/r \qquad (2.5)$$

where $\Lambda_{CSR}(r)$ is the expected lacunarity statistic at box size r under the condition of complete spatial randomness (CSR), and p is the pattern density of the binary set. Lacunarity curves that lie above or fall below $\Lambda(r)$ expected under CSR (set A) indicate

the kind, magnitude, and scale of nonrandomness. For example, curves E, D, C, and F all lie above CSR and display, in ascending order, increasing quantities and scales of spatial aggregation. Curve E exhibits the least amount of coarse-scale aggregation, because gaps are relatively small, homogeneous in size, and uniformly dispersed across the set. Set F, on the other hand, is composed of one large gap, and displays the greatest amount of aggregation at all spatial scales. Curve B falls substantially below CSR and therefore indicates the presence of spatial uniformity at all measurement scales.

2.2.3. A lacunarity-based clumping index $\Omega_{LAC}(\theta)$

The conifer shoot or twig is generally considered to be the minimum resolvable canopy object or element size in gap-fraction and gap-size analyses, because optical instruments are unable to capture the infinitely small gaps that separate individual needles at these finer scales of spatial organization (Gower and Norman, 1990; Chen and Cihlar, 1995). Broad leaves, however, because of their relatively large size and arrangement, generally represent the basic foliage unit in deciduous stands (Baldocchi et al., 1985). $\Omega(\theta)$ is a spatially integrated measure of the kind and quantity of scale-dependent spatial dispersion that exists at all scales greater than the shoot or leaf within the optical sensor's FOV. For example, values of $\Omega(\theta) > 1$, $\Omega(\theta) < 1$, and $\Omega(\theta) \approx 1$ denote spatial uniformity, spatial aggregation or clumping, and CSR, respectively (Chen et al., 1997). Foliage clumping at spatial scales finer than the shoot is determined independently of $\Omega(\theta)$ using direct manual sampling (Fassnacht et al., 1994; Stenberg, 1996; Chen et al., 1997; Gower et al., 1999).

The strong angular dependence of $\Omega(\theta)$ is well described by Kucharik et al. (1999), and recent studies by Walter et al. (2003) and Leblanc et al. (2005) demonstrate various methods for retrieving estimates of $\Omega(\theta)$ from fisheye photos. Binary sets composed of black and white pixels are easily extracted from 1-bit digital fisheye photos using a circular sample transect that connects pixels of equal θ (Fig. 2.3). Black and white pixels indicate the presence (occupied sites = 1) and absence (unoccupied sites = 0) of canopy elements, respectively. Lacunarity analysis is a useful statistical technique to study these binary sets, because it is a multiscale spatial method and does not require the user to dismantle the set into a statistical distribution of gap sizes or run lengths prior to

analysis (e.g., Chen and Cihlar, 1995). Therefore, lacunarity analysis has the potential to capture the coarser-scale patterns of clumping created by the nonrandom spatial distribution of stem densities.

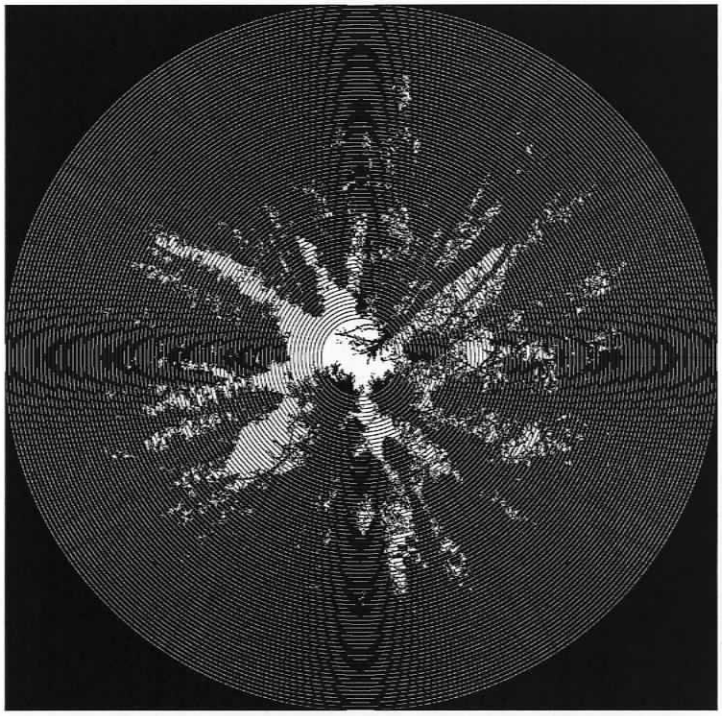

FIGURE 2.3. Equiangular overlay of circular sample transects placed every 1° of θ between $10° \leq \theta \leq 90°$. Binary sets are created by sampling pixels sequentially along lines of equal θ using all 360° of azimuth angle. Transect lengths are exceedingly short at $\theta < 10°$, and canopy gaps often become infrequent to nonexistent at $\theta > 70°$ in closed canopies. Therefore, estimates of $P(\theta)$ and $\Omega(\theta)$ are necessarily restricted to only a subset of θ angles.

From the brief description and examples of lacunarity analysis outlined in the previous sections, it is evident that the integrated cross-scale differences between observed estimates of $\Lambda(r)$ and those expected under CSR provide both the conceptual and analytical bases for the derivation of $\Omega(\theta)$. Three important analytical steps were necessary to develop this index. First, binary sets extracted from fisheye photos have no logical start or end due to the circular nature of the sample transect. Nevertheless, there are implications to and rules for selecting a starting point: (*i*) sets must always start at a gap edge to avoid the potential fragmentation of discrete gaps or clumps; (*ii*) $\Lambda(r)$ can be

sensitive to the set's start point, because at coarse measurement scales the gliding-box algorithm samples pixels (gridcells) in the middle of the set more often than ones near the start or end (Cheng, 1997). It is, therefore, imperative to resample the set using randomly or regularly placed start points and to compute the mean observed lacunarity statistic $\overline{\Lambda_{Obs}(r)}$ for all resampled sets:

$$\overline{\Lambda_{Obs}(r)} = \frac{1}{m}\sum_{t=1}^{m}\Lambda_t(r) \tag{2.6}$$

where $\Lambda_t(r)$ is the lacunarity statistic estimated at r for each resampled transect t, and m is the total number of resampled transects. Short, spatially heterogeneous sets require more resampling than long, homogeneous sets; however, we found that resampling the set 4 to 8 times using regularly spaced start points was usually sufficient to stabilize $\overline{\Lambda_{Obs}(r)}$.

Second, the magnitude of $\Lambda(r)$ is a function of p and its spatial variability or dispersion across the binary set. Lacunarity curves generated for sets with identical lengths n and different densities p are therefore not directly comparable unless the effect of density p on $\Lambda(r)$ is first eliminated. Normalization to a common Y intercept can be accomplished by dividing each value of $\Lambda(r)$ by $\Lambda(r = 1)$. Doing so, removes the effect of the first statistical moment $Z_Q^{(1)}$ on all values of $\Lambda(r)$ and allows direct comparison of the scale-dependent variation in lacunarity for sets with identical lengths n and different densities p (Plotnick et al., 1996; Feagin, 2003).

Last, the integrated area between normalized $\overline{\Lambda_{Obs}(r)}$ and $\Lambda_{CSR}(r)$ across all measurement scales r gives a quantitative estimate of a set's departure from CSR, where areas below and above $\Lambda_{CSR}(r)$ indicate the amount of spatial uniformity and clumping, respectively. Knowing also the area beneath a hypothetical curve of 'maximal clumping' allows us to derive an estimate of $\Omega(\theta)$:

$$\Omega_{LAC}(\theta) = \left[\frac{Area_{Max}(\theta) - Area_{Obs}(\theta)}{Area_{Max}(\theta) - Area_{CSR}(\theta)}\right] \tag{2.7}$$

where $Area_{Obs}(\theta)$, $Area_{CSR}(\theta)$, and $Area_{Max}(\theta)$ are, respectively, the integrated areas under the normalized $\overline{\Lambda_{Obs}(r)}$, $\Lambda_{CSR}(r)$, and 'maximally clumped' $\Lambda_{Max}(r)$ lacunarity curves

computed for a binary set extracted at θ (Fig. 2.4). Values of $\Omega_{LAC}(\theta)$ range from greater than unity for uniform sets, unity at CSR, and less than unity for clumped sets. Previous work by Plotnick et al. (1996) indicates that a binary set defining $\Lambda_{Max}(r)$ will have two important properties: (*i*) all occupied sites (black pixels) will be completely separate from all unoccupied sites (white pixels), and (*ii*) p will approach zero. To understand this conceptually, imagine that all shoots or leaves visible in a fisheye photo at θ were rearranged so that they appear at only one point in the hemispherical object region, with a single foliage unit obstructing the view of all other units stacked behind it. Although this kind and degree of clumping is unlikely to occur in natural forests, $\Lambda_{Max}(r)$ does represent a reasonable endpoint for spatial clumping from a purely geometrical perspective. We found that $Area_{Max}(\theta)$ reached its maximum value when p was equal to 0.01.

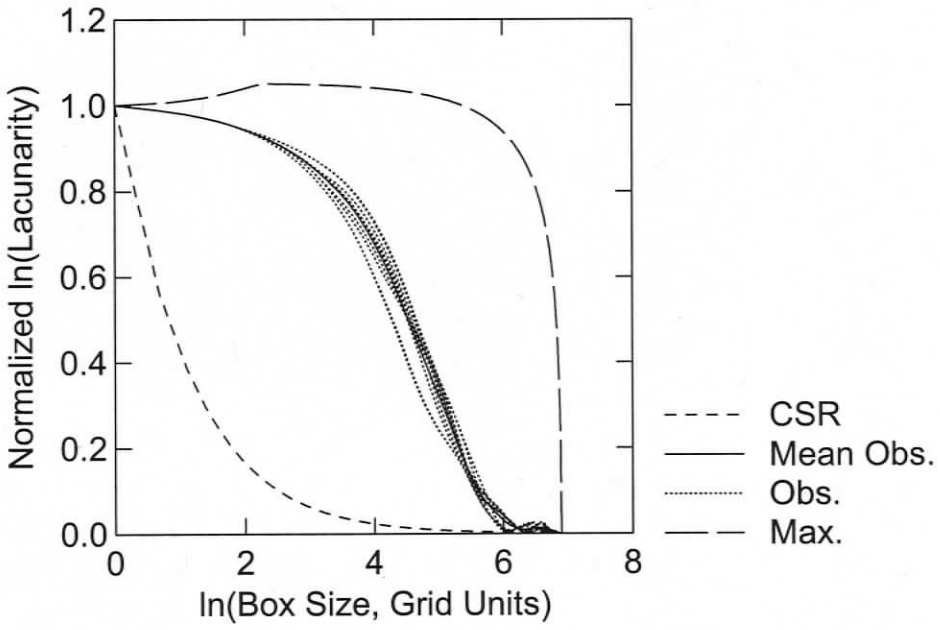

FIGURE 2.4. Normalized lacunarity curves identifying the position of the mean 'observed' curve (set C in Fig. 2.1) relative to CSR and maximal clumping. We divide the integrated area between maximal clumping and the mean 'observed' curve by the integrated area between maximal clumping and CSR to estimate $\Omega_{LAC}(\theta)$. The range of variation in the 14 'observed' curves is due to the resampling of transect start and end points. The estimated mean and standard deviation of $\Omega_{LAC}(\theta)$ for set C are 0.36±0.01 ($0.34 \leq \Omega_{LAC}(\theta) \leq 0.40$) using all 14 possible transect start and end points.

2.3. Materials and Methods

2.3.1. Description of hemispherical canopy photosets

We analyzed a number of simulated and real fisheye canopy photos to examine the angular response of $\Omega_{LAC}(\theta)$ and its ability to improve the accuracy of optically derived estimates of LAI. The first dataset consisted of 12 simulated fisheye canopy photos, each having a known and unique combination of LAI (2, 4, and 6 m^2/m^2) and spatial clumping (Fc = 0.0 (CSR), 0.2, 0.4, 0.6) (Fig. 2.5). The second dataset was composed of 29 real fisheye canopy photos collected in three well-documented experimental forest sites in Canada and Germany (Fig. 2.6).

2.3.1.1. Simulated fisheye canopy photos

We utilized the three-dimensional (3-D) modelling and ray-tracing techniques developed by Fournier et al. (1996) and Walter et al. (2003) to simulate 12 fisheye canopy photos with known values of LAI and spatial clumping. Five main steps were required to generate each of these simulated images. First, we constructed a 3-D canopy volume V with a vertical height of 10 m and square horizontal base of 5 m × 5 m (25 m^2) following a method similarly proposed by Castro and Fletcher (1999). V was divided into 2.5×10^6 discrete equal-sized volume elements (voxel), each with a vertical height of 1 cm, horizontal widths of 10 cm, and surface area of 0.024 m^2. Second, following the definition of LAI specified in this paper, we randomly populated the 3-D array or matrix of voxels with a specific number (N) of opaque or occupied cells (leaves) to create a V of pseudo-randomly distributed leaves with known LAI (Fig. 2.7). To produce LAIs of approximately 2, 4, and 6 m^2/m^2 (LAI = $N \times [0.5 \times 0.024\ m^2] / 25\ m^2$), we set N = 4167, 8333, and 12500 leaves, respectively. Third, we arbitrarily chose 15 cluster seeds (CS) or centroids to place randomly within V, each leaf was assigned to the closest CS, and the Euclidean distance d between each leaf and its closest CS was measured. We then allowed each leaf to migrate towards its assigned CS by applying a scale or clumping factor (Fc) of 0.2, 0.4, and 0.6 ($d' = d \times [1 - Fc]$) to each d (Fig. 2.7). Leaves were shifted along the original vectors used to measure d, and two or more leaves were never permitted to occupy the same voxel so that a constant LAI was maintained at all values of Fc.

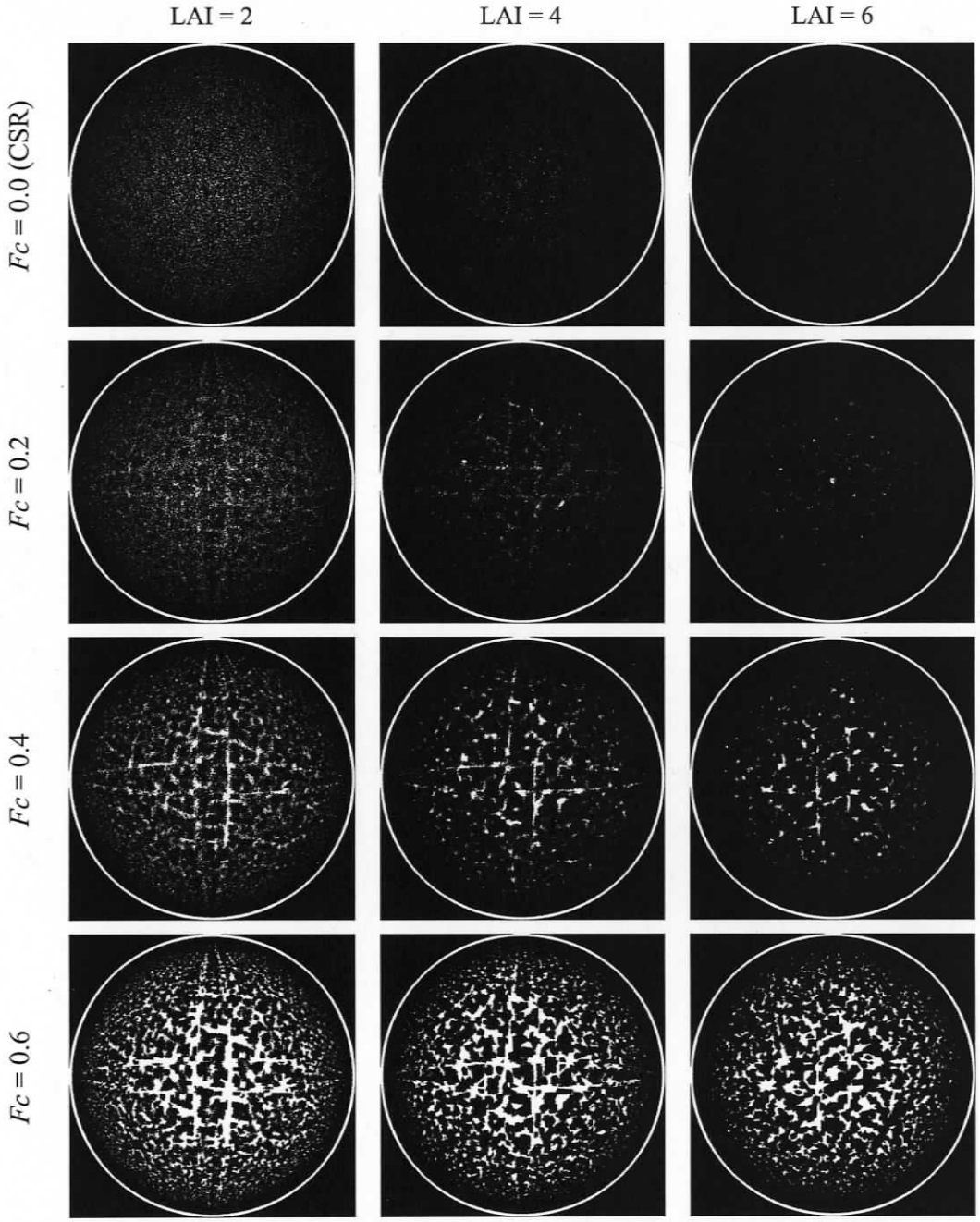

FIGURE 2.5. Simulated hemispherical canopy photos with known values of LAI (2, 4, and 6) and *Fc* (0.0 (CSR), 0.2, 0.4, and 0.6). Photos were generated by ray-tracing through a 600 m (width) × 600 m (length) × 20 m (height) simulated volume of square, horizontal, flat leaves. Leaves were spatially restricted to vertical heights between 10 m and 20 m. The simulated image resolution was 1024 × 1024 pixel.

BOREAS, black spruce

Hartheim, Scots pine

St. Gilles, sugar maple

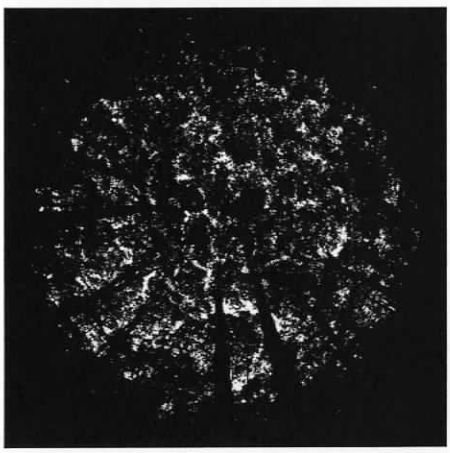

FIGURE 2.6. Examples of hemispherical canopy photos representing each of the three experimental forest sites.

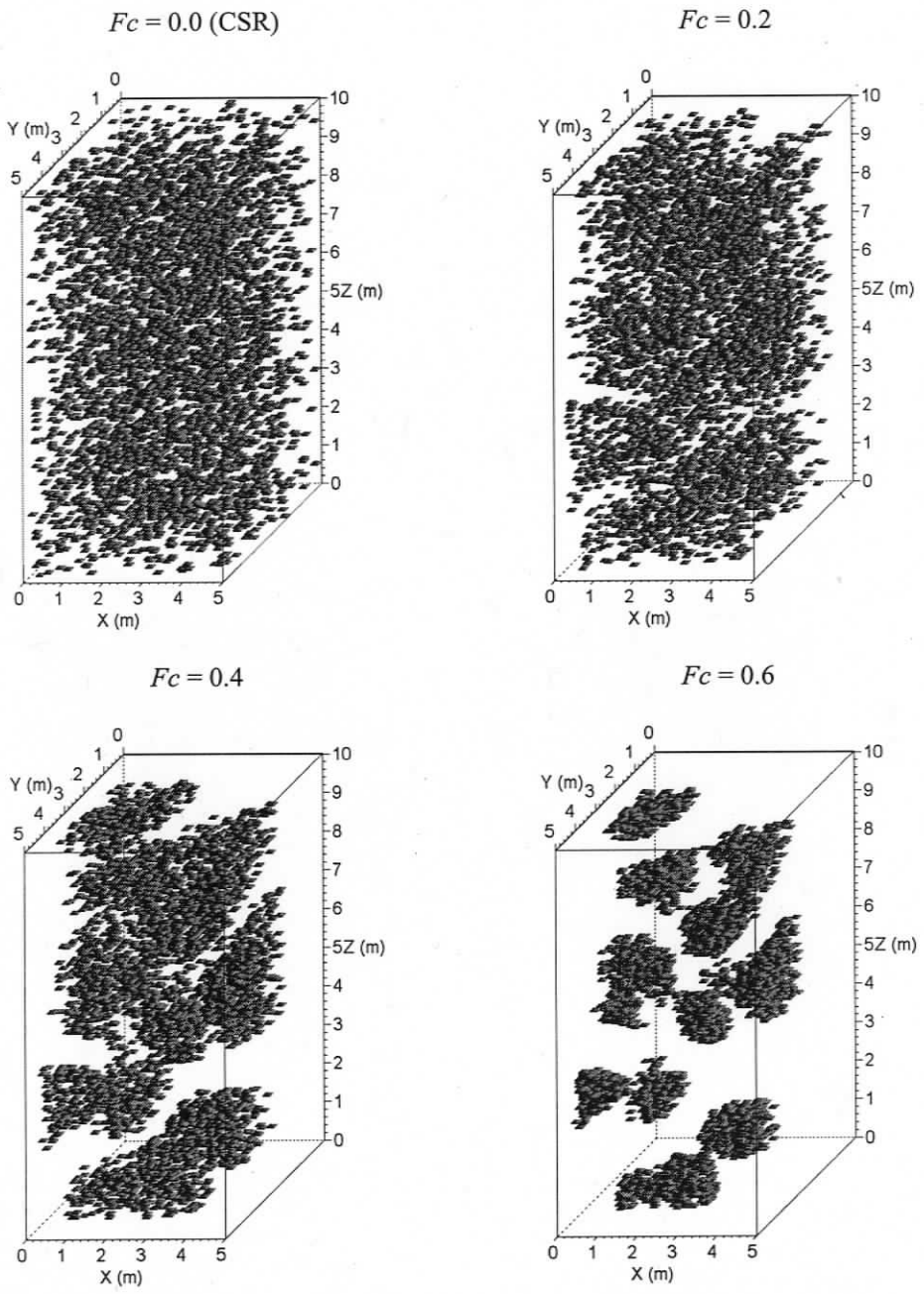

FIGURE 2.7. A single simulated 5 m (width) × 5 m (length) × 10 m (height) canopy volume *V* displaying increasing amounts of spatial aggregation (*Fc* = 0.0, 0.2, 0.4, 0.6). *V* is composed of 2.5 × 10^6 discrete voxels, each with a vertical height of 1 cm, width and length of 10 cm, and surface area of 0.024 m^2. *V* was randomly populated with 15 centroids that became points of attraction for the closest surrounding leaves to migrate as *Fc* increased. We used a 120 × 120 array of randomly rotated *V* to generate a contiguous 600 m × 600 m forest canopy.

Fourth, we generated a large, spatially contiguous (600 m × 600 m) forest canopy of known LAI and *Fc* by placing multiple copies of *V* side by side (similar to the 'toroidal edge correction' used in point pattern analysis; see Dale, 1999: 215). Before placement, each *V* was randomly rotated in the horizontal plane by 0, 90, 180, or 270° to help alleviate some of the repetition (uniformity) in spatial pattern created by this approach. The bottom of each *V* was elevated to a height of 10 m so that the vertical distribution of leaves ranged from 10 to 20 m. Last, we used the ray-tracing program ULooPS (Upward-Looking Photography Simulator) developed by R. Fournier to generate skyward-looking, hemispherical (fisheye) views from the centre of the spatially extended *V* and at 1.5 m above the ground (Fig. 2.5).

2.3.1.2. Fisheye photos from experimental forest sites

We chose three separate sets of existing fisheye canopy photographs collected in well-documented experimental forest sites located near (1) Thompson, Manitoba, Canada (55° 53′ N, 98° 29′ W) as part of the Boreal Ecosystem-Atmosphere Study (BOREAS) (Sellers et al., 1997; Leblanc et al., 2005); (2) Hartheim, Germany (47° 56′ N, 7° 37′ E), as part of the Meteorological Institute of University of Frieburg (Walter et al., 2003), and (3) St. Gilles, Quebec, Canada (46° 26′ N, 71° 25′ W), as part of the Canadian Forest Service, ECOLEAP project (Bernier et al., 1999). All three experimental forest sites had distinctively different stand and canopy structures due to differences in species composition, stand age, disturbance history, and climate (Table 2.1; Fig. 2.6). The BOREAS forest site was a mature (~69 yr.), even-aged, *Picea mariana* (Miller) Britton (black spruce) stand that originated naturally after wildfire. The Hartheim forest site was located in an intensively managed, even-aged, *Pinus sylvestris* L. (Scots pine) plantation that was established after harvesting in 1961. The forest site at St. Gilles also originated after harvesting, and was predominantly (72%) composed of mature (65 yr.), even-aged *Acer saccharum* Marshall (sugar maple), with some lesser components of *Fagus grandifolia* Ehrh. (American beech), and *Betula alleghaniensis* Britton (yellow birch). The photographic equipment and field sampling methods used to collect the three separate sets of fisheye photos are well described by Leblanc et al. (2005) for BOREAS and by Walter et al. (2003) for Hartheim and St. Gilles sites. Due to differences in

sampling design, photographic equipment, and exposure settings, each photoset differed by number of photos, image resolution, image quality, and projection distortion (Table 2.1).

TABLE 2.1. Description of selected stand and fisheye-photo characteristics for three experimental forest sites

Attributes	BOREAS[a]	Hartheim	St. Gilles
Dominant species	black spruce	Scots pine	sugar maple
Age (yr.)	69	34	65
Basal area (m^2/ha)	36.7	33.0	28.2
Stand height (m)	12[b]	12[c]	23[d]
Mean DBH (cm)	4.4	9.4	24.2
Stem density (n/ha)	15850	6400	644
LAI (m^2/m^2)	6.80[e]	4.08[f]	6.06[g]
L_W (m^2/m^2)	1.02[h]	0.69[i]	-
γ_E	1.4[h]	1.25[i]	1
No. of photos	11	10	8
Lens projection[j]	Polar	Orthographic	polar
Camera type	digital/RGB	film/B&W	film/B&W
Image size (pixel)	1377 × 1377	1709 × 1709	2004 × 2004

a Identified as Plot D1930 in Bond-Lamberty et al. (2002a,b) and T04 in Leblanc et al. (2005).
b Mean height of dominant trees.
c Maximum tree height.
d Mean tree height.
e Derived from site-specific allometric equation (Bond-Lamberty et al., 2002b).
f Derived from site-specific allometric equation (Walter et al., 2003).
g Derived from litterfall data (Bernier et al., 1999).
h Source Leblanc et al. (2005).
i Source Walter et al. (2003).
j See Herbert (1987) for details.
L_W is the woody area index (WAI); not estimated for the St. Gilles site.
γ_E is the needle-to-shoot-area ratio; $\gamma_E = 1$ for deciduous tree species.

2.3.2. Image pre-processing and extraction of binary sets

We followed five main image-processing steps before retrieving estimates of gap size, $P(\theta)$, and $\Omega(\theta)$ from the real fisheye photos. First, we extracted the RED plane from the 24-bit (RGB) digital photos taken at BOREAS to increase the grayscale contrast between sky and non-sky (canopy) components of the image. Second, we used the software, *SideLook*, developed by Nobis and Hunziker (2005) to automatically determine a single threshold value for each grayscale (8-bit) image. This threshold value was used to separate each photo into discrete classes of sky (white) and canopy (black) pixels. *SideLook* uses an edge-detection algorithm to find the 'optimal' threshold value that provides the highest local contrast between pixels classified as sky and canopy. We used an automatic threshold procedure rather than a manual one to avoid the subjectivity and variability known to be introduced by the latter approach (Rich, 1990). Third, we resized the original grayscale images using the 'bicubic' interpolation method implemented in Adobe Photoshop Version 5.1 to create two replicate photosets with arbitrarily chosen, lower spatial resolutions: 750 × 750 pixel and 1000 × 1000 pixel. We applied the same threshold values determined for original, full-resolution photos to these lower-resolution replicates. We used these two new image sets to determine the sensitivity of our clumping algorithms to image (spatial) resolution. Four, we applied either a polar or orthographic projection (Herbert, 1987) to extract binary sets at 1° intervals of θ between $10° \leq \theta \leq 90°$ using all 360° of azimuth angle. Last, each binary set was spatially rearranged so that its starting point began at the edge of the first gap encountered along the length of the set. We used these resampled binary sets to derive estimates of gap size, $P(\theta)$, and $\Omega(\theta)$ for each photo.

2.3.3. Estimation of LAI and canopy openness

The plant area index of a forest canopy at θ can be estimated by inverting the Beer-Lambert model (Eq. 2.1) and solving for $L_t(\theta)$:

$$L_t(\theta) = -\frac{\ln[P(\theta)]\cos\theta}{G(\theta)\Omega(\theta)} \tag{2.8}$$

where $P(\theta)$ is estimated as the fraction of sky (white) pixels found within a set at θ. In homogeneous canopies, where leaf position and azimuthal direction are randomly and independently distributed, $G(\theta)$ is determined solely by the orientation of foliage angles (Norman and Campbell, 1989; Welles and Norman, 1991; Stenberg, 2006). However, when canopies are spatially heterogeneous, $G(\theta)$ is also strongly influenced by the scale and geometry (size, shape, and orientation) of foliage clumps (i.e., branches, whorls, and crowns) (Black et al., 1991; Chen and Black, 1991):

$$G(\theta) = -\frac{\ln[P(\theta)]\cos\theta}{L_t \Omega(\theta)} \tag{2.9}$$

Miller (1967) demonstrated that the mean value of G was largely independent of foliage orientation and equivalent to 0.5 when $G(\theta)$ was integrated between $0° \leq \theta \leq 90°$:

$$G = \int_0^{\pi/2} G(\theta)\sin(\theta)d(\theta) = 0.5 \tag{2.10}$$

Therefore, in the absence of angle-dependent $G(\theta)$ data, L_t is more readily calculated through inversion of the Beer-Lambert model following Miller's (1967) theorem (Leblanc et al., 2005):

$$L_t = -2\int_0^{\pi/2} \frac{\ln[P(\theta)]}{\Omega(\theta)}\cos\theta\sin\theta d\theta \tag{2.11}$$

Under the assumption that leaves are spatially randomly distributed ($\Omega(\theta) = 1$), or if $\Omega(\theta)$ is unknown, Miller's theorem provides an estimate of the "effective" plant area index (L_e) (Chen et al., 1997):

$$L_e = \Omega L_t = -2\int_0^{\pi/2} \ln[P(\theta)]\cos\theta\sin\theta d\theta \tag{2.12}$$

where Ω is the mean clumping index derived from numerical integration of $\Omega(\theta)$ between the limits $0° \leq \theta \leq 90°$:

$$\Omega = \int_0^{\pi/2} \Omega(\theta)\sin\theta d\theta \tag{2.13}$$

Two additional parameters are required to convert optically derived estimates of L_t to LAI (L): (1) the woody area index (L_W), defined as one-half the total branch plus bole surface area (m^2) per unit of ground surface area (m^2) (Chen et al., 1997, Gower et al., 1999, Barclay et al., 2000); (2) the needle-to-shoot-area ratio (γ_E), defined as one-half the total needle surface area contained in a shoot divided by one-half the total 'imaginary' shoot surface area (Fassnacht et al., 1994; Stenberg et al., 1994; Chen et al., 1997). The final equation needed to convert L_t to L is given by Leblanc et al. (2005):

$$L = \gamma_E (L_t - L_W) = L_t \gamma_E (1 - \alpha) \tag{2.14}$$

where α is L_W expressed as a fraction of L_t (the woody-to-total-plant-area ratio).

Numerical integration of L_e and L_t between $0° \leq \theta \leq 90°$ is often not possible or prescribed in closed canopies for two main reasons. First, $P(\theta)$ at $\theta > 70°$ will usually be zero in dense stands, and the logarithm of zero is undefined. Second, one of the main assumptions needed for reliable inversion of gap fraction data is that leaves (and foliage clumps) are small relative to the sensor's FOV (Welles and Norman, 1991). Circular sample transects, however, become limited in length (scale) relative to the size of foliage clumps at $\theta < 10°$. This is particularly noticeable when canopy photos are captured using an equiangular (polar) or stereographic (equal-angle) fisheye lens (Herbert, 1991). Also, the amount and spatial distribution of foliage found at $\theta < 10°$ is often highly variable and more directly related to camera placement and local canopy conditions rather than general structural characteristics of the stand (Fournier et al., 1997; Leblanc and Chen, 2001).

We completed the numerical integrations of L_e (Eq. 2.12) and L_t (Eq. 2.11) using a fixed lower limit of $\theta = 10°$ and a variable upper limit ($69° \leq \theta \leq 80°$) that depended on the θ at which $P(\theta) = 0$. Others (e.g., Warren Wilson, 1960; Neumann et al., 1989; Weiss et al., 2004; Leblanc et al., 2005) have suggested that L_e and L_t can also be accurately retrieved at $\theta = 57.5°$, because $G(\theta)$ is equivalent to 0.5 at this exact θ for any leaf-angle distribution (Chen and Black, 1991). Therefore, for comparative purposes, we also computed L_t between $55° \leq \theta \leq 60°$. In addition, we calculated the mean % canopy openness (CO) for each image using the integral (Frazer et al., 1997):

$$CO = 100 \int_{0}^{\pi/2} P(\theta)\sin(\theta)d(\theta) \qquad (2.15)$$

CO is defined as the percentage of open or unobstructed sky observed from a single point beneath the canopy at all possible view angles and directions within a 180° FOV.

2.3.4. Photo-based estimates of $\Omega(\theta)$

2.3.4.1. Lacunarity-based clumping index, $\Omega_{LAC}(\theta)$

The derivation of $\Omega_{LAC}(\theta)$ can be computationally intensive, because it involves repeated measurements at different spatial scales using a potentially large number and range of box sizes r. For example, a transect length of n = 1000 pixels would require 1000 iterations to estimate $\Lambda(r)$ for $1 \leq r \leq n$. In an effort to reduce processing time, we chose to measure $\Lambda(r)$ using a maximum of 75 approximately equal intervals of $\ln(r)$. We divided each extracted sample transect into four equal segments (quadrants) of azimuth angle: 0 to 90°, 90 to 180°, 180 to 270°, and 270 to 360°, and established a new start point at the edge of the first gap found within each quadrant. This step produced four separate sets that differed only by their starting and ending azimuth angles. We then used Eq. 2.6 to compute $\overline{\Lambda_{Obs}(r)}$ from analyses of these four resampled sets. We estimated $\Lambda_{CSR}(r)$ for the same 75 box sizes using Eq. 2.5, while $\Lambda_{Max}(r)$ was derived from analysis of a single set containing one large, spatially contiguous gap of size $n \times 0.99$ (p = 0.01). We computed the total area found under each of these three separate lacunarity curves by assuming linearity between known points and through numerical integration by the 'trapezoidal rule' (Press et al., 1986) using a constant step value of 0.01 (in $\ln(r)$ units) between the limits ln(1) and $\ln(n)$. Finally, $\Omega_{LAC}(\theta)$ was estimated for each θ using Eq. 2.7.

2.3.4.2. Chen and Cihlar (CC) clumping index, $\Omega_{CC}(\theta)$

The method we used to compute $\Omega_{CC}(\theta)$ was based on the gap-size analysis theory originally developed by Chen and Cihlar (1995) for the TRAC. TRAC was designed to record the size, intensity, and spatial pattern of sunflecks measured along a sample transect located beneath the canopy. The size (width) of discrete gaps extracted from

these sunfleck data are sorted in descending order, converted to an 'observed' gap-size distribution or accumulation function $F_m(\lambda,\theta)$ (Chen and Cihlar, 1995: Appendix B), and then compared to the theoretical gap-size-accumulation function $F_{CSR}(\lambda,\theta)$ expected under CSR (Chen and Cihlar, 1995; Leblanc et al., 2005):

$$F_{CSR}(\lambda,\theta)=\left[1+L_p(\theta)\frac{\lambda}{W_p(\theta)}\right]\exp\left[-L_p(\theta)\left(1+\frac{\lambda}{W_p(\theta)}\right)\right] \qquad (2.16)$$

where $F_{CSR}(\lambda,\theta)$ represents the fraction of the total transect length measured at θ occupied by gap sizes larger than λ for a spatially random canopy; $L_p(\theta)$ is the projected foliage-element (leaf or shoot) area index estimated from the gap fraction at θ, and $W_p(\theta)$ is the mean shadow width of a single leaf or shoot (i.e., mean foliage element size) projected on a horizontal surface at θ.

We derived $F_m(\lambda,\theta)$ for each fisheye photo using the measured widths (in pixel units) of discrete canopy gaps found along the length of a binary set retrieved at θ. $W_p(\theta)$ is difficult to estimate directly from digital photos because of the complex geometrical relationship between pixel size and foliage element size (Leblanc et al., 2005; Chen et al., 2006). We therefore employed an alternative gap-removal algorithm modified from the original procedure developed by Walter et al. (2003) to estimate $F_{CSR}(\lambda,\theta)$. This modified gap-removal algorithm required three main steps: (1) discrete gap sizes retrieved from the set extracted at θ were sorted into descending order to compute $F_m(\lambda,\theta)$; (2) a single gap, starting with the first largest gap, was removed and a new 'compacted' accumulation function $F_{mr}(\lambda,\theta)$ was calculated; (3) the difference (epsilon) in $F_{mr}(\lambda,\theta)$ between successive iterations of the gap-removal algorithm was calculated, and the process was halted when epsilon equaled 0.005 (i.e., further gap removal would have very little effect on $F_{mr}(\lambda,\theta)$). We arbitrarily chose an epsilon of 0.005 based on a condition proposed by Chen and Cihlar (1995: 6214) for stopping the gap-removal process (i.e., $F_{mr}(\lambda,\theta)$ would approximate $F_{CSR}(\lambda,\theta)$ when epsilon was less than 0.01). We derived $\Omega_{CC}(\theta)$ directly from the accumulated gap fractions associated with $F_m(\lambda,\theta)$ and $F_{mr}(\lambda,\theta)$ (Leblanc et al., 2005):

$$\Omega_{CC}(\theta)=\frac{\ln[F_m(0,\theta)]\,[1-F_{mr}(0,\theta)]}{\ln[F_{mr}(0,\theta)]\,[1-F_m(0,\theta)]} \qquad (2.17)$$

where $F_m(0,\theta)$ is the total accumulated gap fraction associated with all gap sizes λ larger than 0 for $F_m(\lambda,\theta)$, and $F_{mr}(0,\theta)$ is the total accumulated gap fraction associated with all gap sizes λ larger than 0 for $F_{mr}(\lambda,\theta)$.

2.3.4.3. Lang and Xiang (LX) clumping index, $\Omega_{LX}(\theta)$

Estimation of $\Omega_{LX}(\theta)$ is based on the finite-length averaging technique developed by Lang and Xiang (1986) for optical measurements of LAI in spatially heterogeneous canopies. These authors proposed that the logarithmic average of $P(\theta)$ measured over several short segment lengths would provide a more accurate estimate of LAI than the linear average of $P(\theta)$ integrated over an entire transect. Lang and Xiang (1986) recommended this approach for two principal reasons: (1) the inverted formulation of the Beer-Lambert model (Eq. 2.8) implies that L_t is proportional to the logarithm of $P(\theta)$ rather than $P(\theta)$ itself, and (2) the required assumption of CSR is more likely to hold true over short rather than long segment lengths in heterogeneous forest canopies.

The choice of segment length used for finite-length averaging has been largely arbitrary (e.g., van Gardingen et al., 1999; Walter et al., 2003; Leblanc et al., 2005). Shorter segment lengths, however, are known to produce higher LAI estimates (van Gardingen et al., 1999), and are also associated with higher probabilities that $P(\theta) = 0$ (the logarithm of zero is undefined). We therefore chose to divide each set extracted at θ into eight equal-arc-length (45°) segments as a way to minimize the number of sample lengths where the logarithm of $P(\theta)$ would be undefined. We computed $\Omega_{LX}(\theta)$ following the procedure outlined by Leblanc et al. (2005):

$$\Omega_{LX}(\theta) = \frac{\ln[P(\theta)]}{\frac{1}{q}\sum_{i=1}^{q}\ln[P_i(\theta)]} \qquad (2.18)$$

where $P_i(\theta)$ is the gap fraction measured for one of $q = 8$ segment lengths i at θ. In the case that no gaps were found in segment i ($P_i(\theta) = 0$), we arbitrarily inserted one-half of a single gap (i.e., 0.5 pixel divided by the segment length in number of pixels) following the method proposed by Leblanc et al. (2005).

2.3.4.4. Pielou's coefficient of segregation (PCS) clumping index, $\Omega_{PCS}(\theta)$

The Pielou (1962) coefficient of segregation was initially used to detect and describe the kind and degree of spatial nonrandomness or segregation that occurred between two plant species (A and B) found along a narrow sample transect. Walter et al. (2003), by analogy, used PCS to quantify the spatial nonrandomness found in binary sets of black (B, foliage) and white (W, canopy gaps) pixels extracted at equal θ angles from fisheye canopy photos. The spatial arrangement of B and W pixels within a set is considered (with 95% probability) to be random when (Pielou, 1962):

$$\hat{b} + \hat{w} = \frac{1}{\overline{m_W}} + \frac{1}{\overline{m_B}} = 1 \pm 1.96\sqrt{s_b^2 + s_w^2} \qquad (2.19)$$

where $\hat{b}$ and $\hat{w}$ are estimates of the maximum likelihoods of encountering individual B and W pixels, respectively; $\overline{m_W}$ and $\overline{m_B}$ are the average run lengths of W and B pixels, respectively; s_b^2 and s_w^2 are estimates of the sample variances associated with the probabilities b and w of encountering individual B and W pixels, respectively (Pielou, 1962):

$$s_b^2 = \frac{1}{n_W}\frac{\overline{m_W} - 1}{\overline{m_W}^3} \text{ and } s_w^2 = \frac{1}{n_B}\frac{\overline{m_B} - 1}{\overline{m_B}^3} \qquad (2.20)$$

where n_W and n_B are the total numbers of discrete runs (sequences) of W and B pixels, respectively. Estimates of PCS that are significantly less than unity indicate positive spatial segregation or clumping (i.e., average run lengths of B and W pixels are longer than expected), while those significantly larger than unity denote negative spatial segregation or overdispersion (i.e., average run lengths of B and W pixels are shorter than expected). We therefore calculated $\Omega_{PCS}(\theta)$ from Eq. 2.19 using the formula (Walter et al., 2003):

$$\Omega_{PCS}(\theta) = \frac{1}{\overline{m_W}} + \frac{1}{\overline{m_B}} = \frac{n_W}{T_W} + \frac{n_B}{T_B} \qquad (2.21)$$

where T_W and T_B are the total numbers of W and B pixels contained within a set extracted at θ. n_W and n_B are always equal when a circular transect starts and ends at the same gap edge.

2.3.5. Statistical analysis

We used (1) linear and non-linear regression to study the statistical relationship between estimates of $\Omega(\theta)$ and various gap-size statistics; (2) paired-sample t tests to determine whether mean differences between L estimated by Miller's theorem and at 57.5° were statistically significant, and (3) single-factor analysis of variance (ANOVA) and Tukey's post-hoc test for pairwise comparisons to determine whether image resolution had any statistically significant effect on photo-based estimates of L_e, Ω, or L. We used the 5% significance level to reject the null hypothesis of "no mean differences" between samples. We examined each of our samples for normality prior to analysis using a normal probability plot. We used SYSTAT Version 10.2 for all statistical analyses.

2.4. Results and Discussion

2.4.1. Estimates of L_e, CO, and L from simulated canopies

Our results from the analysis of the 12 simulated fisheye photos clearly illustrate the impact of foliage clumping on estimates of L_e derived using the Beer-Lambert model (Eq. 2.12; Table 2.2). Estimates of L_e were similar to expected values of LAI when leaves were randomly and independently distributed ($Fc = 0$) within the simulated canopy volume. However, when leaves became increasingly more clumped ($Fc > 0$), measures of L_e substantially underestimated LAI, particularly for those canopy volumes with larger leaf areas (LAI > 2). The magnitude and rate of decline in L_e with increasing foliage clumping was markedly nonlinear and varied strongly with LAI. For example, the disparity between L_e and LAI for any given Fc was always larger for LAI = 6 than LAI = 2 or 4, and all estimates of L_e converged towards a similar low value ($1.17 \leq L_e \leq 1.92$) for LAI = 2, 4, and 6 when Fc reached 0.6. The largest % difference between L_e and LAI ($[L_e/\text{LAI} - 1] \times 100\%$) occurred when the canopy volume was maximally clumped (Fc = 0.6): L_e underestimated LAI = 2, 4, and 6 by 41.7%, 61.2%, and 68.1%, respectively.

TABLE 2.2. Summary of percent canopy openness, element clumping, and LAI calculations for the 12 simulated fish-eye photos

					CC			LAC			LX			PCS		
LAI	*Fc*	*%CO*	L_e	%Diff.	Ω_{CC}	*L*	%Diff.	Ω_{LAC}	*L*	%Diff.	Ω_{LX}	*L*	%Diff.	Ω_{PCS}	*L*	%Diff.
2	0.0	17.5	1.94	−2.8	0.98	1.98	−1.0	0.97	2.01	0.6	0.99	1.96	−1.9	0.79	2.45	22.5
	0.2	18.7	1.86	−6.9	0.97	1.92	−4.2	0.95	1.96	−2.0	0.99	1.89	−5.7	0.76	2.45	22.6
	0.4	22.4	1.64	−17.9	0.91	1.80	−10.1	0.88	1.87	−6.6	0.97	1.69	−15.6	0.61	2.69	34.4
	0.6	33.7	1.17	−41.7	0.73	1.60	−20.1	0.76	1.54	−23.1	0.96	1.21	−39.4	0.34	3.40	69.9
4	0.0	3.2	3.89	−2.8	0.99	3.94	−1.5	0.98	3.95	−1.2	0.97	3.99	−0.1	0.89	4.39	9.7
	0.2	4.2	3.57	−10.8	0.98	3.65	−8.8	0.96	3.72	−7.1	0.96	3.70	−7.5	0.82	4.35	8.8
	0.4	9.3	2.67	−33.3	0.89	3.00	−25.0	0.85	3.12	−22.0	0.94	2.83	−29.3	0.54	4.98	24.5
	0.6	24.1	1.55	−61.2	0.67	2.33	−41.7	0.73	2.13	−46.8	0.93	1.66	−58.5	0.24	6.39	59.8
6	0.0	0.6	5.99	−0.2	0.98	6.13	2.2	1.00	5.96	−0.7	0.99	6.04	0.6	0.97	6.15	2.5
	0.2	1.0	5.24	−12.7	0.97	5.38	−10.3	0.98	5.34	−11.0	0.96	5.47	−8.8	0.86	6.07	1.2
	0.4	4.4	3.62	−39.6	0.88	4.13	−31.2	0.86	4.22	−29.7	0.91	3.98	−33.7	0.49	7.32	22.0
	0.6	18.2	1.92	−68.1	0.67	2.86	−52.3	0.74	2.59	−56.8	0.93	2.07	−65.5	0.22	8.84	47.3

LAI is the expected or known (modelled) LAI in m^2/m^2.
L_e is the 'effective' LAI in m^2/m^2 determined by gap fraction inversion using Miller's theorem (Eq. 2.12).
L is the LAI in m^2/m^2 integrated over zenith angles 10° to 80° using 4 different estimates of $\Omega(\theta)$ (Eq. 2.11).
Fc is the fractional clumping factor (higher values of *Fc* denote greater spatial clumping).
%CO is the percentage canopy openness integrated over zenith angles 10° to 80° (Eq. 2.15).
%Diff. is the percentage difference between observed L_e or *L* (optical) and expected LAI (%Diff. = [Obs/Exp − 1] × 100%).
CC-Chen and Cihlar method; LAC-lacunarity method; LX-Lang and Xiang method; PCS-Pielou coefficient of segregation method.

CO increased nonlinearly for all values of LAI as the canopy became more spatially clumped (Table 2.2), and at $Fc = 0.6$ all simulated fisheye photos, irrespective of LAI, exhibited a large *CO* ($18.2\% \leq CO \leq 33.7\%$) compared to that expected under CSR (Fig. 2.7). Castro and Fetcher (1999), using transmittance (the probability that an infinitely narrow beam of light would penetrate the canopy from all possible view angles) rather than *CO*, found that transmittance approached 1 ($CO = 100\%$) for all values of LAI ranging from 1 to 9 when the canopy approached maximum clumping (i.e., all leaves were packed into their closest cluster seed). Thus, under conditions of extreme 3-D spatial clumping ($Fc > 0.6$), we expect that 2-D hemispherical projections of the canopy gap fraction will display similar amounts and patterns of *CO* no matter how much leaf area the simulated canopy volume holds.

Under the condition of CSR ($Fc = 0$), canopy gaps became progressively smaller and less frequent when leaf area increased from LAI = 2 to LAI = 6 (Fig. 2.5). At LAI = 6, for example, *CO* was only 0.6% when leaves were randomly and independently distributed within the simulated canopy volume. Adding any more leaves to this volume would have caused the remaining gaps to disappear (the 'saturation' point; Gower et al., 1999) and reliable estimates of LAI based on gap fraction analysis would no longer be possible (Jonckheere et al., 2004). At certain thresholds of leaf density and spatial clumping, saturation also occurs locally within hemispherical canopy photos, whereby discrete foliage clumps become completely opaque (no gaps). Once gaps disappear from within individual clumps, there is no way of estimating the amount of mutual shading or leaf area contained in a single clump from gap fraction data (Chen et al., 1997). Another compounding problem related to local saturation was that higher values of *Fc* produced discrete clumps with smaller projected areas, while the leaf area associated with these clumps remained unchanged. The rapid, nonlinear decline and convergence of L_e at higher levels of spatial clumping ($Fc > 0$) for LAI = 2, 4, and 6 indicated that local saturation had occurred at lower values of *Fc* for LAI = 6 than LAI = 2 or 4 due to differences in leaf area density. It is well known from previous studies (e.g., Chen et al., 1997; Nilson, 1999) that when local saturation occurs (often within individual branches or crowns in real forests), gap fraction analysis provides only an estimate of one-half the

total 'imaginary' surface area of clumps and not the surface area of individual leaves or shoots.

We found that measurements of L, which included the angle-dependent effect of $\Omega(\theta)$ (Eqs. 2.11 and 2.14), had generally improved LAI estimates in the presence of spatial clumping ($Fc > 0$) (Table 2.2). However, the magnitude and extent of this improvement was limited and largely determined by the methods (CC, LAC, LX, PCS) used to compute $\Omega(\theta)$; the number and density of leaves, and the degree of spatial clumping (Fc). CC, LAC, and LX, for example, minimized the % difference between L and LAI, but all three methods still underestimated LAI, especially at higher values of LAI and Fc. The mean % difference (median in parentheses) between L_e and LAI for all 12 simulated fisheye photos was reduced from 24.8% (15.3%) to 17.3% (10.2%) with CC, 17.3% (9.0%) with LAC, and 22.2% (12.2%) with LX. The largest underestimation between L and LAI for CC (−52.3%), LAC (−56.8%), and LX (−65.5%) occurred at LAI = 6 and $Fc = 0.6$. In contrast, L exceeded LAI for all simulated LAI and Fc values when the PCS method was introduced. The mean % difference (median in parentheses) between L and LAI for PCS was 27.1% (22.6%), which was larger than the original mean % difference between L_e and LAI. Also, the influence of leaf area and density on the % difference between L and LAI was reversed when PCS was used: % differences (overestimations) between L and LAI were greatest for LAI = 2 (22.5% ≤ %Diff. ≤ 69.9%) and lowest for LAI = 6 (1.2% ≤ %Diff. ≤ 47.3%). The disparity between L and LAI was always at its maximum for all four clumping methods when $Fc = 0.6$.

2.4.2. Estimates of L_e, CO, L_t, and L from real forest canopies

Mean estimates of L_e for each of the three experimental forest sites were similar in magnitude despite substantial between-site differences in species composition, stand structure, and LAI (Table 2.1; Fig. 2.6). Mean L_e computed for the black spruce stand (BOREAS) was 2.87 ± 0.30 s.d. ($2.35 \leq L_e \leq 3.27$), 2.87 ± 0.27 s.d. ($2.46 \leq L_e \leq 3.45$) for the Scots pine stand (Hartheim), and 2.89 ± 0.39 s.d. ($2.39 \leq L_e \leq 3.65$) for the sugar maple stand (St. Gilles). The black spruce stand exhibited the highest mean CO (10.2% ± 1.6% s.d.), but also supported the largest LAI (6.80) of the three sites. The lowest mean CO (7.2% ± 2.0% s.d.) was recorded for the sugar maple stand, which had a measured

LAI of 6.06. The Scots pine stand had a moderately high *CO* (9.4% ± 1.7% s.d.) and the lowest LAI (4.08). The % difference between mean L_e and LAI was greatest for the black spruce (−57.8%) and sugar maple stands (−52.3%), and lowest for Scots pine stand (−29.7%).

Other published studies that have compared optical L_e estimates with direct LAI in black spruce stands at BOREAS revealed a similar magnitude of underestimation. Chen et al. (1997) and Kucharik et al. (1999), for example, reported underestimates that ranged from −45% to −66% for LAI-2000 and MVI measurements of L_e taken in mature stands of black spruce ($5 \leq \text{LAI} \leq 7.9$). Stenberg et al. (1994) and Jonckheere et al. (2005) showed that photo- and LAI-2000-based measurements of L_e underestimated direct LAI ($2 \leq \text{LAI} \leq 5.5$) by 37.7% to 54.4% in Scots pine stands. The comparatively low % difference (−29.7%) between L_e and LAI recorded for the Hartheim Scots pine site can be attributed to the spatially uniform and homogeneous canopy created by intensive thinning and forest management at this site (Kessler and Jaeger, 1999). Published studies comparing L_e with LAI in sugar maple stands are rare; however, optical LAI data collected at another ECOLEAP site (Duchesnay) of similar height, basal area, and species composition suggest that our estimates of L_e at St. Gilles are unusually low. At Duchesnay, the % difference between mean L_e (3.53) estimated by fisheye photos and LAI (5.38) derived from litterfall was −34.4% (pers. comm., R. Boutin). Therefore, we believe that the low mean L_e measured at St. Gilles may be due in part to the close proximity of a high-contrast stand edge.

Measurements of L_t, which include the angle-dependent effect of $\Omega(\theta)$, improved optical estimates of LAI only when CC, LAC, and LX methods were introduced (Table 2.3). PCS produced L_t estimates that were substantially larger ($74\% \leq \%\text{Diff.} \leq 147.4\%$) than the expected LAI at each of the sites, and the magnitude of these differences was always larger than the % differences between L_e and LAI ($29.7\% \leq \%\text{Diff.} \leq 57.8\%$). Overestimation by PCS was most apparent at the Hartheim Scots pine site, where the % difference between L_t and LAI was 147.4%. In contrast, estimates of L_t based on CC, LAC, and LX methods consistently underestimated LAI, although LAC produced the smallest ($-6.6\% \geq \%\text{Diff.} \geq -39.6\%$) of these underestimates compared to CC ($-24.4\% \geq \%\text{Diff.} \geq -47.8\%$) and LX ($-19.8\% \geq \%\text{Diff.} \geq -48.9\%$) methods. CC,

LAC, and LX methods were least able to compensate for clumping in the most spatially heterogeneous and highest LAI stands such as BOREAS ($-39.6\% \geq$ %Diff. $\geq -48.9\%$) and St. Gilles ($-35\% \geq$ %Diff. $\geq -46.4\%$), and most effective in the least clumped and lowest LAI stand at Hartheim ($-6.8\% \geq$ %Diff. $\geq -24.4\%$). All four clumping methods correctly identified the BOREAS black spruce as the most spatially clumped ($0.22 \leq \Omega \leq 0.83$), the Hartheim Scots pine as the least spatially clumped ($0.28 \leq \Omega \leq 0.93$), and the St. Gilles sugar maple as somewhere in-between these two ($0.27 \leq \Omega \leq 0.89$).

Correcting CC-, LAC-, and LX-based estimates of L_t for clumping at the shoot level (γ_E) and for the total wood fraction (α) further reduced the underestimation of LAI at the BOREAS ($-28.1\% \geq$ %Diff. $\geq -39.2\%$) and Hartheim ($-3.1\% \geq$ %Diff. $\geq -21.5\%$) sites. Estimates of L derived from PCS-based L_t values, however, were shifted even further beyond their expected LAI by 125.1% at BOREAS and 156.6% at Hartheim. The best optical estimates of LAI (L) at the three experimental sites were derived using LAC-based L_t values: $L = 4.89 \pm 0.51$ s.d. (%Diff. $= -28.1\%$) at BOREAS black spruce (LAI = 6.8), 3.95 ± 0.29 s.d. (%Diff. $= -3.1\%$) at Hartheim Scots pine (LAI = 4.08), and 3.94 ± 0.42 s.d. (%Diff. $= -35\%$) at the St. Gilles sugar maple (LAI = 6.06) sites. No estimate of α was available for the St. Gilles stand, thus L is expected to underestimate LAI by slightly more than the amounts shown for CC, LAC, or LX methods ($-35\% \geq$ %Diff. $\geq -46.4\%$; Table 2.3).

TRAC measurements collected by Leblanc et al. (2005) at the BOREAS site at the same time our fisheye photos were taken resulted in an $L(39°)$ of 3.98 (where 39° was the solar zenith angle used by TRAC to sample $P(\theta)$ and $F_m(\lambda,\theta)$; $L_e(39°) = 3.06$, $\Omega_{CC}(39°) = 0.91$, $\gamma_E = 1.40$, $\alpha = 0.15$). TRAC-derived L was smaller than any of our photo-based estimates of L ($4.13 \leq L \leq 4.89$) computed using CC, LAC, or LX methods and Miller's theorem. We expect that the lower L measured by TRAC was the result of two main factors: (1) TRAC estimates of L_e and Ω_{CC} were based on measurements taken at only one solar position rather than several, and (2) Ω_{CC} (0.91) measured by TRAC at 39° was substantially larger than the photo-based estimates of Ω_{CC} (0.81), Ω_{LAC} (0.70), and Ω_{LX} (0.83) integrated between $10° \leq \theta \leq 70°$ using all 360° of azimuth.

TABLE 2.3. Summary of Ω, L_t, and L for CC, LAC, LX, and PCS clumping methods

		BOREAS (LAI = 6.80)			Hartheim (LAI = 4.08)			St. Gilles (LAI = 6.06)		
Method	Statistic	Ω	L_t	L	Ω	L_t	L	Ω	L_t	L*
CC	Mean	0.81	3.55	4.22	0.93	3.09	3.20	0.89	3.25	3.25
	s.d.	0.03	0.39	0.47	0.02	0.26	0.27	0.02	0.38	0.38
	min.	0.75	2.98	3.54	0.91	2.66	2.76	0.86	2.76	2.76
	Max.	0.85	4.22	5.02	0.97	3.56	3.70	0.93	4.03	4.03
	%Diff.	n.a.	-47.8	-37.9	n.a.	-24.4	-21.5	n.a.	-46.4	-46.4
LAC	Mean	0.70	4.11	4.89	0.75	3.81	3.95	0.73	3.94	3.94
	s.d.	0.03	0.43	0.51	0.02	0.28	0.29	0.03	0.42	0.42
	min.	0.64	3.50	4.16	0.73	3.28	3.40	0.70	3.35	3.35
	Max.	0.74	4.71	5.61	0.79	4.37	4.53	0.77	4.79	4.79
	%Diff.	n.a.	-39.6	-28.1	n.a.	-6.6	-3.1	n.a.	-35.0	-35.0
LX	Mean	0.83	3.47	4.13	0.88	3.27	3.40	0.86	3.38	3.38
	s.d.	0.03	0.44	0.52	0.02	0.27	0.28	0.03	0.51	0.51
	min.	0.78	2.79	3.32	0.85	2.79	2.89	0.82	2.69	2.69
	Max.	0.87	3.90	4.64	0.91	3.81	3.95	0.89	4.38	4.38
	%Diff.	n.a.	-48.9	-39.2	n.a.	-19.8	-16.8	n.a.	-44.2	-44.2
PCS	Mean	0.22	12.86	15.31	0.28	10.09	10.47	0.27	10.54	10.54
	s.d.	0.02	1.90	2.27	0.01	0.56	0.59	0.03	0.75	0.75
	min.	0.19	10.81	12.86	0.27	8.84	9.17	0.24	9.76	9.76
	Max.	0.27	17.09	20.33	0.32	10.86	11.26	0.31	11.81	11.81
	%Diff.	n.a.	89.1	125.1	n.a.	147.4	156.6	n.a.	74.0	74.0

CC-Chen and Cihlar; LAC-lacunarity; LX-Lang and Xiang; PCS-Pielou coefficient of segregation.

Ω is the element-clumping index integrated across all possible angles of zenith (Eq. 2.13).

L_t is the plant area index in m^2/m^2 corrected for clumping at spatial scales larger than the shoot or leaf (Eq. 2.11).

L is the leaf area index in m^2/m^2 corrected for the wood (branch and bole) fraction and clumping at all spatial scales (Eq. 2.14).

*Not corrected for woody fraction.

s.d. is the standard deviation.

%Diff. is the % difference between optical (observed) and direct (expected) LAI estimates ([Obs./Exp − 1] × 100%).

A comparison of optical estimates of L (corrected for clumping and wood fraction) and direct LAI presented by Gower et al. (1999) for a variety of deciduous and coniferous forests generally showed a strong linear (1:1) relationship between the two techniques; however, this relationship became markedly more variable and biased once direct LAI values reached 4 or 5. Optical measurements of L (manually scaled from Fig. 3 in Gower et al., 1999: 37), for example, often underestimated direct LAI by 25% or more in forest stands when direct LAI values exceeded 4 or 5. The largest underestimates (~45%) of optical L in coniferous forests have been reported for mature black spruce at BOREAS ($6.3 \leq \text{LAI} \leq 8$) southern study area (SOBS) by Chen et al. (1997) and Gower et al. (1999). Chen et al. (1997) suggested two reasons for such large differences. First, the patchy, discontinuous nature of the canopy at SOBS made comparisons between the two techniques difficult, since each method measured a somewhat different part of a strongly spatially heterogeneous forest. Second, black spruce crowns were long and narrow, and often appeared opaque to optical sensors because of the dense packing of needle area into the upper, conical portion of the crown (see Fig. 2.6 as an example). Large underestimates of LAI have also been reported by Gower et al. (1999) for optical measurements of L taken in mature sugar maple stands ($5.6 \leq \text{LAI} \leq 8.4$) in northern Wisconsin (Fassnacht and Gower, 1997). Optical L underestimated LAI in these nine stands by an average of 19.6% ± 10.2 s.d. ($-1.8\% \geq \%\text{Diff.} \geq -30.2\%$), with the largest underestimates ($-19.8\% \geq \%\text{Diff.} \geq 30.2\%$) occurring in the four stands with the greatest LAI ($6.6 \leq \text{LAI} \leq 8.4$).

Matching the spatial footprint of an optical sensor, such as TRAC, LAI-2000, or hemispherical photography, with direct LAI field measurements is often a challenge because of the large FOV of these instruments. This methodological difficulty may have little consequence in spatially extensive and homogeneous stands (e.g., Hartheim); however, it can lead to substantial differences between optical and direct estimates of LAI in highly fragmented or horizontally discontinuous (patchy) forests (e.g., SOBS; Chen et al., 1997). In the case of St. Gilles, we believe that some portion of the disparity between L and LAI was due to the 180° FOV of the fisheye lens and close proximity of a forest edge. A visible forest edge may alter $P(\theta)$ in one of two ways: (1) $P(\theta)$ will be smaller than expected at $\theta > 50°$ if the adjacent forest is taller or more dense than the

overhead canopy, or (2) $P(\theta)$ may be larger than expected at $\theta > 50°$ if the adjacent stand is short, sparse, or non-existent (e.g., St. Gilles).

2.4.3. Angular dependence of optical LAI measurements

The size-frequency distribution, spatial arrangement, and magnitude of canopy gaps vary strongly with θ (Kucharik et al., 1999; Walter et al., 2003; Leblanc et al., 2005), because θ alters the linear distance (pathlength) and line of sight (perspective) through the canopy, as well as the spatial extent or footprint (FOV) of the optical sensor. At small θ angles, for example, pathlengths are relatively short ($1/\cos\theta$), the perspective view is near vertical, and the spatial footprint of the optical sensor encompasses only one or a few canopy trees. Large θ angles, on the other hand, produce longer pathlengths, oblique views of the canopy, and a much larger FOV (optical instruments view many trees). Pathlength and line of sight directly affect $P(\theta)$, $F_m(\lambda,\theta)$, $G(\theta)$, and $\Omega(\theta)$ (Black et al., 1991; Kucharik et al., 1999; Leblanc et al., 2005), while instrument FOV and image resolution determine the potential range of spatial scales over which these attributes can be measured (Walter et al., 2003).

Scattergrams displaying selected gap statistics plotted against θ for the simulated photoset clearly demonstrate the strong angular dependence of these attributes (Fig. 2.8). $P(\theta)$, for instance, generally declined with increasing θ (Fig. 2.8A–C), because longer pathlengths through a horizontally continuous forest canopy reduced the probability of light transmittance (Welles and Norman, 1991). The number (frequency) of discrete canopy gaps (Fig. 2.8D–F) tended to rise with increasing θ in response to the longer length (or circumference) of circular sample transects and the fragmentation of large gaps into smaller ones as the line of sight was obscured by more and more vegetation. Gap frequency, however, reached a maximum at some larger value of θ and then rapidly declined towards zero once the pathlength became long enough to eliminate gaps altogether. Both the mean (Fig. 2.8G–I) and coefficient of variation (COV) (Fig. 2.8J–L) of the canopy gap-size distribution generally declined with increasing θ due to the combined influences of pathlength, line of sight, and FOV. For example, both large (between-clump) and small (within-clump) gaps tended to be preserved at $\theta < 50°$, because near vertical views from beneath the simulated canopy resulted in fewer canopy

layers to fragment the sky view. More oblique views ($\theta > 50°$), on the other hand, eliminated many of the larger between-clump gaps, thereby producing gap-size distributions dominated by small openings. The pattern of angular variation in $P(\theta)$ and $F_m(\lambda,\theta)$ was ultimately determined by all aspects of stand-level canopy structure, including species composition and spatial arrangement (Kucharik et al., 1999).

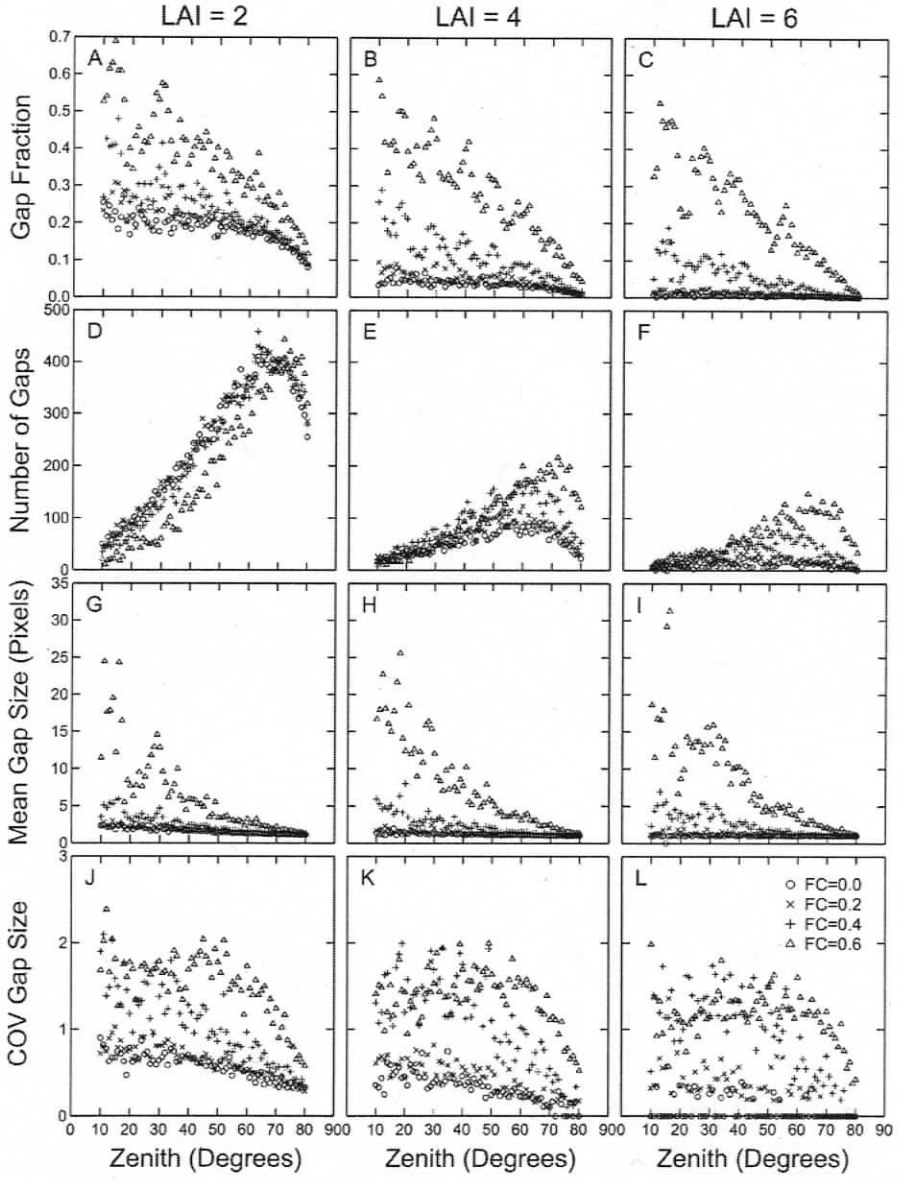

FIGURE 2.8. Angular variation of (A-C) the canopy gap fraction, (D-F) gap frequency, (G-I) mean gap size, and (J-L) coefficient of variation (COV) of gap size data derived from the simulated fisheye photoset.

Quantitative estimates of $\Omega(\theta)$ are either implicitly or explicitly linked to the size-frequencies and spatial distribution of canopy gaps (Section 2.3.4), and therefore also strongly influenced by θ. Results from our simulated photoset generally showed that $\Omega(\theta)$ increased nonlinearly from a minimum near the zenith towards a maximum value of approximately unity (CSR) closer to the horizon (Fig. 2.9). However, the range and pattern of angular variation in $\Omega(\theta)$ were markedly different for each of the four clumping indices. Lower values of $\Omega(\theta)$ always occurred at small values of θ in response to the patchy distribution of larger between-clump gaps, while larger $\Omega(\theta)$ estimates near the horizon were associated with the smaller, less frequent, and more randomly dispersed canopy gaps (Fig. 2.6). The same general pattern of angular variation in $\Omega(\theta)$ has been previously reported by Kucharik et al. (1999), Walter et al. (2003), and Leblanc et al. (2005).

Variation in the magnitude and angular pattern of $\Omega(\theta)$ among each of the four clumping methods can be explained by inherent algorithmic differences. PCS was derived from the sum of multiplicative inverses (reciprocals) of average run lengths of white (gap) and black (canopy) pixels (Eq. 2.21), and was therefore highly nonlinearly correlated (R^2 = 0.97) with the mean size of canopy gaps (Fig. 2.10). As a result, PCS estimates of $\Omega(\theta)$ declined with increasing mean gap size more rapidly and to substantially lower values compared to all other methods. LX, in contrast, generally produced the highest $\Omega(\theta)$ estimates and was least responsive to changes in spatial clumping (Fc) and mean gap size (R^2 = 0.37). The limited responsiveness of LX was a direct consequence of the long (45°) segment length used to sample $P_i(\theta)$ (van Gardingen et al., 1999). Segment length (measurement scale) is critical, because it determines (1) how discrete objects (i.e., foliage clumps and canopy gaps) in the photo are spatially aggregated into a single gap fraction, and (2) the likelihood of finding adjacent segment lengths with similar gap fractions (see Marceau et al., 1994 for general discussion on the scale and spatial aggregation problem). LX estimates of $\Omega(\theta)$ approached unity when $P_i(\theta)$ varied little among discrete segment lengths i, while large segment-to-segment differences in $P_i(\theta)$ produced $\Omega(\theta)$ values substantially less than unity (Welles and Norman, 1991). Insertion of a partial (0.5) gap into segments where $P_i(\theta) = 0$ resulted in LX estimates of $\Omega(\theta) > 1$.

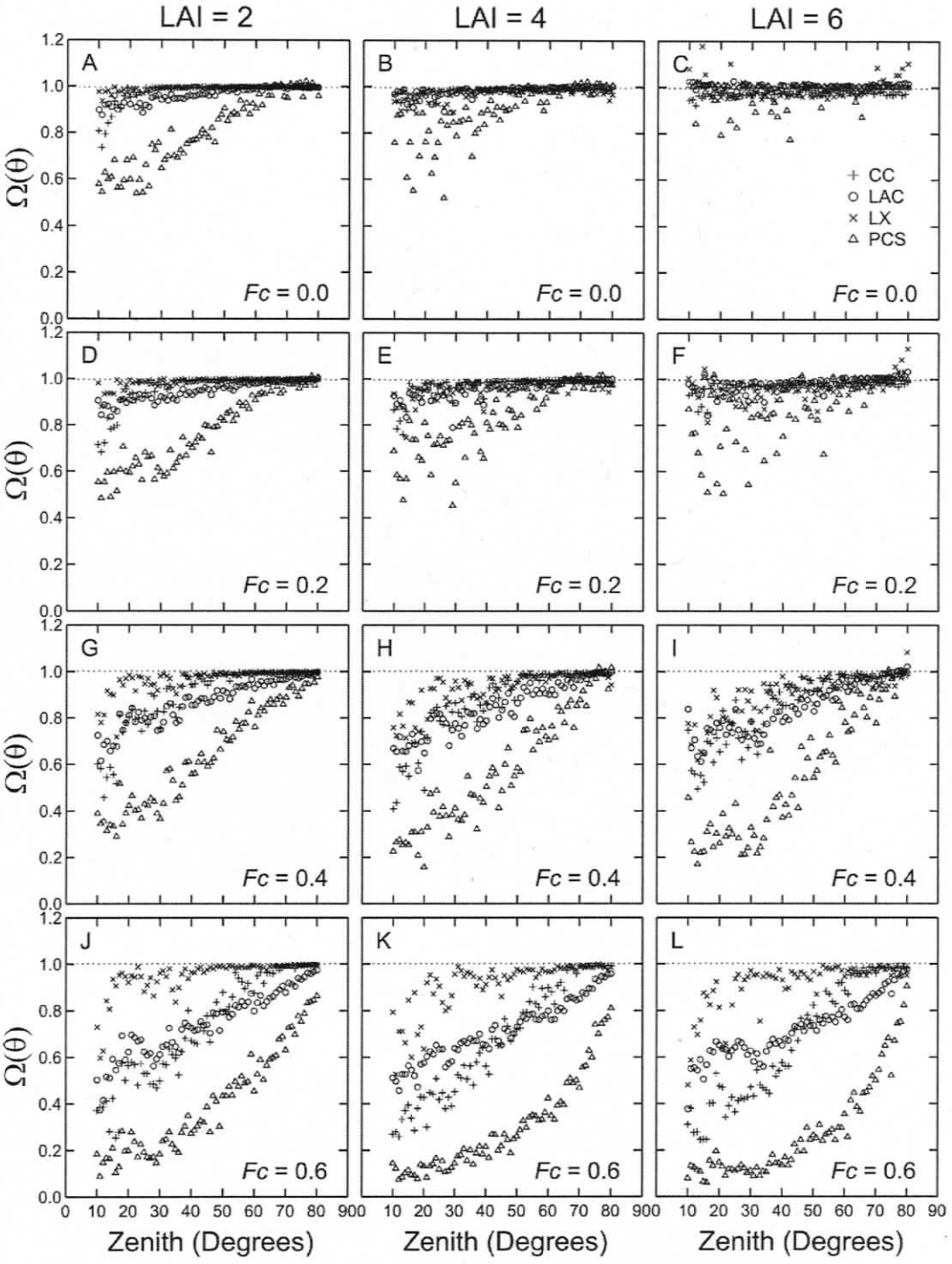

FIGURE 2.9. Scatterplots displaying the angular response of $\Omega(\theta)$ estimated by four different clumping methods (CC, LAC, LX, PCS) applied to the simulated photoset. LAI influences leaf density, the opacity of discrete foliage clumps, and interacts strongly with Fc to determine the angular pattern of $\Omega(\theta)$.

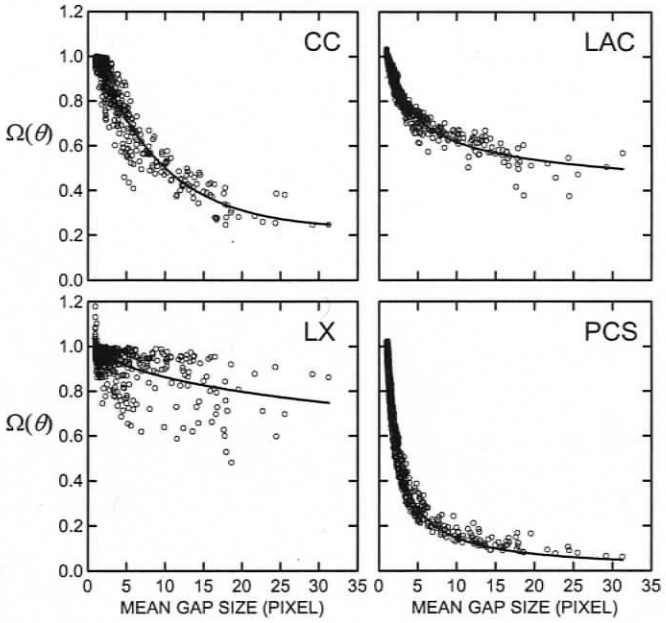

FIGURE 2.10. Nonlinear relationship between $\Omega(\theta)$ and mean gap size: CC, $R^2 = 0.92$; LAC, $R^2 = 0.96$; LX, $R^2 = 0.37$; PCS, $R^2 = 0.97$. These data were derived from the simulated fisheye photoset. The weak relationship between $\Omega_{LX}(\theta)$ and mean gap size is due to the long segment lengths used to estimate $P_i(\theta)$.

Both CC and LAC estimates of $\Omega(\theta)$ were generally lower than LX and higher than PCS at $Fc > 0$ (Fig. 2.9). However, CC and LAC were distinct from one another in their angular pattern of response to changes in the size-frequency and spatial distributions of canopy gaps. LAC, for example, was more sensitive than CC to increases in gap size when the average gap size was relatively small (near the horizon), largely because the normalized lacunarity curves used to compute $\Omega(\theta)$ resided in log-log rather than Cartesian coordinate space (Fig. 2.4). As a result, small increases in gap size caused the normalized $\overline{\Lambda_{Obs}(r)}$ curve to shift rapidly (logarithmically) away from CSR when the average gap size was small, and more slowly when the average gap size was large. CC estimates of $\Omega(\theta)$, on the other hand, were often lower than LAC at small values of θ for two reasons. First, LAC explicitly measures the degree of spatial nonrandomness across a range of spatial scales, and was therefore sensitive to the coarser-scale (*i*) random pattern of clumps within a single simulated canopy volume V, and (*ii*) uniform spatial

distribution of foliage clumps created by the side-by-side placement of multiple copies of V to produce a spatially contiguous forest canopy. Second, any single large gap removed using CC accounted for a substantially large portion of the canopy gap fraction when the instrument FOV was limited to only a small part of the canopy.

Estimates of $P(\theta)$, $\Omega(\theta)$, $G(\theta)$, and $L_t(\theta)$ extracted from fisheye photos taken at the three experimental forests also revealed a strong angular dependence that was noticeably site specific (Fig. 2.11). The black spruce stand at BOREAS, for example, exhibited (*i*) the largest and most rapid decline in mean $P(\theta)$ with increasing θ, (*ii*) the greatest change in mean $\Omega(\theta)$ between $10° \leq \theta \leq 70°$, (*iii*) a slightly erectophile (vertical) to near spherical ($G(\theta) = 0.5$) distribution of shoot, branch, and crown angles, and (*iv*) mean estimates of $L_e(\theta)$ and $L_t(\theta)$ that generally increased towards the horizon. The magnitude and angular pattern of variation in $P(\theta)$, $\Omega(\theta)$, $G(\theta)$, and $L_t(\theta)$ was markedly different for the St. Gilles sugar maple site: (*i*) mean $P(\theta)$ was low near the zenith and declined slowly with increasing θ, (*ii*) mean $\Omega(\theta)$ varied little between $10° \leq \theta \leq 70°$, (*iii*) the vertical distribution of leaf, branch, and crown angles was dominantly planophile (horizontal), and (*iv*) mean $L_e(\theta)$ and $L_t(\theta)$ declined sharply towards the horizon. CC, LAC, LX, and PCS methods produced estimates of $\Omega(\theta)$ that differed by magnitude and angular pattern, and these differences further contributed to the angular variability and uncertainty of $G(\theta)$ and $L_t(\theta)$.

The angular dependence of $P(\theta)$, $\Omega(\theta)$, $G(\theta)$, and $L_t(\theta)$ has implications for optical estimates of L, especially in forest stands that display substantial vertical and horizontal heterogeneity. First, optical measurements of L derived by Miller's theorem (Eq. 2.11) using estimates of $\Omega(\theta)$ obtained at only one or a few arbitrarily selected θ angles will be biased if those estimates differ greatly from the value of Ω integrated between $0° \leq \theta \leq 90°$ (Eq. 2.13). Second, when the vertical distribution of foliage, branch, and crown angles deviates from a spherical (random) arrangement towards planophile (horizontal), erectophile (vertical), plagiophile (oblique), or extremophile (vertical and horizontal) patterns, measurements of L based on $P(\theta)$ and $\Omega(\theta)$ sampled at 55° to 60° ($L_{57.5°}$) can be significantly different from L computed using Miller's theorem (L_{Miller}). At BOREAS, for example, LAC- and LX-based estimates of $G(\theta)$ displayed a slightly erectophile behaviour (Fig. 2.11G), and as a result have produced estimates of $L_{57.5°}$ that were larger

($p < 0.03$) than L_{Miller} (Table 2.4). Similar patterns (Fig. 2.11H) and results occurred for the Hartheim site, although the difference between $L_{57.5°}$ and L_{Miller} were only statistically significant for LX. In contrast, the vertical distribution of leaf and clump angles at St. Gilles appeared strongly planophile (Fig. 2.11I), and CC, LAC, LX, and PCS estimates of L_{Miller} were all significantly ($p \leq 0.02$) larger than $L_{57.5°}$.

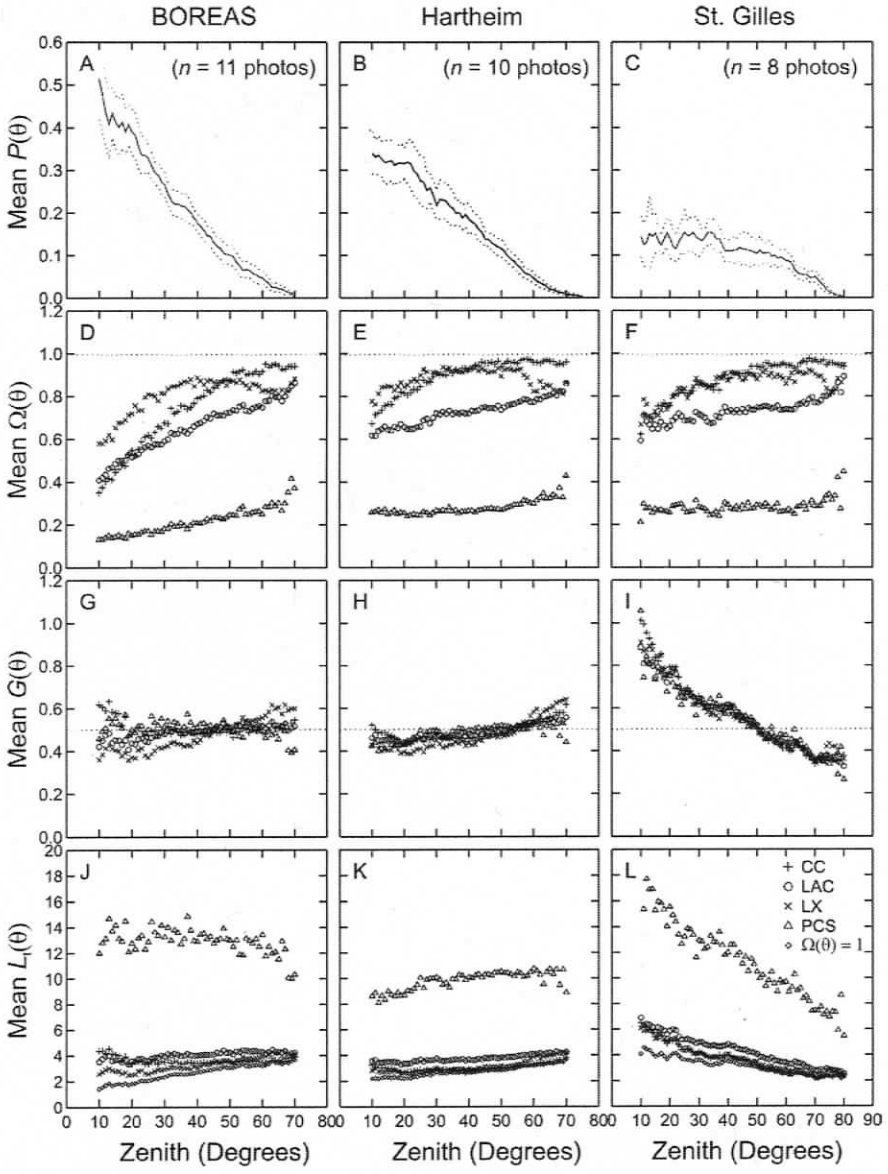

FIGURE 2.11. Line and scatterplots showing the strong angular variation in mean (A-C) $P(\theta)$, (D-F) $\Omega(\theta)$, (G-I) $G(\theta)$, (J-L) $L_e(\theta)$ and $L_t(\theta)$ retrieved from the three experimental forest sites. Dotted lines represent (A-C) 95% confidence limits; (D-F) CSR; (G-I) spherical vertical distribution of leaf and clump angles.

TABLE 2.4. Summary of L estimated by Miller's theorem and at 57.5°

		Plot Mean		Difference				
Site	Method	L_{Miller}	$L_{57.5°}$	Mean	s.d.	t	df	*Prob.*
BOREAS	CC	4.22	4.21	0.01	0.28	0.16	10	0.88
	LAC	4.89	5.13	–0.24	0.32	–2.54	10	0.03
	LX	4.13	4.55	–0.42	0.41	–3.40	10	0.01
	PCS	15.31	15.45	–0.14	2.00	–0.24	10	0.82
Hartheim	CC	3.20	3.35	–0.14	0.33	–1.40	9	0.19
	LAC	3.95	4.15	–0.19	0.29	–2.12	9	0.06
	LX	3.40	3.67	–0.27	0.34	–2.50	9	0.03
	PCS	10.54	10.80	–0.32	0.66	–1.56	9	0.15
St. Gilles	CC	3.25	2.74	0.50	0.18	7.83	7	0.00
	LAC	3.94	3.49	0.45	0.26	4.93	7	0.00
	LX	3.38	2.94	0.44	0.31	4.00	7	0.01
	PCS	10.54	9.67	0.87	0.86	2.86	7	0.02

CC-Chen and Cihlar; LAC-lacunarity; LX-Lang and Xiang; PCS-Pielou coefficient of segregation.
L_{Miller} is optical L measured using all possible zenith angles ≥ 10° (Eqs. 2.11 and 2.14).
$L_{57.5°}$ is optical L integrated using Eq. 2.11 between zenith angles 55 to 60°.
Mean and s.d. are the mean and standard deviation of paired differences.
t is the Student's t statistic computed by paired t test.
df is the degrees of freedom (n-1).
Prob. is the probability that the mean difference is zero (critical $\alpha = 0.05$).

2.4.4. Impact of image resolution on $\Omega(\theta)$ and L

Image resolution (the number and size of pixels) can have a significant impact on photo-based estimates of L_e, Ω, and L (Frazer et al., 2001; Walter et al., 2003), because pixel size determines the minimum gap or canopy element size that can be retrieved, and also influences the number and proportion of pure (canopy or sky) and mixed (canopy and sky) pixels contained within a single image. Pixel mixing specifically interferes with image classification (separation of pixels into discrete sky and canopy classes) and the accurate delineation and measurement of gap size, while pixel size alone arbitrarily defines the lower size limit of the gap-size-frequency distribution. We expect that higher

image resolutions will facilitate the capture of smaller (within-crown) canopy gaps, alleviate some occurrences of local saturation, and improve the overall accuracy of gap size and gap fraction data retrieved from canopy photos.

A comparison of mean differences in L_e, Ω, and L extracted from low- (750 × 750 pixel), medium- (1000 × 1000 pixel), and high-resolution (Full) photosets collected at the three experimental sites revealed a number of significant trends (Table 2.5). First, mean Ω_{LAC} and Ω_{PCS} both declined as image resolution increased from low to high at each site; however, the magnitude of decline in mean Ω_{PCS} (~ 0.11) was approximately twice that of Ω_{LAC}. In contrast, mean estimates of Ω_{CC} increased significantly for the Hartheim and St. Gilles photosets as image resolution increased. The magnitude of difference in mean Ω_{CC} (~ 0.05) between high and low resolutions was similar to Ω_{LAC}. No significant mean differences were found for Ω_{LX} over this range of image resolutions. Second, the large decline in Ω_{PCS} with increasing image resolution also produced substantial mean differences in L_{PCS} at each of the three sites: mean L_{PCS} increased from 10.54 (750 × 750 pixel) to 15.31 (1377 × 1377 pixel) at BOREAS, 7.5 (750 × 750 pixel) to 10.47 (1709 × 1709 pixel) at Hartheim, and 8.26 (750 × 750 pixel) to 10.54 (2004 × 2004 pixel) at St. Gilles. Because the effect of image resolution on the magnitude of Ω_{CC}, Ω_{LAC}, and Ω_{LX} was small compared to Ω_{PCS}, any variation in mean L_{CC}, L_{LAC}, and L_{LX} across the range of image resolutions was found to be relatively small and statistically insignificant.

Both Ω_{LAC} and Ω_{PCS} declined with increasing image resolution, because these two indices depend, in varying degrees, on the spatial relationship (random, aggregated, or uniform) found between black and white pixels. The primary weakness associated with LAC and PCS methods is that the number of pixels comprising any discrete canopy gap or foliage clump will increase with image resolution. Thus, sequences of black and white pixels naturally appear more spatially clumped at higher resolutions (more pixels of the same type are found together). Ω_{PCS} was particularly sensitive to changes in image resolution, because PCS is based solely on the average run lengths of black and white pixels. Ω_{LAC}, on the other hand, is derived from both the mean and variance of black- and white-pixel counts extracted at numerous spatial scales, and was thus far less sensitive to shifts in image resolution. Ω_{CC} is also affected by image resolution, because pixel size arbitrarily defines the minimum gap size of $F_m(\lambda,\theta)$. For example, coarser (lower) image

TABLE 2.5. Summary of L_e, Ω, and L for different image resolutions

		Image Resolution							
		750		1000		Full			
Site	Attribute	Mean	s.d.	Mean	s.d.	Mean	s.d.	*F*	*Prob.*
BOREAS	L_e	2.91	0.31	2.87	0.30	2.87	0.30	0.07	0.93
	Ω_{CC}	0.79	0.03	0.80	0.03	0.81	0.03	1.58	0.22
	Ω_{LAC}	0.74	0.03	0.73	0.03	0.70	0.03	7.13	0.00[1]
	Ω_{LX}	0.83	0.02	0.83	0.03	0.83	0.03	0.21	0.81
	Ω_{PCS}	0.33	0.03	0.28	0.03	0.22	0.02	35.32	0.00[2]
	L_{CC}	4.40	0.48	4.27	0.48	4.22	0.47	0.43	0.66
	L_{LAC}	4.65	0.49	4.71	0.49	4.89	0.51	0.69	0.51
	L_{LX}	4.16	0.50	4.11	0.50	4.13	0.52	0.02	0.98
	L_{PCS}	10.54	1.41	12.14	1.71	15.31	2.27	19.37	0.00[3]
Hartheim	L_e	2.92	0.29	2.86	0.28	2.87	0.27	0.15	0.86
	Ω_{CC}	0.89	0.02	0.91	0.02	0.93	0.02	12.15	0.00[3]
	Ω_{LAC}	0.80	0.02	0.78	0.02	0.75	0.02	12.64	0.00[3]
	Ω_{LX}	0.87	0.02	0.87	0.02	0.88	0.02	0.14	0.87
	Ω_{PCS}	0.40	0.03	0.38	0.03	0.28	0.01	63.88	0.00[3]
	L_{CC}	3.40	0.29	3.27	0.27	3.20	0.26	1.41	0.26
	L_{LAC}	3.80	0.29	3.78	0.28	3.95	0.29	1.08	0.35
	L_{LX}	3.48	0.30	3.40	0.28	3.40	0.28	0.27	0.77
	L_{PCS}	7.50	0.30	7.89	0.38	10.47	0.59	135.21	0.00[3]
St. Gilles*	L_e	3.14	0.50	3.05	0.47	2.89	0.39	0.58	0.57
	Ω_{CC}	0.83	0.03	0.85	0.03	0.89	0.02	10.53	0.00[3]
	Ω_{LAC}	0.79	0.03	0.77	0.03	0.73	0.03	9.15	0.00[3]
	Ω_{LX}	0.85	0.02	0.85	0.02	0.86	0.03	0.55	0.58
	Ω_{PCS}	0.38	0.04	0.35	0.04	0.27	0.03	15.54	0.00[3]
	L_{CC}	3.79	0.47	3.57	0.44	3.25	0.38	3.14	0.06
	L_{LAC}	3.96	0.51	3.93	0.48	3.94	0.42	0.01	0.99
	L_{LX}	3.71	0.63	3.61	0.61	3.38	0.51	0.68	0.52
	L_{PCS}	8.26	0.59	8.67	0.56	10.54	0.75	29.13	0.00[3]

CC-Chen and Cihlar; LAC-lacunarity; LX-Lang and Xiang; PCS-Pielou coefficient of segregation.
Ω is the clumping index integrated across all possible angles of zenith (Eq. 2.13).
L is the leaf area index in m^2/m^2 corrected for the wood (branch and bole) fraction and clumping at all spatial scales (Eq. 2.14).
*All estimates of L at St. Gilles were not corrected for the effect of branch and bole area.
Mean and s.d. are the site means and standard deviations computed for each attribute using n photos.
Image resolution: 750×750 pixel; 1000×1000 pixel; Full: 1377×1377 pixel (BOREAS); 1709×1709 pixel (Hartheim); 2004×2004 pixel (St. Gilles).
Prob. is the probability that there are no mean differences between image resolutions (critical $\alpha = 0.05$).
[1]Mean differences were only statistically significant between 750 and Full.
[2]Mean differences were statistically significant between all resolutions.
[3]Mean differences were not statistically significant between 750 and 1000.

resolutions truncate $F_m(\lambda,\theta)$ at larger minimum gap sizes, and thus have the potential to reduce the magnitude of the accumulated gap fraction $F_m(0,\theta)$, especially if the canopy contains many small gaps (e.g., St. Gilles). Since image resolution has little effect on the removed portion (gap fraction associated with the largest canopy gaps) of the 'compacted' gap fraction $F_{mr}(0,\theta)$, estimates of Ω_{CC} from low-resolution images will usually be smaller than those retrieved from high-resolution images. Interestingly, a decline in image resolution will typically produce higher estimates of L_e (Frazer et al., 2001; Walter et al., 2003) and lower values of Ω_{CC}, which in turn amplifies the disparity of mean L_{CC} between high and low resolutions (e.g., St. Gilles). Ω_{LX} was insensitive to any variation in image resolution because of the long segment lengths used to compute $P_i(\theta)$; however, we expect that estimates of Ω_{LX} derived using shorter segment lengths would be more responsive to changes in image resolution.

2.5. Conclusions

Results from our simulated fisheye photoset demonstrate the validity of the Beer-Lambert model when the spatial arrangement of foliage satisfies the required assumption of CSR. At LAI > 6, canopy gaps are rare to nonexistent under the condition of CSR, and the Beer-Lambert model becomes ineffective because the logarithm of $P(\theta) = 0$ is infinite and undefined. Therefore, a stand LAI of 5 or 6 has been widely considered the practical upper limit for optical measurements of L (Gower et al., 1999). We found that the Beer-Lambert model increasingly underestimated LAI when the simulated pattern of leaves departed from CSR towards progressively more clumped spatial arrangements. Two principal factors contributed to this underestimation: (1) in the presence of spatial clumping, the canopy gap fraction was markedly larger than what would have been expected under CSR, and (2) individual foliage clumps 'saturated' at substantially lower values of Fc when the number and density of leaves were high (LAI > 2). The opacity of discrete clumps was particularly limiting, because once saturation occurred there was no way to quantify the amount or spatial pattern of LAI contained within individual foliage clumps.

Inclusion of $\Omega(\theta)$ in the Beer-Lambert model reduced the underestimation of LAI for both the simulated and real photosets only when CC, LAC, or LX methods were used. PCS led to substantial overestimates of LAI, often by an amount that was larger than the relative difference between L_e and LAI. We, therefore, do not recommend the use of PCS as a direct measure of $\Omega(\theta)$ until modifications to the algorithm are made. LAC consistently produced the lowest underestimate of L in each of the three experimental sites, and it was the only technique that explicitly measured the integrated effect of spatial nonrandomness across a broad range of spatial scales. This multiscale measurement approach also conveniently helped to minimize any impact of image resolution on the retrieval of $\Omega_{LAC}(\theta)$. LX was the simplest technique algorithmically; however, segment length and azimuthal position are critical methodological inputs that will influence the magnitude of $\Omega_{LX}(\theta)$ in heterogeneous forest canopies. van Gardingen et al. (1999) suggested that the 'optimal' segment length would occur when measurement scale maximized the total number of segment lengths i, while still minimizing the number of occurrences where $P_i(\theta) = 0$. $\Omega_{CC}(\theta)$ was derived from the statistical distribution of gap sizes rather than directly from the original spatial pattern of canopy openings (or sunflecks). As a result, CC may not capture coarser-scale patterns of clumping that occur when stem and crown densities vary spatially within a forest stand. Lacunarity analysis may therefore provide a more direct and purely spatial approach to estimate $\Omega(\theta)$ from TRAC-derived sunfleck data.

There are two principal reasons why optical measurements of L continue to underestimate LAI even with the inclusion of $\Omega(\theta)$. First, saturation will always occur at different spatial scales and locations within a fisheye photo when the forest canopy supports a large LAI or is spatially clumped at one or more organizational levels (i.e., branch, whorl, crown, stand, etc.). Once saturation occurs, optical methods ignore the LAI contained within discrete clumps and, instead, measure only the 'imaginary' surface area of the clumps themselves. Second, the reduced spatial dimensionality of 1-D sequences of black and white pixels extracted from 2-D fisheye photos is unlikely to fully describe the complex spatial patterns of clumping that occur within the original three dimensions of canopy space. We expect that the saturation problem can be alleviated to some extent by using (1) photographic lenses with slightly longer focal lengths and

smaller FOV (120°), (2) higher spatial image resolutions, (3) non-binary threshold methods (Leblanc et al., 2005), and (4) more intensive sampling throughout the plot (Kucharik et al., 1999). The reduced spatial dimensionality of optical data is a limitation currently shared by all indirect LAI methods; however, the design of more elaborate vertical and horizontal sampling strategies and inversion models may compensate for this shortcoming.

The range of θ angles over which optical estimates of L_e and L_t are integrated is an important consideration because of the strong angular dependence of $P(\theta)$, $G(\theta)$, and $\Omega(\theta)$ in all forest canopies. Integration of L_e and L_t following Miller's theorem or using 57.5° is convenient when G is unknown. However, we found that strict adherence to Miller's theorem was never possible due to the limited length of transects at $\theta < 10°$ and absence of gaps at $\theta > 70°$. Moreover, integration of L_e and L_t across the full 180° FOV may be subject to additional measurement errors induced by steep slopes (Walter and Torquebiau, 2000) and forest-edge effects (e.g., St. Gilles) in horizontally discontinuous canopies. Limiting optical LAI estimates to a smaller range of θ angles near 57.5° may offer several advantages: (1) photographic lenses other than 180° FOV fisheyes could be used to collect canopy images; (2) longer focal-length lenses would improve image resolution because they project a smaller FOV; (3) a more restricted FOV would lessen the potential for terrain and forest-edge effects, and may perhaps improve comparisons between optical and direct LAI measurements; (4) extraction of $P(\theta)$ and $\Omega(\theta)$ at fewer θ angles would also reduce processing time. Further validation work is needed to determine how well these photo-based clumping techniques operate in other closed and discontinuous forest canopies, and also to identify the most efficient and unbiased LAI integration procedure.

2.6. References

Allain, C., Cloitre, M., 1991. Characterizing the lacunarity of random and deterministic fractal sets. Physical Review A 44, 3552–3558.

Asner, G.P., Scurlock, J.M.O., Hicke, J.A., 2003. Global synthesis of leaf area observations: Implications for ecological and remote sensing studies. Global Ecology & Biogeography 12, 191–205.

Baldocchi, D.D., Hutchison, B.A., Matt, D.R., McMillen, R.T., 1985. Canopy radiative transfer models for spherical and known leaf inclination angle distributions: A test in an oak-hickory forest. Journal of Applied Ecology 22, 539–555.

Barclay, H.J., Goodman, D., 2000. Conversion of total to projected leaf area index in conifers. Canadian Journal of Botany 78, 447–454.

Barclay, H.J., Trofymow, J.A., 2000. Relationship of readings from the LI-COR canopy analyzer to total one-sided leaf area index and stand structure in immature Douglas-fir. Forest Ecology and Management 132, 121–126.

Barclay, H.J., Trofymow, J.A., Leach, R.I., 2000. Assessing bias from boles in calculating leaf area index in immature Douglas-fir with the LI-COR canopy analyzer. Agricultural and Forest Meteorology 100, 255–260.

Bernier, P.Y., Fournier, R.A., Ung, C.H., Robitaille, G., Larocque, G.R., Lavigne, M.B., Boutin, R., Raulier, F., Paré, D., Beaubien, J., Delisle, C., 1999. Linking ecophysiology and forest productivity: an overview of the ECOLEAP project. Forestry Chronicle 75, 417–421.

Black, T.A., Chen, J.M., Lee, X., Sagar, R.M., 1991. Characteristics of shortwave and longwave irradiances under a Douglas-fir forest stand. Canadian Journal of Forest Research 21, 1020–1028.

Blumenfeld, R., Mandelbrot, B.B., 1997. Lévy dusts, Mittag–Leffler statistics, mass fractal lacunarity, and perceived dimension. Physical Review E 56, 112–118.

Bonan, G.B., 1993. Importance of leaf area index and forest type when estimating photosynthesis in boreal forests. Remote Sensing of Environment 43, 303–314.

Bond-Lamberty, B., Wang, C., Gower, S.T., 2002a. Aboveground and belowground biomass and sapwood area allometric equations for six boreal tree species of northern Manitoba. Canadian Journal of Forest Research 32, 1441–1450.

Bond-Lamberty, B., Wang, C., Gower, S.T., Norman, J., 2002b. Leaf area dynamics of boreal black spruce fire chronosequence. Tree Physiology 22, 993–1001.

Bréda, N.J.J., 2003. Ground-based measurements of leaf area index: a review of methods, instruments and current controversies. Journal of Experimental Botany 54, 2403–2417.

Castro, F., Fetcher, N., 1999. The effect of leaf clustering in the interception of light in vegetal canopies: theoretical considerations. Ecological Modelling 116, 125–134.

Cescatti, A., 1998. Effects of needle clumping in shoots and crowns on the radiative regime of a Norway spruce canopy. Annals of Forest Science 55, 89–102.

Chason, J.W., Baldocchi, D.D., Huston, M.A., 1991. A comparison of direct and indirect methods for estimating forest canopy leaf area. Agricultural and Forest Meteorology 57, 107–128.

Chen, J.M., Black, T.A., 1991. Measuring leaf area index of plant canopies with branch architecture. Agricultural and Forest Meteorology 57, 1–12.

Chen, J.M., Black, T.A., 1992. Defining leaf area index for non-flat leaves. Plant, Cell and Environment 15, 421–429.

Chen, J.M., Cihlar, J., 1995. Plant canopy gap-size theory for improving optical measurements of leaf-area index. Applied Optics 34, 6211–6222.

Chen, J.M., Govind, A., Sonnentag, O., Zhang, Y., Barr, A. Amiro, B., 2006. Leaf area index measurements at Fluxnet Canada forest sites. Agricultural and Forest Meteorology 140, 257–268.

Chen, J.M., Rich, P.M., Gower, S.T., Norman, J.M., Plummer, S., 1997. Leaf area index of boreal forests: theory, techniques, and measurements. Journal of Geophysical Research 102(D24), 29429–29443.

Cheng, Q., 1997. Multifractal modeling and lacunarity analysis. Mathematical Geology 29, 919–932.

Cooper, C.F., 1961. Pattern in ponderosa pine forests. Ecology 42, 493–499.

Dale, M.R.T., 1999. Spatial Pattern Analysis in Plant Ecology. Cambridge University Press, Cambridge, U.K.

Dale, M.R.T., 2000. Lacunarity analysis of spatial pattern: a comparison. Landscape Ecology 15, 467–478.

Deblonde, G., Penner, M., Royer, A., 1994. Measuring leaf area index with the LI-COR LAI-2000 in pine stands. Ecology 75, 1507–1511.

Fassnacht, K.S., Gower, S.T., 1997. Interrelationships among the edaphic and stand characteristics, leaf area index, and aboveground net primary production of upland forest ecosystems in north central Wisconsin. Canadian Journal of Forest Research 27, 1058–1067.

Fassnacht, K.S., Gower, S.T., Norman, J.M., McMurtrie, R.E., 1994. A comparison of optical and direct methods for estimating foliage surface area index in forests. Agricultural and Forest Meteorology 71, 183–207.

Feagin, R.A., 2003. Relationship of second-order lacunarity, Hurst exponent, Brownian motion, and pattern organization. Physica A 328, 315–321.

Fournier, R.A., Landry, R., August, N.M., Fedosejevs, G., Gauthier, R.P., 1996. Modelling light obstruction in three conifer forests using hemispherical photography and fine tree architecture. Agricultural and Forest Meteorology 82, 47–72.

Fournier, R.A., Mailly, D., Walter, J-M. N., Soudani, K., 2003. Indirect measurement of forest canopy structure from *in situ* optical sensors. In: Wulder, M.A., Franklin, S.E. (Eds.), Remote Sensing of Forest Environments: Concepts and Case Studies. Kluwer Academic Press, Norwell, Massachusetts.

Fournier, R.A., Rich, P.M., Landry, R., 1997. Hierarchical characterization of canopy architecture for boreal forest. Journal of Geophysical Research 102, 29,445–29,454.

Frazer, G.W., Canham, C.D., Lertzman, K.P., 2000. Gap Light Analyzer (GLA), Version 2.0: Image processing software to analyze true-colour, hemispherical canopy photographs. Bulletin of the Ecological Society of America 81, 191–197.

Frazer, G.W., Fournier, R.A., Trofymow, J.A., Hall, R.J., 2001. A comparison of digital and film fisheye photography for analysis of forest canopy structure and gap light transmission. Agricultural and Forest Meteorology 109, 249–263.

Frazer, G.W., Trofymow, J.A., and Lertzman, K.P., 1997. A method for estimating canopy openness, effective leaf area index, and photosynthetically active photon flux density using hemispherical photography and digital image analysis techniques. Can. For. Ser., Pac. For. Cent., Inf. Rep. No. BC-X-373.

Frazer, G.W., Wulder, M.A., Niemann, K.O., 2005. Simulation and quantification of the fine-scale spatial pattern and heterogeneity of forest canopy structure: A lacunarity-based method designed for continuous canopy heights. Forest Ecology and Management 214, 65–90.

Geffen, Y., Meir, Y., Mandelbrot, B.B., Aharony, A., 1983. Geometric implementation of hypercubic lattices with noninteger dimensionality by use of low lacunarity fractal lattices. Physical Review Letters 50, 145–148.

Gower, S.T., Kucharik, C.J., Norman, J.M., 1999. Direct and indirect estimation of leaf area index, f_{APAR}, and net primary productivity of terrestrial ecosystems. Remote Sensing of Environment 70, 29–51.

Gower, S.T., Norman, J.M., 1991. Rapid estimation of leaf area index in conifer and broad-leaf plantations. Ecology 72, 1896–1900.

Herbert, T.J., 1987. Area projections of fisheye photographic lenses. Agricultural and Forest Meteorology 39, 215–223.

Jonckheere, I., Fleck, S., Nackaerts, K., Muys, B., Coppin, P., Weiss, M., Baret, F., 2004. Review of methods for in situ leaf area index determination Part I. Theories, sensors and hemispherical photography. Agricultural and Forest Meteorology 121, 19–35.

Jonckheere, I., Muys, B., Coppin, P., 2005. Allomtery and evaluation of in situ optical LAI in Scots pine: a case study in Belgium. Tree Physiology 25, 723–732.

Kessler, A., Jaeger, L., 1999. Long-term changes in net radiation and its components above a pine forest and a grass surface in Germany. International Journal of Climatology 19, 211–226.

Kirkpatrick, L.A., and Weishampel, J.F., 2005. Quantifying spatial structure of volumetric neutral models. Ecological Modelling 186, 312–325.

Kucharik, C.J., Norman, J.M., Gower, S.T., 1999. Characterization of radiation regimes in nonrandom forest canopies: theory, measurements, and a simplified modeling approach. Tree Physiology 19, 695–706.

Kucharik, C.J., Norman, J.M., Murdock, L.M., Gower, S.T., 1997. Characterizing canopy nonrandomness with a multiband vegetation imager (MVI). Journal of Geophysical Research 102, 29,455–29,473.

Lang, A.R.G., 1991. Application of some of Cauchy's theorems to estimation of surface area of leaves, needles and branches of plants, and light transmittance. Agricultural and Forest Meteorology 55, 191–212.

Lang, A.R.G., Xiang, Y., 1986. Estimation of leaf area index from transmission of direct sunlight in discontinuous canopies. Agricultural and Forest Meteorology 37, 229–243.

Law, B.E., Van Tuyl, S., Cescatti, A., Baldocchi, D.D., 2001. Estimation of leaf area index in open-canopy ponderosa pine forests of different successional stages and management regimes in Oregon. Agricultural and Forest Meteorology 108, 1–14.

Leblanc, S.G., Chen, J.M., 2001. A practical scheme for correcting multiple scattering effects on optical LAI measurements. Agricultural and Forest Meteorology 110, 125–139.

Leblanc, S.G., Chen, J.M., Fernandes, R., Deering, D.W., Conley, A., 2005. Methodology comparison for canopy structure parameter extraction from digital hemispherical photography in boreal forests. Agricultural and Forest Meteorology 129, 187–207.

Marceau, D.J., Howarth, P.J., Gratton, D.J., 1994. Remote sensing and the measurement of geographical entities in a forested environment. 1. The scale and spatial aggregation problem. Remote Sensing of Environment 49, 93–104.

Miller, J.B., 1967. A formula for average foliage density. Australian Journal of Botany 15, 141–144.

Neumann, H.H., den Hartog, G., Shaw, R.H., 1989. Leaf area measurements based on hemispheric photographs and litter-collection in a deciduous forest during autumn leaf-fall. Agricultural and Forest Meteorology 45, 325–345.

Nilson, T., 1971. A theoretical analysis of the frequency of gaps in plant stands. Agricultural Meteorology 8, 25–38.

Nilson, T., 1999. Inversion of gap frequency data in forest stands. Agricultural and Forest Meteorology 98-99, 437–448.

Nilson, T., Kuusk, A., 2004. Improved algorithm for estimating indices from gap fraction data. Agricultural and Forest Meteorology 124, 157–169.

Nobis, M., Hunziker, U., 2005. Automatic thresholding for hemispherical canopy-photographs based on edge detection. Agricultural and Forest Meteorology 128, 243–250.

Norman, J.M., Campbell, G.S., 1989. Canopy structure. In: R.W. Pearcy, J. Ehleringer, H.A. Mooney, and P.W. Rundel (Eds.), Plant Physiological Ecology: Field Methods and Instrumentation. Chapman and Hall, London, pp. 301–326.

Oker-Blom, P., Kaufmann, M.R., Ryan, M., 1991. Performance of a canopy light interception model for conifer shoots, trees and stands. Tree Physiology 9, 227–243.

Parker, G.G., 1995. Structure and microclimate of forest canopies. In: M.D. Lowman and N.N. Nadkarni. (Eds.), Forest Canopies, Academic Press, San Diego, CA, pp. 73-106.

Pielou, E.C., 1962. Runs of one species with respect to another in transects through plant populations. Biometrics 18, 579–593.

Planchais, I., Pontailler, J.-Y., 1999. Validity of leaf areas and angles estimated in a beech forest from analysis of gap frequencies, using hemispherical photography and a plant canopy analyzer. Annals of Forest Science 56, 1–10.

Plotnick, R.E., Gardner, R.H., O'Neill, R.V., 1993. Lacunarity analysis as measures of landscape texture. Landscape Ecology 8, 201–211.

Plotnick, R.E., Gardner, R.H., Hargrove, W.W., Prestegaard, K., Perlmutter, M., 1996. Lacunarity analysis: a general technique for the analysis of spatial patterns. Physical Review E 53, 5461–5468.

Press, W.H., Flannery, B.P., Teukolsky, S.A., Vetterling, W.T., 1986. Numerical recipes: the art of scientific computing. Cambridge University Press, New York, NY.

Rich, P.M., 1990. Characterizing plant canopies with hemispherical photographs. Remote Sensing Reviews 5, 13–29.

Saunders, S.C., Chen, J., Drummer, T.D., Gustafson, E.J., Brosofske, K.D., 2005. Identifying scales of pattern in ecological data: a comparison of lacunarity, spectral and wavelet analyses. Ecological Complexity 2, 87–105.

Sellers, P.J., Hall, F.G., Kelly, R.D., Black, T.A., Baldocchi, D.B., Berry, J., Ryan, M., Ranson, K.J., Crill, P.M., Lettenmaier, D.P., Margolis, H., Cihlar, J., Newcomer, J., Fitzjarrald, D., Jarvis, P.G., Gower, S.T., Halliwell, D., Williams, D., Goodison, B., Wickland, D.E., Guertin, F.E., 1997. BOREAS in 1997: Experiment Overview, Scientific Results and Future Directions. Journal of Geophysical Research 102, 28,731–28,770.

Smith, N.J., 1993. Estimating leaf area index and light extinction coefficients in stands of Douglas-fir (*Pseudotsuga menziesii*). Canadian Journal of Forest Research 23, 317–321.

Smith, N.J., Chen, J.M., Black, T.A., 1993. Effects of clumping on estimates of stand leaf area index using the LI-COR LAI-2000. Canadian Journal of Forest Research 23, 1940–1943.

Smolander, H., Stenberg, P., 1996. Response of LAI-2000 estimates to changes in plant surface area index in a Scots pine stand. Tree Physiology 16, 345–349.

Smolander, H., Stenberg, P., Linder, S., 1994. Dependence of light interception efficiency of Scots pine shoots on structural parameters. Tree Physiology 14, 971–980.

Spanner, M., Johnson, L., Miller, J., McCreight, R., Freemantle, J., Runyon, J., and Gong, P., 1994. Remote sensing of seasonal leaf area index across the Oregon transect. Ecological Applications 4, 258–271.

Stenberg, P., 1996. Correcting LAI-2000 estimates for the clumping of needles in shoots of conifers. Agricultural and Forest Meteorology 79, 1–8.

Stenberg, P., 2006. A note on the *G*-function for needle leaf canopies. Agricultural and Forest Meteorology 136, 76–79.

Stenberg, P., Linder, S., Smolander, H., Flower-Ellis, J., 1994. Performance of the LAI-2000 plant canopy analyzer in estimating leaf area index of some Scots pine stands. Tree Physiology 14, 981–995.

Stenberg, P., Nilson, T., Smolander, H., Voipio, P., 2003. Gap fraction based estimation of LAI in Scots pine stands subjected to experimental removal of branches and stems. Canadian Journal of Remote Sensing 29, 363–370.

van Gardingen, P.R., Jackson, G.E., Hernandez-Daumas, S., Russell, G., Sharp, L., 1999. Leaf area estimates obtained for clumped canopies using hemispherical photography. Agricultural and Forest Meteorology 94, 243–257.

Walter, J-M.N., 2002. CIMES©: A package of programs for the assessment of canopy geometry through hemispherical photographs. Faculté des Sciences de la Vie, Université Louis Pasteur, Strasbourg, France.

Walter, J-M.N., Fournier, R.A., Soudani, K., Meyer, E., 2003. Integrating clumping effects in forest canopy structure: an assessment through hemispherical photographs. Canadian Journal of Remote Sensing 29, 388–410.

Walter, J-M.N., Torquebiau, E.F., 2000. The computation of forest leaf area index on slope using fish-eye sensors. C.R. Academy of Science Paris, Life Sciences 323, 801–813.

Warren-Wilson, J., 1960. Inclined point quadrats. New Phytologist 59, 1–8.

Weiss, M., Baret, F., Smith, G.J., Jonckheere, I., Coppin, P., 2004. Review of methods for in situ leaf area index (LAI) determination Part II. Estimation of LAI, errors and sampling. Agricultural and Forest Meteorology 121, 37–53.

Welles, J.M., Cohen, S., 1996. Canopy structure measurement by gap fraction analysis using commercial instrumentation. Journal of Experimental Botany 47, 1335–1342.

Welles, J.M., Norman, J.M., 1991. Instrument for indirect measurement of canopy architecture. Agronomy Journal 83, 818–825.

Whitford, K.R., Colquhoun, I.J., Lang, A.R.G., Harper, B.M., 1995. Measuring leaf area index in a sparse eucalypt forest: a comparison of estimates from direct measurement, hemispherical photography, sunlight transmittance and allometric regression. Agricultural and Forest Meteorology 74, 237–249.

CHAPTER 3

Simulation and Quantification of the Fine-scale Spatial Pattern and Heterogeneity of Forest Canopy Structure: A Lacunarity-Based Method Designed for Analysis of Continuous Canopy Heights

3.0 Abstract

Forests canopies are dynamic, continuously varying, three-dimensional structures that display substantial heterogeneity in their spatial arrangement at many scales. At the stand-level, fine-scale spatial heterogeneity influences key canopy processes and contributes to the diversity of niche space and maintenance of forest biodiversity. We present a quantitative method that we developed based on a novel application of two well-established statistical techniques—lacunarity analysis and principal component analysis (PCA)—to determine the fine-scale (0.5 to 33 m) spatial heterogeneity found in the outer surface of a forest canopy. This method was specifically designed for the analysis of continuous canopy height data generated by airborne LiDAR systems or digital photogrammetry; however, in this study we demonstrate our method using a large, well-documented dataset composed of simulated canopy surfaces only. We found that the magnitude of the lacunarity statistic was strongly associated with canopy cover (R^2 = 0.85) and gap volume (R^2 = 0.84), while the pattern of decline in lacunarity across discrete measurement scales was related to many size- and density-related attributes of stand and canopy structure ($0.27 \leq R^2 \leq 0.58$) and their diverse vertical and horizontal spatial distributions. PCA uncovered two major gradients of spatial heterogeneity from the 10 dimensions of our original lacunarity dataset. The stronger of these two gradients reflected the continuous variation in canopy cover and gap volume, while a second, more subtle gradient was associated with the array of possible vertical and horizontal spatial configurations that might define any one measure of canopy cover. We expect that this quantitative method can be used to support a broad range of practical applications in

sustainable forest management, long-term ecological monitoring, and forest science. Further research is required to understand how these statistical estimates and gradients of measured spatial heterogeneity relate to other ecologically relevant patterns of forest composition, structure, and function.

3.1. Introduction

Heterogeneity is an inherent, ubiquitous, and critical property of ecological systems, and is thought to sustain many aspects of ecosystem function and biodiversity across space and through time (Kolasa and Pickett, 1991; Caldwell and Pearcy, 1994; Pickett et al., 1997). Heterogeneity, as an ecological concept and system property, has many definitions, occurs in many forms (Kolasa and Rollo, 1991), and is strongly dependent on the spatiotemporal scales of observation and methods of measurement (Legendre and Fortin, 1989; Gardner, 1998; Gustafson, 1998; Dale, 1999). Forest ecosystems are often described by attributes of composition, structure, and function (Franklin et al., 2002), and heterogeneity arises when any or all of these attributes vary in space, time, or both (Duttilleul and Legendre, 1993; Li and Reynolds, 1995; Franklin and Van Pelt, 2004).

A precise definition of spatial heterogeneity depends upon the nature of the ecological pattern and entities of interest (Dutilleul and Legendre, 1993; Gustafson, 1998). For example, discontinuous spatial phenomena (e.g., individual tree locations, nest sites, etc.) form distinctive point patterns that are a result of their distribution throughout a region of space (Dale, 1999). In this case, spatial heterogeneity is defined by variability in density of the discrete objects or entities (referred to as events in point pattern literature) in space, and by their degree of departure from complete spatial randomness (CSR) towards aggregation or overdispersion (regularity or uniformity). CSR occurs when discrete events are dispersed both randomly and independently of one another (Diggle, 2003). Many ecological processes and system attributes, on the other hand, occur more continuously over space or time (e.g., photosynthesis, temperature, humidity, canopy density, etc.). Continuous spatial phenomena are considered to be heterogeneous when one or more ecosystem attributes vary across discrete subregions of space in an

irregular or nonrandom manner (Dutilleul and Legendre, 1993). Measures of spatial heterogeneity are almost always tied to variability in time, because ecosystems are by definition inherently dynamic in both space and time (Gustafson, 1998).

Forest canopies are dynamic, continuously varying, three-dimensional (3-D) spatial structures composed mostly of leaves, twigs, branches, and the open spaces (gaps) among them (Parker, 1995). Canopies are shaped by all components of stand structure including live tree-size and age distributions, stem density, species composition, crown widths and depths, leaf area and density, growth form, and the spatial arrangement of individual boles (Spies, 1998). The fine-scale spatial structure of forest canopies is often conceptualized within a hierarchical framework (Fournier et al., 1997), where individual leaves are organized into increasingly coarser-scale structures, such as shoots or twigs, branches, whorls, crowns, and finally into spatial neighbourhoods of individual crowns (Parker, 1995; Song et al., 1997; Cescatti, 1998). At coarser spatial scales, discrete neighbourhoods of individual crowns coalesce to form homogeneous stands (patches), which may be similar in disturbance history, age class, species composition, and site productivity, and between-patch rather than within-patch spatial heterogeneity emerges as the dominant characteristic of forest structure (Lertzman and Fall, 1998).

Fine-scale canopy structure and its vertical and horizontal spatial heterogeneity play key roles in regulating the spatial and temporal variability of stand microclimate (Chen et al., 1999), light interception, photosynthesis, carbon gain, and primary production (Parker, 1995), atmosphere–biosphere exchanges of energy, matter, and trace gases (Parker et al., 2004a), nutrient and hydrological cycles (Prescott, 2002; Nadkarni and Sumera, 2004), stand dynamics (Canham et al., 1994; Herwitz et al., 2000), and biodiversity (Carey, 2003; Ishii et al., 2004; Spies, 2004). Fine-scale canopy patterns, processes, and dynamics naturally scale across larger aggregates of time and space, and therefore also contribute to broader-scale ecological patterns, processes, and dynamics (Ehleringer and Field, 1993; Saunders et al., 1998).

Despite the significance of spatial heterogeneity in theoretical and applied ecology, few methods exist to determine this key attribute of forest canopy structure. Quantification of spatial heterogeneity has been hampered in the past by four main factors. First, consensus on an operational definition of spatial heterogeneity did not exist

in ecology until recently (Kolasa and Rollo, 1991; Dutilleul and Legendre, 1993; Li and Reynolds, 1995). Second, those relying on analytical techniques that measure spatial pattern or texture at only one, arbitrarily defined, observation scale have ignored the fact that pattern is often highly scale dependent (Gardner, 1998; Dale, 1999). Third, limited access to the forest canopy has forced many researchers to rely on ground-based sampling, datasets of restricted dimensionality (i.e., points and transects), and aspatial metrics (e.g., Shannon's Index; Staudhammer and LeMay, 2001) to characterize the spatial heterogeneity associated with 3-D patterns of canopy structure. Last, many of the statistical techniques (e.g., semivariance, Moran's I, Geary's c, and Grey Level Co-occurrence Matrix) commonly used to quantify spatial pattern in ecological or remotely sensed data depend, in varying degrees, on the unlikely assumption of second-order stationarity[2] to remain unbiased (Henebry and Kux, 1995; Weishampel et al., 2001; Perry et al., 2002).

Efforts to quantify the spatial heterogeneity of forest canopies have focused on three distinct methodological approaches. The first approach relies on skyward-looking, ground-based optical instruments such as solar radiation sensors (Baldocchi and Collineau, 1994; Brown and Parker, 1994; Montgomery and Chazdon, 2001), fisheye photography (Walter and Himmler, 1996; Trichon et al., 1998; Frazer et al., 2000), and range-finding lasers (Parker et al., 2004b) to characterize canopy structure. Aspatial statistical descriptions of these field data include mean values of key canopy variables (e.g., gap fraction, openness, leaf area index) and their variances (Trichon et al., 1998; Frazer et al., 2000), and diversity indices describing vertical distributions of canopy elements (Parker et al., 2004b). The scale-dependent structure of sunflecks, gaps, leaf area, and canopy height over a given spatial domain has been investigated using semivariance, spectral analysis, wavelets, and local quadrat variances (Bradshaw and

[2] Second-order stationarity exists when an attribute of interest is normally distributed with the same mean and variance over the entire sampling area (Legendre and Legendre, 1998). Under conditions of second-order stationarity, covariance between a pair of random variables is only dependent on the distance of separation between sample points and not on location within the study area. Spatial stationarity is often an unreasonable assumption for heterogeneous forest canopies because of continuously varying local and regional influences of resource and environmental heterogeneity, community composition, successional processes, and disturbance regimes on all aspects of stand and canopy structure.

Spies, 1992; Baldocchi and Collineau, 1994; Walter and Himmler, 1996; Bartemucci et al., 2002).

The second methodological approach utilizes the simulated or real point pattern of tree locations coupled with 3-D crown models or spatial tessellations (e.g., Zenner and Hibbs, 2000) to explore the continuously varying structure of forest canopies (Van Pelt and North, 1996; Song et al., 1997; Chen and Bradshaw, 1999; Van Pelt and Franklin, 2000; Silbernagel and Moeur, 2001; Song et al., 2004; Van Pelt and Nadkarni, 2004). In forest research, nearest-neighbour and Ripley's K statistical analyses are commonly used to determine if a pattern of discrete events (stem locations) or points between the events are spatially random, aggregated, or overdispersed (Moeur, 1993; Stoyan and Penttinen, 2000). Ripley's K was specifically designed to identify the scale dependence of these point patterns. In addition, vertical and hemispherical projections of canopy crown models (Van Pelt and North, 1996; Song et al. 1997; Silbernagel and Moeur, 2001) and the size-distribution of patches (polygons) generated by spatial tessellation (Zenner and Hibbs, 2000) have facilitated the measurement of canopy patchiness in the horizontal domain. Sampling 3-D canopy models in the vertical dimension has been used to determine the spatial variability of intercrown gaps and crown volume from the top of forest canopy to the forest floor (Van Pelt and North, 1996; Song et al., 2004).

Finally, the fine-scale spatial pattern and structure of forest canopies have been studied from above using air- and space-borne optical (Cohen et al., 1990; Treitz and Howarth, 2000), radar (Sun and Ranson, 1998), and laser (LiDAR - light detection and ranging) remote sensing (Drake and Weishampel, 2000; Weishampel et al., 2000; Ollier et al., 2003; Parker and Russ, 2004). Small-footprint, discrete-return LiDAR has been identified as a particularly useful remote sensing technology in forest studies (Lefsky et al., 2002; Lim et al., 2003), because of its unique ability to accurately measure fine-scale (<1 m) canopy structure in both vertical and horizontal spatial domains (Zimble et al., 2003; Koukoulas and Blackburn, 2004; Parker et al., 2004a; Parker and Russ, 2004).

The main purpose of this paper is to describe a quantitative method that we devised for measuring the fine-scale (<50 m) spatial heterogeneity or texture found in the surface topography of a forest canopy. This technique is based on a novel application of two well-established statistical techniques: lacunarity analysis and principal component

analysis (PCA). We used the lacunarity statistic as a scale-dependent estimate of canopy texture and spatial non-stationarity, while PCA facilitated the separation of individual sample units along unique gradients of spatial pattern and canopy structure based on differences in lacunarity measured at nine discrete spatial scales. Our method was designed specifically for the analysis of 2-D canopy height models extracted from airborne LiDAR data; however, in this study we demonstrate its application using simulated canopy surfaces only. We have five principal objectives in this paper:

(1) To provide a brief introduction to lacunarity as a concept and analytical method, and to describe its potential application to 2-D quantitative canopy height data.

(2) To present a detailed case study illustrating the scale-dependent response of the lacunarity statistic to five different simulated canopy surface patterns.

(3) To demonstrate how lacunarity analysis and PCA can be combined to effectively separate a large number of canopy surface patterns in reduced ordination space based on cross-scale differences in spatial heterogeneity.

(4) To identify specific attributes of canopy structure that contributed to the unique spatial and structural gradients uncovered by lacunarity analysis and PCA.

(5) To suggest a number of potential ecological applications for this research.

3.2. Spatial Pattern Analysis

3.2.1. Lacunarity as a scale-dependent measure of spatial heterogeneity in forest canopies

Lacunarity derives from the Latin word, *lacuna*, meaning 'gap', and was first introduced by Mandelbrot (1983: 310) to describe the 'gapiness' or texture of fractals. The concept of lacunarity, however, applies equally to non-fractals (Allain and Cloitre, 1991), and is more formally defined as the scale-dependent deviation of a geometrical object or pattern from translational invariance or homogeneity (Gefen et al., 1983; Cheng, 1997). Geometrical patterns with low lacunarity are finely textured and homogeneous with respect to the size distribution and spatial arrangement of gaps. In contrast, coarsely textured patterns that show substantial heterogeneity in the size distribution and spatial arrangement of gaps are described as being highly 'lacunar'

(Blumenfeld and Mandelbrot, 1997). Statistical estimates of lacunarity are strongly dependent on both the spatial scale (i.e., grain or resolution) and extent of observation (Plotnick et al., 1993; Dale, 2000). For example, a spatial pattern that is heterogeneous at one observation scale may appear homogeneous at finer or coarser measurement scales. Similarly, one region of space may reveal a very different scale-dependent pattern of heterogeneity than another region. Lacunarity has therefore become a useful concept and analytical technique to study the scale-dependent heterogeneity of a broad range of spatiotemporal phenomena in ecology and remote sensing (e.g., Plotnick et al., 1996; Sun and Ranson, 1998; Weishampel et al. 2000; Saunders et al., 2005).

The spatial pattern and structure of the outer surface of a forest canopy is determined by the size, shape, abundance, and spatial distribution of canopy trees (or overstory), as well as by the varied gap sizes found within and among tree crowns. Spatial heterogeneity in the height of the outer canopy surface can be observed at many different scales. For example, leaf display, branch geometry, and within-crown gaps contribute to the finest scales of canopy height variation. At coarser spatial scales, heterogeneity is created by differences in the size and geometry of individual crowns and intercrown gaps. Finally, local variations in stem density, species composition, and spatial aggregation among crowns of similar size and height (patches of regeneration, biological legacies, or dominant canopy trees), and major tree-fall gaps produce the coarsest scales of stand-level spatial heterogeneity in forest canopy height.

We created two separate sets of simulated 50 m × 50 m (0.25 ha) forest canopy height models (CHM) to demonstrate how lacunarity analysis can be used to examine the cross-scale spatial pattern and heterogeneity of forest canopies. The first simulated dataset included five CHMs, while the second consisted of 187 separate CHMs (Appendix 3A). The size of each of these datasets was arbitrarily chosen. We utilized the first dataset to briefly illustrate and explain the scale-dependent response of the lacunarity statistic to a few simple and complex canopy surface patterns. We then used the larger, second dataset to show how lacunarity analysis and PCA facilitated the separation and comparison of sample units in reduced ordination space based on cross-scale differences in canopy surface pattern. We chose a 3-D simulation approach rather than LiDAR-generated CHMs to develop this quantitative method, because simulation permitted us

strict control over the composition and spatial arrangement of stand structure, and it also allowed us to quickly generate a large, well-documented dataset covering a broad range of canopy surface patterns. Nevertheless, we recognize that simulated CHMs lack the fine-scale detail (i.e., foliage and branch architecture, and within-crown gaps) and coarse-scale realism of natural forest patterns (i.e., dispersion of tree locations), as well as the measurement error or noise inherent in all remotely sensed data. However, our intent here was not to derive an ecological interpretation of these simulated data, but rather only to illustrate and explain the statistical behaviour of lacunarity as a potentially useful quantitative measure of spatial heterogeneity in forest canopy research.

3.2.2. Lacunarity analysis using the 'gliding-box' algorithm and 2-D quantitative data

The 'gliding-box' algorithm (see Plotnick et al., 1993, 1996 for description) was first introduced by Allain and Cloitre (1991) to compute the lacunarity of random or deterministic fractal sets composed of binary (i.e., occupied ($M = 1$) or unoccupied ($M = 0$)) patterns. However, the method was later expanded to include scale-dependent measures of lacunarity for fractal and non-fractal sets (binary patterns) and fields (quantitative spatial data) of one or more Euclidean dimensions (Plotnick et al., 1996; Cheng, 1997; Kirkpatrick and Weishampel, 2005). Here, we use the gliding-box algorithm to compute lacunarity at discrete measurement scales s (0.5 m $\leq s \leq$ 33 m) by sampling the distribution of mass across a regularized m (columns) $\times$ n (rows) grid of quantitative canopy heights x_{ij}. In this application, mass M (box mass) is defined as the sum or integral of all canopy heights x_{kl} contained within a square gliding box of linear size r; where, r is the box size measured in grid-cell units (i.e., r = 1, 2, 3, . . .), and subscripts k and l are unique column and row identifiers for each cell height x_{ij} summed within the bounds of the gliding box. The frequency distribution of mass at box size r is sampled by gliding a box of size r one grid-cell position at a time starting at the origin of the grid until all columns i and rows j of the $m \times n$ grid have been sampled. The total number of boxes $N(r)$ of size r required to cover the entire $m \times n$ grid is given by Sun and Ranson (1998):

$$N(r) = (m - r + 1)(n - r + 1) \tag{3.1}$$

The frequency distribution of mass M at box size r is converted to a probability function $Q(M,r)$ by dividing the frequency of each mass M by $N(r)$ (Allain and Cloitre, 1991). The first and second statistical moments of the probability function $Q(M,r)$ are estimated using the following equations (Cheng, 1997; Dale, 2000):

$$Z_Q^{(1)}(r) = \frac{1}{N(r)} \sum_{i=1}^{m-r+1} \sum_{j=1}^{n-r+1} \sum_{k=1}^{i+r-1} \sum_{l=1}^{j+r-1} x_{kl} \tag{3.2}$$

$$Z_Q^{(2)}(r) = \frac{1}{N(r)} \sum_{i=1}^{m-r+1} \sum_{j=1}^{n-r+1} \left(\sum_{k=1}^{i+r-1} \sum_{l=1}^{j+r-1} x_{kl} \right)^2 \tag{3.3}$$

Finally, lacunarity at box size r is computed as a dimensionless statistic using the equation:

$$\Lambda(r) = \frac{Z_Q^{(2)}(r)}{\left[Z_Q^{(1)}(r)\right]^2} = 1 + \frac{\sigma_Q^2(r)}{\left[Z_Q^{(1)}(r)\right]^2} \tag{3.4}$$

where $\sigma_Q^2(r)$ is the sample variance, and $Z_Q^{(1)}(r)$ is the mean of the probability function $Q(M,r)$ (Plotnick et al., 1996; Cheng, 1997). Repeating the lacunarity calculations at box sizes ranging from $r = 1$ to some proportion of the shortest length of the grid map reveals a unique scale-dependent pattern of decline in the logarithm of the lacunarity statistic when plotted against the logarithm of box size.

3.2.3. Five examples illustrating the application of lacunarity analysis to forest CHMs

Canopy surface patterns have been simulated by others using a combination of spatial point processes and 3-D crown modeling techniques (e.g., Song et al., 2004; Van Pelt and Nadkarni, 2004). Three of the five simulated CHMs presented here are examples of random, aggregated, and uniform (overdispersed) point patterns each composed of 100 trees (Fig. 3.1; Table 3.1). The first three examples (Figs. 3.1A–C) are represented by different point patterns with identical tree heights and crown dimensions, while the last two examples (Figs. 3.1D and E) have the same random pattern as Fig. 3.1A, but with variable tree heights and crown sizes. In the last example (Fig. 3.1E), the stand table used

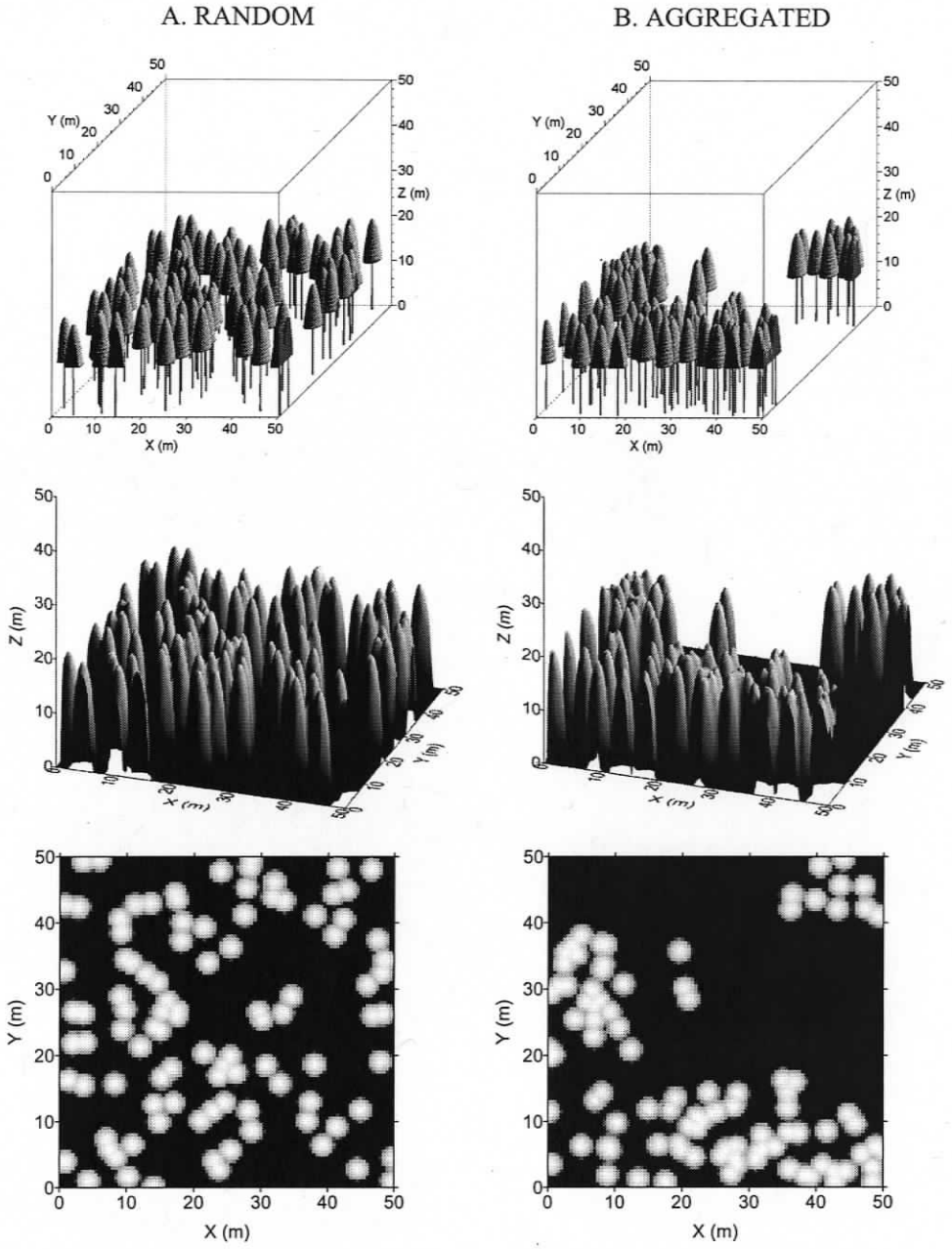

FIGURE 3.1. Five examples of simulated 3-D stand models (top graphic) and canopy height models (middle and bottom graphics) developed for A) Random, B) Aggregated, and C) Uniform distributions of tree locations. We used the stem locations generated for the Random model to create two other more complex canopy patterns by (D) randomly assigning a range of tree sizes to the random stem locations, and (E) by spatially sorting these variable tree sizes so that tree height increased with decreasing distance along the *X* axis of the plot. All five canopy height models contain the same number of trees (n = 100), and have a spatial resolution of 0.5 m.

C. UNIFORM

D. RANDOM (DIVERSE)

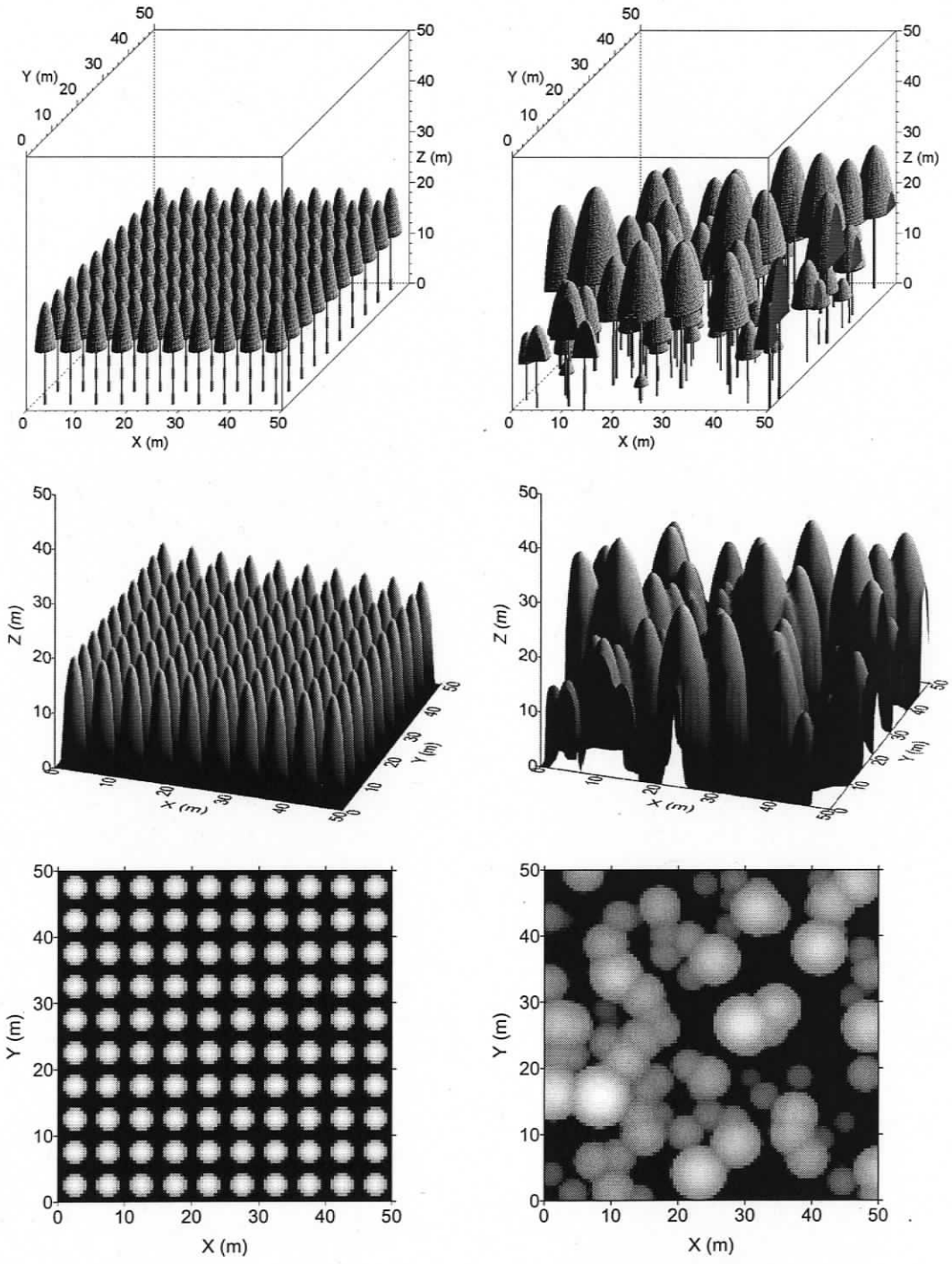

FIGURE 3.1. (Cont'd)

E. RANDOM (DIVERSE, SORTED)

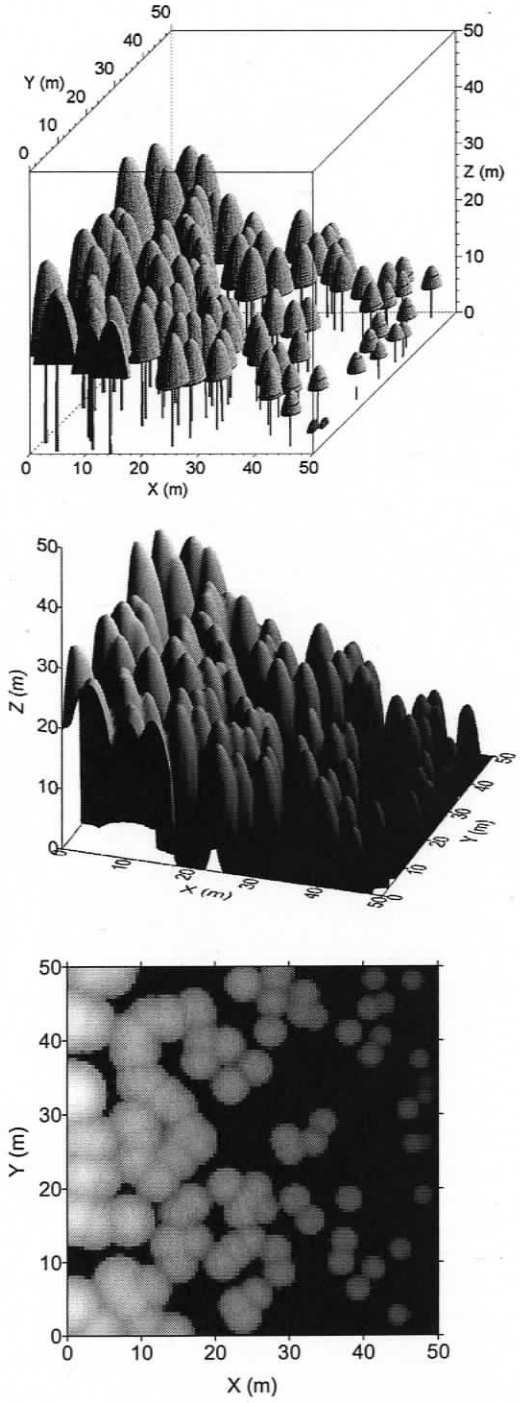

FIGURE 3.1. (Cont'd.)

TABLE 3.1. Stand attributes and spatial characteristics of five simulated forest canopies

	Examples of Simulated Canopy Height Models				
Stand Attributes	Model A. (Random)	Model B. (Aggregated)	Model C. (Uniform)	Model D. (Diverse)	Model E. (Sorted)
Tree Height (m):					
Min.	20.00	20.00	20.00	4.14	4.14
Max.	20.00	20.00	20.00	36.00	36.00
Avg.[a]	20.00	20.00	20.00	19.35	19.35
COV[b]	0	0	0	0.37	0.37
DBH (cm):					
Min.	23.50	23.50	23.50	4.02	4.02
Max.	23.50	23.50	23.50	58.60	58.60
Avg.[a]	23.50	23.50	23.50	24.89	24.89
COV[b]	0	0	0	0.48	0.48
Crown Diameter (m):					
Min.	5.32	5.32	5.32	2.08	2.08
Max.	5.32	5.32	5.32	9.57	9.57
Avg.[a]	5.32	5.32	5.32	5.37	5.37
COV[b]	0	0	0	0.31	0.31
Crown Depth (m):					
Min.	9.00	9.00	9.00	1.48	1.48
Max.	9.00	9.00	9.00	17.11	17.11
Avg.[a]	9.00	9.00	9.00	8.24	8.24
COV[b]	0	0	0	0.42	0.42
No. of Trees	100	100	100	100	100
Stem Density (n/ha)	400	400	400	400	400
Lorey's Height[c] (m)	20.00	20.00	20.00	25.26	25.26
Basal Area (m^2/ha)	17.35	17.35	17.35	23.90	23.90
Pollard's Statistic[d]	1.009	3.546	0.119	1.006	1.049
SHDI[e]	0	0	0	2.41	2.41
Canopy Cover[f] (%)	41.55	32.87	52.00	68.46	60.95
Gap Volume[g] (%)	73.04	77.63	69.04	37.69	49.48

[a] Arithmetic mean.
[b] Coefficient of variation (standard deviation divided by the mean).
[c] Lorey's height is the basal-area-weighted mean stand height.
[d] Origin-to-point nearest-neighbour statistic (random: $P_O \approx 1$; aggregated: $P_O > 1$; uniform: $P_O < 1$).
[e] Shannon's Height Diversity Index (values >0 indicate increasing height diversity).
[f] Number of canopy heights > 2 m divided by total number of grid cells times 100 %.
[g] Percentage volume of empty (gap) space between the height of the tallest tree and the height of the upper canopy surface (see Table 3.2).

to generate Fig. 3.1D was spatially sorted so that tree height increased with decreasing distance along the *X* dimension of the plot.

Lacunarity analyses of these five CHMs produce very distinct curves when logarithmic transforms of lacunarity $\Lambda(r)$ and box size r are plotted against one another (Fig. 3.2). All double-log curves show a decline in lacunarity with increase in box size; however, all curves differ in magnitude at their maxima, some decline more rapidly than others (e.g., A, C, F), and all show subtle breaks in slope at different measurement scales. Self-similar fractals produce lacunarity curves that are straight lines, with slopes equal to fractal dimension *D* minus Euclidean dimension *E* (Allain and Cloitre, 1991; Plotnick et al., 1996). Lacunarity is determined by the proportion of the grid map covered by vegetative canopy, and by the mean and variance of the distribution of canopy heights across the plot (Feagin, 2003). Dividing each value of lacunarity $\Lambda(r)$ by $\Lambda(1)$ eliminates the effect of the first statistical moment (mean), thereby normalizing the lacunarity curve to a common *Y*-intercept of 1 (Plotnick et al., 1996; Feagin, 2003). Normalization of the lacunarity statistic $\Lambda(r)$ allows direct comparison of curves between sample plots of different canopy height, cover, and spatial pattern (bottom graph, Fig. 3.2).

Three general characteristics of the lacunarity statistic $\Lambda(r)$ emerge from analysis of these five CHMs and through other published studies (e.g., Plotnick et al., 1996; Dale, 2000). First, lacunarity at box size $r = 1$ will increase as the percentage of canopy cover decreases and gap volume increases. For example, Model B (Fig. 3.1B) has the highest lacunarity ($\Lambda(1) = 3.669$), lowest canopy cover (32.9%), and highest gap volume (77.6%) of all five models, while Model D (Fig. 3.1D) has the lowest lacunarity ($\Lambda(1) = 1.733$), highest canopy cover (68.5%), and lowest gap volume (37.7%). In general, larger values of the lacunarity statistic observed at a given spatial scale imply greater spatial heterogeneity or texture (patchiness) of the canopy surface at that scale. On the other hand, lacunarity values approaching 1 indicate low spatial variability in canopy heights and therefore greater translational invariance or homogeneity in the canopy surface at that scale of measurement.

Second, the rate of decline in lacunarity with increasing box size depends on the presence and heterogeneity of coarser-scale patterns. Lacunarity curves that decline more slowly with increasing spatial scale indicate the occurrence of coarser-scale patterns

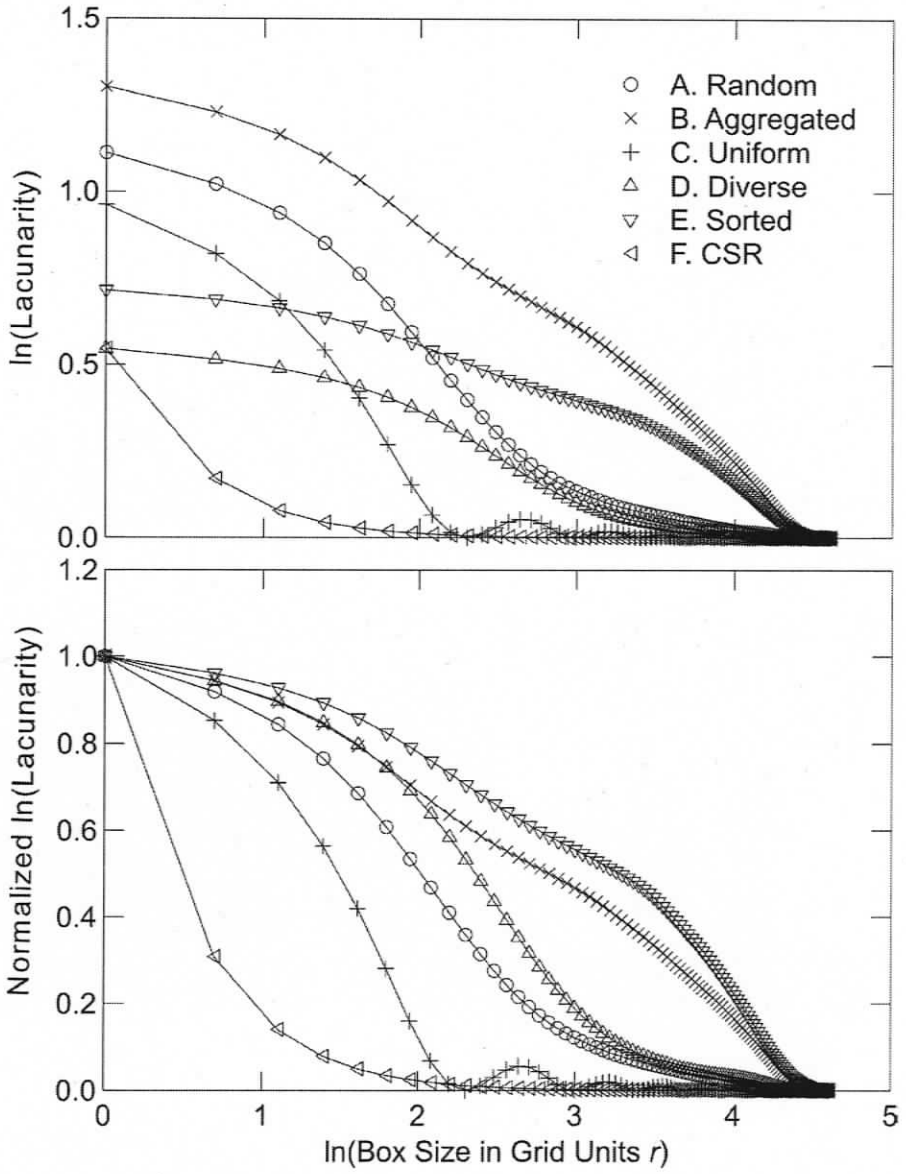

FIGURE 3.2. Line- and scatterplots showing the natural logarithm of the lacunarity statistic plotted against the natural logarithm of box size *r*. The top graphic reveals the true magnitude of the lacunarity statistic at each measurement scale and the overall shape of the lacunarity curve, while the normalized lacunarity curve (bottom graphic) removes the effect of the first statistical moment (mean) and allows direct comparison of all six curve shapes. Lacunarity curves that decline more slowly with increasing box size indicate the presence of spatial structure or pattern at coarser measurement scales (e.g., curves B and E). In contrast, lacunarity curves exhibiting rapid decline imply randomness or uniformity at coarser spatial scales (e.g., curves A, C, and F). We derived lacunarity curve F from the analysis of a spatially randomized model (CSR) generated from Model D.

(Plotnick et al., 1993, 1996). Alternatively, lacunarity curves showing a rapid decline with increasing box size imply spatial randomness or uniformity at coarser measurement scales. Dale (2000) suggests using randomization procedures (see Manly, 1997) and CSR as the null model if tests of statistical significance are required. Lacunarity curves B and E are examples of curve forms that diminish more slowly with increasing spatial scale (Fig. 3.2). These curves decline more slowly in response to the aggregation of crowns at various levels of organization within the two CHMs (Model B and E). Model E (Fig. 3.1E), for example, was constructed using a random pattern of stem locations; however, tree heights were spatially sorted to create a strong gradient of canopy height, density, and gap size along the *X* dimension of the plot. As a result, all of the largest canopy trees coalesce to form a very dense, tall canopy on the left side of the plot, while the right side is dominated by a sparse, low canopy composed of short trees, small crowns, and large intercrown gaps. Models A and C are represented by lacunarity curves that decline more rapidly with increasing scale due to the random and uniform distributions of stem positions and tree sizes of identical height and crown form. Lacunarity curve F (CSR) was generated by analyzing the pseudo-randomized canopy heights of Model D.

Third, breaks in slope along the lacunarity curve mark scale-dependent peaks in variance that signify the transition from one discrete scale of pattern to another (Plotnick et al., 1996; Dale, 2000). Here, pattern is formed by the alternating patches of local high points surrounded by low points (outliers), and local low points surrounded by high points (inliers). Variation in pattern across scale is strongly linked to the hierarchical clumping of foliage into individual crowns of variable sizes and shapes, and the aggregation of trees of similar size into distinct neighbourhoods (e.g., regeneration in tree-fall gaps). Patterns of foliage clumping also influence the presence and spatial character of canopy gaps, and so discrete scales of pattern are a consequence of the spatial structure contributed by both foliage clumps and canopy gaps (Dale, 2000). Scale-dependent peaks in variance (and lacunarity) occur when the scale of measurement approximately matches the mean size and mass of unique structural features present within the canopy surface (Marceau et al., 1994; Dale, 2000). For example, all canopy models, with the exception of the pseudo-randomized model (CSR), are represented by

lacunarity curves that remain relatively high over the first few box sizes because of the clumping of foliage into discrete crowns. In the case of Model B, small crowns are further aggregated into small clumps of randomly distributed trees, and these clumps are in turn randomly distributed within the plot. As a result, the normalized lacunarity curve for Model B reveals a subtle break in the slope at approximately box size $\ln(r) = 3.1$, due to the aggregation of tree clusters in the lower half of the plot. Model E also shows a similar break in slope at box size $\ln(r) = 3.5$, due to the clumping of large trees in one half of the plot.

3.3. Forest Canopy Simulation and Pattern Ordination

3.3.1. Development of simulated CHMs

We constructed all of our 3-D stand models and their derivative CHMs from simulated stand tables that described the stem location, height, and diameter, crown width and depth, and species for each tree contained in the list. We chose *Pseudotsuga menziesii* (Mirb.) Franco var. *menziesii* (Douglas-fir) as the dominant and only tree species to include in these stand tables for two reasons: (1) this study was part of a larger research project designed to evaluate the utility of airborne LiDAR as a potential forest inventory and ecological monitoring tool in the coastal *Pseudotsuga-Tsuga* forests of southeastern Vancouver Island, British Columbia, and (2) use of a single tree species greatly simplified the modelling process without compromising any of our objectives. We created four distinct stand classes based largely on differences in mean height and standard deviation (s.d.): Short (7.89 m ± 0.25 s.d.; $n = 48$), Medium (19.70 m ± 4.79 s.d.; $n = 56$), Tall (27.73 m ± 10.07 s.d.; $n = 48$), and Natural (14.19 m ± 4.22 s.d.; $n = 35$) classes. Unlike other stand classes, the Natural class was constructed using the unpublished tree heights, diameters, and crown depths sampled by the senior author in 12 young (35 yr.) to old (>250 yr.), 0.25 ha forest plots established in managed and natural *Pseudotsuga-Tsuga* forests on southeastern Vancouver Island, BC.

We manipulated three stand attributes to simulate a wide range of canopy surface patterns: the spatial point pattern of tree locations, tree-height distribution, and stand density. We used the binomial, Poisson clustering, and Sequential Spatial Inhibition

models implemented in S+SpatialStats Version 2.0 (Kaluzny et al., 1998) to compute a variety of random, aggregated, and uniform point patterns, respectively. We assigned stem heights to each tree in the stand table using pseudo-random heights drawn from normal, uniform, and Weibull distributions generated by random variate functions in SYSTAT Version 10.2. Diameter at breast height (DBH) and crown depth were predicted for each tree using linearized forms of a combined exponential and power function:

$$\ln(DBH) = -0.05318 + 0.96275\ln(HT) + 0.01872HT \tag{3.5}$$

and multiplicative model:

$$\ln(CD) = -1.08100 + 0.35274\ln(DBH) + 0.69334\ln(HT) \tag{3.6}$$

where *DBH* is the stem diameter at breast height (1.4 m) in centimetre, *HT* is tree height in metre, and *CD* is the crown depth in metre. Both models were fit by ordinary least squares regression using a subset of the unpublished heights, diameters, and crown depths mentioned above for 830 sampled Douglas-fir trees ranging in height from 1.3 to 55 m. The coefficients of determination, R^2, associated with Equations (5) and (6) were 0.91 and 0.77, respectively. Maximum crown widths were predicted using two published equations developed from 925 Douglas-fir trees measured near Corvallis, Oregon (Hann, 1999):

$$MCW = 1.4081 + 0.22111DBH - 0.00053438DBH^2 \tag{3.7}$$

$$LCW = MCW \times CR^{\left(0.0143149CD + 0.0722402\frac{DBH}{HT}\right)} \tag{3.8}$$

where *MCW* is the maximum crown width of an open-grown tree in metre; *LCW* is the largest crown width of a stand-grown tree in metre, and *CR* is the crown ratio (crown depth divided by tree height). The crown profile was modelled as a parabola using the quadratic function:

$$f(x) = a(x-h)^2 + k \tag{3.9}$$

where x is the crown radius in m ($x \geq 0$); h is the vertical axis of symmetry ($h = 0$); k is the maximum tree or crown height in m ($k > 0$); (h, k) represents the vertex of the parabola in Cartesian coordinates, and a is a shape factor controlling the rate and

direction of crown profile curvature ($a < 0$). The shape factor a is determined by the crown's maximum depth and radius:

$$a = \frac{-CD}{(0.5LCW)^2}. \tag{3.10}$$

We constructed our 3-D stand models by slicing a continuous 50 m (length) × 50 m (width) × 60 m (height) canopy volume (1.5×10^5 m^3) into discrete 10 cm (0.001 m^3) volume elements (voxels), and then populating each voxel with the value 1 for canopy or 0 for gap, based on the tree positions and crown dimensions defined in the stand table (see top graphic in Fig. 3.1). A simulated CHM was generated by extracting the maximum canopy height at each *XY* position of the 3-D stand model using a 0.5 m grid overlay (middle and bottom graphics, Fig. 3.1). We chose to sample the canopy surface at a spatial resolution of 0.5 m, because this resolution approximates the density and post spacing of many of today's small-footprint, discrete-return LiDAR systems.

3.3.2. Attributes of forest canopy structure and spatial pattern

We used 12 plot-level attributes to describe the structural composition and pattern of each of the 187 simulated 0.25 ha CHMs (Table 3.2). Ten of these attributes were calculated directly from the stand tables, while the remaining two were extracted from the CHMs. Those attributes calculated from stand tables were Lorey's height (H_L), quadratic mean crown width (*CW*), quadratic mean crown depth (*CD*), quadratic mean diameter (*QMD*), basal area (*BA*), total stem volume (*VOL*), stem density (*SD*), Curtis' relative density (*RD*), Shannon's Height Diversity Index (*SHDI*), and modified Pollard's statistic (P_O) (all defined below). Canopy cover (*CC*) and gap volume (*GAP*) were both computed using the CHMs. We used the quadratic mean (i.e., square-root of the arithmetic mean of squared values) instead of the arithmetic mean to calculate average crown width, crown depth, and DBH, because the quadratic method provides a more accurate estimate of the mean sizes of canopy trees observed from above.

TABLE 3.2. Formulae for plot-level attributes used to describe forest canopy structure

Attribute	Unit	Formula
Lorey's Height	m	$H_L = \sum_{i=1}^{n} d_i^2 h_i \Big/ \sum_{i=1}^{n} d_i^2$
Quadratic Mean	m, cm	$QM = \sqrt{\frac{1}{n}\sum_{i=1}^{n} b_i^2}$
Basal Area	m^2/ha	$BA = (\pi/40000) \times \left(\frac{1}{a}\sum_{i=1}^{n} d_i^2\right)$
Total Volume	m^3/ha	$VOL = \frac{1}{a}\sum_{i=1}^{n} \frac{1}{3}\pi\left(\frac{0.5d_i}{100}\right)^2 h_i$
Stem Density	n/ha	$SD = n/a$
Curtis' Relative Density	m^2/ha/cm	$RD = BA/QMD^{0.5}$
Shannon's Height Diversity Index	None	$SHDI = -\sum_{z=1}^{H} p_z \ln p_z$
Pollard's Statistic	None	$P_O = 12l^2 v \left[v \ln\left(\sum_{k=1}^{v} x_{kl}^2 / v\right) - \sum_{k=1}^{v} \ln\left(x_{kl}^2\right)\right] \Big/ \left[(6lv + v + 1)(v - 1)\right]$
Canopy Cover	%	$CC = \left[1 - \frac{n_g}{(n_g + n_c)}\right] \times 100$
Gap Volume	%	$GAP = \left[\sum_{q=1}^{s}\sum_{r=1}^{t}\left(h_{\max} - h_{qr}\right) \Big/ \sum_{q=1}^{s}\sum_{r=1}^{t} h_{\max}\right] \times 100$

NOTES: n, s, t, and v are total number of samples; d_i is the diameter at breast height (DBH, cm) of tree i; h_i is the height (m) of tree i; b_i is the crown width (m), crown depth (m), or DBH (cm) of tree i; a is the sample plot area (a = 0.25 ha in this study); QMD is the quadratic mean diameter (cm); p_z is the proportion of basal area found in each height class z, and H is the total number of height classes (2-m height classes were used in this study); x_{kl} is the linear distance from the kth random point to its lth nearest neighbour; l is the first to third nearest neighbour (stem position) to random point k; v is the total number of random points k overlaid on the stem map (k = 175 in this study); n_g is the total number of grid cells with a canopy height ≤ 2 m (classified as ground); n_c is the total number of grid cells with a canopy height > 2 m (classified as canopy); h_{max} is the maximum canopy height (m) within the sample plot, and h_{qr} is the canopy height at column q and row r of the canopy height model.

H_L is Lorey's mean stand height, defined as the height of the tree of average basal area (Magnussen and Boudewyn, 1998). Similarly, *QMD* is the mean diameter of the tree of arithmetic mean basal area (Curtis and Marshall, 2000). *BA*, *VOL*, and *SD* are frequently used estimates of stand occupancy measured on a per-hectare basis. *RD* is a diameter-based measure of stand density developed for even-aged coastal Douglas-fir, commonly defined as the average area available to the tree of average basal area relative to either an open-grown condition or "normal" stand density (Curtis, 1982). *RD* varies along a continuous scale ranging from zero for a basal area of zero to some biological maximum at $RD = 14$ for even-aged Douglas-fir. Shannon's index, H', is a statistic frequently used by ecologists to represent the probability that any two individuals sampled independently and at random from a community will belong to the same species (Pielou, 1975). We used a modified version of H' (*SHDI*) to describe the vertical diversity of basal-area-weighted tree heights (Staudhammer and LeMay, 2001). The modified Pollard's statistic (P_O) uses the distance measured from a random point to its jth-nearest neighbour to detect spatial pattern in point data (Liu, 2001). We used estimates of P_O with $j = 3$ to quantify the departure of stem positions from CSR. Values of P_O significantly less than 1 indicate uniformity, while values significantly greater than 1 suggest aggregation; a pattern approaches CSR when P_O equals unity. *CC* is the fraction of horizontal ground surface covered by the vertical projection of tree crowns (Jennings et al., 1999). In this study, *CC* was estimated as the percentage of heights in the CHM greater than some arbitrary height threshold (i.e., 2 m; Brokaw, 1982). *GAP* is the empty intercrown space that exists between the height of the tallest tree and the top of the outer canopy surface, expressed as a percentage of the total gap plus canopy volumes. Thus, *GAP* is the volumetric equivalent of the intercrown canopy gap fraction.

3.3.3. Statistical analyses

We used principal component analysis (PCA), Pearson correlation, and linear and non-linear regression analyses to facilitate the comparison and interpretation of the scale-dependent lacunarity statistics generated for each of the 187 simulated canopies. PCA was specifically used to create a smaller number of uncorrelated composite variables (components) from a linear combination of the lacunarity statistic estimated at different

spatial scales. Pearson correlation and regression analyses were used to examine the statistical relationship between each of these new synthetic components and the 12 attributes of stand structure and spatial pattern described above. Principal components were extracted directly from a correlation matrix derived from an original data table that consisted of n sample units (187 rows) by p variables (10 columns). Where, p is one of nine scale-dependent estimates of lacunarity $\Lambda(r)$ measured at approximately equal-log intervals of box size r (r = 1, 2, 3, 5, 9, 15, 24, 40, 66 in grid-cell units), and n identifies the corresponding CHM for which these p variables have been measured. The 10th variable that we included in the main data table was a simple integrated measure of cross-scale spatial heterogeneity, computed as the sum of the normalized lacunarity statistic estimated at nine discrete box sizes r:

$$\Lambda_{TOTAL} = \frac{1}{\Lambda(1)} \sum \Lambda(r) \qquad (3.11)$$

where $\Lambda(r)$ is the lacunarity statistic computed at the nine box sizes listed above, and $\Lambda(1)$ is the lacunarity statistic estimated for box size r = 1. Small values of Λ_{TOTAL} (<3.25) generally indicate uniformity or randomness in canopy heights at coarser spatial scales, while larger values (>4.25), in contrast, denote the presence of spatial structure at coarser scales. Theses two values of Λ_{TOTAL} correspond to the 25th and 75th percentiles of the sampled statistic, respectively. We transformed all ten variables independently of one another using a rank-preserving (monotonic) power transformation to improve linearity and normality. We subsequently rescaled each of the transformed variables to a mean of 0 and variance of 1, so that all ten variables had equivalent weight in the PCA. We used PC-ORD Version 4.27 (McCune and Mefford, 1999) for PCA and SYSTAT Version 10.2 for correlation and regression analyses. All other spatial modelling and analysis software used in this study was developed by the senior author.

3.4. Results

3.4.1. Structural characteristics of the simulated 3-D stand models and derived CHMs

All four stand classes (i.e., Short, Medium, Tall, and Natural) exhibited substantial variation in structural composition and spatial pattern, thus contributing to marked overlap between most classes for many of the 12 attributes of stand and canopy structure (Fig. 3.3). There were, however, a number of distinct structural characteristics that distinguished these four stand classes from one another. For example, the Short class had the lowest median and narrowest range of H_L, *CW*, *CD*, *QMD*, *BA*, *VOL*, and *SHDI*, and also showed the greatest variation in *SD*, *CC*, and P_O. Approximately 25% of the stand models found within the Short class had P_O values that exceeded 4, indicating that some CHMs in this class had substantially higher levels of nearest-neighbour spatial aggregation than those in other stand classes.

Simulated CHMs within the Medium class also exhibited substantial variation in *CC*, P_O, and *SHDI*, and had the greatest range of *GAP* values. Although this stand class was limited in its range of H_L, it still displayed moderate variability in *CW* and *CD*. The Tall class contained CHMs with the largest H_L, *CW*, *CD*, and *QMD*, and also revealed substantial variation in *CW*, *CD*, *QMD*, *BA*, *VOL*, *RD*, *CC*, and *GAP*. *RD*, *CC*, and *GAP* all varied considerably within the Tall class, despite the narrow range and low median value of *SD*. The Natural class produced the highest median *BA*, *VOL*, *RD*, *SHDI*, and *CC*; however, the range of *SHDI* and *CC* within this class was extremely limited, and more so than any other stand class. The Natural class also had the lowest median and narrowest range of *GAP*, because of its very high median *CC* and generally uniform to random ($0.21 \leq P_O \leq 1.38$) stem point patterns.

3.4.2. Scale-dependent estimates of the lacunarity statistic

Minimum, maximum, and median estimates of the lacunarity statistic computed at box size $r = 1$ for all 187 simulated CHMs were 1.01, 11.92, and 1.54, respectively. The lacunarity statistic was always at its maximum value at the finest scale of measurement

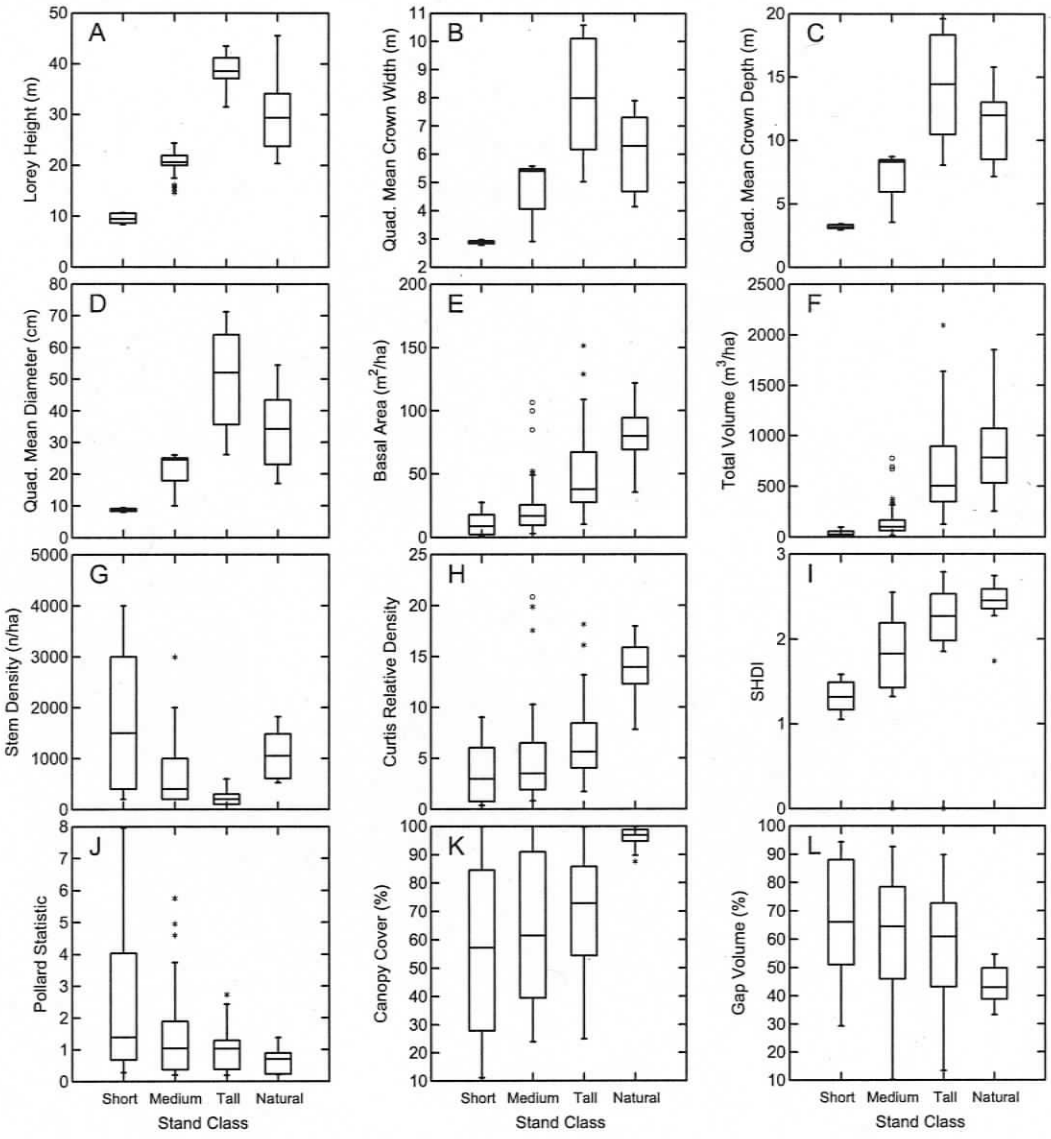

FIGURE 3.3. Boxplots summarizing the frequency distributions of 12 different attributes of stand and canopy stratified by stand class. The lower and upper bounds of the boxplot represent the 25th and 75th percentiles, the horizontal line within the box is the median value of the distribution, and box whiskers identify the range of extreme values.

(i.e., box size r = 1), indicating that all CHMs generally became more spatially homogeneous at coarser measurement scales. The rate and pattern of decline in lacunarity at larger measurement scales was solely determined by the canopies' hierarchical spatial structure and scale-dependent patchiness (i.e., the clumping of foliage into individual crowns and then into groups of crowns of variable sizes and patterns). The Short class exhibited the widest range of lacunarity estimates across the first seven measurement scales (0.5 m $\leq s \leq$ 12 m), indicating substantial variation in the magnitude and pattern of spatial aggregation at these finer spatial scales (Fig. 3.4). In contrast, the Natural class had the narrowest range and lowest median value of the lacunarity statistic at all nine measurement scales, largely because of their characteristic high levels of canopy cover (density) and the limited size and depth of intercrown gaps. The Medium class also revealed substantial variation in lacunarity across the first five measurement scales (0.5 m $\leq s \leq$ 4.5 m), but the median and range of the lacunarity statistic were more similar to the Short and Tall classes at coarser spatial scales.

Minimum, maximum, and median values of Λ_{TOTAL} computed in this study were respectively 1.74, 5.56, and 3.89. Larger values of Λ_{TOTAL} generally denote both the presence and persistence of spatial structure or aggregation at increasingly coarser measurement scales. The Tall class displayed the largest median value of Λ_{TOTAL} (4.29), followed in descending order by the Natural (3.92), Medium (3.60), and Short (3.22) classes. The Medium class revealed the greatest range of variation in Λ_{TOTAL} ($1.74 \leq \Lambda_{TOTAL} \leq 5.35$), while the Natural class showed the least amount of variation ($3.09 \leq \Lambda_{TOTAL} \leq 4.60$). The larger values of Λ_{TOTAL} exhibited by the Tall and Natural classes are due to their coarser-scale structure (bigger crowns and gaps) and greater variation in crown and gap sizes. The wide variation in Λ_{TOTAL} associated with Medium class was due to substantial spatial variability in vertical and horizontal canopy structure as indicated by the broad ranges of *CC*, *GAP*, *SHDI*, and P_O. The range of Λ_{TOTAL} estimates was limited in the Natural class, due to very high levels of canopy cover, the limited size and depth of intercrown gaps, and their predominantly random to uniform stem patterns.

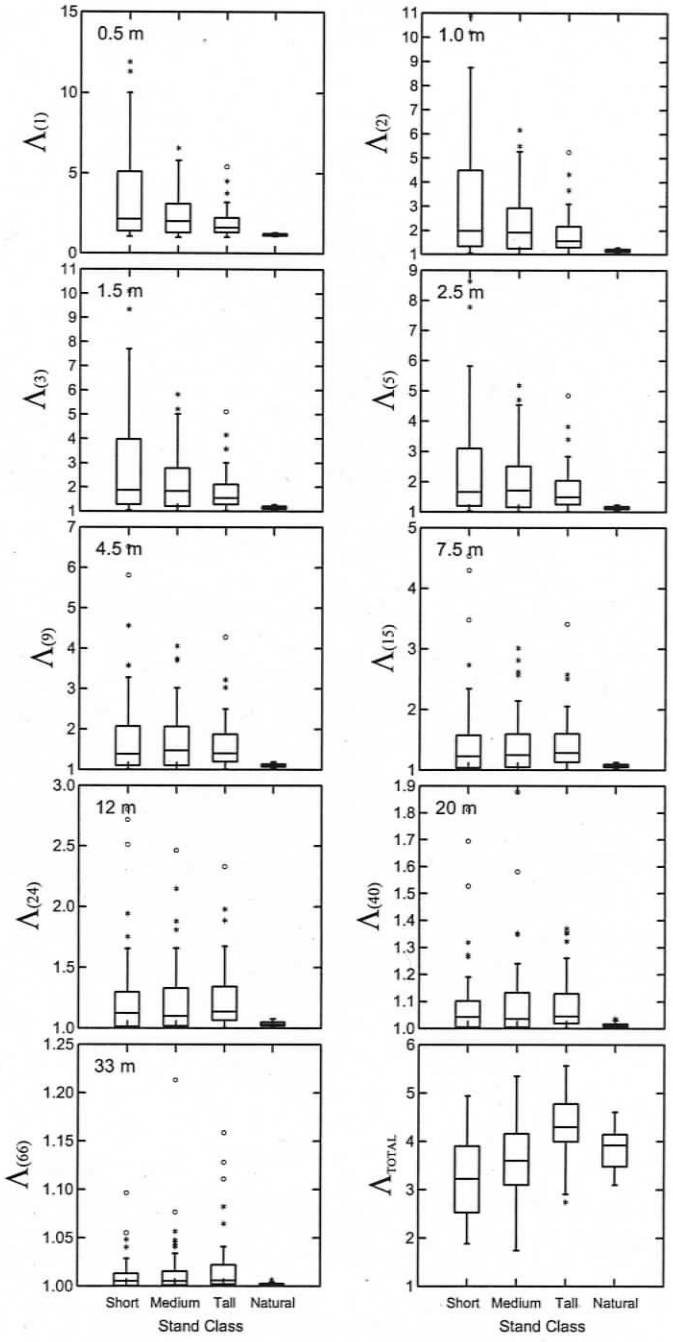

FIGURE 3.4. Boxplots showing the frequency distributions of the lacunarity statistic $\Lambda(r)$ stratified by linear box size r and stand class. Measurement scale is identified in grid-cell units on the Y-axis and as an absolute unit of measure (in metre) in the top left-hand corner of each graph. Λ_{TOTAL} is a simple integrated measure of cross-scale spatial heterogeneity.

3.4.3. Ordination of lacunarity statistics using PCA

The first two principal components accounted for 98.4% of the total variance found in the original scale-dependent lacunarity data, with 89.3% and 9.1% of total variance explained by the first (PC1) and second (PC2) principal components, respectively. The third principal component (PC3) accounted for only 1.1% of the total variance, and was therefore excluded from further analyses. PC1 had a strong negative correlation with the lacunarity statistic at all nine discrete spatial scales ($0.865 \leq R^2 \leq 0.990$), and moderate negative correlation ($R^2 = 0.496$) with Λ_{TOTAL} (Table 3.3). The sign and strength of the Pearson coefficient of correlation, R, between the scale-dependent lacunarity statistic and PC2 declined from a low positive value of $R = 0.321$ at scale $r = 1$, to $R = 0.074$ at scale $r = 7$, and finally to a small negative value of $R = -0.231$ at scale $r = 60$. Λ_{TOTAL} was also moderately negatively correlated with PC2 ($R^2 = 0.474$). Three main conclusions were drawn from these patterns of correlation. First, strong negative correlations between PC1 and lacunarity at all spatial scales indicated that PC1 scores declined as the magnitude of the lacunarity statistic increased. Second, PC2 scores increased and decreased when simulated CHMs were dominated by fine-scale and coarse-scale spatial patterns, respectively. Third, PC1 and PC2 scores both declined when the cross-scale spatial heterogeneity (Λ_{TOTAL}) exhibited by the CHMs increased.

A scatterplot of PC1 versus PC2 scores revealed the spatial distribution of simulated CHMs in reduced ordination space (Fig. 3.5). PCA attempts to preserve the relative Euclidean distances that separated sample units in the multi-dimensional space of the original descriptors (Legendre and Legendre, 1998). Therefore, simulated CHMs found at close proximity in ordination space will likely have lacunarity curves of similar magnitude and shape, while those far apart will have curves that are dissimilar in these same two characteristics. Despite the substantial overlap among the four different stand classes for many of the 12 attributes of stand and canopy structure, each stand class occupied a relatively distinct region of ordination space. For example, stand classes tended to stratify vertically, with the Short class dominating the top of the scatterplot, the Medium class in the middle, and the Tall and Natural classes on the bottom. The Short, Medium, and Tall classes occupied the largest regions of ordination space, largely because these classes varied widely in *CC*, *GAP*, *SHDI*, and P_O. In contrast, the Natural

class was limited in its ranges of these same four attributes, and therefore filled a relatively small, but unique region of ordination space.

TABLE 3.3. Principal component loadings and Pearson correlations between principal components and lacunarity statistics

	PC1			PC2		
Attribute[a]	loadings[b]	R	R^2	loadings[b]	R	R^2
$\Lambda(1)$	−0.317	−0.946	0.896	0.337	0.321	0.103
$\Lambda(2)$	−0.320	−0.956	0.913	0.306	0.292	0.085
$\Lambda(3)$	−0.323	−0.964	0.928	0.278	0.264	0.070
$\Lambda(5)$	−0.330	−0.978	0.956	0.212	0.202	0.041
$\Lambda(9)$	−0.333	−0.994	0.988	0.078	0.074	0.006*
$\Lambda(15)$	−0.333	−0.995	0.990	−0.058	−0.055	0.003*
$\Lambda(24)$	−0.329	−0.984	0.969	−0.157	−0.150	0.022
$\Lambda(40)$	−0.322	−0.963	0.927	−0.222	−0.211	0.045
$\Lambda(66)$	−0.311	−0.930	0.865	−0.243	−0.231	0.053
Λ_{TOTAL}	−0.236	−0.704	0.496	−0.727	−0.689	0.474

[a]All attributes except Λ_{TOTAL} were log transformed.
[b]Principal component loadings (eigenvector coefficients) of the original variables.
*Not significant at 0.05 level.

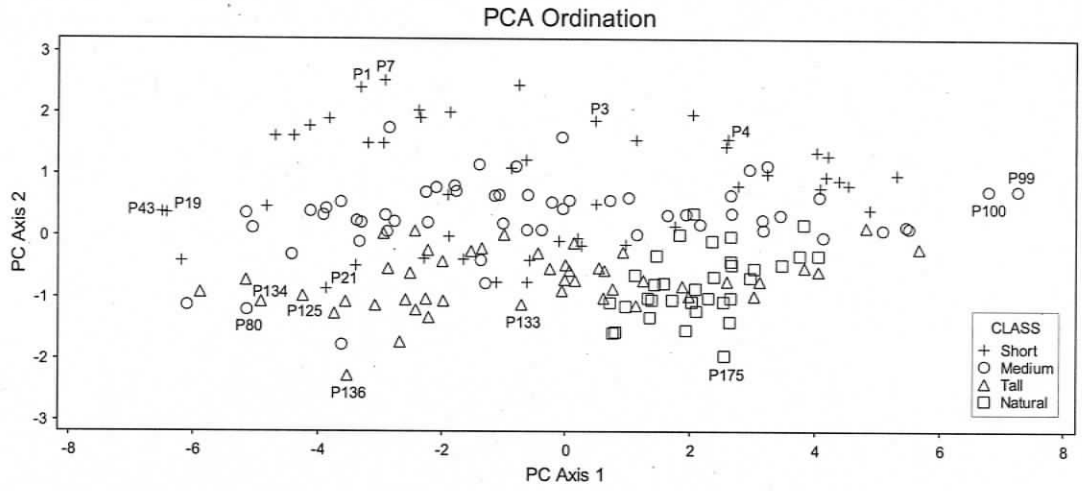

FIGURE 3.5. Ordination diagram showing the distribution of sample points in reduced ordination space. PCA attempts to preserve the distances that separated sample units in the multidimensional space of the original descriptors, therefore CHMs located in close proximity of one another are likely to have similar scale-dependent spatial patterns. The labels marked P1, P3, etc. correspond to the 15 selected examples of simulated CHMs shown in Figure 3.7.

3.4.4. Correlations between principal components, lacunarity, and attributes of forest stand and canopy structure

PCA uncovered a number of gradients in the original lacunarity dataset that were associated with the vertical and horizontal patchiness (texture) of the canopy and other more specific size- and density-related attributes of stand and canopy structure (Fig. 3.6). We found that PC1 was strongly positively correlated with estimates of CC (R^2 = 0.848) and negatively correlated with *GAP* (R^2 = 0.842) (Table 3.4). For example, P99 and P100 are two paired examples of simulated CHMs having the highest PC1 scores, while P19 and P43 are characterized by the two lowest PC1 scores (Fig. 3.7). P99 recorded the lowest $\Lambda(1)$ statistic (1.01), highest *CC* (99.99%), and lowest *GAP* (10.2%) of all simulated CHMs, while P43, in contrast, had the highest $\Lambda(1)$ statistic (11.92), lowest *CC* (11.10%), and highest *GAP* (94.3%). Regression analyses revealed a strong negative linear relationship between the logarithm of $\Lambda(1)$ and logarithm of *CC* (R^2 = 0.982), and a

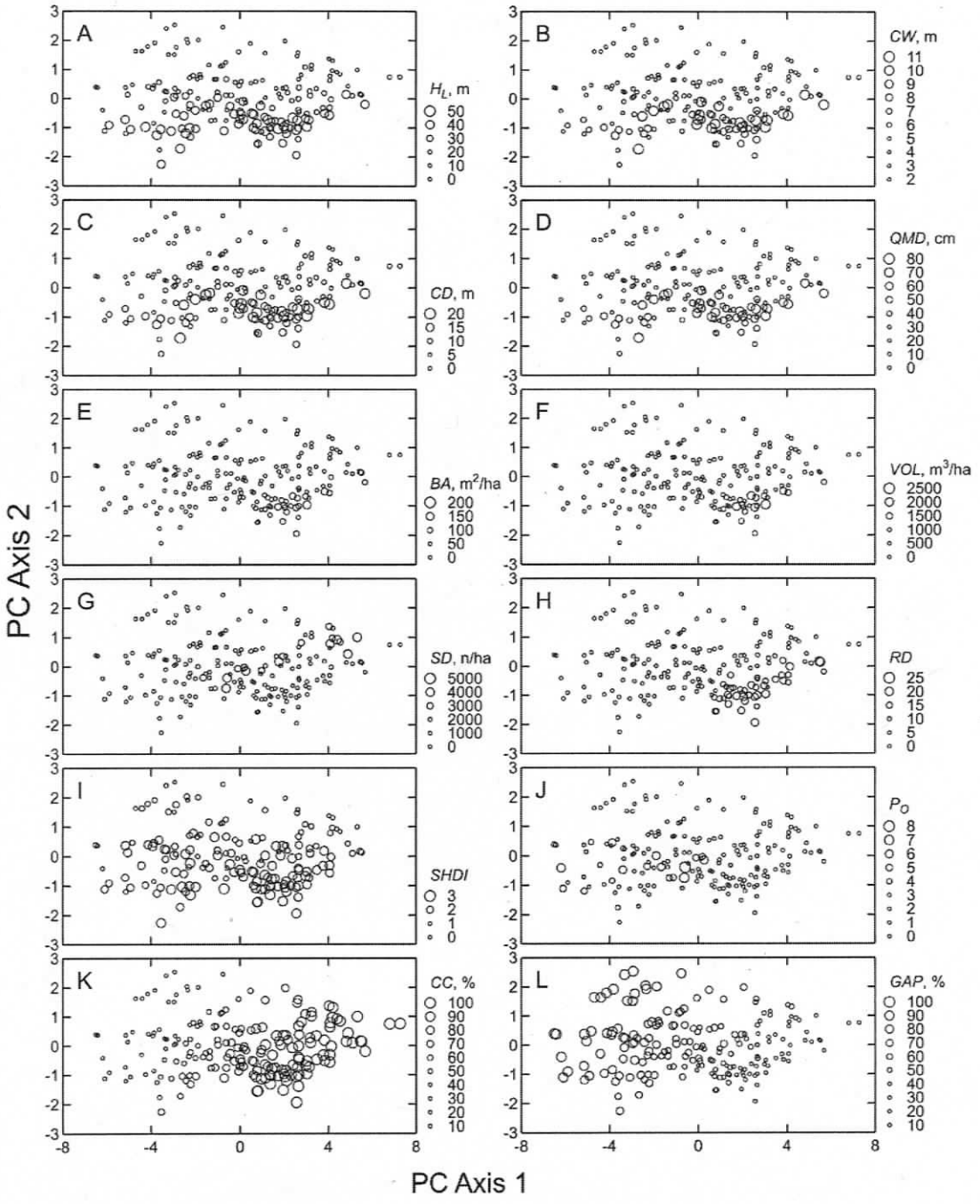

FIGURE 3.6. Overlay plot summarizing the relationship between attributes of stand and canopy structure and the first (PC1) and second (PC2) principal components. The diameter of the circular plot symbol is proportional to magnitude of the attribute. Gradients of variation in these structural attributes are defined by a monotonic increase or decrease in symbol size. The direction of this change defines the statistical association between the variable and each of the two principal components.

strong positive exponential relationship between the logarithm of $\Lambda(1)$ and *GAP* ($R^2 = 0.959$). PC1 was poorly correlated with many of the size-related attributes such as H_L, *CW*, *CD*, and *QMD* ($0.004 \leq R^2 \leq 0.032$), but positively correlated ($0.271 \leq R^2 \leq 0.584$) with density-related attributes of stand structure, such as *RD*, *BA*, *SD*, and *VOL*. PC1 also revealed a moderate negative correlation with P_o ($R^2 = 0.229$), because higher levels of nearest-neighbour spatial aggregation, particularly in the Short and Medium classes, generally produced more patchy or open canopy structures.

TABLE 3.4. Pearson correlations between principal components and attributes of stand structure

	PC1		PC2	
Attributes	*R*	R^2	*R*	R^2
H_L	0.061	0.004*	−0.703	0.495
CW[a]	0.164	0.027	−0.629	0.395
CD[a]	0.179	0.032	−0.660	0.436
QMD[a]	0.143	0.020*	−0.663	0.440
BA[a]	0.669	0.448	−0.682	0.465
VOL[a]	0.521	0.271	−0.739	0.546
SD[a]	0.594	0.352	0.107	0.011*
RD[a]	0.764	0.584	−0.595	0.354
SHDI[b]	0.109	0.012*	−0.652	0.425
P_O[a]	−0.479	0.229	−0.046	0.002*
CC	0.921	0.848	−0.320	0.102
GAP	−0.918	0.842	0.294	0.087

[a]Transformed using natural log.
[b]Zero values of *SHDI* excluded from correlation.
*Not significant at 0.05 level.

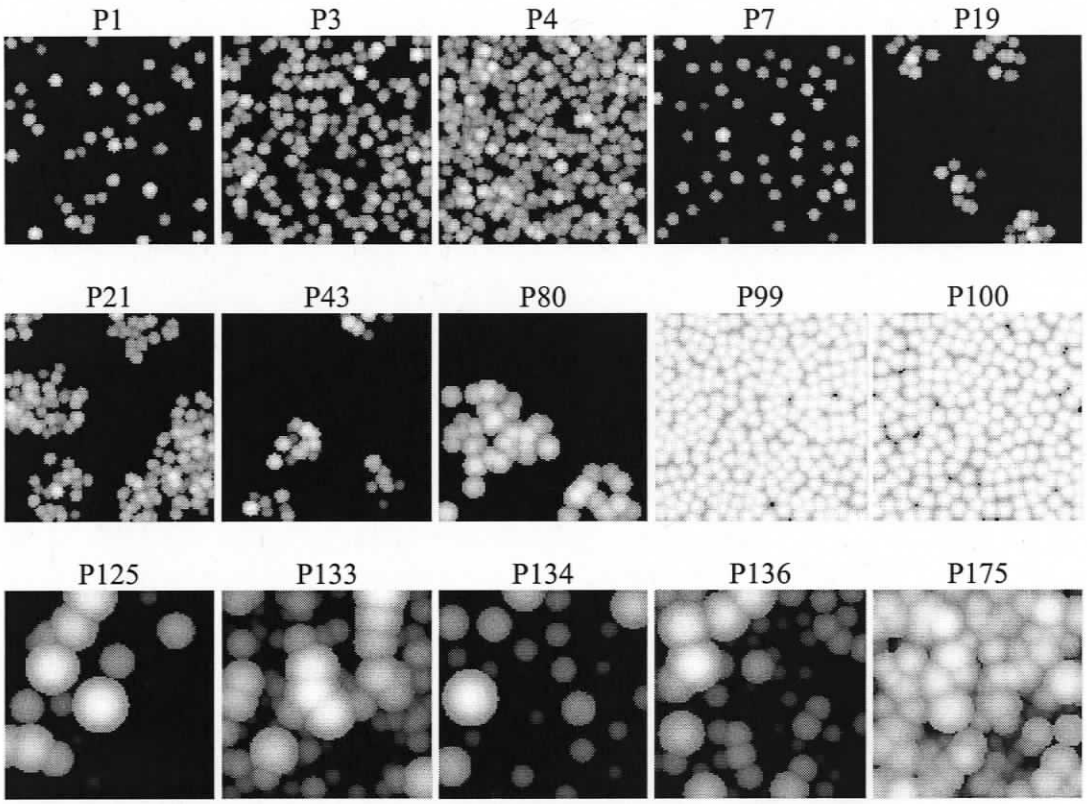

FIGURE 3.7. Selected examples of the 187 simulated CHMs. P99 and P43 represent the highest and lowest PC1 scores, respectively. P7 and P136 recorded the highest and lowest PC2 scores, respectively. P100 and P136 represent the minimum and maximum values of Λ_{TOTAL}, respectively. See Figure 3.5. for the positions of these 15 examples in PCA ordination space.

Correlations between PC2 and attributes of stand and canopy structure were distinct from those associated with PC1. For example, PC2 was negatively correlated with size-related attributes such as H_L, *CW*, *CD*, and *QMD* ($0.395 \leq R^2 \leq 0.543$) and *SHDI* ($R^2 = 0.425$). PC2 was weakly negatively correlated with *CC* ($R^2 = 0.102$) and weakly positively correlated with *GAP* ($R^2 = 0.087$), because larger and more variable tree and crown sizes generally create larger, deeper, and more diverse intercrown gaps. Like PC1, PC2 was also correlated with *VOL*, *BA*, and *RD* ($0.354 \leq R^2 \leq 0.546$), largely because these three attributes of stand structure are all strongly dependent on both tree size and density. P7 and P136 were associated with the highest and lowest PC2 scores, respectively (Fig. 3.7). P7 is characterized by a sparse, uniform pattern of very small trees

(H_L = 8.43 m), with little variation in crown size and height. P136, on the other hand, is also composed of a sparse, uniform pattern of trees, but these trees are much larger (H_L = 37.71 m), vary substantially in size and height, and show coarser-scale patterns of aggregation among some of the larger crowns. P4 and P175 have higher *CC* estimates than P7 and P136, but reveal similar between-CHM differences in tree size and spatial pattern. Approximately 16 CHMs from the Short and Medium classes were found interspersed in the same region of ordination space as CHMs from substantially taller classes (Fig. 3.5): 12 belonged to the Short class, while the rest were from the Medium class. For example, P80 (Medium) was located very close to P134 (Tall), and P21 (Short) was located adjacent to P125 (Tall), yet both sets of pairs are obviously dissimilar in stand structure and pattern (Fig. 3.7). Interestingly, all of these 16 plots exhibited an unusually strong hierarchical arrangement of crowns into discrete randomly distributed clusters ($2.76 \leq P_o \leq 7.95$; see Fig. 3.6J).

3.5. Discussion and Conclusions

Lacunarity is a quantitative measure of texture increasingly used to characterize the cross-scale heterogeneity associated with a broad range of spatiotemporal phenomena. We used the lacunarity statistic estimated at nine discrete measurement scales to examine the spatial heterogeneity found in the outer canopy surface of 187 simulated CHMs. The lacunarity statistic has a theoretical range from a minimum value of 1 to some infinite positive number, where 1 represents spatial homogeneity (zero spatial variance), and increasingly larger values of the statistic imply increasing heterogeneity. We found that the magnitude of the lacunarity statistic was strongly associated with canopy cover and gap volume, while the pattern of decline in lacunarity across discrete measurement scales was related to many size- and density-related attributes of stand and canopy structure and their diverse vertical and horizontal spatial distributions. These general findings are supported by other published studies that have reported a strong positive correlation between stand-level canopy texture or patchiness and scale-dependent estimates of lacunarity (Sun and Ranson, 1998; Weishampel et al., 2000).

We used PCA explicitly to uncover gradients of scale-dependent spatial heterogeneity in the surface pattern and structure of our simulated CHMs. PCA revealed that a substantial portion (98.34%) of the total variance contained in the ten dimensions of the original lacunarity dataset could be explained by two synthetic, orthogonal components. The first component (PC1) captured 89.3% of the total variance in the original lacunarity data, while the second (PC2) accounted for the remaining 9.1%. Pearson correlation showed that PC1 scores were largely determined by the magnitude of the lacunarity statistic estimated at each of nine discrete measurement scales ($0.865 \leq R^2 \leq 0.990$). In contrast, PC2 showed very little correlation with the lacunarity statistic at any of the measurement scales ($0.003 \leq R^2 \leq 0.103$), and was instead related to rates of decline, subtle breaks in slope, and other scale-dependent variations in the shape of the lacunarity curve. Further analyses showed that PC1 and the magnitude of the lacunarity statistic at box size $r = 1$ were both strongly correlated with canopy cover and gap volume, while PC2 was negatively correlated with size-related attributes of stand structure (i.e., mean height, crown width and depth, DBH, and height diversity). Both PC1 and PC2 were moderately correlated with density-related attributes of stand structure (i.e., volume, basal area, and relative density), because all of these forest measurements are influenced by both tree size and stem density. Even though most of the variance (approximately 75%) found in the original lacunarity dataset could be explained solely by canopy cover or gap volume, a sufficient amount of variance still remained to effectively separate CHMs in ordination space along other diverse gradients of forest canopy structure and scale-dependent spatial pattern.

Detailed 3-D views of the forest canopy looking down from above have helped to reshape our thinking about canopy structure and the ways in which it can be quantified and studied. Measures of canopy cover have traditionally been regarded as dichotomous (i.e., canopy or gap), rather than reflecting the true continuous nature of canopy height, depth, density, porosity, and pattern (Lieberman et al., 1989; Dial et al., 2004). In this study, the forest canopy was treated as a continuous surface of varying height, where gaps were physically defined by the empty spaces of variable depth, width, and shape that separated neighbouring crowns. Consequently, the hierarchical arrangement of canopy elements in both vertical and horizontal spatial domains determined the size, shape, and

patchy distribution of filled and empty canopy spaces, and therefore the kind, magnitude, and scale of spatial heterogeneity. Two distinctively different, yet complementary gradients of spatial heterogeneity emerged from analyses of these canopy height data. The stronger of these two gradients reflected the continuous variation in canopy cover and intercrown gap volume, while a second, more subtle gradient was associated with the array of possible vertical and horizontal spatial configurations that might define any one measure of canopy cover.

Canopy cover and other related measures of site occupancy (e.g., stem density, basal area, volume, etc.) are well known to be negatively correlated with mean values of the understory light environment (Baldocchi and Collineau, 1994; Lieffers et al., 1999). Vertical and horizontal spatial distributions of canopy cover, on the other hand, play key roles in structuring spatiotemporal patterns of light and other critical forest resources (Trichon et al., 1998; Wirth et al., 2001; Parker et al., 2002), and have therefore been considered an important driver of many key ecosystem processes and functions, including stand dynamics (Canham et al., 1994; Nicotra et al., 1999; Van Pelt and Franklin, 2000; Herwitz et al., 2000), stand productivity, niche diversification, and biodiversity (Franklin et al., 2002; Carey, 2003; Ishii et al., 2004). Spatial characteristics of canopy structure are also known to vary markedly throughout stand succession, with the most substantial and unique patterns of vertical and horizontal spatial heterogeneity often occurring in the later stages of stand development (Brown and Parker, 1994; Franklin and Van Pelt, 2004; Parker and Russ, 2004).

The kinds of spatiotemporal pattern that we are able to observe in nature are constrained by the grain (resolution) and extent of our measurements (Marceau et al., 1994; Gardner, 1998; Dale, 1999). The horizontal extent of our simulated forest canopy view was restricted to 50 m × 50 m (0.25 ha), and the grain of our measurements ranged from 0.5 to 33 m. We would, however, expect different scale-dependent patterns of spatial heterogeneity to emerge if the grain or extent of our models and measurements of lacunarity were reduced or enlarged. Larger sample plots, for example, are generally expected to exhibit substantially more spatial heterogeneity in canopy structure over the same fixed range of measurement scales than smaller plots (Zenner, 2005). In real forests, stand structure and species composition vary considerably both locally and regionally in

response to fine- and coarse-scale variations in edaphic factors, disturbance regime, and successional processes (Franklin et al., 2002). Consequently, increasing the spatial extent over which canopy heights and lacunarity are measured is likely to reveal different scale-dependent patterns of spatial heterogeneity. It is, therefore, imperative that both the grain and extent of spatial observation, measurement, and analysis match as closely as possible the ecological phenomenon of interest.

Accurate, high-spatial-resolution (<1 m) canopy heights can be readily acquired with airborne LiDAR instruments (Lefsky et al., 2002; St-Onge et al., 2003) or from high-resolution aerial photos and digital photogrammetry (Miller et al., 2000). We propose two different potential sampling strategies to extract fine-scale estimates of lacunarity from a regularly spaced, rectangular array of quantitative canopy heights. First, a sample window (quadrat) of fixed size and geometry could be moved in either an overlapping or non-overlapping manner to cover an entire array of canopy heights. The sample quadrat may be equivalent in size to the 50 m × 50 m (0.25 ha) horizontal footprint of the simulated CHMs used in this study, or it could be smaller or larger depending on the objectives of the research and the grain and extent of the data. At each quadrat position, the lacunarity statistic is then estimated at a number of discrete spatial scales within the bounds of the quadrat. Alternatively, forest cover maps identifying the distinct boundaries of individual stands may provide the spatial context for undertaking a stratified-random-sampling approach. For example, sample quadrats of some predetermined size could be randomly placed within the confines of each stand boundary to avoid the arbitrariness and boundary issues inherent in the first sampling approach. Spatial boundaries or ecotones can, however, represent a legitimate and interesting ecological phenomenon. Therefore, both sampling strategies will likely have merit depending on the study objectives.

Lacunarity provides a simple conceptual and methodological framework to study the scale-dependent spatial heterogeneity of forest canopies. Ordination techniques, especially those that are unconstrained and distance-preserving, facilitate the comparison of cross-scale spatial heterogeneity by separating CHMs in reduced ordination space along unique gradients of pattern and structure. When used together, these two techniques provide substantial opportunity for forest scientists to study a broad range of ecological

and forest management problems. For example, pooling scale-dependent lacunarity estimates collected from local managed and natural forests into a single statistical ordination would allow forest managers to assess the potential impact of specific silvicultural practices on both fine- and coarse-scale patterns of spatial heterogeneity. Ordination diagrams are helpful in this respect, because they show the overall variation of points in sample space, as well as identify both the distance and direction separating any two sample units or classes of interest. Target plots representing some kind of ideal structural condition or habitat may be identified prior to analysis, as a way to establish a frame of reference to compare all other sample units in reduced ordination space.

The current shift towards an ecosystem-based approach to sustainable forest management in North America has created a demand for cost-effective forest measurement and monitoring technologies, analytical methods, and relevant scientific data (Lindenmayer and Franklin, 2002). We expect that our novel methodological approach could be used in conjunction with high-spatial-resolution airborne LiDAR data or digital photogrammetry to support a broad range of ecological applications. For example, this method could be used to study the fine-scale spatial heterogeneity of 'natural' forest canopies as a blueprint for developing new stand-level gap- or retention-based silvicultural systems (Coates and Burton, 1997). Second, homogeneous or heterogeneous forest patterns may be identified as targets for structural restoration or retention, respectively (Carey, 2003). Third, this technique could be used to monitor stand-level spatial aspects of forest canopies for adaptive forest management and certification purposes (Kremsater et al., 2003). Fourth, quantitative estimates of scale-dependent spatial heterogeneity may help to identify unique ecosystems or wildlife habitats (e.g., riparian or old-growth forests, etc.) suitable for designation as special management areas or reserves. Fifth, this method would facilitate the segmentation of LiDAR or other kinds of remotely sensed data into unique structural classes based on quantitative estimates of fine-scale spatial heterogeneity. Last, because lacunarity is well correlated with more traditional measurements of stand structure (i.e., canopy cover, height, crown size, volume, basal area, and relative density), we expect that synthetic variables generated by PCA from the original lacunarity dataset may become useful

predictors of stand structure in regression analyses when combined with some percentile of canopy height.

Studies in ecology, spatial pattern analysis, and remote sensing have demonstrated that there is no single, 'optimum' scale or window size that can be prescribed to analyze the complex spatial patterns and hierarchical structure of heterogeneous forest canopies (Marceau et al., 1994; Coburn and Roberts, 2004). In this study, we found that the spatial heterogeneity associated with canopy heights varied substantially with measurement scale, and it was this cross-scale pattern of variation that distinguished one CHM from another. Lacunarity analysis appears to offer several advantages over other spatial statistical approaches. First, lacunarity is a multiscaled method and does not depend on the existence of a single, 'optimum' measurement scale. Second, lacunarity does not require the unlikely assumption of spatial stationarity to remain unbiased. Third, lacunarity is computed simply and efficiently, and is easily applied to binary or quantitative datasets of any Euclidean dimension. Last, when applied to 2-D quantitative canopy heights, lacunarity becomes an integrated, scale-dependent measure of vertical and horizontal spatial heterogeneity. Further research is required to understand how these statistical estimates and gradients of measured heterogeneity relate to other ecologically relevant patterns of forest composition, structure, and function.

3.6. References

Allain, C., Cloitre, M., 1991. Characterizing the lacunarity of random and deterministic fractal sets. Physical Review A 44, 3552–3558.

Baldocchi, D., Collineau, S., 1994. The physical nature of solar radiation in heterogeneous canopies: spatial and temporal attributes. In: Caldwell, M.M., Pearcy, R.W. (Eds.), Exploitation of Environmental Heterogeneity by Plants: Ecophysiological Processes Above- and Below-Ground. Academic Press, San Diego, pp. 21–71.

Bartemucci, P., Coates, K.D., Harper, K.A., Wright, E.F., 2002. Gap disturbances in northern old-growth forests of British Columbia, Canada. Journal of Vegetation Science 13, 685–696.

Blumenfeld, R., Mandelbrot, B.B., 1997. Lévy dusts, Mittag-Leffler statistics, mass fractal lacunarity, and perceived dimension. Physical Review E 56, 112–118.

Bradshaw, G.A., Spies, T.A., 1992. Characterizing canopy gaps in forests using wavelet analysis. Journal of Ecology 80, 205–215.

Brokaw, N.V.L., 1982. The definition of treefall gap and its effect on measures of forest dynamics. Biotropica 14, 158–160.

Brown, M.J., Parker, G.G., 1994. Canopy light transmittance in a chronosequence of mixed-species deciduous forests. Canadian Journal of Forest Research 24, 1694–1703.

Caldwell, M.M., Pearcy, R.W., 1994. Exploitation of Environmental Heterogeneity by Plants: Ecophysiological Processes Above- and Below Ground. Academic Press, San Diego.

Canham, C.D., Finzi, A.C., Pacala, S.W., Burbank, D.H., 1994. Causes and consequences of resource heterogeneity in forests: interspecific variation in light transmission by canopy trees. Canadian Journal of Forest Research 24, 337–349.

Carey, A.B., 2003. Biocomplexity and restoration of biodiversity in temperate coniferous forests: inducing spatial heterogeneity with variable-density thinning. Forestry 76, 127–136.

Cescatti, A., 1998. Effects of needle clumping in shoots and crowns on the radiative regime of a Norway spruce canopy. Annals of Forest Science 55, 89–102.

Chen, J., Bradshaw, G.A., 1999. Forest structure in space: a case study of an old growth spruce-fir forest in Changbaishan Natural Reserve, PR China. Forest Ecology and Management 120, 219–233.

Chen, J., Saunders, S.C., Crow, T.R., Naiman, R.J., Brosofske, K.D., Mroz, G.D., Brookshire, B.L., Franklin, J.F., 1999. Microclimate in forest ecosystem and landscape ecology. BioScience 49, 288–297.

Cheng, Q., 1997. Multifractal modeling and lacunarity analysis. Mathematical Geology 29, 919–932.

Coates, K.D., Burton, P.J., 1997. A gap-based approach for development of silvicultural systems to address ecosystem management objectives. Forest Ecology and Management 99, 337–354.

Coburn, C.A., Roberts, A.C.B., 2004. A multiscaled texture analysis procedure for improved stand classification. International Journal of Remote Sensing 20, 4287–4308.

Cohen, W.B., Spies, T.A., Bradshaw, G.A., 1990. Semivariograms of digital imagery for analysis of conifer canopy structure. Remote Sensing of Environment 34, 167–178.

Curtis, R.O., 1982. A simple index of stand density for Douglas-fir. Forest Science 28, 92–94.

Curtis, R.O., Marshall, D.D., 2000. Why quadratic mean diameter? Western Journal of Applied Forestry 15, 137–139.

Dale, M.R.T., 1999. Spatial Pattern Analysis in Plant Ecology. Cambridge University Press, Cambridge, U.K.

Dale, M.R.T., 2000. Lacunarity analysis of spatial pattern: a comparison. Landscape Ecology 15, 467–478.

Dial, R., Bloodworth, B., Lee, A., Boyne, P., Heys, J., 2004. The distribution of free space and its relation to canopy composition at six forest sites. Forest Science 50, 312–325.

Diggle, P.J., 2003. Statistical analysis of spatial point patterns. Oxford University Press, New York, NY.

Drake, J.B., Weishampel, J.F., 2000. Multifractal analysis of canopy height measures in a longleaf pine savanna. Forest Ecology and Management 128, 121–127

Dutilleul, P., Legendre, P., 1993. Spatial heterogeneity against heteroscedasticity: an ecological paradigm versus a statistical concept. Oikos 66, 152–171.

Ehleringer, J.R., Field, C.B., 1993. Scaling Physiological Processes: Leaf to Globe. Academic Press, San Diego, CA.

Feagin, R.A., 2003. Relationship of second-order lacunarity, Hurst exponent, Brownian motion, and pattern organization. Physica A 328, 315–321.

Fournier, R.A., Rich, P.M., Landry, R., 1997. Hierarchical characterization of canopy architecture for boreal forests. Journal of Geophysical Research 102, 29445–29454.

Franklin, J.F., Spies, T.A., Van Pelt, R., Carey, A.B., Thornburgh, D.A., Berg, D.R., Lindenmayer, D.B., Harmon, M.E., Keeton, W.S., Shaw, D.C., Bible, K., Chen, J., 2002. Disturbances and structural development of natural forest ecosystems with silvicultural implications, using Douglas-fir as an example. Forest Ecology and Management 155, 399–423.

Franklin, J.F., Van Pelt, R., 2004. Spatial aspects of structural complexity in old-growth forests. Journal of Forestry 102, 22–28.

Frazer, G.W., Trofymow, J.A., Lertzman, K.P., 2000. Canopy openness and leaf area in chronosequences of coastal temperate rainforests. Canadian Journal of Forest Research 30, 239–256.

Gardner, R.H., 1998. Pattern, process, and the analysis of spatial scales. In: Peterson, D.L., Parker, V.T. (Eds.), Ecological Scale: Theory and Applications. Columbia University Press, New York, pp. 17–34.

Geffen, Y., Meir, Y., Mandelbrot, B.B., Aharony, A., 1983. Geometric implementation of hypercubic lattices with noninteger dimensionality by use of low lacunarity fractal lattices. Physical Review Letters 50, 145–148.

Gustafson, E.J., 1998. Quantifying landscape spatial pattern: what is the state of the art? Ecosystems 1, 143–156.

Hann, D.W., 1999. An adjustable predictor of crown profile for stand-grown Douglas-fir trees. Forest Science 45, 217–225.

Henebry, G.M., Kux, H.J.H., 1995. Lacunarity as a texture measure for SAR imagery. International Journal of Remote Sensing 16, 565–571.

Herwitz, S.R., Slye, R.E., Turton, S.M., 2000. Long-term survivorship and crown area dynamics of tropical rain forest canopy trees. Ecology 81, 585–597.

Ishii, H.T., Tanabe, S., Hiura, T., 2004. Exploring the relationships among canopy structure, stand productivity, and biodiversity of temperate forest ecosystems. Forest Science 50, 342–355.

Jennings, S.B., Brown, N.D., Sheil, S., 1999. Assessing forest canopies and understorey illumination: canopy closure, canopy cover and other measures. Forestry 72, 59–73.

Kaluzny, S.P., Vega, S.C., Cardoso, T.P., Shelly, A.A., 1998. S+SpatialStats, User's Manual for Windows® and Unix®. Springer-Verlag, New York, NY.

Kirkpatrick, L.A., Weishampel, J.F., 2005. Quantifying spatial structure of volumetric neutral models. Ecological Modelling 186, 312–325.

Kolasa, J., Pickett, S.T.A., 1991. Ecological Heterogeneity. Springer-Verlag, New York.

Kolasa, J., Rollo, C.D., 1991. Introduction: the heterogeneity of heterogeneity: a glossary. In: Kolasa, J., Pickett, S.T.A. (Eds.), Ecological Heterogeneity. Springer-Verlag, New York, pp. 1–23.

Koukoulas, S., Blackburn, G.A., 2004. Quantifying the spatial properties of forest canopy gaps using LiDAR imagery and GIS. International Journal of Remote Sensing 25, 3049–3071.

Kremsater, L., Bunnell, F., Huggard, D., Dunsworth, G., 2003. Indicators to assess biological diversity: Weyerhaeuser's coastal British Columbia forest project. Forestry Chronicle 79, 590–601.

Lefsky, M.A., Cohen, W.B., Parker, G.G., Harding, D.J., 2002. LiDAR remote sensing for ecosystem studies. BioScience 52, 19–30.

Legendre, P., Fortin, M.-J., 1989. Spatial pattern and ecological analysis. Vegetatio 80, 107–138.

Legendre, P., Legendre, L., 1998. Numerical Ecology. Elsevier Science, Amsterdam.

Lertzman, K.P., Fall, J.G., 1998. From forest stands to landscapes: spatial scales and the roles of disturbance. In: Peterson, D.L., Parker, V.T. (Eds.), Ecological Scale: Theory and Applications. Columbia University Press, New York, pp. 339–367.

Li, H., Reynolds, J.F., 1995. On definition and quantification of heterogeneity. Oikos 73, 280–284.

Lieberman, M., Lieberman, D., Peralta, R., 1989. Forests are not just Swiss cheese: canopy stereogeometry of non-gaps in tropical forests. Ecology 70, 550–552.

Lim, K., Treitz, P., Wulder, M., St-Onge, B., Flood, M., 2003. LiDAR remote sensing of forest structure. Progress in Physical Geography 27, 88–106.

Lindenmayer, D.B., Franklin, J.F., 2002. Conserving Forest Biodiversity: A Comprehensive Multiscaled Approach. Island Press, Washington, D.C.

Lui, C., 2001. A comparison of five distance-based methods for spatial pattern analysis. Journal of Vegetation Science 12, 411–416.

Magnussen, S., Boudewyn, P., 1998. Derivations of stand heights from airborne laser scanner data with canopy-based quantile estimators. Canadian Journal of Forest Research 28, 1016–1031.

Mandelbrot, B.B., 1983. The fractal geometry of nature. W.H. Freeman and Company, New York, NY.

Manly, B.F.J., 1997. Randomization, Bootstrap and Monte Carlo Methods in Biology. Chapman and Hall, London.

Marceau, D.J., Howarth, P.J., Gratton, D.J., 1994. Remote sensing and the measurement of geographical entities in a forested environment. 1. The scale and spatial aggregation problem. Remote Sensing of Environment 49, 93–104.

McCune, B., Mefford, M.J., 1999. PC-ORD Version 4 for Windows®. MjM Software Design, Gleneden, OR.

Miller, D.R., Quine, C.P., Hadley, W., 2000. An investigation of the potential of digital photogrammetry to provide measurements of forest characteristics and abiotic damage. Forest Ecology and Management 135, 279–288.

Moeur, M., 1993. Characterizing spatial patterns of trees using stem-mapped data. Forest Science 39, 756–775.

Montgomery, R.A., Chazdon, R.L., 2001. Forest structure, canopy architecture, and light transmittance in tropical wet forests. Ecology 82, 2707–2718.

Nadkarni, N.M., Sumera, M.M., 2004. Old-growth forest canopy structure and its relationship to throughfall interception. Forest Science 50, 290–298.

Nicotra, A.B., Chazdon, R.L., Iriarte, S., 1999. Spatial heterogeneity of light and woody seedling regeneration in tropical wet forests. Ecology 80, 1908–1926.

Ollier, S., Chessel, D., Couteron, P., Pélissier, R., Thioulouse, J., 2003. Comparing and classifying one-dimensional spatial patterns: an application to laser altimeter profiles. Remote Sensing of Environment 85, 453–462.

Parker, G.G., 1995. Structure and microclimate of forest canopies. In: Lowman, M.D., Nadkarni, N.M. (Eds.), Forest Canopies. Academic Press, Orlando, Florida., pp. 73–78.

Parker, G.G., Davis, M.M., Chapotin, S.M., 2002. Canopy light transmittance in Douglas-fir–western hemlock stands. Tree Physiology 22, 147–157.

Parker, G.G., Russ, M.E., 2004. The canopy surface and stand development: assessing forest canopy structure and complexity with near-surface altimetry. Forest Ecology and Management 189, 307–315.

Parker, G.G., Harding, D.J., Berger, M.L., 2004b. A portable LiDAR system for rapid determination of forest canopy structure. Journal of Applied Ecology 41, 755–767.

Parker, G.G., Harmon, M.E., Lefsky, M.A., Chen, J., Van Pelt, R., Weiss, S.B., Thomas, S.C., Winner, W.E., Shaw, D.C., Franklin, J.F., 2004a. Three-dimensional structure of an old-growth *Pseudotsuga-Tsuga* canopy and its implications for radiation balance, microclimate, and gas exchange. Ecosystems 7, 440–453.

Perry, J.N., Liebhold, A.M., Rosenberg, M.S., Dungan, J., Miriti, M., Jakomulska, A., Citron-Pousty, S., 2002. Illustrations and guidelines for selecting statistical methods for quantifying spatial pattern in ecological data. Ecography 25, 578–600.

Pickett, S.T.A., Ostfeld, R.S., Shachak, M., Lickens, G.E., 1997. The Ecological Basis of Conservation: Heterogeneity, Ecosystems, and Biodiversity. Chapman and Hall, New York.

Pielou, E.C., 1975. Ecological diversity. John Wiley & Sons, Inc., New York, NY.

Plotnick, R.E., Gardner, R.H., Hargrove, W.W., Prestegaard, K., Perlmutter, M., 1996. Lacunarity analysis: a general technique for the analysis of spatial pattern. Physical Review E 53, 5461–5468

Plotnick, R.E., Gardner, R.H., O'Neill, R.V., 1993. Lacunarity indices as measures of landscape texture. Landscape Ecology 8, 201–211.

Prescott, C.E., 2002. The influence of the forest canopy on nutrient cycling. Tree Physiology 22, 1193–1200.

Saunders, S.C., Chen, J., Crow, T.R., Brosofske, K.D., 1998. Hierarchical relationships between landscape structure and temperature in a managed forest landscape. Landscape Ecology 13, 381–395.

Saunders, S.C., Chen, J., Drummer, T.D., Gustafson, E.J., Brosofske, K.D., 2005. Identifying scales of pattern in ecological data: a comparison of lacunarity, spectral and wavelet analyses. Ecological Complexity 2, 87–105.

Silbernagel, J., Moeur, M., 2001. Modeling canopy openness and understory gap patterns based on image analysis and mapped tree data. Forest Ecology and Management 149, 217–233.

Song, B., Chen, J., Desenker, P.V., Reed, D.D., Bradshaw, G.A., Franklin, J.F., 1997. Modeling canopy structure and heterogeneity across scales: from crowns to canopy. Forest Ecology and Management 96, 217–229.

Song, B., Chen, J., Silbernagel, J., 2004. Three-dimensional canopy structure of an old-growth Douglas-fir forest. Forest Science 50, 376–386.

Spies, T.A., 1998. Forest structure: a key to ecosystems. In: Trofymow, J.A., MacKinnon, A. (Eds.), Structure, Process, and Diversity in Successional Forests of Coastal British Columbia. Northwest Science 72, 34–39.

Spies, T.A., 2004. Ecological concepts and diversity of old-growth forests. Journal of Forestry 102, 14–20.

Staudhammer, C., LeMay, V., 2001. Introduction and evaluation of possible indices of stand structural diversity. Canadian Journal of Forest Research 31, 1105–1115.

St-Onge, B., Treitz, P., Wulder, M.A., 2003. Tree and canopy height estimation with scanning LiDAR. In: Wulder, M.A., and Franklin, S.E. (Eds.), Remote sensing of forest environments: concepts and case studies. Kluwer Academic Publishers, Boston, pp. 489–509.

Stoyan, D., Penttinen, A., 2000. Recent applications of point process methods in forestry statistics. Statistical Science 15, 61–78.

Sun, G., Ranson, K.J., 1998. Radar modeling of forest spatial patterns. International Journal of Remote Sensing 19, 1769–1791.

Treitz, P., Howarth, P., 2000. High spatial resolution remote sensing data for forest ecosystem classification: an examination of spatial scale. Remote Sensing of Environment 72, 268–289.

Trichon, V., Walter, J-M., Laumonier, Y., 1998. Identifying spatial patterns in tropical rainforest structure using hemispherical photographs. Plant Ecology 137, 227–244.

Van Pelt, R., Franklin, J.F., 2000. Influence of canopy structure on the understory environment in tall, old-growth, conifer forests. Canadian Journal of Forest Research 30, 1231–1245.

Van Pelt, R., Nadkarni, N.M., 2004. Development of canopy structure in *Pseudotsuga menziesii* forests in the southern Washington Cascades. Forest Science 50, 326–341.

Van Pelt, R., North, M.P., 1996. Analyzing canopy structure in Pacific Northwest old-growth forests with a stand-scale crown model. Northwest Science 70, 15–30.

Walter, J.-M., Himmler, C.G., 1996. Spatial heterogeneity of a Scots pine canopy: an assessment by hemispherical photographs. Canadian Journal of Forest Research 26, 1610–1619.

Weishampel, J.F., Blair, J.B., Knox, R.G., Dubayah, R., Clark, D.B., 2000. Volumetric LiDAR return patterns from an old-growth tropical rainforest canopy. International Journal of Remote Sensing 21, 409–415.

Weishampel, J.F., Godin, J.R., Henebry, G.M., 2001. Pantropical dynamics of 'intact' rain forest canopy texture. Global Ecology & Biogeography 10, 389–397.

Wirth, R., Weber, B., Ryel, R.J., 2001. Spatial and temporal variability of canopy structure in a tropical moist forest. Acta Oecologica 22, 235–244.

Zenner, E.K., 2005. Investigating scale-dependent stand heterogeneity with structure-area-curves. Forest Ecology and Management 209, 87–100.

Zenner, E.K., Hibbs, D.E., 2000. A new method for modeling the heterogeneity of forest structure. Forest Ecology and Management 129, 75–87.

Zimble, D.A., Evans, D.L., Carlson, G.C., Parker, R.C., Grado, S.C., Gerard, P.D., 2003. Characterizing vertical forest structure using small-footprint airborne LiDAR. Remote Sensing of Environment 87, 171–182.

Appendix 3

Catalogue of simulated canopy height models[3]

[3] Bitmaps are composed of 100 columns and 100 rows and represent 50 m × 50 m ground-reference plot with outer surface canopy heights measured on a 0.5 m grid.

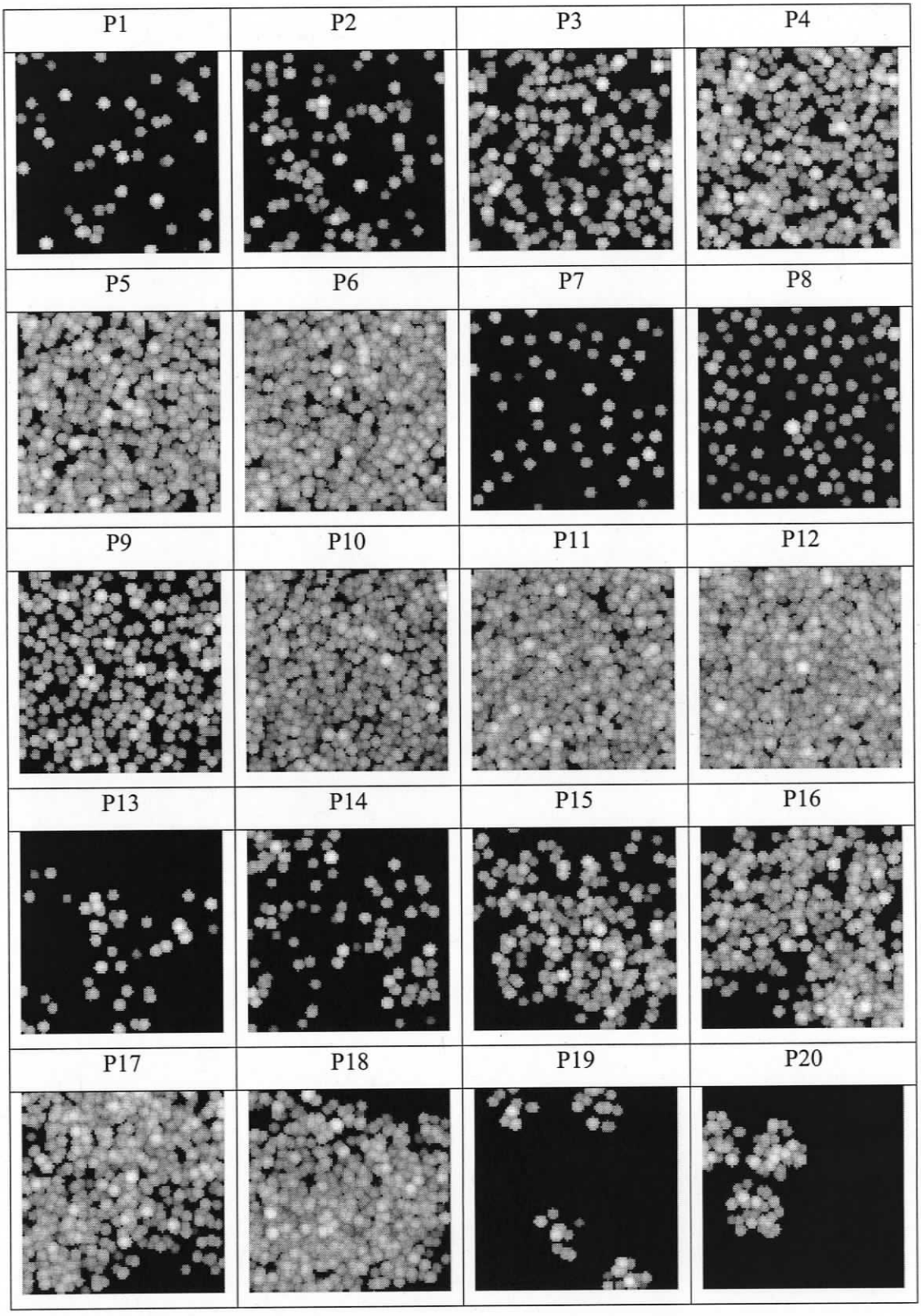
P1
P2
P3
P4
P5
P6
P7
P8
P9
P10
P11
P12
P13
P14
P15
P16
P17
P18
P19
P20

P21	P22	P23	P24
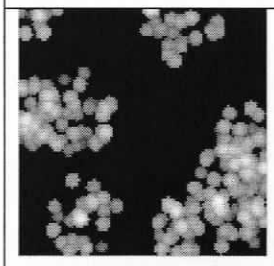	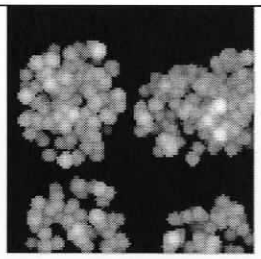	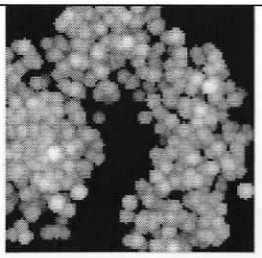	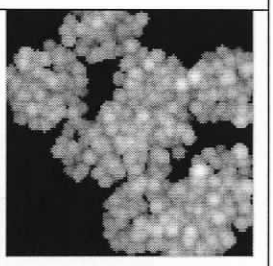
P25	P26	P27	P28
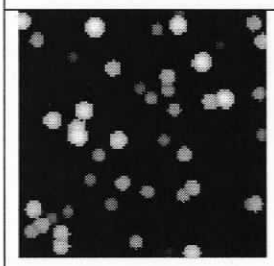	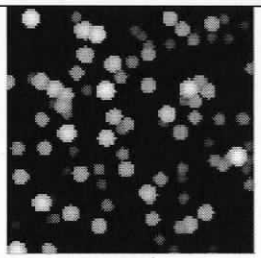	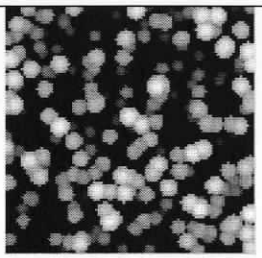	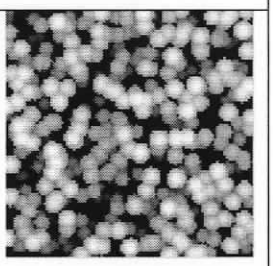
P29	P30	P31	P32
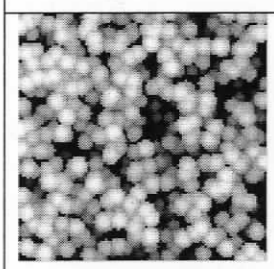	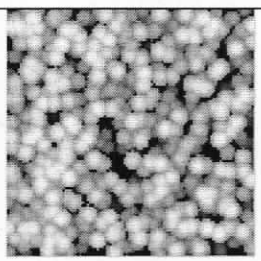	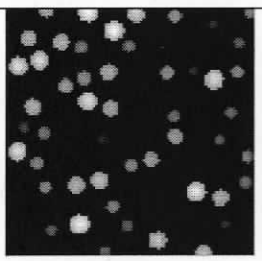	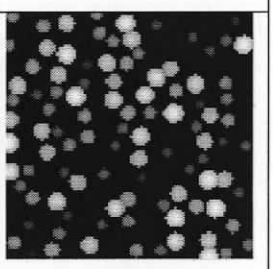
P33	P34	P35	P36
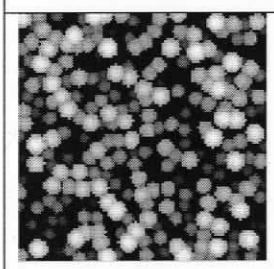	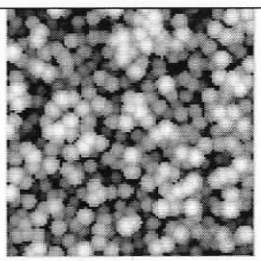	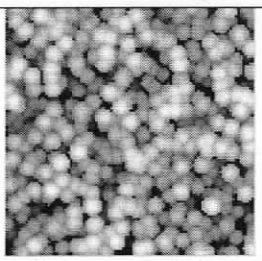	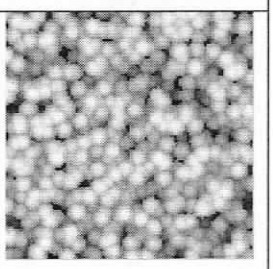
P37	P38	P39	P40
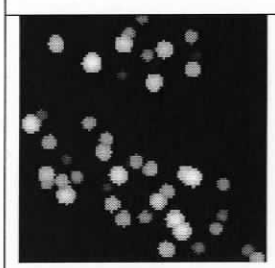	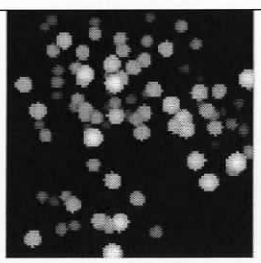	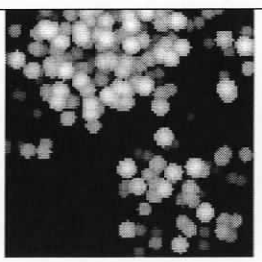	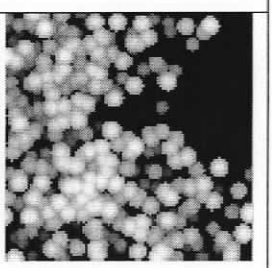

P41	P42	P43	P44
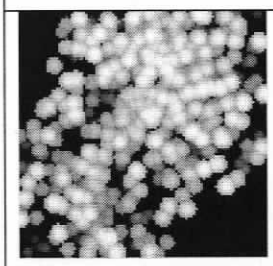	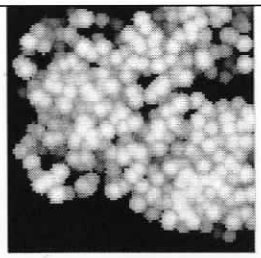	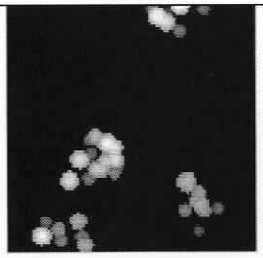	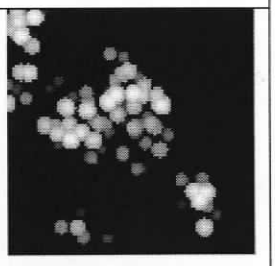
P45	P46	P47	P48
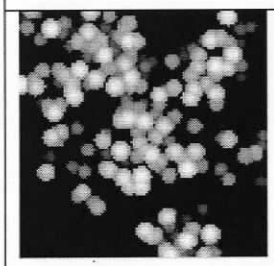	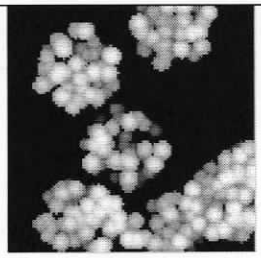	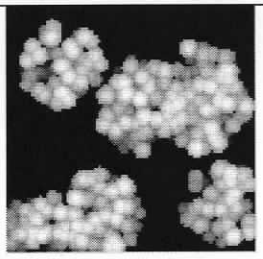	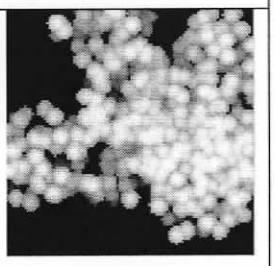
P49	P50	P51	P52
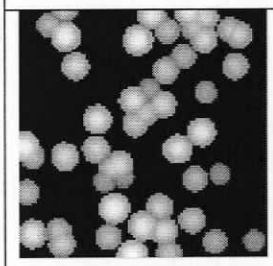	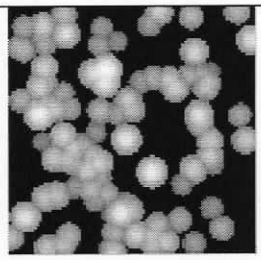	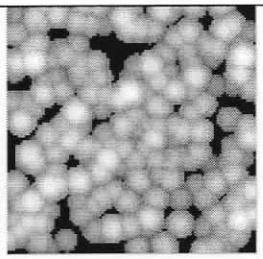	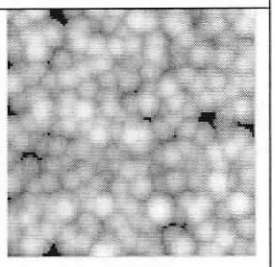
P53	P54	P55	P56
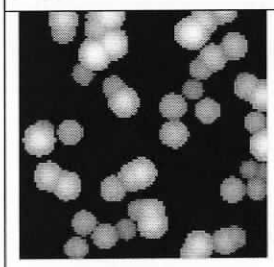	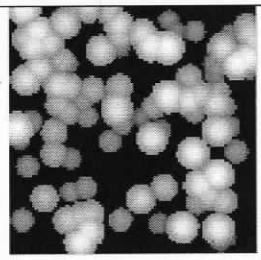	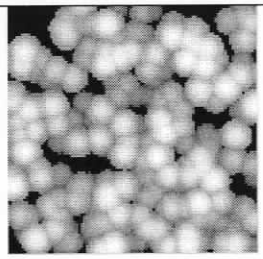	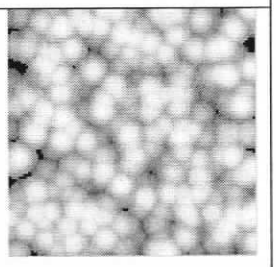
P57	P58	P59	P60
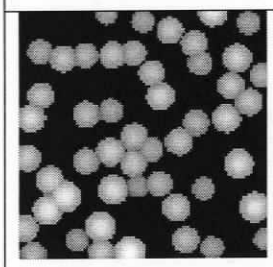	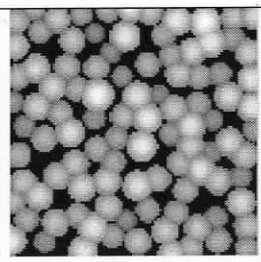	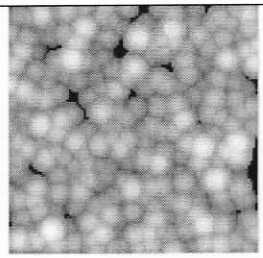	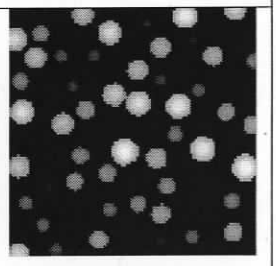

P61	P62	P63	P64
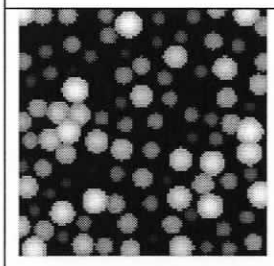	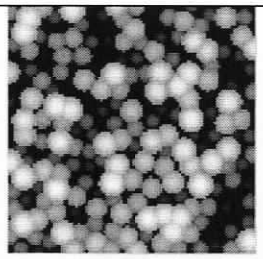	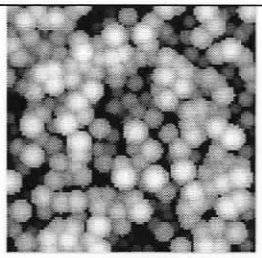	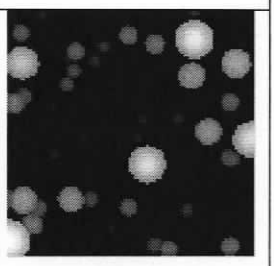
P65	P66	P67	P68
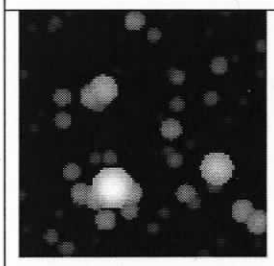	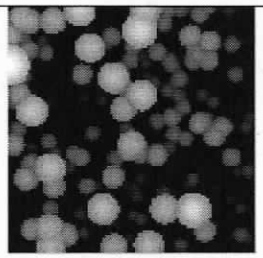	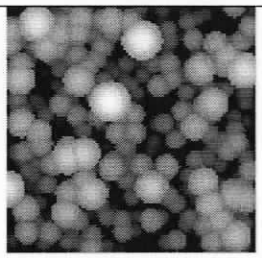	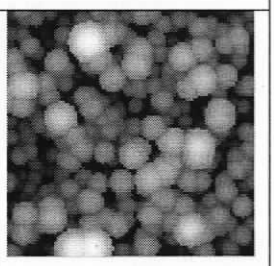
P69	P70	P71	P72
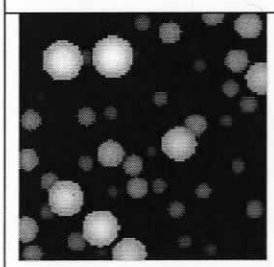	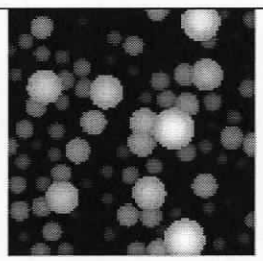	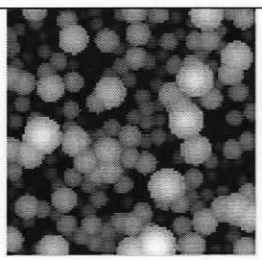	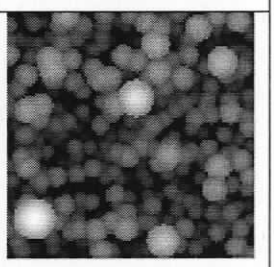
P73	P74	P75	P76
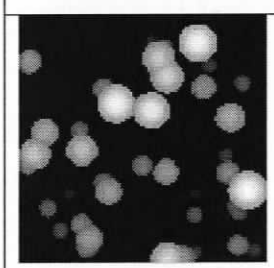	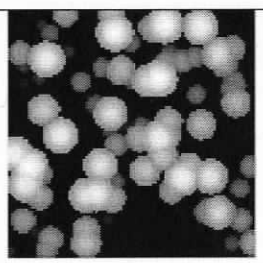	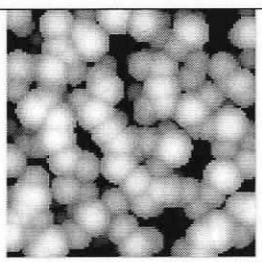	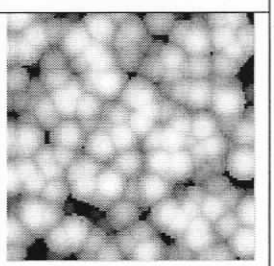
P77	P78	P79	P80
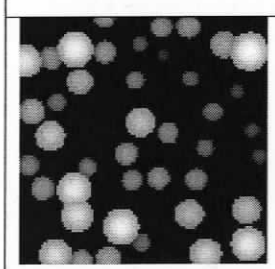	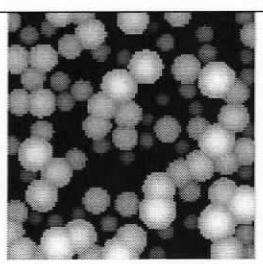	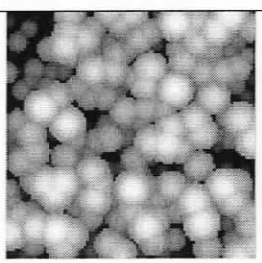	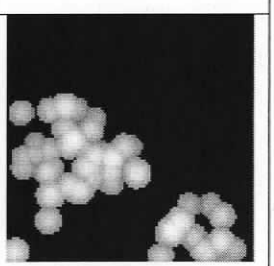

P81	P82	P83	P84
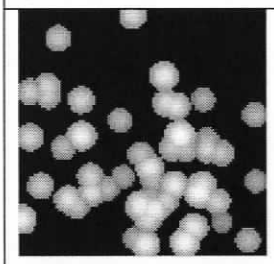	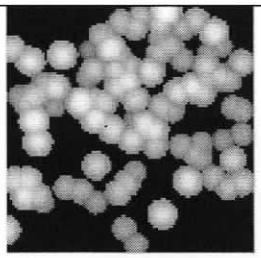	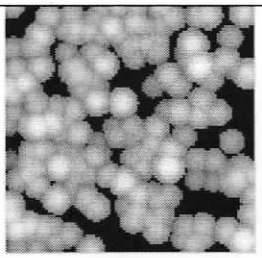	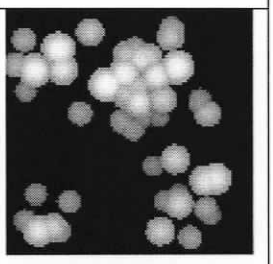
P85	P86	P87	P88
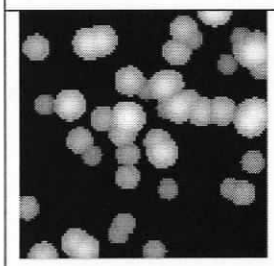	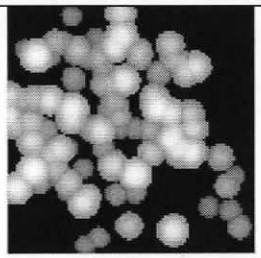	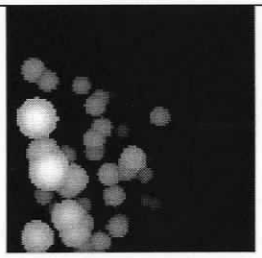	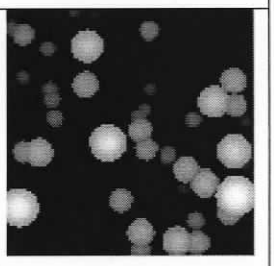
P89	P90	P91	P92
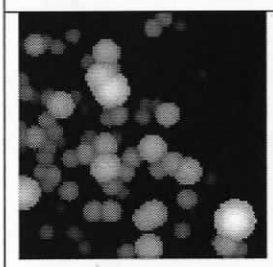	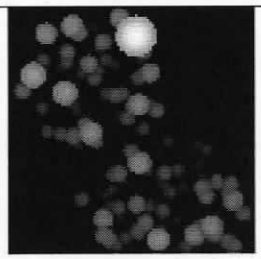	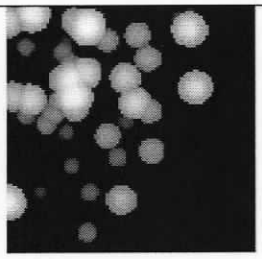	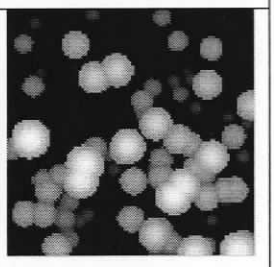
P93	P94	P95	P96
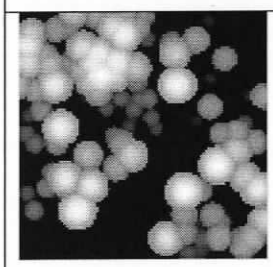	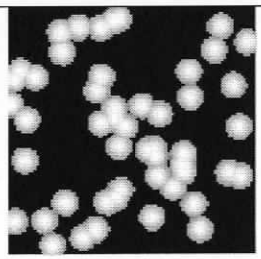	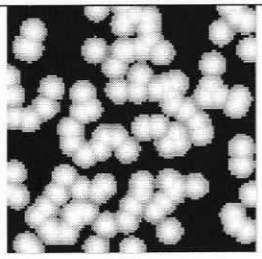	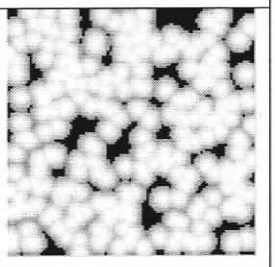
P97	P98	P99	P100
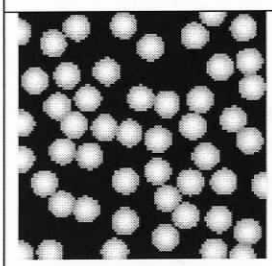	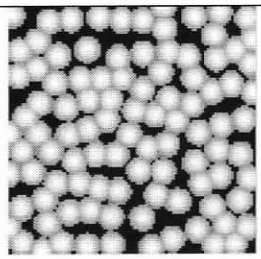	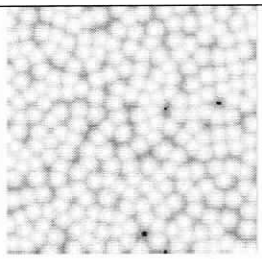	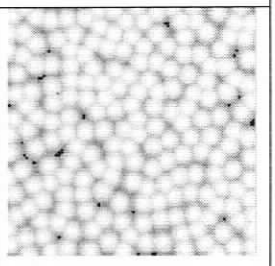

P101	P102	P103	P104
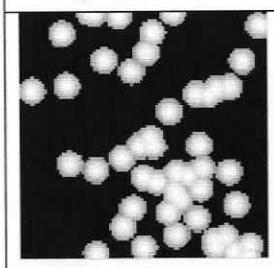	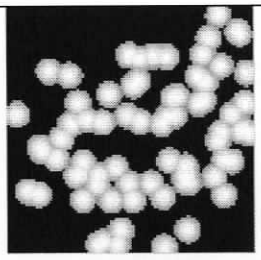	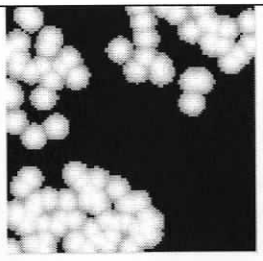	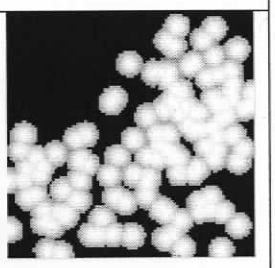
P105	P106	P107	P108
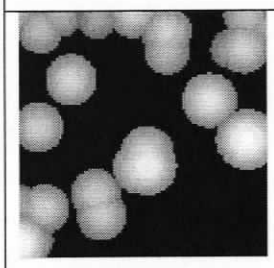	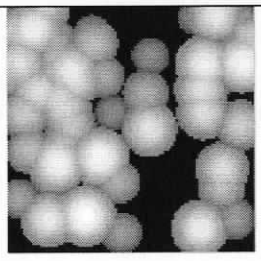	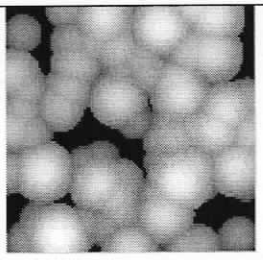	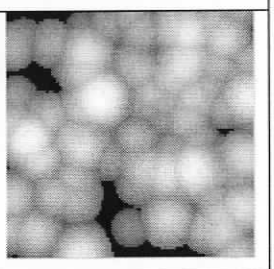
P109	P110	P111	P112
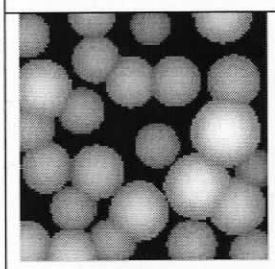	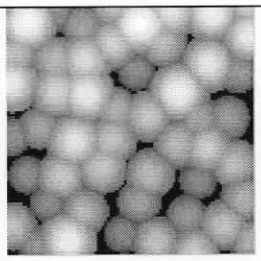	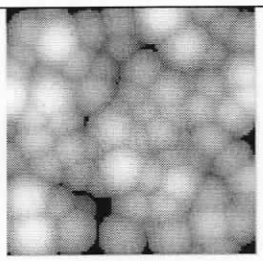	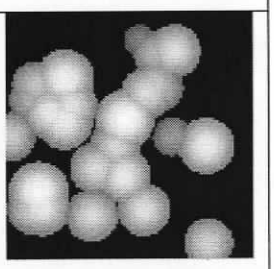
P113	P114	P115	P116
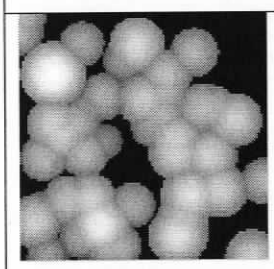	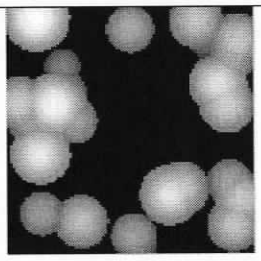	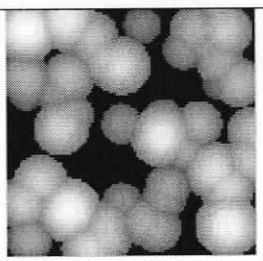	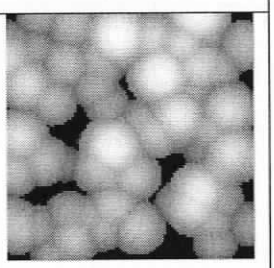
P117	P118	P119	P120
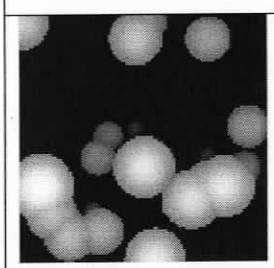	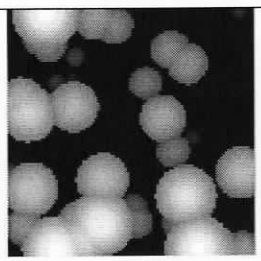	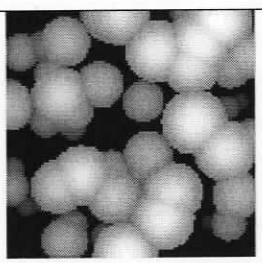	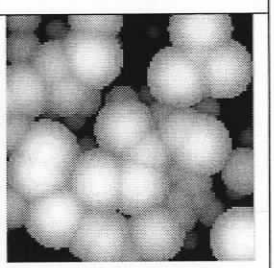

P121	P122	P123	P124
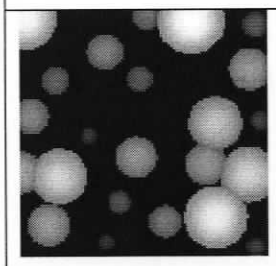	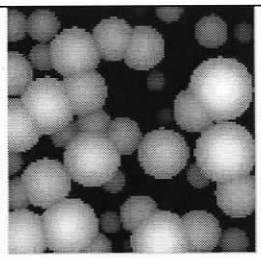	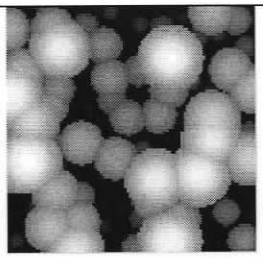	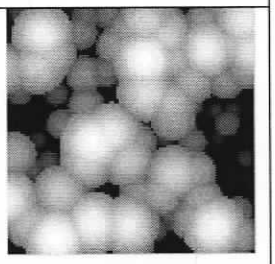
P125	P126	P127	P128
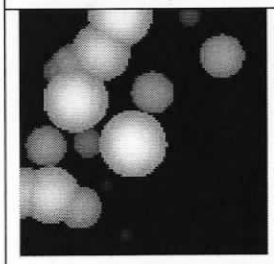	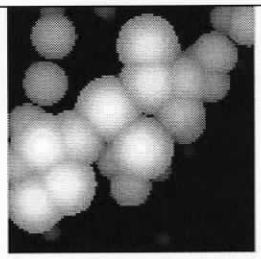	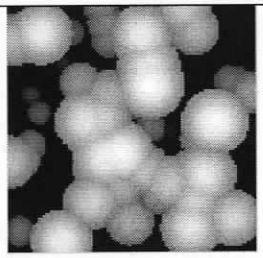	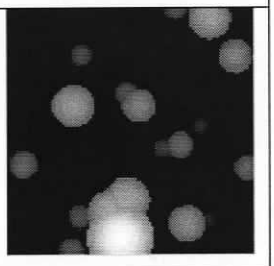
P129	P130	P131	P132
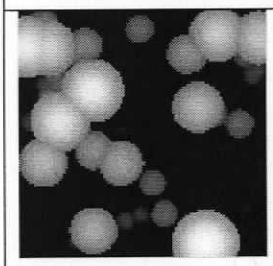	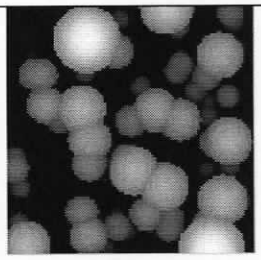	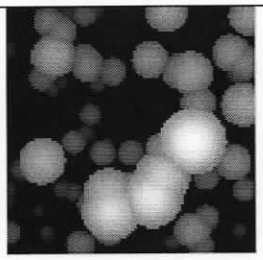	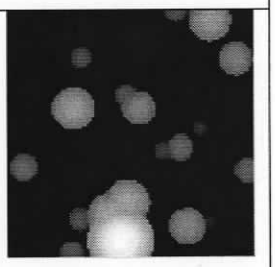
P133	P134	P135	P136
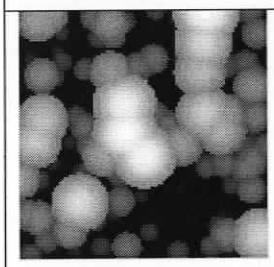	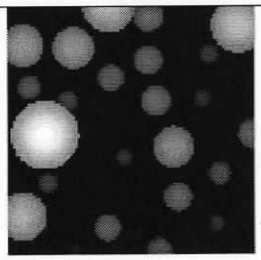	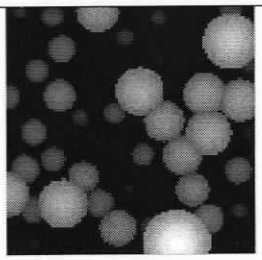	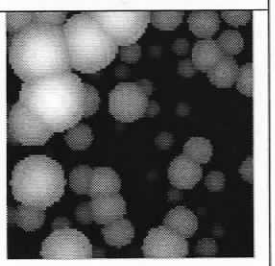
P137	P138	P139	P140
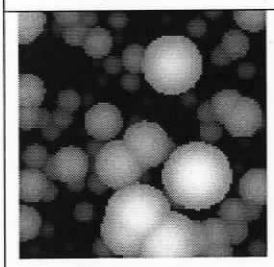	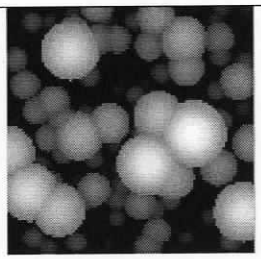	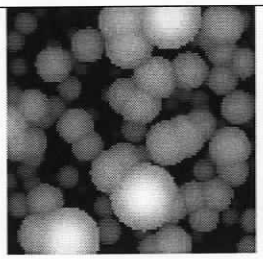	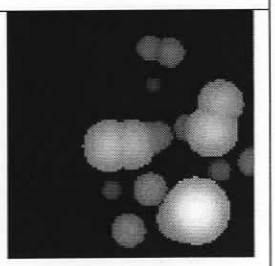

P141	P142	P143	P144
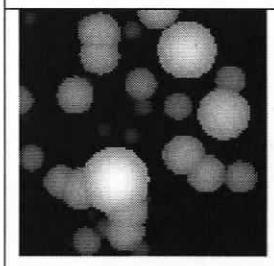	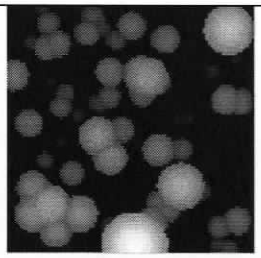	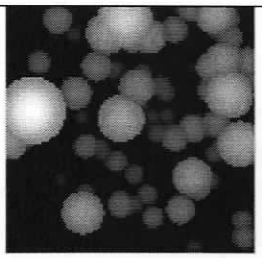	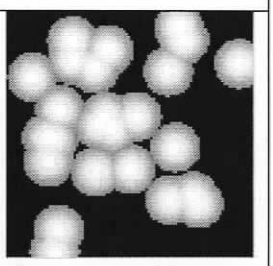
P145	P146	P147	P148
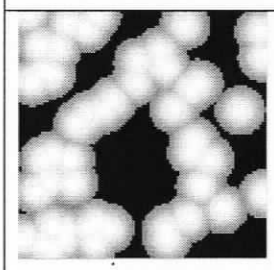	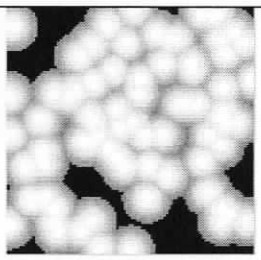	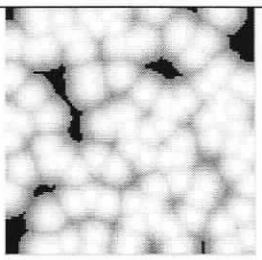	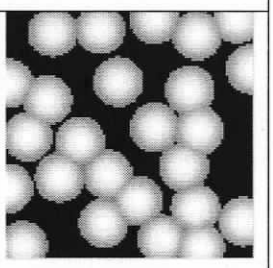
P149	P150	P151	P152
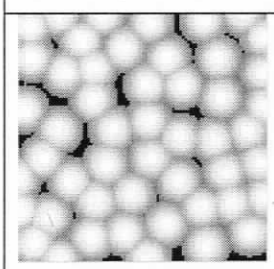	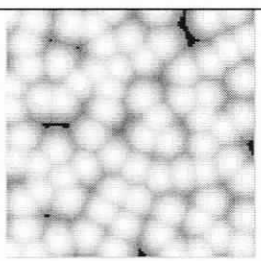	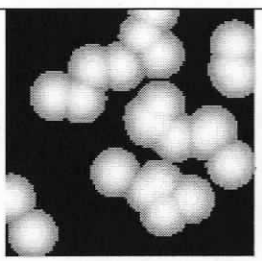	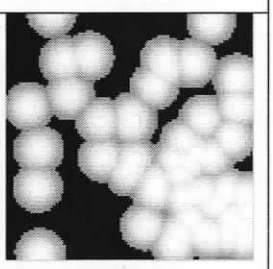
P153	P154	P155	P156
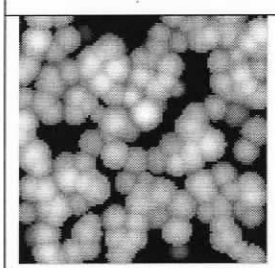	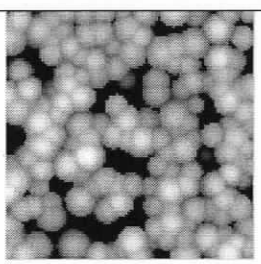	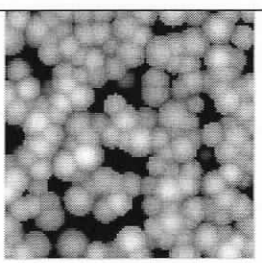	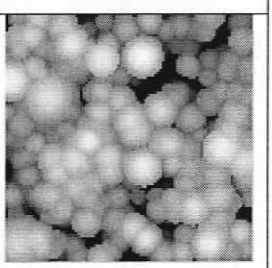
P157	P158	P159	P160
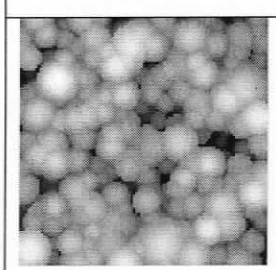	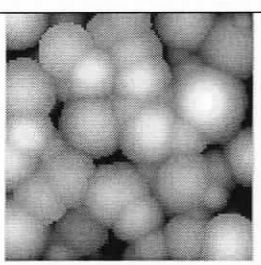	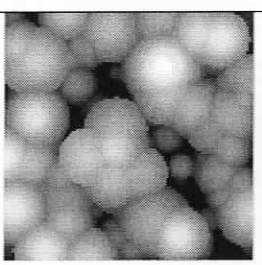	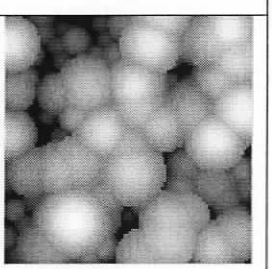

P161	P162	P163	P164
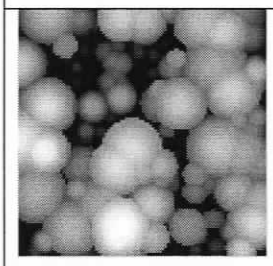	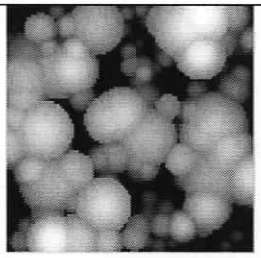	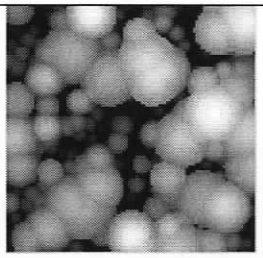	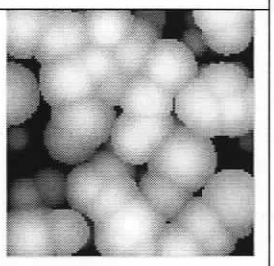
P165	P166	P167	P168
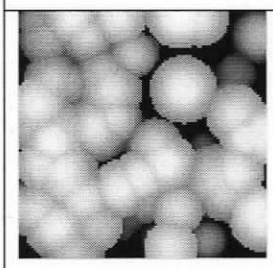	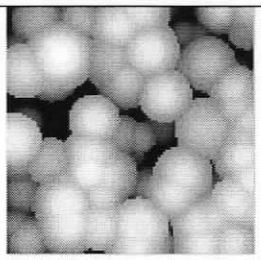	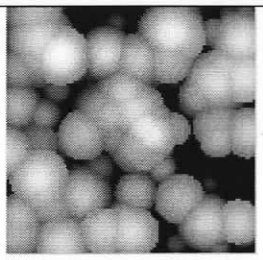	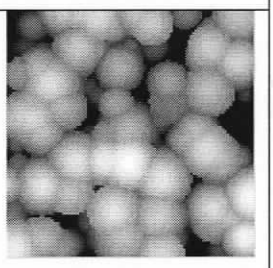
P169	P170	P171	P172
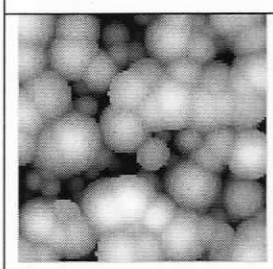	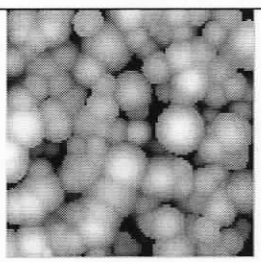	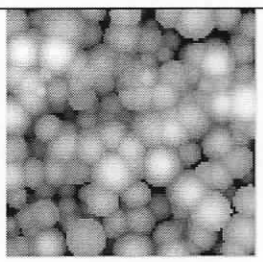	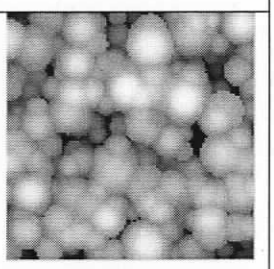
P173	P174	P175	P176
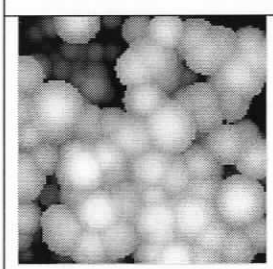	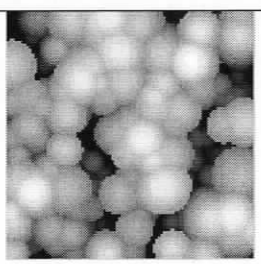	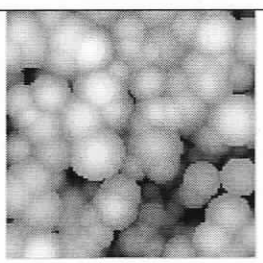	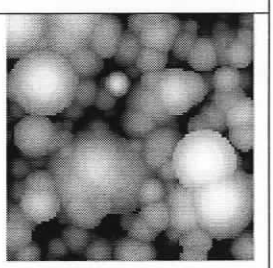
P177	P178	P179	P180
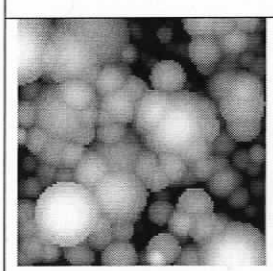	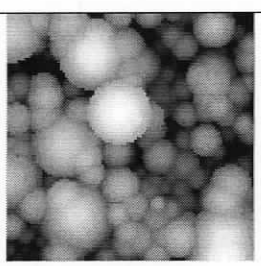	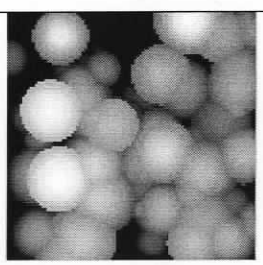	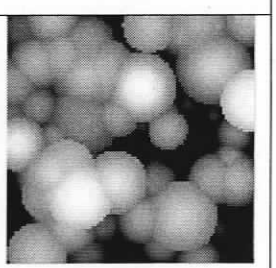

181	P182	P183	P184
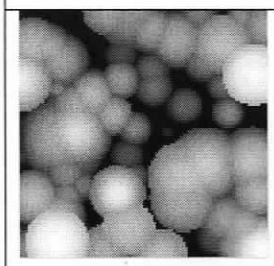	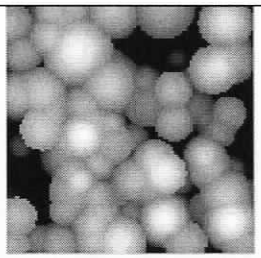	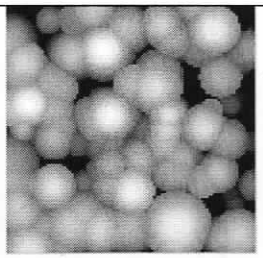	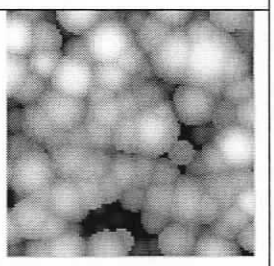
P185	P186	P187	
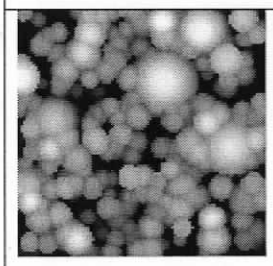	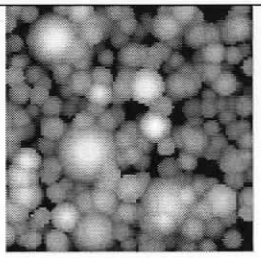	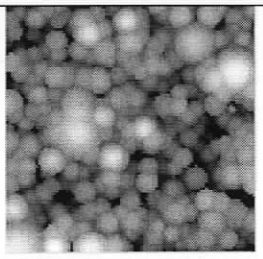	

CHAPTER 4

Use of Airborne LiDAR to Characterize Fine-Scale Vertical and Horizontal Patterns of Canopy Structure in *Pseudotsuga-Tsuga* Forests of Varying Stand Age and Structural Complexity

4.0 Abstract

Forest structure is widely regarded as an important, unifying variable in conservation biology, ecosystem science, and forest management because of its direct link to biodiversity (habitat), ecosystem function, and timber production. In this study, we describe how an airborne discrete-return, small-footprint LiDAR (Light Detection And Ranging) instrument was used to capture detailed vertical and horizontal measurements of canopy structure over a coastal *Pseudotsuga-Tsuga* forest on southeastern Vancouver Island, British Columbia. We also examine age-related developmental changes in canopy structure at decadal and century time scales using a pseudo 'space-for-time substitution' sampling approach. Finally, we show how non-hierarchical cluster analysis by *k*-means partitioning was applied to generate a purely structure-based classification as an ecologically relevant and practical alternative to stand age class. Our findings revealed that there were significant structural differences between very young (≤20 yr.), young (>20–80 yr.), mature (>80–200 yr.), and old-growth (>200 yr.) forest canopies, and that these age-class differences were generally consistent with the structures, patterns, and processes described by conceptualized models of stand and canopy development for coastal *Pseudotsuga-Tsuga* forests of northwestern North America. *k*-means partitioning identified seven to nine unique vertical and horizontal canopy structural classes within the dataset. We expect that this methodology will be used to segment landscapes into discrete classes of forest canopy structure, and that the resultant map products and data will support further scale-dependent explorations of the theoretical links between forest ecosystem structure, composition, and function, including the maintenance of forest biodiversity.

4.1. Introduction

The ecological properties (i.e., composition, structure, and function) of a forest stand change markedly as the stand advances in age from young to old growth (Spies, 1997). Structural and successional pathways of stand development following stand-initiating disturbances are well described for many general forest types (Oliver, 1981; West et al., 1981; Pickett and White, 1985; Oliver and Larson, 1996; Franklin et al., 2002), while the functional implications of these ecological changes at local, regional, and global scales still remain poorly known (Pacala and Deutschman, 1995; Perry, 1998; Parker et al., 2004; Pregitzer and Euskirchen, 2004; Ogunjemiyo et al., 2005). Structural trajectories of forest stand development are usually defined by the temporal dynamics of easily measured forest attributes (Spies, 1998), such as the size distributions of live trees (Oliver and Larson, 1996); stand density, volume, and biomass (Acker et al., 1998); and abundances of snags and coarse woody debris (Spies et al., 1988). Attributes of canopy structure, on the other hand, have been far more difficult to measure, due to problems with physical access and the overwhelming complexity of forest canopies in both space and time (Lowman and Rinker, 2004). Consequently, much less is known about the stand-level spatial organization and developmental pathways of forest canopies (Ishii et al., 2004a,b; Parker and Russ, 2004; Van Pelt and Nadkarni, 2004).

The three-dimensional (3-D) spatial arrangement and temporal dynamics (the fourth dimension) of tall woody plants, including all of their aboveground component parts (e.g., foliage, twigs, branches, boles, seeds, cones, flowers, epiphytes, etc.) and the open interstitial spaces (gaps) separating them are all considered the domain of forest canopy structure (Parker, 1995; Connell et al., 1997; Dial et al., 2004; Nadkarni et al., 2004). Forest canopies are widely recognized as the fundamental site for many key ecosystem processes and functions, such as regulation of the stand microclimate, primary production, biogeochemical cycles, atmosphere-biosphere interactions, and biodiversity (Parker, 1995; Chen et al., 1999; Chapin et al., 2002; Ozanne et al., 2003). Biological, physiological, and ecological properties of forest canopies have therefore become subjects of considerable research interest (Ryan, 2002; Lowman and Rinker, 2004).

Stand-level studies of canopy structure have generally focused on patterns and processes occurring within vertical and horizontal dimensions of a forest. Vertical patterns of canopy structure arise from within-stand differences in vegetation height, age, architecture, and species composition (Parker et al., 1989; McComb et al., 1993; Dubrasich et al., 1997; Ishii et al., 2000), and have been linked to vertical gradients of microclimates, materials (i.e., phytomass, nutrients, gases, water, pollutants, etc.), processes, and organisms (Brokaw and Lent, 1999; Lewis et al., 2000; Parker et al., 2004; Winchester, 2006). Horizontal structure describes the spatial organization of forest canopies in the *XY*-plane (Bradshaw and Spies, 1992; Bartemucci et al., 2002; Song et al., 2004), and has been closely associated with aboveground productivity, stand dynamics, dispersal of organisms, and spread of natural disturbances (Pacala and Deutschman, 1995; Lertzman and Fall, 1998; Spies and Turner, 1999; Chen et al., 2004). Vertical and horizontal patterns of canopy structure, however, are not entirely spatially independent of one another (Brokaw and Lent, 1999), since vertical structure varies with measurement location and extent (plot size) in the *XY*-plane, and horizontal structure changes markedly with canopy height (Song et al., 1997; Chen and Bradshaw, 1999; Ishii et al., 2004b; Song et al., 2004; Parker et al., 2004).

Although numerous field techniques have been developed for fine-scale *in situ* measurements of forest canopy structure (Fournier et al., 2003), all remain impractical for spatially continuous mapping of canopy structure over broad geographic areas. Airborne discrete-return, small-footprint Light Detection And Ranging (LiDAR) systems, on the other hand, hold considerable promise for 3-D characterizations of forest canopy structure at very high spatial resolutions (multiple returns per square metre) and over relatively large areas (Lefsky et al., 2002; Lim et al., 2003; Reutebuch et al., 2005). These active sensors emit short (4–10 ns), narrowly collimated (0.15–3 mrad) pulses of laser energy (850–1060 nm) at very high frequencies (10–100 kHz), and then record the return-time-of-flight (range) and amplitude (intensity) of selected backscatter events (typically first, last, and/or intermediate peaks in the return signal). A scanning mechanism deflects pulses of laser energy (10–160 scans per second) in an across-track direction beneath the aircraft, while an onboard GPS and inertial measurement unit allow accurate 3-D (*XYZ*) georeferencing of each recorded backscatter event.

Sample quantiles derived from the height distribution of LiDAR canopy returns have been widely used in regression to predict several attributes of stand structure (Means et al., 2000; Næsset, 2002; Lim and Treitz, 2004). Others have shown that the vertical distribution of LiDAR canopy heights is well correlated with the vertical arrangement of canopy structure (Magnussen and Boudewyn, 1998; Blair and Hofton, 1999; Lovell et al., 2003; Parker and Russ, 2004; Maltamo et al., 2005; Coops et al., 2007). Therefore, we expect that sample quantiles, along with dispersion (scale) and shape-related statistical properties of the LiDAR canopy height distribution, will provide a distinctive multivariate signature and basis for characterizing vertical canopy structure (Zimble et al., 2003; Jerez et al., 2005; Kao et al., 2005; Lefsky et al., 2005; van Aardt et al., 2006). Analytical techniques explicitly used to characterize fine-scale horizontal patterns of forest canopy structure have been far less well developed in the LiDAR remote sensing literature, and only a few published methodological examples currently exist (e.g., Koukoulas and Blackburn, 2004; Parker et al., 2004; Frazer et al., 2005). Here, we expand on the lacunarity-based approach presented by Frazer et al. (2005) to quantify scale-dependent patterns of canopy structure in the horizontal domain.

Our primary objective for this paper is to present a methodological framework for quantifying, classifying, and comparing fine-spatial-scale vertical and horizontal patterns of forest canopy structure derived from airborne LiDAR data. This methodology is demonstrated using a discrete-return LiDAR dataset collected over managed and natural, very young to old-growth *Pseudotsuga-Tsuga* (Douglas-fir/western hemlock) forests on Vancouver Island, British Columbia. We also apply this novel technique to explore the following questions: (1) What are the key attributes of vertical and horizontal canopy structure that separate and define young, mature, and old-growth *Pseudotsuga-Tsuga* forests?; (2) Are age-class differences consistent with the structural characteristics, patterns, and dynamics predicted by generalized, process-based models of forest stand development for Pacific Coast *Pseudotsuga-Tsuga* forests of western North America (i.e., Spies, 1997; Franklin et al., 2002; Franklin and Van Pelt, 2004); (3) Is it possible to partition sample units and landscapes into other ecologically relevant classes based solely on the fine-spatial-scale measurements of vertical and horizontal canopy structure derived from an airborne LiDAR?

4.2. Materials and Methods

4.2.1. Study area description

Our study area was located (48°35' N, 123°42' W) within the northern portion (3,746 of total 8,613 ha) of the Sooke Lake watershed (SLW) on southeastern Vancouver Island, British Columbia, Canada (Fig. 4.1). SLW is part of the Victoria Highland physiographic region of Vancouver Island (Yorath and Nasmith, 1995), and falls within the Very Dry Maritime subzone (variants CWHxm1 and CWHxm2) of the Coastal Western Hemlock (CWH) biogeoclimatic zone (Trofymow et al., 1997). The terrain is characterized by low (elevations 190–850 metre above sea level), well-rounded, gently to moderately sloping hills and mountains. Forest soils are typically loamy to coarse-skeletal Dystric Brunisols or Humo-Ferric Podzols that have developed on a well-drained, gravelly sandy till deposited during the last glacial event (Fraser Glaciation, 10,000–29,000 BP yr.). Bedrock is exposed at several locations throughout the watershed in the form of minor bluffs, cliffs, benches, knolls, and other local prominences.

SLW experiences relatively warm, dry summers and mild, wet winters (mean annual temperature is 9.4° C), with approximately 75% of the total mean annual precipitation (1500 mm) falling as rain during the months of October to March. The proportion of total precipitation falling as snow is generally less than 15% (Trofymow et al., 1997). The most common floristic site association in SLW is the Douglas-fir (*Pseudotsuga menziesii* (Mirb) Franco)-western hemlock (*Tsuga heterophylla* (Raf.))-salal (*Gaultheria shallon* Pursh) association. Here, early-seral, shade-intolerant Douglas-fir dominates the overstory in most stands, while more shade-tolerant, late-successional species such as western hemlock and western redcedar (*Thuja plicata* Donn.) often occupy lower canopy positions. Other common, but less-abundant tree species of varying shade tolerance include grand fir (*Abies grandis* (Dougl.) Lindl.), shore pine (*Pinus contorta* Dougl. ex loud.), western white pine (*Pinus monticola* Dougl.), western yew

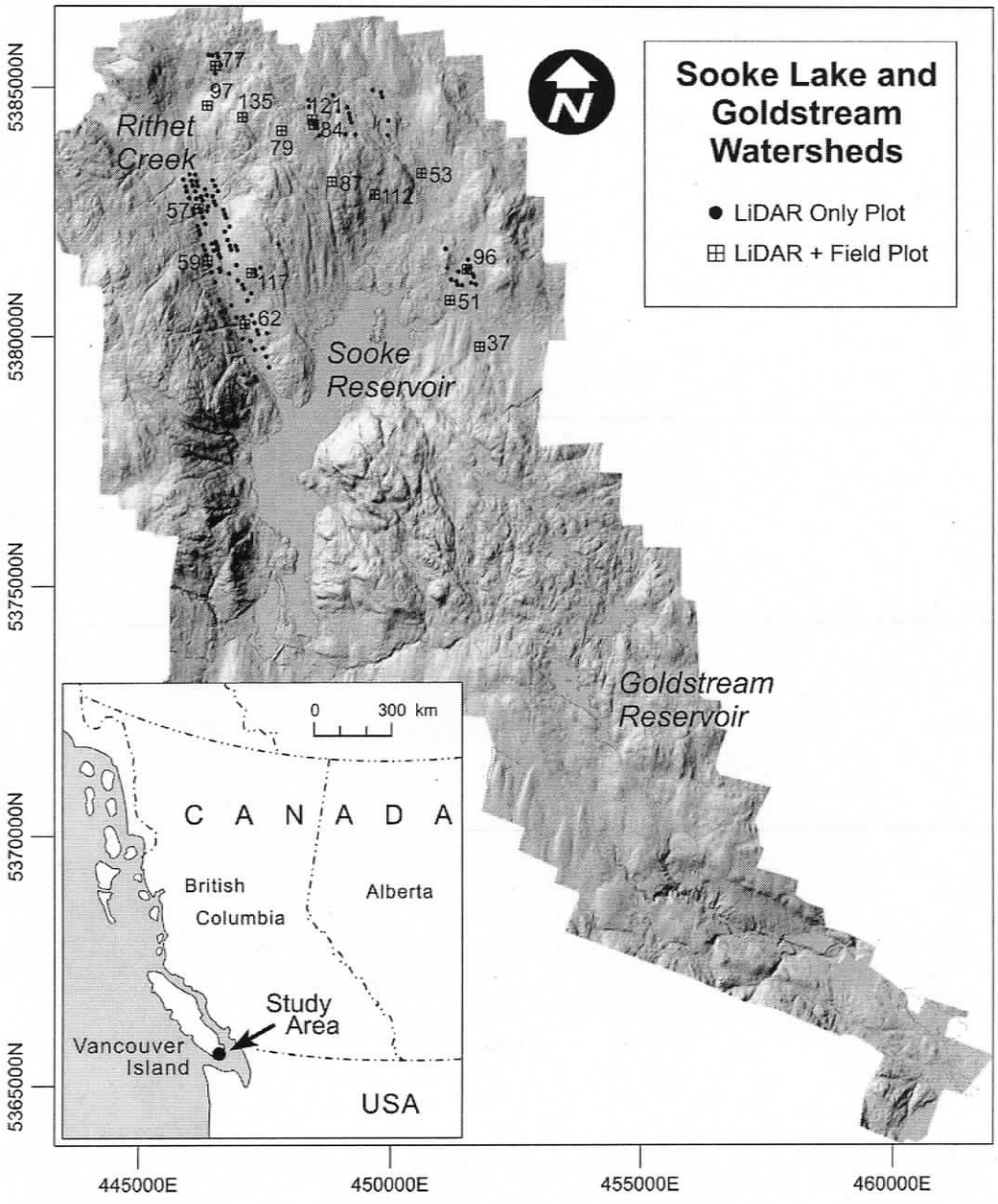

FIGURE 4.1. Site map showing the location of 152 square (0.25 ha) sample plots within the Sooke Lake watershed (SLW). LiDAR flight lines were restricted to the northern portion of SLW. Flight-lines were spatially discontinuous due to high winds at the time of the LiDAR survey (November 2001). Sample sites located along Rithet Creek were either young plantations (<60 yr.) or original old-growth (>200 yr.) forest cover. Mature stands (>80–200 yr.) were restricted to areas surrounding field plots # 84, 97, 77, 96, and 51 (see Table 4.2). The 2 m digital elevation model used as the base map was constructed using LiDAR ground returns from a more recent survey flown in August 2006.

(*Taxus brevifolia* Nutt.), red alder (*Alnus rubra* Bong.), big leaf maple (*Acer macrophyllum* Pursh), and arbutus (*Arbutus menziesii*). The prevalence and mix of these different species within SLW is strongly dependent on site productivity, topographic position, disturbance history, and stand age.

SLW has been an important water supply area for Greater Victoria since 1914, and has therefore been subject to a number of long-standing regulatory policies governing public access, land-use, road construction, logging, and fire suppression. Nevertheless, limited salvage, selective (removal of cedar poles), and clear-cut logging have occurred in many parts of the watershed over the past 70 years. Approximately 38% of the study area is covered by young (≤80 yr.) managed plantations of harvest origin (established between 1956 and 1997), while the remaining forest cover is composed of late-successional mature (12%; >80–200 yr.) and old-growth (50%; >200 yr.) stands that established naturally after wildfire (Capital Regional District, *unpublished data*). Old fire scars, charred bark, charcoal, live veterans, and other relic evidence of past fires found throughout SLW indicate the historical importance of mixed-severity fires in the development and maintenance of these relatively dry, east-side island CWH forests. Pathogens, insects, and windthrow are also prevalent and active agents of forest disturbance throughout SLW.

4.2.2. Sampling design and plot selection

Airborne LiDAR data were collected over a five-day period beginning 01 November 2001 using a helicopter-mounted (Eurocopter AS350 A-Star), pulsed laser scanner (Riegl LMS-Q140i-60) system that was designed and operated by Mosaic Mapping Systems Inc., Ottawa. Survey flight characteristics and LiDAR instrument settings are summarized in Table 4.1. High winds at the time of the survey prevented complete sampling of all planned flight lines, and resulted in discontinuous, patchy LiDAR coverage for the northern portion of SLW. Only sections of individual flight lines that appeared straight and exhibited a relatively uniform spatial pattern of individual returns were considered potential sites for the placement of LiDAR and ground-reference sample plots. We used these two criteria as reliable evidence that the helicopter and

LiDAR sensor were stable and unaffected by wind turbulence at the time of data acquisition.

TABLE 4.1. Summary of LiDAR flight and instrument settings

Parameter	Setting
Flight altitude	220 m (AGL)
Swath width	220 m
Flight-line spacing	120 m
Flight-line overlap	40%
Laser wavelength	900 nm (NIR)
Pulse frequency	28 kHz
Scan angle	± 30°
Scan rate	34 Hz
Mirror type	Rotating, unidirectional
Scan pattern	Diagonal, parallel
Post spacing	0.4 m (across track), 1.0 m (along track)
Beam divergence	3.0 mrads (0.9 m @ 300 m)
Collection mode*	First pulse, last pulse, intensity (8-bit)

*Alternating first pulse and last pulse detection.

Our sampling strategy was similar to the "space-for-time substitution" approach of Pickett (1989); however, our intent here was not to create a true successional chronosequence, but rather to establish a strong gradient of forest canopy structure, ranging from simple (young plantations) to complex (natural old-growth canopies). We recognized that there were many ecological, environmental, and historical factors that would contribute to the development of complex forest structures and patterns (Lertzman and Fall, 1998; Spies and Turner, 1999; White and Jentsch, 2001; Franklin and Van Pelt,

2004). Therefore, we sampled young through old riparian and upland forests with different site productivities, topographic positions, and disturbance histories as a way to capture part of this natural structural variability. We adopted the broad age classes of Spies and Franklin (1991) to define young (≤80 yr.), mature (>80–200 yr.), and old-growth (>200 yr.) forests, because of their association with major stand developmental stages in *Pseudotsuga-Tsuga* forests of coastal Oregon, Washington, and British Columbia (Franklin et al., 2002). However, we further split the "young" age class into two other discrete classes to try and distinguish between young forest canopies before (very young: ≤20 yr.) and after canopy closure (young: >20–80 yr.).

We relied on the LiDAR flight lines that were minimally affected by wind; forest cover maps; aerial photographs; inventory age-classes, and some field reconnaissance to systematically locate 152 0.25 ha (50 m × 50 m) sample plots. Our choice of plot size was based on the need to balance two methodological requirements: (1) the plot had to be large enough to reliably capture an adequate portion of the within-stand structural variability inherent in late-successional *Pseudotsuga-Tsuga* forests (Zenner, 2005b), while (2) still remaining small enough that ground-reference measurements did not become too laborious. We located all sample plots on flight-line centres to avoid large (>10°) scan angles (Holmgren et al., 2003), and as far away from stand boundaries as possible to minimize forest-edge influences on stand structure and composition (Harper et al., 2005). We tried to balance the number of early-successional plots (n = 74) with late-successional plots (n = 78), but were unable to allocate sample units evenly across very young (n = 12), young (n = 62), mature (n = 28), and old-growth (n = 50) classes, due to the discontinuous LiDAR coverage and rarity of mature stands in SLW.

4.2.3. Ground-reference plots and field measurements

From the 152 sample plots selected, 16 were identified as ground-reference plots, based on their broad range of stand structures and relative ease of access (proximity to roads). We located the centre position of each field plot using a Trimble-Pro-XRB Global Positioning System receiver (Trimble Navigation, Ltd., California, USA) and real-time differential corrections transmitted by the Canadian Coast Guard, Richmond, BC. We used an Impulse 200 laser range finder (Laser Technology Inc., Colorado, USA),

reflective target, and magnetic compass adjusted for local magnetic declination (19°4' E, 2002 A.D.) to establish the orientation, boundaries, and overall layout for each ground-reference plot (Fig. 4.2). We further subdivided each ground-reference plot into four 625 m^2 quadrants, and then centred a fixed-radius (8 m) subplot over the plot centre and each of the four quadrant centres (total area equal to 1005 m^2 or approximately 40% of the 0.25 ha plot footprint). We used the fixed-radius subplots for mensurational purposes only in the very dense, young stands (P37, P53, P57, P62). Otherwise, we censused all live trees >2 m tall located within the square 0.25 ha ground-reference plot. We relied on inventory data collected in these limited number of ground-reference plots to help guide the development and interpretation of our LiDAR-based measurements of canopy structure, rather than for purposes of statistical validation and inference.

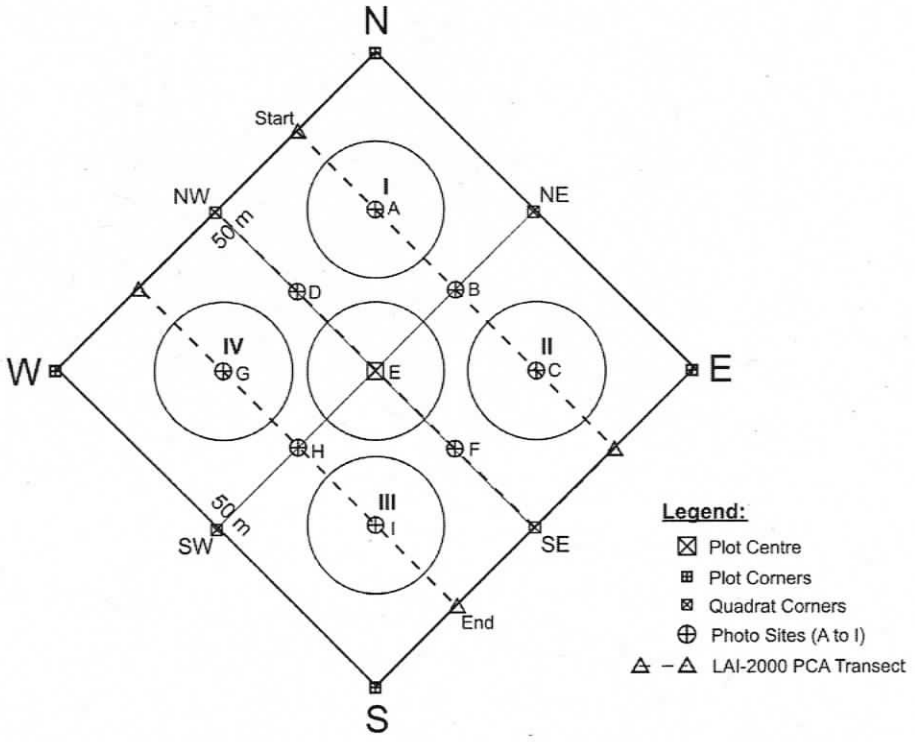

FIGURE 4.2. Dimensions and layout of 0.25 ha (50 m × 50 m) ground-reference plots used for inventory sampling and other indirect canopy measurements. Plots were further subdivided into four separate 25 m × 25 m quadrants identified by roman numerals I-IV, and five (8 m) circular subplots positioned at the centres of the plot and each of the four quadrants (total area equal to 1005 m^2 or approximately 40% of the entire plot area). We used the circular subplots to subsample four of the more densely stocked young stands (Table 4.2).

4.2.3.1. Tree inventory and stand attributes

From May to September 2002, we inventoried a total of 4891 trees for species, height, height to live crown, diameter at breast height (1.3 m; DBH), crown class (dominant, codominant, intermediate, suppressed; Avery and Burkhart, 2002: 163), and crown condition (dead, damaged, or intact) in the 16 ground-reference plots. Heights were estimated using the Impulse 200 laser range finder, and DBH was measured directly by diameter tape. For each live tree, we computed its basal area (m^2) and gross volume (m^3) using species- and region-specific taper equations implemented in TREEVOL software (BC Ministry of Forests and Range, Victoria). We also computed the following stand-level summary statistics for each ground-reference plot using live trees ≥ 2 m tall (Table 4.2): basal area (BA, m^3/ha); stem density (SD, n/ha); gross volume (VOL, m^3/ha); species abundance (measured as a percentage of total BA); quadratic mean diameter (QMD, cm; Curtis and Marshall, 2000); mean and standard deviation of tree diameter (cm); Lorey's mean height (h_L, m; Curtis and Marshall, 2000); mean, standard deviation, and percentiles of tree height (m). Lastly, we computed the Shannon index (H') as an indicator of tree diameter (H'_d) and height (H'_h) diversity (Staudhammer and LeMay, 2001):

$$H' = -\sum_{i=1}^{S} p_i \ln p_i , \qquad (4.1)$$

where p_i is the proportion of BA per hectare in diameter or height class i, and S is the total number of 3-cm (i.e., Class 1: 0 to <3 cm; Class 2: 3 to <6 cm, etc.) diameter or 2 m (i.e., Class 1: 2 to <4 m; Class 2: 4 to <6 m, etc.) height classes. Maximum size classes were determined by the largest tree diameter and height measured in each plot. Empty size classes were set to $\ln p_i = 0$, since the logarithm of zero is infinite and undefined.

TABLE 4.2. Summary of live-tree (≥2 m tall) stand attributes for 16 ground-reference plots (0.25 ha) established in Sooke Lake watershed, Vancouver Island, BC.

						Species				DBH				Height				
Plot ID	Age Class	CC %	BA m^2/ha	SD n/ha	VOL m^3/ha	Cw %	Fdc %	Hw %	Other %	QMD cm	Avg. cm	s.d. cm	H'_d	h_L m	h_{95} m	Avg. m	s.d. m	H'_h
P37	Y	93.9	41.0	4307	267.0	1.9	90.8	5.7	1.6	11.0	8.7	6.8	2.26	16.6	17.6	9.7	5.7	2.05
P51	M	77.4	37.3	1632	278.8	0.1	86.8	0.0	13.1	17.1	14.3	9.4	2.60	20.3	24.1	13.4	6.5	2.45
P53	Y	97.3	55.1	3882	435.1	5.6	59.0	33.9	1.5	13.7	10.8	8.5	2.57	23.2	25.8	11.7	6.3	2.55
P57	Y	97.8	43.8	3621	365.3	0.7	95.7	3.6	0.0	12.4	9.0	8.5	1.88	21.2	22.3	10.0	8.8	1.81
P59	Y	89.4	36.0	832	302.2	0.1	99.5	0.3	0.1	23.5	20.6	11.2	1.89	23.1	22.9	17.6	8.9	1.76
P62	Y	97.8	45.5	2208	399.7	0.3	94.6	5.1	0.0	16.2	13.5	8.9	2.04	22.5	23.5	14.8	8.9	2.03
P77	M	91.6	70.0	1608	547.8	9.9	86.4	2.4	1.3	23.5	19.6	13.1	2.94	22.7	25.8	14.5	7.9	2.46
P79	O	91.2	69.1	1332	513.5	3.1	82.4	9.8	4.7	25.7	16.5	19.8	3.18	24.3	27.1	10.1	7.7	2.43
P84	M	98.2	62.5	1680	587.2	15.8	61.5	22.7	0.0	21.8	18.3	11.8	2.77	25.0	27.8	16.5	9.0	2.48
P87	O	77.6	78.5	516	630.7	1.7	98.0	0.0	0.3	44.0	39.5	19.5	3.02	26.1	28.8	20.5	8.0	2.31
P96	M	95.9	82.4	1408	791.8	29.8	65.5	2.8	1.9	27.3	19.1	19.5	3.11	30.5	35.2	14.0	10.2	2.75
P97	M	86.2	79.9	736	719.9	7.5	90.7	1.6	0.3	37.2	28.4	24.0	3.06	29.3	32.0	16.2	10.9	2.40
P112	O	75.5	83.7	528	850.1	20.7	78.8	0.3	0.1	44.9	30.6	33.0	3.14	35.0	38.3	16.1	13.6	2.66
P117	O	96.0	105.1	1104	1118.6	15.4	83.8	0.8	0.0	34.8	28.0	20.8	3.18	33.2	37.9	18.7	12.6	2.57
P121	O	92.5	107.5	628	1142.6	11.2	79.2	9.6	0.0	46.7	35.0	31.0	3.04	36.2	39.3	20.0	12.2	2.61
P135	O	95.1	121.8	404	1672.1	2.3	80.6	17.1	0.0	62.0	49.8	37.1	3.00	45.5	47.7	28.6	18.7	2.27

Age classes: Young (Y), >20–80 yr.; Mature (M), >80–200 yr.; Old Growth (O), >200 yr.
CC, canopy cover; BA, basal area; SD, stem density; VOL, total or gross volume.
Species classes: Cw, western redcedar; Fdc, Douglas-fir; Hw, western hemlock (expressed as a percentage of total basal area).
QMD, quadratic mean diameter.
Avg., arithmetic mean; s.d., standard deviation.
H', Shannon's diversity index based on basal area proportions per 3 centimetre DBH class (H'_d) or 2 m height class (H'_h).
h_L, Lorey's mean height; h_{95}, 95th percentile of stand height

4.2.3.2. *In situ* optical measurements of canopy cover

We used the fraction of below-canopy diffuse light (gap fraction) measured with the centre silicon detector ring (Ring 1: 0–12.3°) of two paired LAI-2000 Plant Canopy Analyzers (Li-Cor, Inc., Nebraska, USA) to estimate canopy cover (Chen and Cihlar, 1996). Canopy cover is defined in this study as the "proportion of the forest floor covered by the vertical projection of tree crowns" (Jennings et al., 1999: 62). We placed one stationary LAI-2000 instrument in a clearing outside the stand (above-canopy reference), while the second instrument was used to collect below-canopy skylight measurements every 0.5 m along a continuous 175 m transect located in each ground-reference plot (Fig. 4.2). We assumed that the amount of skylight reaching the below-canopy sensor (1.3 m above the forest floor) at any point along the sample transect was dependent on both within- and between-crown canopy gaps (Fig. 4.3). LAI-2000 measurements were taken immediately after sunset, under perfectly clear skies, and with very little or no wind present. We estimated percent canopy cover (CC_{PCA}) in each plot using the average of 350 discrete CC_{PCA} measurements (Rautiainen et al., 2005):

$$CC_{PCA} = 100 \times \frac{1}{n} \sum_{i=1}^{n} 1 - P_i \,, \tag{4.2}$$

where n is the total number of LAI-2000 measurements, and P_i is the gap fraction derived by Ring 1 of the LAI-2000 optical sensor at transect distance i in the understory (Fig. 4.3).

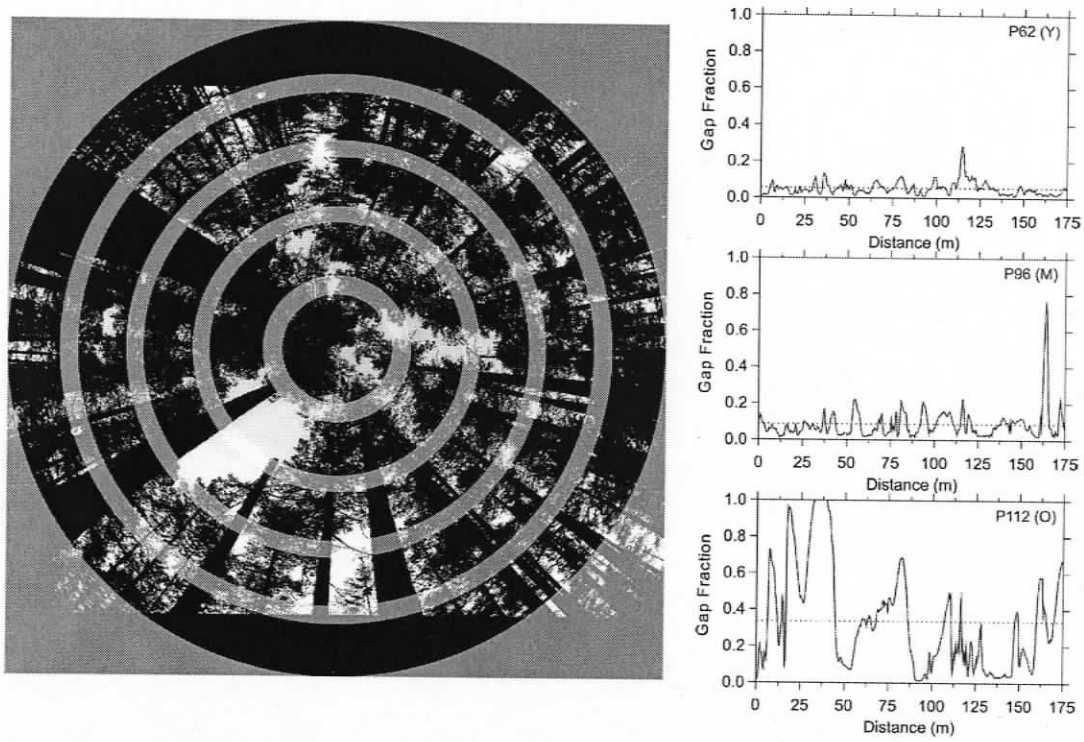

FIGURE 4.3. Geometry of the five silicon detector rings of the LAI-2000 PCA projected onto a hemispherical canopy photograph (left). We used the ratio of below- to above-canopy skylight (gap fraction) measured by the central detector ring (Ring 1: 0–12.3°) of two paired instruments to estimate canopy cover (Eq. 4.2) at regular (0.5 m) spacings along a 175 m transect within the plot. The stacked graphs on the right are examples of the spatial structure of gap fractions collected in young (top), mature (middle), and old-growth (bottom) plots. The broken horizontal line represents the plot-averaged gap fraction.

4.2.4. LiDAR data processing

All LiDAR points were individually classified as ground or vegetation by the data provider using TerraScan software (Terrasolid Ltd., Finland). We used ordinary kriging (Surfer 8, Golden Software, Inc., Colorado, USA) to construct a 2 m bare earth or digital elevation model (DEM) from all LiDAR points classified as ground (Lloyd and Atkinson, 2002; Clark et al., 2004). We converted the Z value (elevation) associated with each LiDAR point into a height (h; m) above the ground surface by computing the vertical distance between the LiDAR point and its interpolated Z value on the DEM. The occurrence of dense shrubs, large coarse woody debris, stumps, windthrow mounds and root wads created by uprooted trees, and mixing of first and last LiDAR returns added

some uncertainty to the classification of points near the ground. We therefore applied a fixed height threshold of 2 m (Næsset et al., 2005) to further separate the LiDAR points into two discrete height classes: canopy ($h \geq 2$ m) versus non-canopy ($h < 2$ m). Brokaw (1982) defined a canopy gap as a hole in the forest canopy that extended all the way down to 2 m above the forest floor. Therefore, our 2 m height threshold also had important implications for LiDAR estimates of canopy cover.

Because the airborne LiDAR system collected alternating first and last returns, exclusive use of either one or the other pulse type would have reduced the point density by approximately half. We therefore decided to pool both kinds of returns under the assumptions that (1) retaining a higher point density would capture more spatial detail within the vertical and horizontal dimensions of the canopy (Thomas et al., 2006), and (2) any height bias associated with using only first or last returns would be somewhat diminished (Lovell et al., 2003). We created two different kinds of datasets from these pooled first and last returns. One dataset was composed of LiDAR point heights (X, Y, h) that were extracted from individual flight lines within the spatial boundaries of each of the 152 sample plots. These point data were specifically used to derive attributes of vertical canopy structure and to estimate canopy cover. The second dataset consisted of LiDAR heights interpolated by ordinary kriging into a 0.5 m regularized grid. We used these gridded or rasterized 'canopy height models' (CHM) to compute horizontal attributes of canopy structure.

4.2.5. LiDAR-based measures of vertical structure

In total, we calculated six different metrics to capture location, dispersion, and shape-related statistical properties of the LiDAR canopy height distribution sampled in each 0.25 ha plot. Four of the metrics were computed directly from order statistics and sample quantiles of LiDAR canopy height, while the remaining two were derived from user-defined height frequencies.

4.2.5.1. Metrics based on order statistics and sample quantiles

We estimated sample quantiles corresponding to the 0, 1, 2, …, 100th percentiles and 1, 2,…, 7th octiles of the LiDAR canopy height ($h \geq 2$ m) distribution following "*Definition 6*" (SAS and SPSS defaults) in Hyndman and Fan (1996):

$$Lh_q = (1-g)X_j + gX_{j+1} \tag{4.3}$$

where Lh_q is the sample quantile of LiDAR canopy height corresponding to sample fraction or probability q ($0 \leq q \leq 1$); X_j is the sorted height or jth order statistic of a LiDAR canopy return with ascending rank order j ($X_1 \leq X_2 \leq \ldots X_n$); g is a weighting coefficient ($0 \leq g \leq 1$) given by $j = \lfloor qn + m \rfloor$ and $g = qn + m - j$, where $\lfloor u \rfloor$ denotes the largest integer not greater than u (i.e., floor function); n is the sample size, and m is a constant set to q. We used estimates of Lh_q to construct one-sample quantile plots of Lh_q versus q (Fig. 4.4), and to compute robust quantile-based estimates of skewness and kurtosis (see below). In particular, we relied on $Lh_{0.85}$ (85th percentile of LiDAR canopy height) as a key measure of canopy height, because of its strong correlation with the average height of dominant and codominant canopy trees (h_{DC}) and several other inventory variables measured in our 16 ground-reference plots (see results).

We calculated Gini's mean difference statistic (David, 1968), also known as the Gini coefficient of inequality (Damgaard and Weiner, 2000) or second L-moment ratio (Hosking, 1990), as a measure of the relative variability (dispersion) found among the heights of reflective canopy surfaces (Latham et al., 1998):

$$G = \frac{1}{\sum X_i (n-1)} \sum_{i=1}^{n} (2i - n - 1) X_i \tag{4.4}$$

where G is an estimate of the mean height difference between every possible pair of LiDAR canopy returns ($h \geq 2$ m), divided by the mean of all LiDAR canopy heights; X_i is the LiDAR height associated with the ith order statistic, and n is the sample size. G ranges from a minimum value of zero (i.e., all LiDAR canopy heights are equal) to a theoretical maximum of one (i.e., all LiDAR canopy heights in an infinite population are equal to zero except one). G is known to be highly correlated with the coefficient of

variation (e.g., $R^2 = 0.99$, $n = 152$ in this study). G, however, is an absolute, not squared deviation measure, and thus considered more robust in the presence of outliers (David, 1968; Knox et al., 1989).

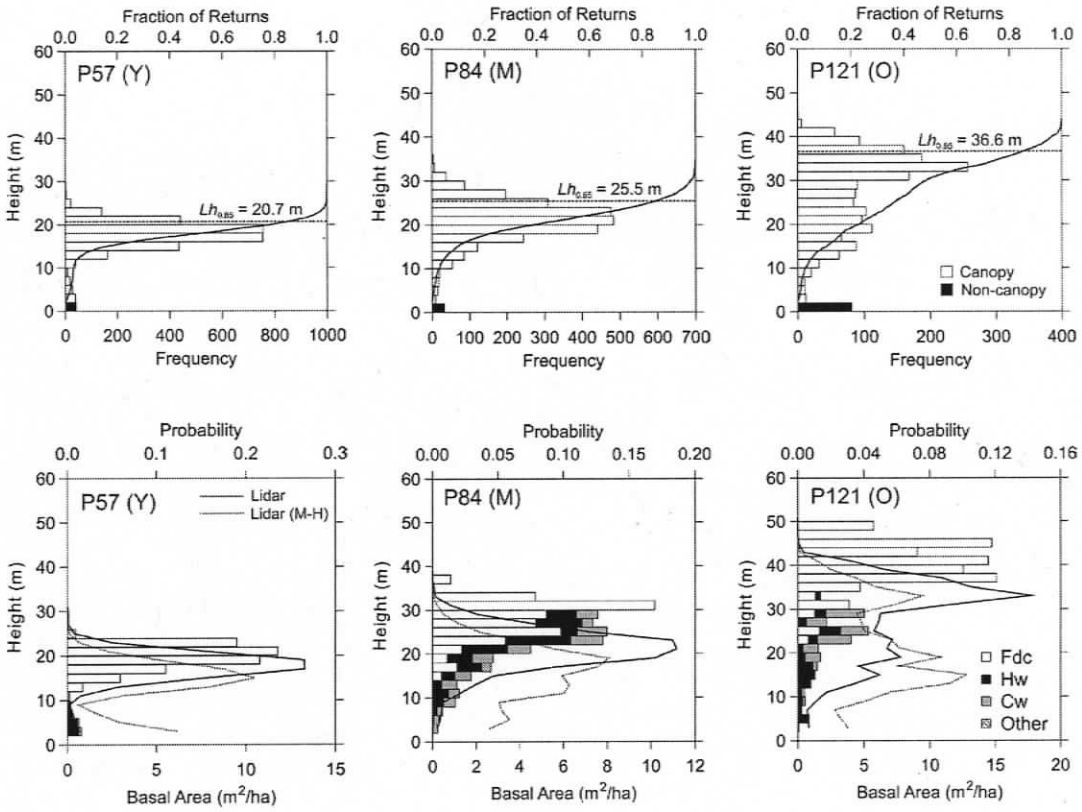

FIGURE 4.4. Examples of one-sample quantile plots (top, lines) and histograms of LiDAR canopy height frequencies (top, bars) and field-measured basal areas per tree height class (bottom, bars) constructed for young (left), mature (middle), and old-growth (right) plots. One-sample quantile plots (top) show the fraction of LiDAR canopy returns found below a certain height. The broken horizontal lines (top) identify the 85th percentile of LiDAR canopy height ($Lh_{0.85}$). Solid and broken lines superimposed on the bottom panel of graphs depict the raw and M-H transformed probabilities derived from the LiDAR-height frequencies. Notice the downward shift and amplification of probability densities in the lower canopy layers produced by the MacArthur-Horn (M-H) transformation. Tree species codes: Douglas-fir (Fdc); western hemlock (Hw); western redcedar (Cw).

We calculated coefficients of skewness (*SK*) and kurtosis (*KR*) as complementary measures of distributional shape (i.e., departures from normality) using two quantile-based estimators (Zar, 1999: 71; Kim and White, 2004):

$$SK = \frac{Lh_{0.75} + Lh_{0.25} - 2Lh_{0.5}}{Lh_{0.75} - Lh_{0.25}} \tag{4.5}$$

$$KR = \frac{(Lh_{0.875} - Lh_{0.625}) + (Lh_{0.375} - Lh_{0.125})}{Lh_{0.75} - Lh_{0.25}} - 1.233 \tag{4.6}$$

where Lh_q are quantiles of LiDAR canopy height estimated from the distribution of LIDAR canopy returns ($h \geq 2$ m) sampled in each plot (Eq. 4.3). *SK* measures distributional asymmetry, and values can range from a minimum of −1 (extreme left skewness) to a maximum of 1 (extreme right skewness). The standard normal distribution has a *SK* equal to zero. Little consensus exists on a formal working definition of *KR*, especially in the presence of distributional asymmetry (Balanda and MacGillivray, 1988; Wyszomirski, 1992). Therefore, we restate Moors' (1988) simple definition of *KR* as a measure of dispersion of probability mass around the 2nd and 6th octiles of the distribution. *KR* has a minimum value of −1.233 (extreme platykurtosis); an infinite maximum (extreme leptokurtosis), and takes on a value of zero for the standard normal distribution (mesokurtic).

4.2.5.2. Metrics derived from canopy height frequencies

We computed a canopy height diversity (CHD) index (MacArthur and MacArthur, 1961; Aber, 1979a) from frequency distributions of LiDAR canopy heights using H' (Eq. 4.1) and two different estimates of p_i. First, we calculated p_i simply as the proportion of LiDAR canopy returns ($h \geq 2$ m) found in each 2 m height class i (i.e., Class 1: 2 to <4 m; Class 2: 4 to <6 m, etc.) (Fig. 4.4). Second, we applied the MacArthur and Horn (1969) transformation (M-H) to compensate for any occluding effect that a dense upper canopy might have on the vertical penetration of LiDAR pulses into successively lower canopy layers (Aber, 1979a; Lefsky et al., 1999; Riaño et al., 2003):

$$p_i = \frac{\ln(N_{i+1}/N_i)}{PAI} \tag{4.7}$$

where p_i is the proportion of the total plant area index (PAI) found in height class i, and N_{i+1} and N_i are the total number of LiDAR returns (both canopy and ground) found below height classes $i + 1$ and i, respectively. PAI is one-half the total plant (i.e., foliage, branches, cones, epiphytes, etc.) surface area (m^2) per unit of ground surface area (m^2) contributed by all canopy height classes i (Aber, 1979a):

$$PAI = \ln\left(N_{Upper} / N_{Lower}\right) \tag{4.8}$$

where N_{Upper} is the total number of LiDAR returns found at or below the maximum canopy height, and N_{Lower} is the total number of LiDAR returns with $h < 2$ m. Lastly, we computed the Shannon evenness index (J') using estimates of CHD derived from the LiDAR-height frequencies and M-H transformed (Eq. 4.7) probabilities (Magurran, 2004):

$$J' = CHD / \ln S \tag{4.9}$$

where ln S is the maximum value of CHD or H' when LiDAR returns are evenly distributed across all height classes i, and S is the total number of 2 m height classes.

4.2.6. LiDAR-based measures of horizontal structure

We calculated another seven metrics to characterize the horizontal arrangement of forest biomass. First, we estimated canopy cover (CC_{LiDAR}) from the fraction of the total number of LiDAR returns classified as non-canopy ($h < 2$ m) (Means et al., 2000; Lovell et al., 2003; Næsset et al., 2005):

$$CC_{LiDAR} = 100 \times \left(1 - \frac{N_{Lower}}{N_{Upper}}\right) \tag{4.10}$$

We computed the remaining six attributes from lacunarity statistics extracted from the rasterized CHMs (Frazer et al., 2005). Lacunarity is a scale-dependent, quantitative measure of heterogeneity (i.e., the degree to which a pattern departs from complete spatial or temporal randomness), and has been increasingly used to describe the multiscale texture or structure of various spatiotemporal phenomena (Plotnick et al., 1996; Saunders et al., 2005). In general, geometric patterns with high lacunarity are coarsely textured and contain a broad range of gap (empty spaces) sizes and shapes,

while patterns with low lacunarity are finely textured, contain few gaps, and appear relatively homogeneous at all measurement scales (Cheng, 1997).

We applied the 'gliding-box' algorithm of Allain and Cloitre (1991) to estimate the lacunarity statistic $\Lambda(r)$ at scales r = 0.5 m to 50 m for each CHM (Frazer et al., 2005):

$$\Lambda(r) = \frac{Z_Q^{(2)}(r)}{\left[Z_Q^{(1)}(r)\right]^2} = 1 + \frac{\sigma_Q^2(r)}{\left[Z_Q^{(1)}(r)\right]^2} \tag{4.11}$$

where $\sigma_Q^2(r)$ and $Z_Q^{(1)}(r)$ are respectively the scale-dependent variance and mean of the probability distribution function $Q(M, r)$, and M is the mass or integral (sum) of canopy height h measured within a square gliding box (window) of scale r (see Plotnick et al., 1993, 1996 for detailed description of the gliding-box algorithm, and Frazer et al., 2005 for application to quantitative canopy heights). Plotting the logarithm of $\Lambda(r)$ against the logarithm of r (i.e., the lacunarity curve) revealed the scale-dependent statistical behaviour of $\Lambda(r)$ that was unique to each CHM (Fig. 4.5).

We selected three separate features of the lacunarity curve to characterize the horizontal distribution of canopy structure. First, we used the magnitude of $\Lambda(r)$ at discrete scales r = 0.5, 1.5, 4.5, and 12 m as a scale-dependent measure of spatial heterogeneity, where $\Lambda(r) \rightarrow 1$ implies increasing spatial homogeneity and $\Lambda(r) \rightarrow \infty$ denotes increasing spatial heterogeneity (Plotnick et al., 1996). Second, we used major breaks in slope (points of inflection) along the lacunarity curve to identify dominant scales of horizontal pattern in each CHM (Sun and Ranson, 1998; Dale, 2000; Butson and King, 2006). We extracted the first derivative (slope) of the lacunarity curve by the secant method (Press et al., 1986), and used the measurement scale r associated with the global slope minimum (Fig. 4.5) as an estimate of the dominant scale of horizontal pattern (Λ_{Scale}). Third, we normalized the lacunarity curve by dividing each estimate of $\Lambda(r)$ by $\Lambda(1)$ (Plotnick et al., 1996; Feagin, 2003), and then numerically derived the integral of the normalized curve ($\Lambda_{Integral}$) by the trapezoid rule (Press et al., 1986). We used $\Lambda_{Integral}$

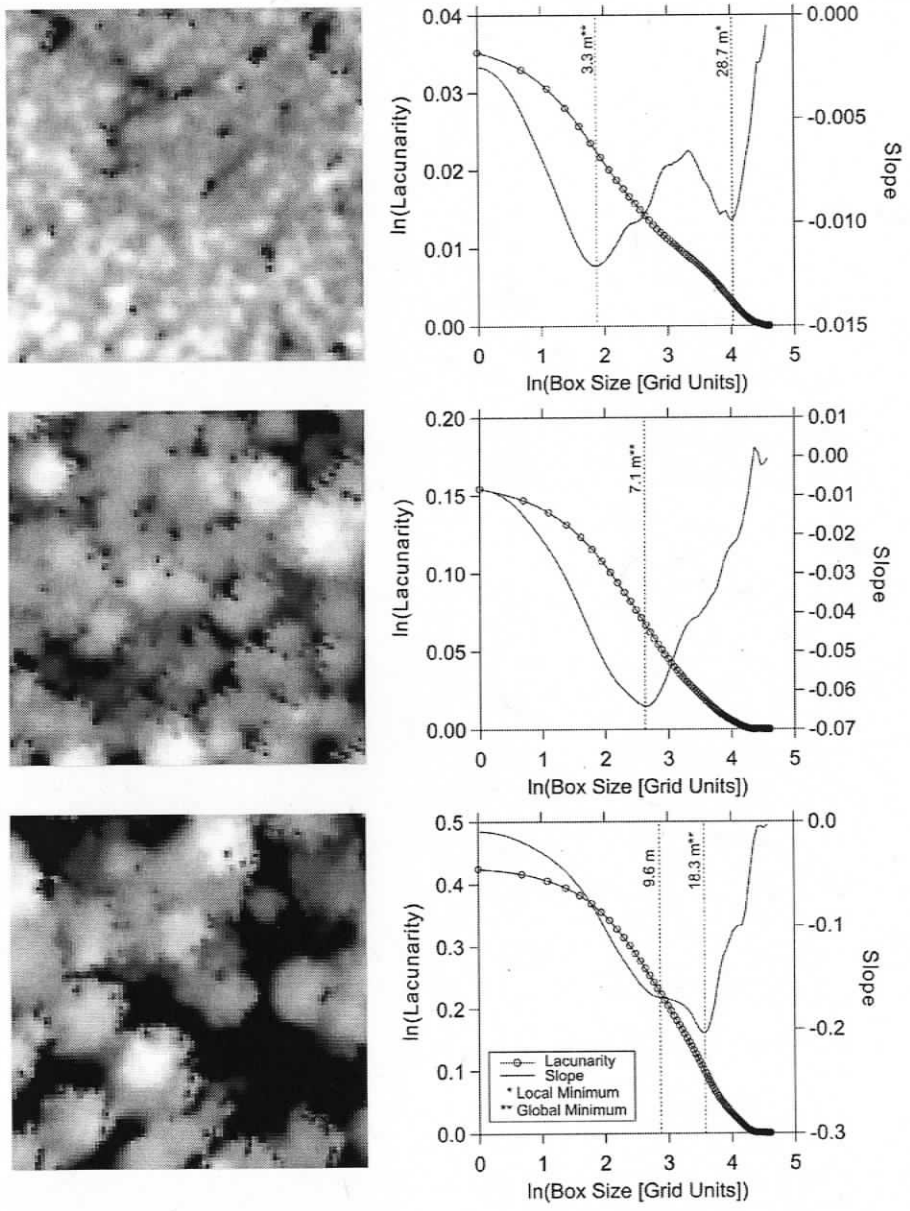

FIGURE 4.5. Multiscale (0.5 m to 50 m) lacunarity statistics $\Lambda(r)$ and curves (right) derived for three separate 50 m × 50 m (0.25 ha), 0.5 m spatial resolution LiDAR-derived CHMs (left): young (P62, top), mature (P96, middle), and old-growth (P112, bottom). Points of inflection in double-log plots of $\Lambda(r)$ against r are marked by local and global slope minima observed in first derivative curves (right). Global minima are often closely associated with mean crown width and tree spacing in closed forest canopies (e.g., top and middle CHMs), but may also reflect patterns of aggregation at finer or coarser spatial scales. For example, global and local slope minima at 3.3 m and 28.7 m, respectively, identified in the top graph reflect the aggregation of canopy heights at the crown scale (3.3 m) and at the plot level (28.7 m). Coarser scale patterns of aggregation may be due to the influence of edaphic factors (top) or tree-fall gaps (bottom).

as an estimate of cross-scale spatial heterogeneity, with larger values of $\Lambda_{Integral}$ indicating the presence of multiple scales of spatial pattern (Frazer et al., 2005).

4.2.7. Canopy density, surface, and volumetric indices

We computed three final attributes of canopy structure using both vertical and horizontal dimensions of the canopy. First, we derived estimates of canopy density (CC_f) at different height fractions from the top of the canopy to the ground surface (Maltamo et al., 2005):

$$CC_f = \left[\frac{n_f}{N}\right] \times 100 \qquad (4.12)$$

where n_f is the total number of LiDAR returns found above a selected fraction ($0 \leq f \leq 1$) of maximum LiDAR canopy height (i.e., 100th percentile of LiDAR canopy height, $Lh_{1.0}$), and N is the total number of LiDAR returns within the sample plot. Second, we calculated the percent gap volume (PGV) found between an 'imaginary' horizontal plane located at $Lh_{1.0}$ and the outer surface of the CHM. PGV is expressed as a percentage of the total plot volume measured between two horizontal planes located at $Lh_{1.0}$ and $h = 0$ (Frazer et al., 2005), and is an equivalent relative measure of the "open gap space" defined by Lefsky et al. (1999). Finally, we calculated the 'rumple index' (RI) as the ratio of outer canopy surface area to horizontal ground surface area (Parker et al., 2004). RI is closely related to the structural complexity index (SCI) developed by Zenner and Hibbs (2000).

4.2.8. Exploratory data analysis

4.2.8.1. *k*-means partitioning of canopy structure metrics

We constructed three original $n \times m$ data tables, each composed of n sample units (152 rows) × m LiDAR-derived attributes of forest canopy structure (m columns): (1) vertical ($Lh_{0.85}$, *G*, *SK*, *KR*, CHD, *J'*); (2) horizontal (CC_{LiDAR}, $\Lambda(0.5)$, $\Lambda(1.5)$, $\Lambda(4.5)$, $\Lambda(12)$, Λ_{Scale}, $\Lambda_{Integral}$); (3) all vertical and horizontal attributes ($m = 13$). We standardized all m columns in each of the three data tables to z scores (mean = 0 and variance = 1) in order to eliminate the numerical weightings arbitrary imposed by different units of

measure (McCune and Grace, 2002). We then used the *k*-means clustering algorithm (SYSTAT Version 10.2, Systat Software Inc., California, USA) to partition *n* sample units within each of the three data tables into *k* statistical groups or clusters (Legendre and Legendre, 1998). Because *k* is user-defined and largely unknown, we relied on consensus among three global stopping rules to identify the optimal *k* number of clusters (Milligan and Cooper, 1985; Gordon, 1999; Wishart, 2005):

$$CH_k = [B_k/(k-1)]/[W_k/(n-k)] \tag{4.13}$$

$$H_k = [(W_k/W_{k+1})-1]\times[n-k-1] \tag{4.14}$$

$$\Delta f_k = \left[(k-1)^{2/p}W_{k-1}\right]-\left[k^{2/p}W_k\right] \quad \text{and} \quad KL_k = \left|\Delta f_k/\Delta f_{k+1}\right| \tag{4.15}$$

where CH_k, H_k, and KL_k are separate objective functions proposed by Caliński and Harabasz (1974), Hartigan (1985), and Krzanowski and Lai (1988), respectively; B_k is the total between-cluster sum of square (Euclidean) distances at *k*, W_k is the total within-cluster sum of square distances at *k*, and *p* is the total number of attributes *m* measured for each sample unit *n*.

An optimal partition of *n* sample units into *k* clusters is found when CH_k and KL_k reach their global maxima or when H_k is at a global minimum over some range of *k*. We, however, adopted an alternative set of rules and procedures to evaluate *k* based on recommendations by Gordon (1999). First, we ran the *k*-means clustering algorithm and computed CH_k, H_k, and KL_k using values of *k* ranging from 2 to 20. Second, we identified discrete values of *k* where all of the following criteria were simultaneously satisfied: (*i*) CH_k and KL_k were local or global maxima, (*ii*) H_k was a local or global minimum, and (*iii*) the minimum cluster membership was ≥3 sample units. We arbitrarily set a minimum membership threshold of three to avoid assigning single sample outliers to cluster classes of their own (analogous to model over-fitting). Last, we used nonmetric multidimensional scaling (see below) to graphically check for any obvious discontinuities in the distribution of sample units that were not captured by *k*-means partitioning using optimal values of *k*.

4.2.8.2. Dissimilarities among samples, age classes, and *k*-means clusters

We employed several graphical and statistical techniques to examine the structural dissimilarities among sample units, forest age classes, and *k*-means clusters. We used nonmetric multidimensional scaling (NMS) to visualize the arrangement and ordering of sample units, age classes, and *k*-means clusters in reduced *p*-dimensional ordination space. NMS is an iterative, nonparametric (ordinal scaling) ordination technique that searches for the best geometrical representation of n sample units on p dimensions (axes) by minimizing the "stress" goodness-of-fit statistic (Legendre and Legendre, 1998). Stress is an estimate of the nonmonotonicity found between the rank order of intersample distances (dissimilarities) measured in the original m-dimensional (feature) space and the rank order of fitted intersample distances established in reduced NMS ordination space (McCune and Grace, 2002). Stress will equal zero when the relationship between these two sets of intersample distances is perfectly monotonic.

We applied the NMS "autopilot-slow and thorough" algorithm implemented in PC-ORD Version 4.41 (McCune and Mefford, 1999) to ordinate three separate dissimilarity (Euclidean distance) matrices constructed from the same standardized $n \times m$ data tables used for *k*-means partitioning (see section above). In autopilot mode, PC-ORD automatically selects a starting configuration (i.e., sample positions and dimensionality) for NMS based on the best *p*-dimensional solution derived from 40 preliminary runs with real data and 50 runs with randomized data (Monte Carlo test). Start points for all preliminary runs were randomly selected, and stress was calculated using the formula 1 variant of the statistic (Legendre and Legendre, 1998: 447). The best solution was one that (1) produced a low and stable stress within the fewest p dimensions (i.e., dimensions were retained only if they reduced stress by 5 or more units), and (2) exhibited significantly more reduction in stress than expected by chance. Because axes in NMS are arbitrarily assigned (i.e., not arranged by maximum orthogonality or ordered by the amount of variance explained), we applied a separate orthogonal (rigid) rotation to each of the final ordinations to maximize the bivariate correlation between scores on the horizontal axis and one of the dominant attributes of canopy structure (i.e., $Lh_{0.85}$ or $\Lambda_{0.5}$).

We did this simply to improve the interpretability of the ordinations from a stand development perspective.

We ran discriminant analysis (DA) in two separate modes using S-Plus Version 6.2 (Insightful Corp., Washington, USA) to further examine differences in vertical and horizontal patterns of canopy structure among age classes. First, we employed stepwise DA as a purely descriptive tool (i.e., canonical analysis of discriminance) to identify key structural variables that contributed most to the separation of age classes in multivariate space (McGarigal et al., 2000). Second, we used the predictive capability of DA to (*i*) evaluate the robustness of derived canonical functions, (*ii*) determine whether certain forest age classes were subject to greater class confusion than others, and (*iii*) evaluate the suite of predictors that was best able to minimize confusion between adjacent age classes and improve the overall classification accuracy.

Prior to running DA, we normalized all skewed variables using a rank-preserving Box-Cox transformation (Legendre and Legendre, 1998: 43) in an effort to improve multivariate normality, equalize group dispersions (i.e., variance/covariance matrices), and eliminate outliers (Tabachnick and Fidell, 2001). Subsequent screening of the transformed variables indicated that all were approximately univariate normal (normal probability plot); however, both univariate (Barlett's test) and multivariate (Box's M test: $p < 0.0001$) group dispersions remained unequal. Scatterplot matrices also revealed high pairwise correlations ($r > 0.7$) among several of the predictors. We eliminated any serious multicollinearity by retaining only weakly correlated variables ($r < 0.5$) with a strong potential for age-class discrimination (McGarigal et al., 2000). The discriminating power of each predictor was estimated *a priori* by univariate, one-way analysis of variance (ANOVA F statistic) and multi-response permutation procedures (MRPP A statistic). MRPP is a nonparametric (distance-based) technique analogous to univariate and multivariate single-factor ANOVA; however, unlike ANOVA and DA, MRPP does not require distributional assumptions of multivariate normality or equality of group dispersions (McCune and Grace, 2002).

DA is considered to be relatively robust even when the key assumption of equality of group dispersions has been moderately violated (Williams, 1983; McGarigal et al., 2000; Tabachnick and Fidell, 2001). Nevertheless, we took a number of

precautions to avoid erroneous interpretations that could result from potentially biased or unstable DA results. First, we based our interpretation of the canonical variates on canonical structure coefficients (total canonical loadings) rather than the standardized (partial) canonical coefficients (Williams, 1983). Second, we verified our initial interpretations of the canonical variates with the distribution of age classes and pattern of pairwise correlations evident in NMS joint plots. Third, we used MRPP to corroborate univariate and multivariate tests of significance for mean group differences estimated by DA. Last, we compared chance-corrected DA classification error rates generated by (*i*) linear versus quadratic classification criteria, and (*ii*) jackknife cross-validation versus direct resubstitution methods to evaluate the overall stability and reliability of the canonical functions (Titus et al., 1984; McGarigal et al., 2000).

4.3. Results

4.3.1. Relationship between inventory and LiDAR-derived metrics

Magnussen and Boudewyn (1998) were the first to formalize the statistical "quantile-quantile relationship" that exists between plot-level LiDAR canopy height and tree height. Here, we found that the largest pairwise linear correlation (R^2 = 0.98) occurred between natural-log transformations of the 95th percentile of field-measured tree height ($h_{0.95}$) and 74th percentile of LiDAR-derived canopy height ($Lh_{0.74}$). Additional pairwise comparisons among log-transformed variables showed that $h_{0.95}$ was maximally correlated (R^2 = 0.98) with the arithmetic mean height of field-measured dominant and codominant trees (h_{DC}) (Fig. 4.6). The largest R^2 (0.99) between our field-measured attributes of stand structure and some quantile of LiDAR canopy height was derived from the linear correlation between h_{DC} and $Lh_{0.83}$. Other maximum pairwise correlations between field measurements and Lh_q were as follows: Lorey's mean height (h_L) versus $Lh_{0.92}$ (R^2 = 0.97); volume (VOL) versus $Lh_{0.81}$ (R^2 = 0.95); basal area (BA) versus $Lh_{0.87}$ (R^2 = 0.85); quadratic mean diameter (QMD) versus $Lh_{0.88}$ (R^2 = 0.83), and stem density (SD) versus $Lh_{0.88}$ (R^2 = 0.64). The average value of q from all above

pairwise correlations was 0.85. Thus, we chose $Lh_{0.85}$ as an important statistical descriptor of canopy and stand structure in this study.

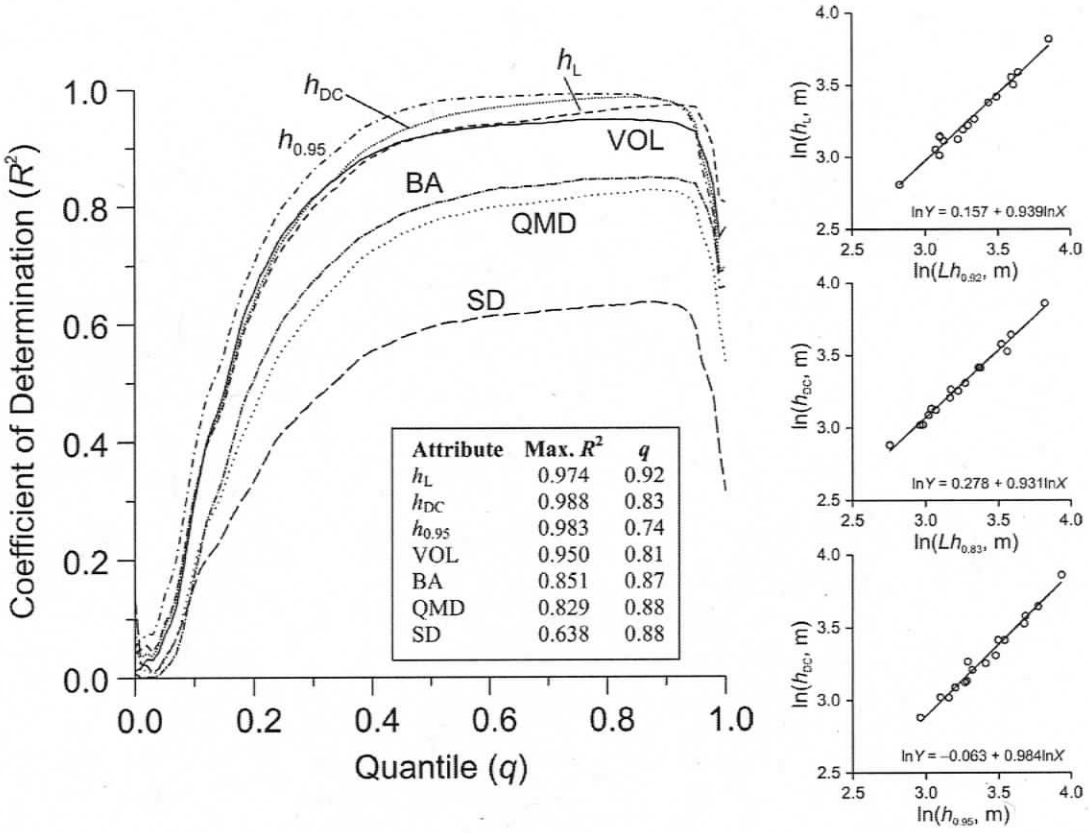

FIGURE 4.6. Pattern of pairwise correlations (R^2) between log-transformed quantiles of laser canopy height Lh_q ($0 \leq q \leq 1$) and log-transformed attributes of stand structure (left): Lorey's mean height (h_L, m); arithmetic mean height of dominant and codominant trees (h_{DC}, m); 95th percentile of tree height ($h_{0.95}$, m); total (gross) stand volume (VOL, m^3/ha); total stand basal area (BA, m^2/ha); quadratic mean diameter (QMD, cm); stem density (SD, stems/ha). Scatterplots and best-fit linear-regression lines (right) highlight the maximum correlations between field-measured stand heights (h_L, $h_{0.95}$, h_{DC}) and LiDAR canopy height (Lh_q).

The general pattern of association (R^2) between field-measured attributes of stand structure and Lh_q (where $0 \leq q \leq 1$) was characterized by three distinct segments of correlation: R^2 rose sharply above zero between $q = 0$ to 0.3, reached maximum values between $q = 0.5$ and 0.9, and then rapidly declined beyond $q > 0.95$ (Fig. 4.6). We

interpreted these three segments of correlation in the following manner. First, estimates of Lh_q at $q = 0$ to 0.3 were weaker correlates of stand height and structure because they only captured the heights of understory canopy layers. In contrast, stand height and structure were well predicted by estimates of Lh_q in the range $q = 0.5$ to 0.9, because this range of Lh_q closely approximated the height of maximum foliage density or crown surface area within the plot (Magnussen and Boudewyn, 1998; Lim and Treitz, 2004). The abrupt decline in R^2 at $q > 0.95$ signified the height transition from the main overstory canopy to the emergent layer of dominant crowns. Correlations between Lh_q and attributes of stand structure were strongest for variables linked directly to tree height (h_L, h_{DC}, $h_{0.95}$, and VOL), moderately high for diameter-based estimates (BA and QMD), and lowest for stem number or density (SD).

LiDAR estimates of canopy cover (CC_{LiDAR}) were strongly linearly correlated ($R^2 = 0.93$) with field measurements of cover (CC_{PCA}) taken with the LAI-2000. However, we found CC_{LiDAR} to be consistently higher than CC_{PCA}, because unlike CC_{PCA}, CC_{LiDAR} was relatively insensitive to the presence of within-crown canopy gaps. The greatest disparity between CC_{LiDAR} and CC_{PCA} occurred in two of the most spatially (horizontally) heterogeneous plots. Measurement bias associated with a spatially restricted and systematic sampling of the canopy gap fraction using the LAI-2000 was the probable source of this disparity. The maximum correlation ($R^2 = 0.94$) between CC_{PCA} and LiDAR estimates of canopy density (CC_f) at relative heights $f = 0$ (ground) to 1 (maximum height) occurred at $f = 0.1$ (Fig. 4.7). Correlations between CC_{PCA} and CC_f were highest ($0.92 \leq R^2 \leq 0.94$) at relative canopy heights f ranging between 0.02 to 0.15. The sharp decline in R^2 at $f < 0.02$ was the result of a substantial increase in number of near-ground (<1 m) LiDAR returns and a concomitant rise in CC_f. Closer inspection of the frequency distributions of these near-ground returns revealed that they were approximately Gaussian, with a mean height slightly >0 m and standard deviation <0.25 m. We therefore regarded these near-ground LiDAR returns as residual measurement (interpolation) error or uncertainty in the vertical position of the ground-canopy interface, rather than any real increase in vegetation cover. Correlations between CC_{PCA} and CC_f also gradually declined at $f > 0.15$, due to the increasing disparity between LAI-2000 instrument height (1.3 m) and f.

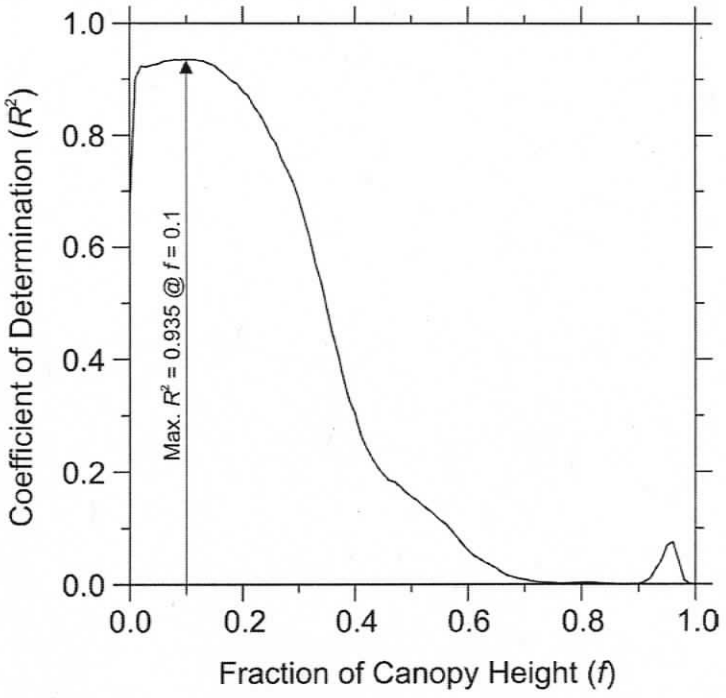

FIGURE 4.7. Pattern of pairwise linear correlations between CC_{PCA} and CC_f at all possible height fractions f. The maximum R^2 between CC_{PCA} and CC_f occurred at $f = 0.1$. The sharp decline in R^2 at $f < 0.02$ was related to the sudden rise in near-ground (± 1 m) returns (noise). A rapid decrease in R^2 at $f > 0.2$ was caused by the increasing disparity between the LAI-2000 instrument height (1.3 m) and f, and the decline in CC_f with canopy height.

We found LiDAR estimates of canopy height diversity (CHD) to be moderately well correlated ($R^2 = 0.71$) with field-derived indices of tree height diversity (H'_h), while CHD computed by the M-H method was more weakly correlated ($R^2 = 0.51$) with H'_h (Fig. 4.8). Visual comparisons of height-frequency distributions and probability density functions of LiDAR canopy height and field-measured BA revealed several obvious similarities and differences. First, frequency distributions of LiDAR canopy heights were often remarkably similar in shape and proportion to vertical distributions of BA (see Fig. 4.4 as an example). We expected some congruence between these two profiles, because the amount of BA found within a particular tree height class should translate into a proportional quantity of foliage, branch, and crown surface area (Turner et al., 2000). Second, the location of modal peaks in LiDAR canopy height profiles was always lower

than the corresponding modal peaks found in height distributions of BA, and the magnitude of this displacement increased with stand height. Two main factors contributed to this modal shift: (1) LiDAR instruments naturally measure canopy height rather than tree height, and (2) crown surfaces are porous and thus allow pulses of laser energy to penetrate deeper into the canopy (Gaveau and Hill, 2003). Last, the M-H transformation produced a substantial downward shift in probability density, reduced the amplitude of overstory modal peaks, and inflated probabilities in the lower canopy layers so that they were no longer proportional to BA. M-H also negatively impacted the correlation between LiDAR and ground-based estimates of J' (i.e., R^2 declined from 0.39 to 0.11 when M-H was applied). We therefore rejected any further use of M-H transformed data in this study.

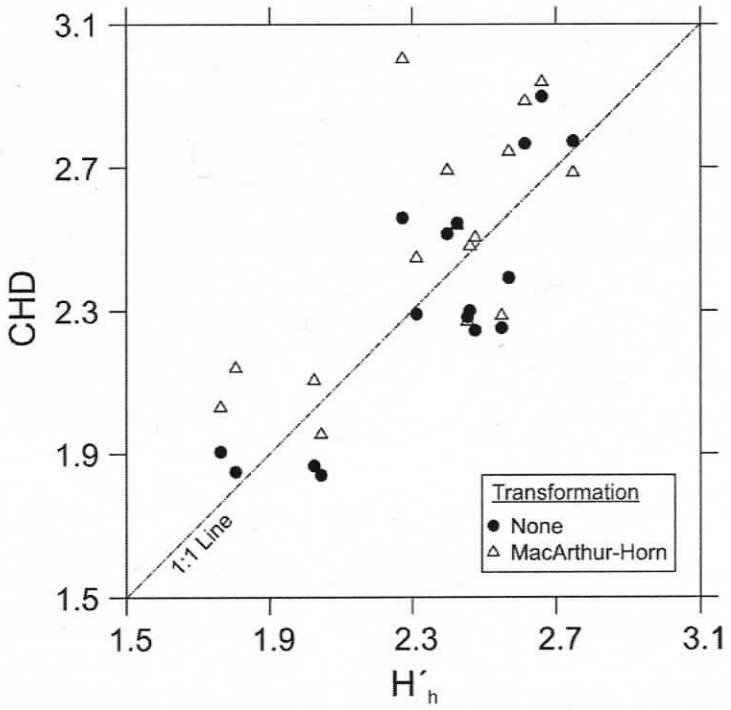

FIGURE 4.8. Scatterplot of canopy height diversity (CHD) computed from LiDAR canopy height frequencies versus field-based measurements of tree height diversity (H'_h). We used the M-H transformation to compensate for any occluding effect that a dense upper canopy might have on the vertical penetration of LiDAR pulses; however, we found that M-H inflated probabilities in the lower canopy layers and diminished the correlation between CHD and H'_h.

4.3.2. Interpretation of lacunarity statistics

We found log-transformations of $\Lambda(r = 0.5, 1.5, 4.5, \text{and } 12 \text{ m})$ to be moderately to strongly negatively correlated ($0.55 \leq R^2 \leq 0.97$) with CC_f at relative canopy heights $f = 0.2$ to 0.25 (Fig. 4.9). At $f < 0.2$ and $f > 0.25$, correlations between $\ln[\Lambda(r)]$ and CC_f diminished rapidly. The largest linear correlation ($R^2 = 0.97$) occurred between $\ln[\Lambda(r = 0.5 \text{ m})]$ and $CC_{0.2}$, and the maximum correlation between $\ln[\Lambda(r)]$ and CC_f declined monotonically with increasing measurement scale r. These findings indicated that $\Lambda(r)$ was most sensitive to the number, size, and spatial arrangement of vertically contiguous gaps, which extended from the top of the canopy to a depth equal to approximately 75–80% of full canopy height. The monotonic decline in R^2 between $\ln[\Lambda(r)]$ and CC_f at

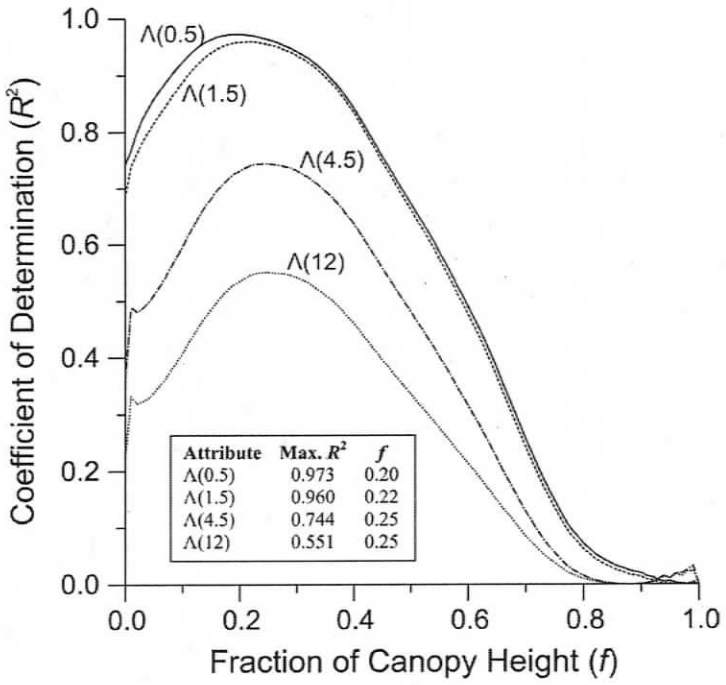

FIGURE 4.9. Patterns of pairwise linear correlations between log-transformed lacunarity statistics $\Lambda(r)$ and untransformed CC_f at all relative canopy heights f. R^2 maxima at $f = 0.2$ to 0.25 indicate that $\Lambda(r)$ was most sensitive to the number, size, and spatial arrangement of vertically contiguous gaps that extended from the top of the canopy to a depth approximately equal to 75-80% of full canopy height. We expect that many of these vertically contiguous gaps were formed by the large intercrown openings that separated individual overstory crowns.

larger measurement scales r resulted from the increasing sensitivity of $\Lambda(r > 0.5$ m) to the cross-scale spatial heterogeneity of canopy cover rather than the amount of cover. This was particularly evident in stands with limited canopy cover (<75%), where estimates of $\Lambda(r > 0.5$ m) were often highly disparate between young and old stands for the same amount of cover. We also found $\ln[\Lambda(r = 0.5$ m)] to be positively and nonlinearly correlated ($R^2 = 0.88$) with PGV, and the strength of correlation between $\ln[\Lambda(r)]$ and PGV also declined monotonically with increasing r. All of these findings, again, support previous studies (e.g., Sun and Ranson, 1998; Frazer et al., 2005) that show $\Lambda(r)$ to be a reliable scale-dependent estimate of canopy 'gapiness', texture, and spatial heterogeneity.

The dominant scale of pattern (Λ_{Scale}) was positively and nonlinearly correlated ($R^2 = 0.63$) with canopy height ($Lh_{0.85}$); however, the relationship between these two attributes became markedly more variable at $Lh_{0.85} > 30$ m (Fig. 4.10). Comparison of nonlinear regression curves derived for $Lh_{0.85}$ versus Λ_{Scale} and tree height versus predicted crown width suggested that Λ_{Scale} might be strongly correlated with the mean diameter and spacing of overstory crowns in many of the stands. In several instances, however, estimates of Λ_{Scale} were substantially larger than the predicted crown widths. In young stands, for example, unusually large estimates of Λ_{Scale} were often associated with the coarser-scale patchiness of edaphic factors (i.e., soil moisture and depth) and its impact on the spatial distribution of tree size and density (e.g., Fig. 4.5: top panel). Coarser-scale spatial patterns formed by tree-fall gaps and the apparent clumping among two or more neighbouring overstory crowns were responsible for large estimates of Λ_{Scale} in older forest canopies (e.g., Fig. 4.5: bottom panel). Several estimates of Λ_{Scale} were also noticeably smaller than predicted mean crown diameters, particularly in the taller, older canopies. We offer two plausible explanations for this: (1) finer branch-scale structures and within-crown gaps formed the dominant scale of pattern in some old-growth canopies (Ishii and McDowell, 2002); (2) $\Lambda(r)$ was sensitive to the high-spatial-frequency variation (noise) in canopy height produced when off-nadir LiDAR pulses directed from a low-flying aircraft (~220 m AGL) penetrated tall old-growth crowns from the side.

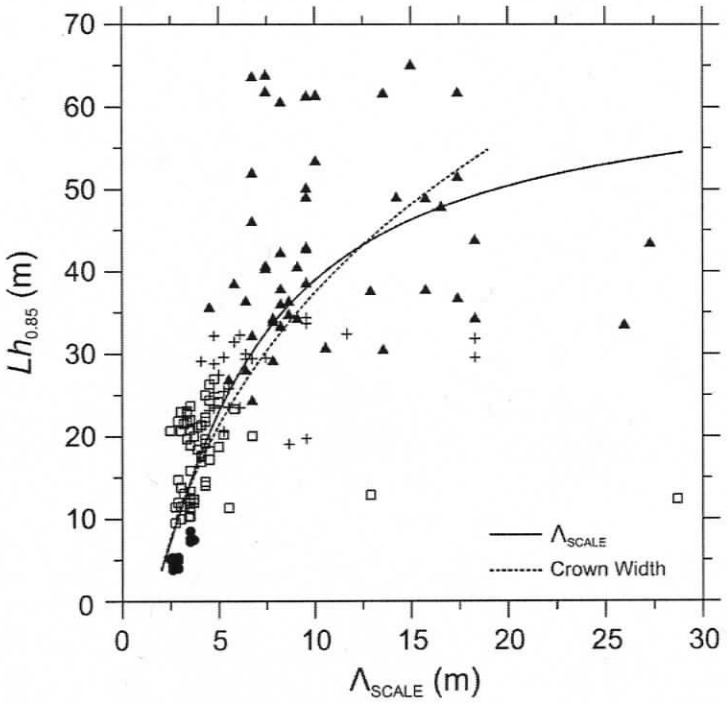

FIGURE 4.10. Scatterplot and best-fit nonlinear regression line (solid) of $Lh_{0.85}$ versus Λ_{Scale}. Superimposed on the scatterplot is a second regression curve (dashed) that relates tree height and crown diameter (Hann, 1999). Similarity between these two regression curves, particularly in very young (solid circle) and young (open square) stands, suggested that Λ_{Scale} may be responding to crown size and spacing. Deviation away from the best-fit line indicated that Λ_{Scale} was also sensitive to branch- and plot-level patterns of spatial aggregation. Mature (plus sign) and old-growth (solid triangles) canopies generally exhibited larger and more variable estimates of Λ_{Scale} than younger forests.

4.3.3. Vertical and horizontal patterns of canopy structure

4.3.3.1. Vertical canopy structure

A two-axis NMS solution (stress = 7.45, $p < 0.02$; final instability = 0.00001; number of iterations = 70) accounted for 97.7% of the total variance in the $n \times n$ dissimilarity (distance) matrix that was constructed using the six LiDAR-derived attributes of vertical canopy structure (Fig. 4.11). The amount of explained variance was estimated by the coefficient of determination (R^2) between intersample (Euclidean) distances measured in p-dimensional NMS space and intersample distances measured in the original m-dimensional (feature) space (McCune and Mefford, 1999). Axis 1

accounted for 71.8% of the total variance, and was positively correlated with CHD (R^2 = 0.89), J (R^2 = 0.76), $Lh_{0.85}$ (R^2 = 0.74), and G (R^2 = 0.43); it was also weakly negatively correlated with SK (R^2 = 0.29). Axis 2 explained a further 25.9% of the total variance; it was moderately positively correlated with KR (R^2 = 0.49), and also negatively correlated with G (R^2 = 0.43) and SK (R^2 = 0.35). The overall pattern of dispersion of individual sample units in NMS ordination space appeared neither random nor uniform, but was instead noticeably clumped and discontinuous.

Stratification of the sample units by age class (VY, very young; Y, young; M, mature; O, old growth) revealed that plots belonging to the same class were often clustered together in NMS space; i.e., forest canopies of the same age class displayed similar patterns of vertical structure. Bivariate confidence ellipses (p = 0.683) fit to the four age classes emphasized several important characteristics related to the pattern of within- and among-group dispersions (Fig. 4.11). First, the centroid of each group occupied a distinct region of NMS space, with age classes principally separated along covarying gradients of $Lh_{0.85}$, CHD, and J (Axis 1). Second, group dispersions did not separate perfectly along either of the two NMS axes, but instead showed varying degrees of overlap between adjacent age classes. Third, the average Euclidean distance between sample units and their group centroid (i.e., within-group variability) was noticeably larger for age-class O (3.36) than VY (2.09), Y (1.44), or M (1.49). Fourth, the differing shapes and orientations of the bivariate confidence ellipses indicated that the covariance structure among the six original descriptors was age-class dependent. Last, spatial discontinuities and clustering among individual sample units within age classes suggested the presence of other structurally unique groups.

Multiple pairwise comparisons using MRPP and Bonferroni-adjusted p values (Legendre and Legendre, 1998: 18) indicated there were significant group differences in vertical canopy structure among all combinations of age classes. Vertical canopy structure differed most between VY vs. M age classes (A = 0.39, $p < 0.0001$), while the least dissimilarity occurred between overlapping age-classes Y vs. M (A = 0.12, $p < 0.0001$) and M vs. O (A = 0.13, $p < 0.0001$). Stepwise DA indicated that the first (CF1) and second (CF2) canonical functions accounted for 95% and 4.3% of the total among-

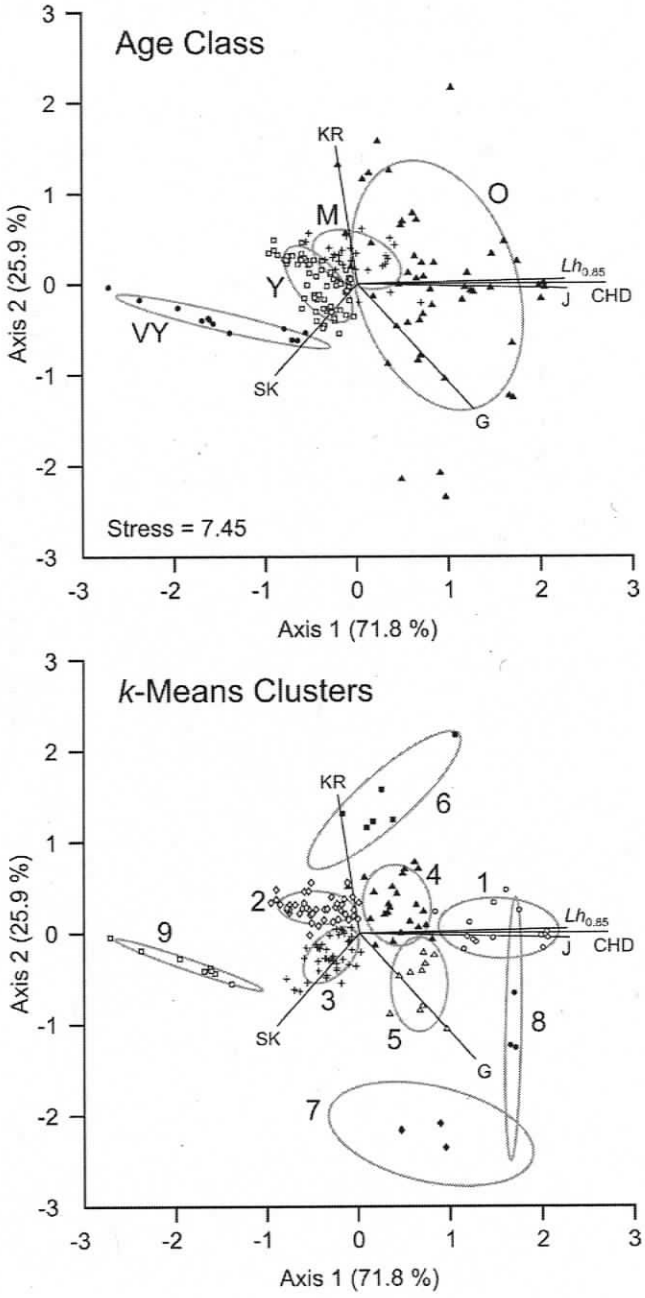

FIGURE 4.11. NMS biplots summarizing the distribution of sample units, age classes (top), and *k*-means clusters (bottom) in reduced ordination space. Vectors define the magnitude and direction of bivariate correlations (Pearson's correlation coefficient *r*) between the original attributes of vertical structure and NMS Axis 1 (x) and Axis 2 (y) scores. Gaussian bivariate confidence ellipses are centred on group (age-class and *k*-means cluster) means of x and y. The unbiased sample standard deviations of x and y determine the length of the ellipse's main axes, while the sample covariance between x and y determine the ellipse's orientation.

group variance, respectively (Table 4.3). Total structure coefficients (canonical loadings) calculated for each canonical function showed that CF1 was positively correlated (R^2 = 0.74) with $Lh_{0.85}$, and CF2 was negatively correlated (R^2 = 0.94) with *G* and moderately positively correlated (R^2 = 0.32) with *KR*. Because $Lh_{0.85}$ was a strong correlate (R^2 = 0.99) of the mean height of dominant-codominant trees (h_{DC}), we concluded that much of the among-group dissimilarity could be explained simply by differences in h_{DC}. Group separation on *G* and *KR* (CF2) was limited because O aged canopies varied widely in these two attributes of vertical canopy structure.

Low cross-validated (jackknifed) and chance-corrected classification error rates (overall accuracy = 89.5%, *kappa* = 0.85) verified both the relative stability and effectiveness of the canonical functions and quadratic classification criterion (Table 4.4). Error rates were generally lower for age-classes VY and Y than for M or O. M-aged canopies were particularly difficult to classify (user's accuracy = 68.6%) because of their substantial overlap with adjacent age-classes Y and O. More class confusion occurred between M and O than with Y and M canopies.

Univariate boxplots revealed several age-class differences and trends in the magnitude and variance of the six original descriptors of vertical canopy structure Fig. 4.12). First, median values of $Lh_{0.85}$, CHD, and *J* all increased monotonically from VY through O, indicating a sustained height growth of the overstory over time. Variances of *J* and *H* in age-class VY were unusually large given the very limited range of $Lh_{0.85}$. Therefore, we suspected that estimates of *J* and *H* in eight of the shortest (<10 m) VY stands were overly sensitive to the small number and arbitrary width (2 m) of height-class intervals. Age-class O exhibited the largest variation in $Lh_{0.85}$. Second, median estimates of *G* declined from VY to Y as stands shifted from an open-grown to closed-canopy environment; *G* then increased from Y through O as forest canopies became taller and more vertically continuous in distribution. *G* reached minimum values at canopy closure in age-class Y, and varied most widely in O. Third, a decline in median *SK* from small positive values in VY to mostly negative values in O, indicated a gradual shift over time of canopy mass from the base of the canopy to its top. Median estimates of *KR* increased steadily from VY to M as crowns continued to differentiate in height and move into opposite tails of a predominantly unimodal height distribution. The within-group

TABLE 4.3. Summary of linear discriminant models, canonical loadings, and univariate and multivariate test statistics

Linear Discriminant Model	Predictor[a]	Total Canonical Loadings			Test Statistics**							
					Univariate[b]				Multivariate			
		CF1	CF2	CF3*	F	p	A^c	p	Pillai[d]	P	A^c	p
Vertical	$Lh_{0.85}$	0.863	0.335	-0.379	199.69	0.000	0.456	0.000	1.076	0.000	0.282	0.000
	G	0.227	-0.965	0.131	24.88	0.000	0.193	0.000				
	KR	-0.004	0.572	0.820	5.19	0.010	0.119	0.000				
	Canonical R^2	0.844	0.196	0.037								
	Eigenvalue	5.394	0.243	0.038								
	% Dispersion	95.04	4.29	0.67								
Horizontal	Λ_{Scale}	0.881	0.473	-	101.53	0.000	0.337	0.000	1.150	0.000	0.316	0.000
	$\Lambda_{0.5}$	-0.133	0.991	-	40.53	0.000	0.323	0.000				
	Canonical R^2	0.708	0.442	-								
	Eigenvalue	2.423	0.793	-								
	% Dispersion	75.35	24.65	-								
All Dimensions	$Lh_{0.85}$	0.885	0.400	-0.238	199.69	0.000	0.456	0.000	1.314	0.000	0.325	0.000
	$\Lambda_{0.5}$	0.057	-0.996	0.069	40.53	0.000	0.323	0.000				
	KR	-0.017	0.297	0.955	5.19	0.010	0.119	0.000				
	Canonical R^2	0.833	0.448	0.034								
	Eigenvalue	4.988	0.810	0.035								
	% Dispersion	85.51	13.89	0.60								

[a] Normalized using Box-Cox transformation (Legendre and Legendre, 1998: 43).
[b] p values adjusted using Bonferroni correction ($p \times k$ independent tests of significance) (Legendre and Legendre, 1998: 18).
[c] Chance-corrected (within-group) agreement statistic derived by MRPP.
[d] Pillai's trace criterion is considered more robust than Wilk's lambda and Hotelling's trace when group sizes are unequal and the assumption of homogeneity of variance-covariance matrices is violated (Tabachnick and Fidell, 2001: 348).
*Not interpreted.
**Tests of significance for F statistics and Pillai's trace criterion are invalid because group dispersions are unequal.

TABLE 4.4. Chance-corrected classification matrices summarizing the cross-validated number and percentage of sample units correctly and incorrectly classified into known forest age classes using three separate sets of quadratic discriminant functions derived from (1) vertical ($Lh_{0.85}$, G, and KR), (2) horizontal ($\Lambda_{0.5}$ and Λ_{Scale}), and (3) multi-dimensional ($Lh_{0.85}$, KR, and $\Lambda_{0.5}$) attributes of canopy structure

Quadratic Discriminant Model	Predicted[a] AGE	Observed AGE[b] VY	Y	M	O	Total	User's[c]
Vertical	VY	11				11	100.0
	Y	1	58	1		60	96.7
	M		4	24	7	35	68.6
	O			3	43	46	93.5
	Total	12	62	28	50	152	
	Producer's[d]	91.7	93.5	85.7	86.0		
						Overall[e]	89.5
						Kappa[f]	0.85
Horizontal	VY	11	2			13	84.6
	Y	1	48	1	1	51	94.1
	M		10	21	7	38	55.3
	O		2	6	42	50	84.0
	Total	12	62	28	50	152	
	Producer's[d]	91.7	77.4	75.0	84.0		
						Overall[e]	80.3
						Kappa[f]	0.72
All Dimensions	VY	12				12	100.0
	Y		57	2		59	96.6
	M		5	23	2	30	76.7
	O			3	48	51	94.1
	Total	12	62	28	50	152	
	Producer's[d]	100.0	91.9	82.1	96.0		
						Overall[e]	92.1
						Kappa[f]	0.89

[a] Determined by cross-validation using jackknife procedure.

[b] Age class: VY (0–20 yr.); Y (>20–80 yr.); M (>80–200 yr.); O (>200 yr.).

[c] User's accuracies (%) denote errors of commission (inclusion); i.e., probability that a classified sample unit located on the ground will belong to the correct age class.

[d] Producer's accuracies (%) indicate errors of omission (exclusion); i.e., probability that a sample unit will be placed into its correct age class by the classification criterion.

[e] Overall accuracy (%) of classification, including the proportion of correct classifications occurring purely by chance assignment.

[f] Cohen's *kappa* (K) statistic is an estimate of classification success taking into account chance assignment; e.g., $K = 0.85$ implies an 85% improvement over chance.

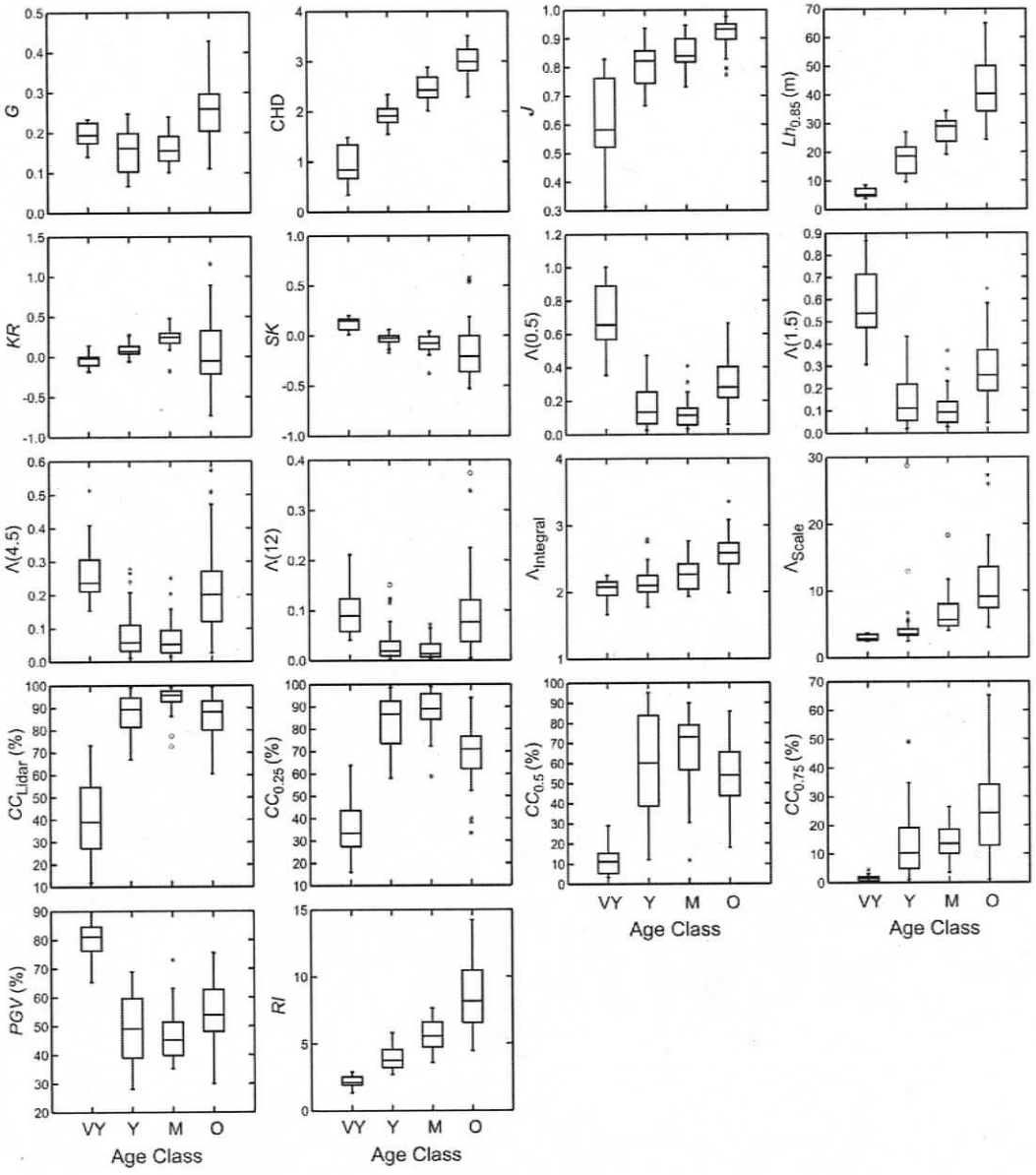

FIGURE 4.12. Univariate box-and-whisker plots (boxplots) summarizing the nonparametric distributional characteristics of 18 separate attributes of vertical and horizontal canopy structure grouped by age class (VY: 0–20 yr.; Y: >20–80 yr.; M: >80–200 yr.; O: >200 yr.). All metrics were derived directly from either LiDAR points or 'rasterized' canopy height models (CHM) measured within 152 0.25 ha (50 m × 50 m) sample plots. The horizontal line within the box represents the median (Q2); lower and upper box edges (hinges) define the first (Q1) and third quartiles (Q3) or interquartile range (IQR = Q3 − Q1); lower and upper vertical lines (whiskers) identify the lower (Q1 − 1.5 × IQR) and upper (Q3 + 1.5 × IQR) inner fences; the open circles and asterisks are near and far outliers, respectively.

variances of *SK* and *KR* were relatively small for VY, Y, and M, and sample units of the same age class generally clustered together in a scatterplot of *SK* against *KR* (not shown). In contrast, estimates of *SK* and *KR* were extremely variable for age-class O, and thus marked the shift away from simple single-layered canopies to more distributionally complex and elaborate vertical arrangements of canopy structure.

Cluster analysis using *k*-means partitioning and three global stopping rules identified ten statistically unique kinds (clusters) of vertical canopy structures within 152 sample units (Fig. 4.11). Because one *k*-means cluster contained only a single sample unit (minimum requirement was 3), we reduced the total number of clusters to nine by placing the lone sample (P151) into its next nearest cluster (Cluster 6). A series of nine quantile plots of mean Lh_q (± one standard deviation) against $0 \leq q \leq 1$ revealed the high degree of within-cluster homogeneity, as well as the characteristic kinds of differences found among the nine groups of vertical canopy structures (Fig. 4.13). Clusters 2, 3, and 4 were the most common (108 of 152) classes of vertical canopy structures. All sample units belonging to these three clusters were predominantly young to mature in age class (89 of 108), relatively short in height (mean Lh_q = 22 m), and unimodal in height distribution. Cluster 9 captured the distinct short stature, bottom-loaded profile typical of very young open-grown crowns. We would expect that these managed VY canopies would grade into Clusters 3 then 2 as continued height growth and self-pruning of lower branch systems led to further crown rise and recession. All of the remaining five *k*-means clusters were associated with tall, vertically heterogeneous O aged canopies: i.e., Cluster 1 (top-loaded bimodal); Cluster 5 (uniform or unimodal); Cluster 6 (top-loaded unimodal); Cluster 7 (bottom-loaded bimodal); Cluster 8 (symmetrically bimodal).

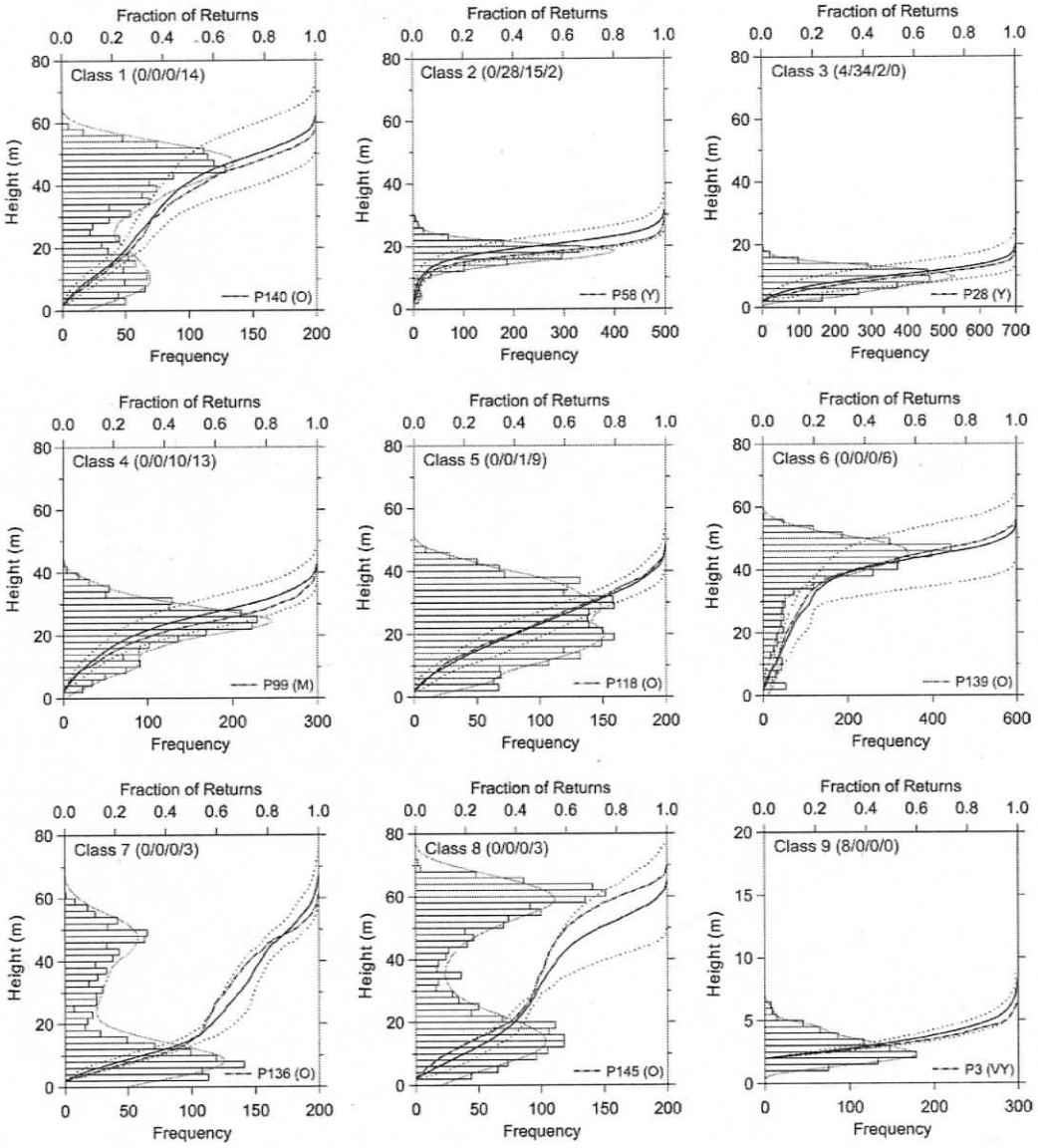

FIGURE 4.13. Examples of nine statistically unique classes of vertical canopy structures identified using *k*-means partitioning. Sample units found closest to their cluster centroid (identified in bottom right corner of each graph) were selected as class examples or exemplars. One-sample quantile curves display the mean (solid line) ± one standard deviation (dotted line) of Lh_q within the cluster. Graphs also depict the estimated Lh_q (dashed and dotted line) and height frequencies (histogram) for the sample unit closest to the centroid. Values in parentheses to the right of the Class ID (top left) represent the number of sample units of each age class (VY/Y/M/O) found within the cluster. Young, managed stands of harvest origin are characteristically short and single layered (Classes 9, 3, and 2), while the older natural stands initiated by wildfire or other natural disturbances (Classes 1, 4, 5, 6, 7, and 8) can be single- or multilayered and highly variable in height and vertical distribution (i.e., uniform, bimodal, top-loaded, or bottom-loaded).

4.3.3.2. Horizontal canopy structure

A two-axis NMS solution (stress = 2.52, $p < 0.02$; final instability = 0.00001; number of iterations = 100) captured 99.8% of the variance in the dissimilarity matrix derived from the seven attributes of horizontal canopy structure (Fig. 4.14). Axis 1 accounted for 84.5% of the among-sample variance and was positively correlated ($0.78 \leq R^2 \leq 0.97$) with $\Lambda(r)$ at all measurement scales r (maximum R^2 at r = 1.5 m) and negatively correlated ($R^2 = 0.65$) with CC_{Lidar}. Axis 2 explained 15.3% of the variance, and was positively correlated with Λ_{Scale} ($R^2 = 0.86$), $\Lambda_{Integral}$ ($R^2 = 0.83$), and Λ(12 m) ($R^2 = 0.36$). The distribution of sample units in NMS space was approximately "V-shaped", with the apex of the "V" located near −0.5 on Axis 1 (i.e., maximum canopy cover and minimum lacunarity) and zero on Axis 2 (i.e., low to medium estimates of Λ_{Scale}).

Sample units mainly clustered together in NMS space according to age class. Age classes Y, M, and some part of O, however, displayed considerable overlap in their group dispersions, while VY remained statistically distinct. A comparison of the bivariate confidence ellipses ($p = 0.683$) fit to each of the four age-classes indicated that the within-group variance-covariance structure was strongly age-class dependent. For example, the average Euclidean distance (dissimilarity) between individual sample units and their group centroid was relatively large for age-classes O (2.85) and VY (2.83) compared to Y (1.80) or M (1.65) aged canopies (i.e., horizontal structure of age-classes VY and O was markedly more heterogeneous than Y or M canopies). As well, the pattern of covariance among several of the original predictors varied along with the suite of processes that dominated during a particular stage of stand development. Prior to canopy closure (VY), for example, rapid height growth, crown expansion, and gap infilling contributed to a moderate negative correlation ($R^2 = 0.30$) between Λ(0.5 m) and Λ_{Scale} (i.e., canopies became less lacunar with height growth). Correlations between these two attributes, however, turned increasingly more positive ($0.06 \leq r \leq 0.28$) after canopy closure (Y, M, and O), as crown differentiation and other gap forming processes created increasingly more lacunar canopies.

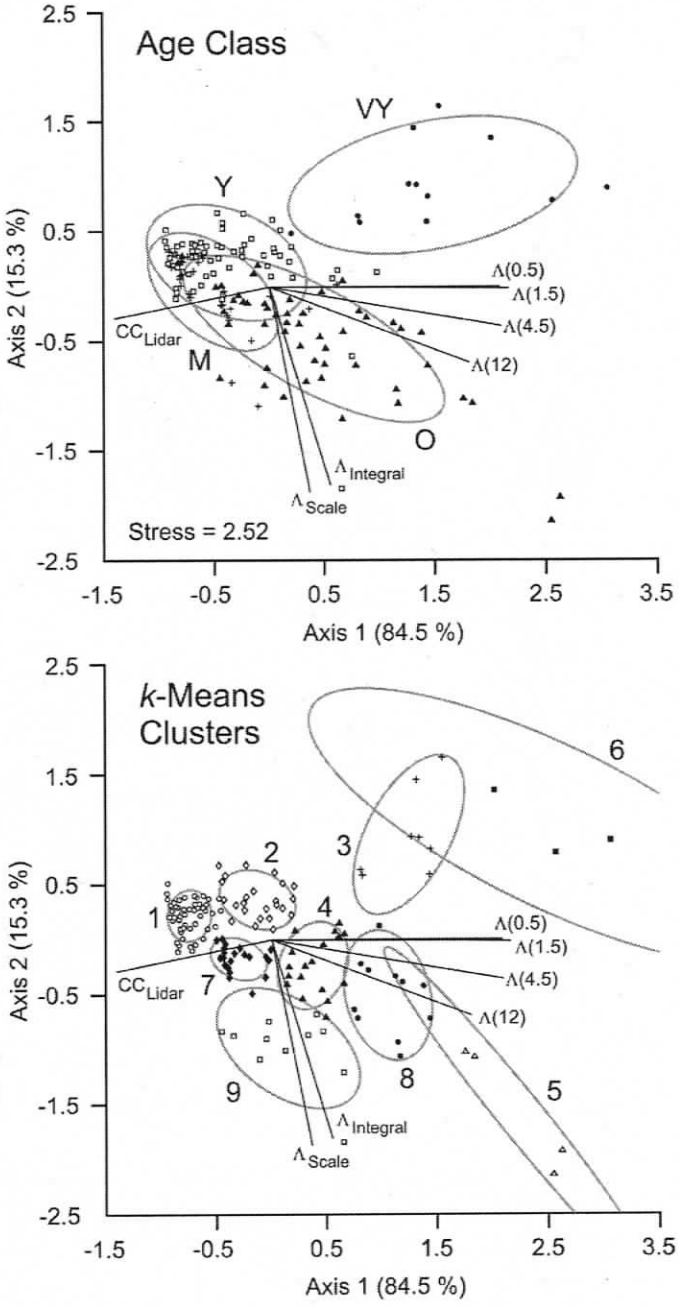

FIGURE 4.14. NMS biplots summarizing the distribution of sample units, age classes (top), and *k*-means clusters (bottom) in two-axis ordination space. Vectors define the magnitude and direction of bivariate correlations (Pearson's correlation coefficient *r*) between the original attributes of horizontal structure and NMS Axis 1 (x) and Axis 2 (y) scores. Gaussian bivariate confidence ellipses are centred on group means of x and y. The unbiased sample standard deviations of x and y determine the length of the ellipse's main axes, while the sample covariance between x and y determine the ellipse's orientation.

Multiple pairwise comparisons using MRPP and Bonferroni-adjusted p values indicated that significant differences in horizontal canopy structure occurred among all four age classes. The greatest pairwise dissimilarity was found between VY and M (A = 0.445, $p < 0.00001$), while Y and M exhibited the least dissimilarity (A = 0.043, p = 0.002). The first (CF1) and second (CF2) canonical functions derived by stepwise DA explained 75.4% and 24.6% of the total among-group variance, respectively (Table 4.3). Total structure coefficients computed for each of the canonical functions showed that CF1 was positively correlated ($R^2 = 0.77$) with Λ_{Scale}, and CF2 was positively correlated ($R^2 = 0.98$) with Λ(0.5 m). Group separation was maximal on CF1 because mean Λ_{Scale} increased nonlinearly with age class, largely in response to the continued height growth and expansion of overstory crowns and canopy gaps. CF2 was less effective at group separation because the pattern of change in mean $\Lambda(r)$ with age class was principally "V-shaped" rather than monotonic; i.e., VY and O classes shared similar high values of $\Lambda(r)$, while Y and M exhibited equally low estimates of $\Lambda(r)$ (Fig. 4.12).

Cross-validated and chance-corrected DA classification error rates were relatively low (overall accuracy = 80.3%, *kappa* = 0.72), but still notably higher than the error rates associated with attributes of vertical canopy structure (Table 4.4). Producer's accuracies were lowest for Y (77.4%) and M (75%) age-classes due to the marked overlap of their dispersions along both canonical axes. Errors of commission (inclusion) were greatest for M-aged canopies (user's accuracy = 55.3%) because of their structural similarity (overlap) with adjacent age classes Y and O.

Cluster analysis using k-means and the three global stopping rules indicated an optimal statistical partition of n sample units into k clusters at k = 14. However, since k = 14 created several clusters with a group membership of less than three sample units, we instead selected the next highest local peak in CH_k and KL_k and local minimum in H_k at k = 9 as the best partition of the dataset (Fig. 4.14). For each of the nine k-means clusters, we selected the sample unit closest in distance to its group centroid as an illustrative example of horizontal canopy structure for that cluster (Fig. 4.15). Clusters generally separated along two mostly orthogonal gradients defined by (1) the dominant scale of horizontal pattern (i.e., Λ_{Scale}), and (2) the amount and heterogeneity of canopy cover (i.e., CC_{Lidar} and Λ(0.5 m)). For example, k-means classes 3 or 6 (fine textured) and

class 5 (coarse textured) defined the range of Λ_{Scale}, while classes 5 or 6 (low cover) and classes 1 (high cover) characterized two end-points along a continuum of canopy cover.

4.3.3.3. Correspondence between vertical and horizontal patterns

A two-way contingency table indicated marked correspondence between several vertical and horizontal *k*-means classes (Table 4.5). For example, 42 (82.4%) of the 51 sample units in horizontal *k*-means Class 1 (Fig. 4.14) also belonged to vertical *k*-means class 2 (Fig. 4.11); 22 (91.7%) of the 24 sample units in horizontal *k*-means Class 2 were associated with vertical *k*-means Class 3; 13 (61.9%) of the 21 sample units in horizontal *k*-means Class 7 were found in vertical *k*-means Class 4. Also, horizontal *k*-means Classes 3 and 6 (age-class VY) were associated with vertical *k*-means Classes 3 and 9 (age-class VY), while horizontal *k*-means Classes 4, 5, 8, and 9 (predominantly age-class O) were widely scattered among vertical *k*-means Classes 1, 5, 6, 7, and 8 (age-class O). The large number of low frequency cells ($n < 5$) and structural zeros (i.e., impossible class combinations) precluded the use of chi-square or log-linear models for statistical tests of significance or association between vertical and horizontal *k*-means classes (Zar, 1999). The apparent lack of pairwise correspondence between the vertical and horizontal *k*-means classes associated with old-growth structures was a consequence of two main factors. First, cluster boundaries established by *k*-means partitioning can be somewhat arbitrary when sample units are uniformly, rather than discontinuously dispersed along a continuum of canopy structure (Legendre and Legendre, 1998). This appears to be more the case with *k*-means clusters derived from attributes of horizontal canopy structure, whereby old-growth canopies separated mainly by the number and spatial distribution of overstory crowns (i.e., canopy cover). Second, the frequency of samples in all old-growth-related *k*-means clusters was limited enough ($3 \leq n \leq 11$) that any potentially significant pairwise correspondence between vertical and horizontal clusters would remain largely undetected.

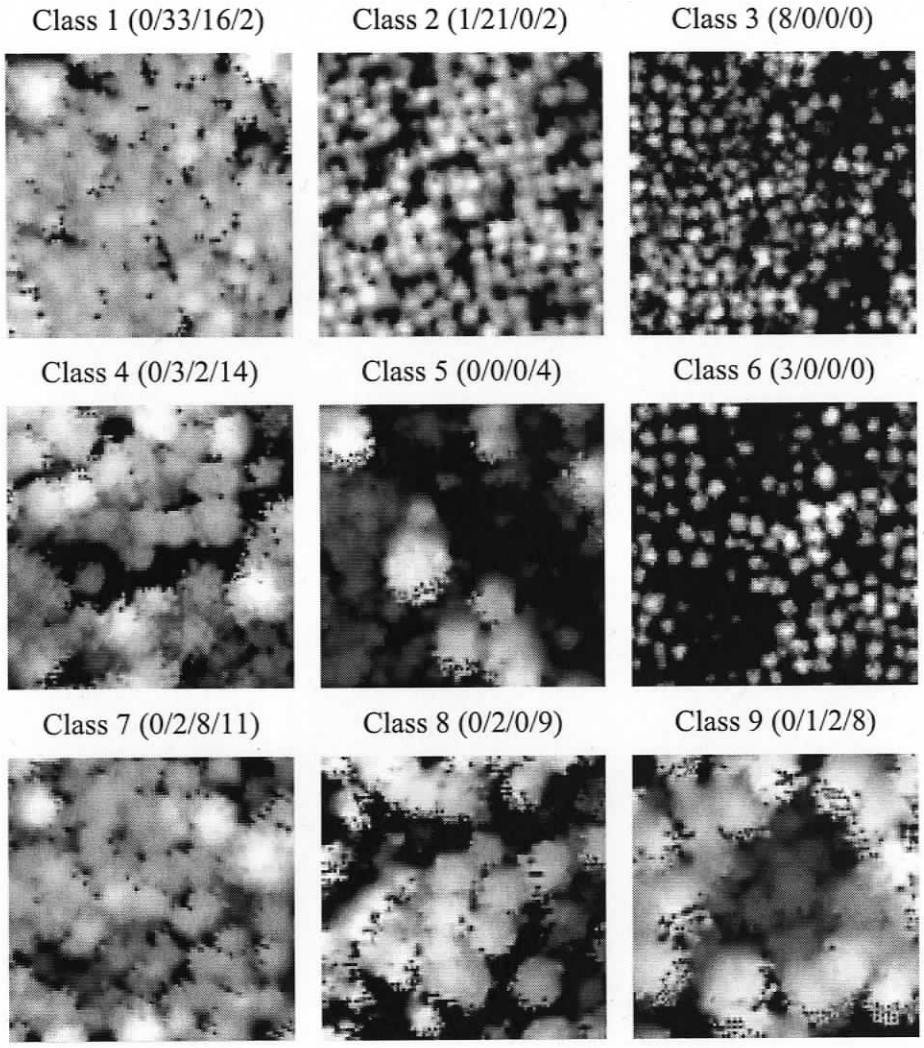

FIGURE 4.15. Examples of nine statistically unique classes of horizontal canopy structure identified using *k*-means partitioning. We chose the sample unit closest to the cluster centroid as an illustrative example for each discrete *k*-mean cluster. Clusters (classes) separated mainly along multivariate gradients related to the amount of canopy cover and its scale-dependent spatial arrangement. The four values in parentheses to the right of the Class ID are the number of sample units belonging to age-classes VY/Y/M/O. Classes 3, 6, and 2 generally capture young, horizontally uniform to patchy, free-growing (open grown) stands of harvest origin; Class 1 included early- and mid-seral closed canopies with high, uniformly distributed cover. Classes 4, 5, 7, 8 and 9 were predominately late-successional canopies with varying levels of spatial heterogeneity. The large variability associated with estimates of Λ_{Scale} lead to considerable age-class confusion (i.e., mixing of young and old canopies within certain *k*-means clusters) within certain clusters (e.g., Class 2).

TABLE 4.5. Two-way contingency table summarizing the frequency of observations for all combinations of vertical (row) and horizontal (column) *k*-means classes. Cells with low (<5 sample units) or zero frequencies are due to our limited sample size (n = 152) and the natural occurrence of structural zeros (i.e., impossible combinations: e.g., vertical classes 1, 4, 5, 6, 7, 8 with horizontal classes 3 and 6)

k-Means Class (Vertical)	*k*-Means Class (Horizontal)									
	1	2	3	4	5	6	7	8	9	Total
1	0	0	0	5	0	0	2	2	5	14
2	42	1	0	0	0	0	1	1	0	45
3	6	22	3	5	0	0	1	2	1	40
4	1	0	0	5	0	0	13	1	3	23
5	0	0	0	2	1	0	2	3	2	10
6	2	1	0	1	0	0	2	0	0	6
7	0	0	0	0	3	0	0	0	0	3
8	0	0	0	1	0	0	0	2	0	3
9	0	0	5	0	0	3	0	0	0	8
Total	51	24	8	19	4	3	21	11	11	152

4.3.3.4. Pooled vertical and horizontal attributes of canopy structure

A two-axis NMS solution (stress = 7.77, $p < 0.02$; final instability = 0.00001; number of iterations = 82) accounted for 97.4% of the total variance in the dissimilarity matrix derived from the 13 pooled attributes of vertical and horizontal canopy structure (Fig. 4.16). Axis 1 explained 68.2% of the total among-sample variance, and was positively correlated with $\Lambda(r)$ at all measurement scales r ($0.76 \leq R^2 \leq 0.89$; max. R^2 at r = 1.5 m) and G (R^2 = 0.42), and negatively correlated with CC_{Lidar} (R^2 = 0.56). Axis 2 accounted for another 29.2% of the total variance, and was negatively correlated with CHD (R^2 = 0.87), $Lh_{0.85}$ (R^2 = 0.72), $\Lambda_{Integral}$ (R^2 = 0.71), J (R^2 = 0.69), and Λ_{Scale} (R^2 = 0.60). The pattern of dissimilarity among sample units was similar to the NMS ordination presented for attributes of horizontal structure (Fig. 4.14), largely because of the strong

covariance among Λ_{Scale}, $\Lambda_{Integral}$, CHD, $Lh_{0.85}$, and J. Sample units, however, exhibited better separation along covarying gradients of CHD, $Lh_{0.85}$, and J than Λ_{Scale}, due to the increased orthogonality between these three attributes of vertical structure and $\Lambda(r)$.

Multivariate group dispersions associated with each of the four age classes were also similar in size, shape, orientation, and location to the group dispersions derived from the seven attributes of horizontal canopy structure. The average dissimilarity between individual sample units and their group centroid was greatest for age-classes O (4.6) and VY (3.7) and smallest for Y (2.4) and M (2.3). The large within-group variability associated with VY was related to the rapid height growth and crown expansion of young, open-grown trees, as well as their characteristic uniform to clumped horizontal arrangements of stem locations; it was also partly a statistical artifact created by the logarithmic increase in J and CHD with canopy height (see Eqs. 4.1 and 4.9). Substantial variation in G, $Lh_{0.85}$, KR, SK, Λ(4.5 m), Λ(12 m), and Λ_{Scale} contributed to the large dispersion of sample units within age-class O (Fig. 4.12). Any marked variation in vertical or horizontal canopy structure was conspicuously absent from classes Y and M.

Multiple pairwise comparisons using MRPP and Bonferroni-adjusted p values indicated that there were significant group differences among all combinations of age classes. The greatest pairwise difference was found between age-classes VY and M (A = 0.41, $p < 0.00001$), while age-classes Y and M displayed the least dissimilarity ($A = 0.08$, $p < 0.00001$). Although VY and O occupied opposite ends of the developmental spectrum, both were highly lacunar and thus displayed only a moderate degree of dissimilarity ($A = 0.23$, $p < 0.00001$). Stepwise DA indicated that CF1 accounted for 85.5% of the total explained between-group variance, and that CF1 was positively correlated ($R^2 = 0.78$) with $Lh_{0.85}$ (Table 4.3). CF2 accounted for another 13.9% of the total explained variance, and was strongly negatively correlated ($R^2 = 0.99$) with Λ(0.5 m).

Cross-validated and chance-corrected DA classification error rates were lower (overall accuracy = 92.1%, *kappa* = 0.89) than error rates produced using either attributes of vertical or horizontal canopy structure alone (Table 4.4). The most notable differences were the improved user's and producer's accuracies for age-classes M (82.1%) and O (94.1%), respectively. Pooling vertical and horizontal attributes of canopy structure

generally helped to relieve confusion between adjacent age-classes Y versus M and M versus O.

Cluster analysis using *k*-means and three global stopping rules indicated an optimal partition of the pooled dataset at $k = 7$ clusters (Fig. 4.16). Again, we used the sample units found closest to their group centroid as illustrative examples of the kinds of vertical and horizontal canopy structures associated with each *k*-means cluster (Fig. 4.17). These seven examples revealed the strong link between vertical and horizontal patterns of canopy structure, as well as the range of canopy structural features that you might generally expect to find in managed and natural *Pseudotsuga-Tsuga* forests of SLW. Many of the sample units within *k*-means classes 1, 3, and 5 were derived from young, even-aged *Pseudotsuga* plantations of harvest origin, while classes 2, 4, 6, and 7 were predominantly composed of late-successional, mixed *Pseudotsuga-Tsuga* canopies that established naturally after partial or complete stand-replacing disturbance.

4.3.3.5. Canopy density, surface, and volumetric indices

Median canopy density (CC_f) profiles constructed for the four separate age classes indicated that canopy cover generally accumulated more gradually and continuously with relative canopy depth in age-classes VY and O compared to Y and M (Fig. 4.18). The vertical continuity of cover in age-class VY was associated with the full, live crowns characteristic of very young, open-grown conifers. For age-class O, however, it was principally the large, dominant-codominant crowns of *Pseudotsuga* and presence of shade-tolerant *Tsuga* and *Thuja* in subordinate canopy positions and tree-fall gaps that contributed to this pattern. The rise in CC_f with increasing relative canopy depth was noticeably more rapid in age-classes Y and M, with most of the accumulated cover occurring in the top two-thirds of these predominantly single-layered canopies. We found that median values of CC_f in the upper portion of the canopy ($f > 0.70$) increased monotonically with age class due to the logarithmic increase in crown size with tree height (i.e., a single old-growth crown will have larger vertically projected surface area than one or even several younger crowns). However, age-classes Y and M had substantially higher median values of CC_f than either VY or O canopies at $f < 0.6$. Median CC_f was consistently low at all relative canopy heights within age-class VY.

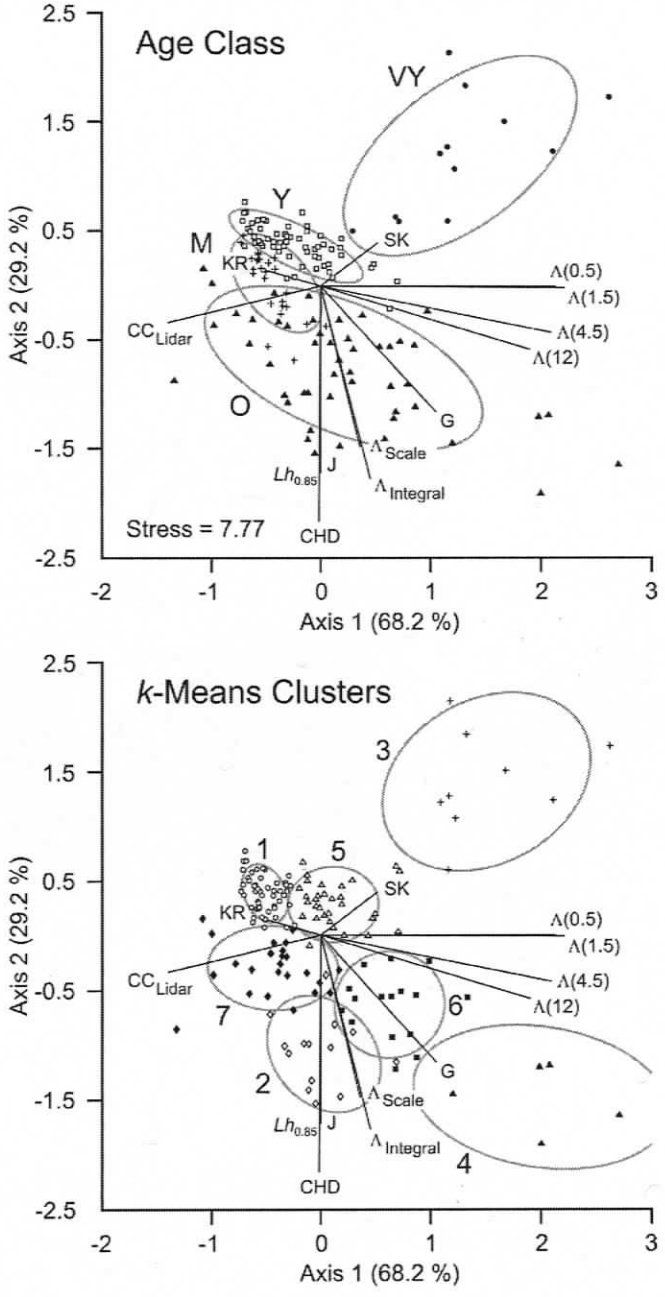

FIGURE 4.16. NMS biplots summarizing the distribution of sample units, age classes (top), and *k*-means clusters (bottom) in two-axis ordination space. Vectors define the magnitude and direction of bivariate correlations (Pearson's correlation coefficient *r*) between the original attributes of vertical and horizontal structure and NMS Axis 1 (*x*) and Axis 2 (*y*) scores. Gaussian bivariate confidence ellipses are centred on group means of *x* and *y*. The unbiased sample standard deviations of *x* and *y* determine the length of the ellipse's main axes, while the sample covariance between *x* and *y* determine the ellipse's orientation.

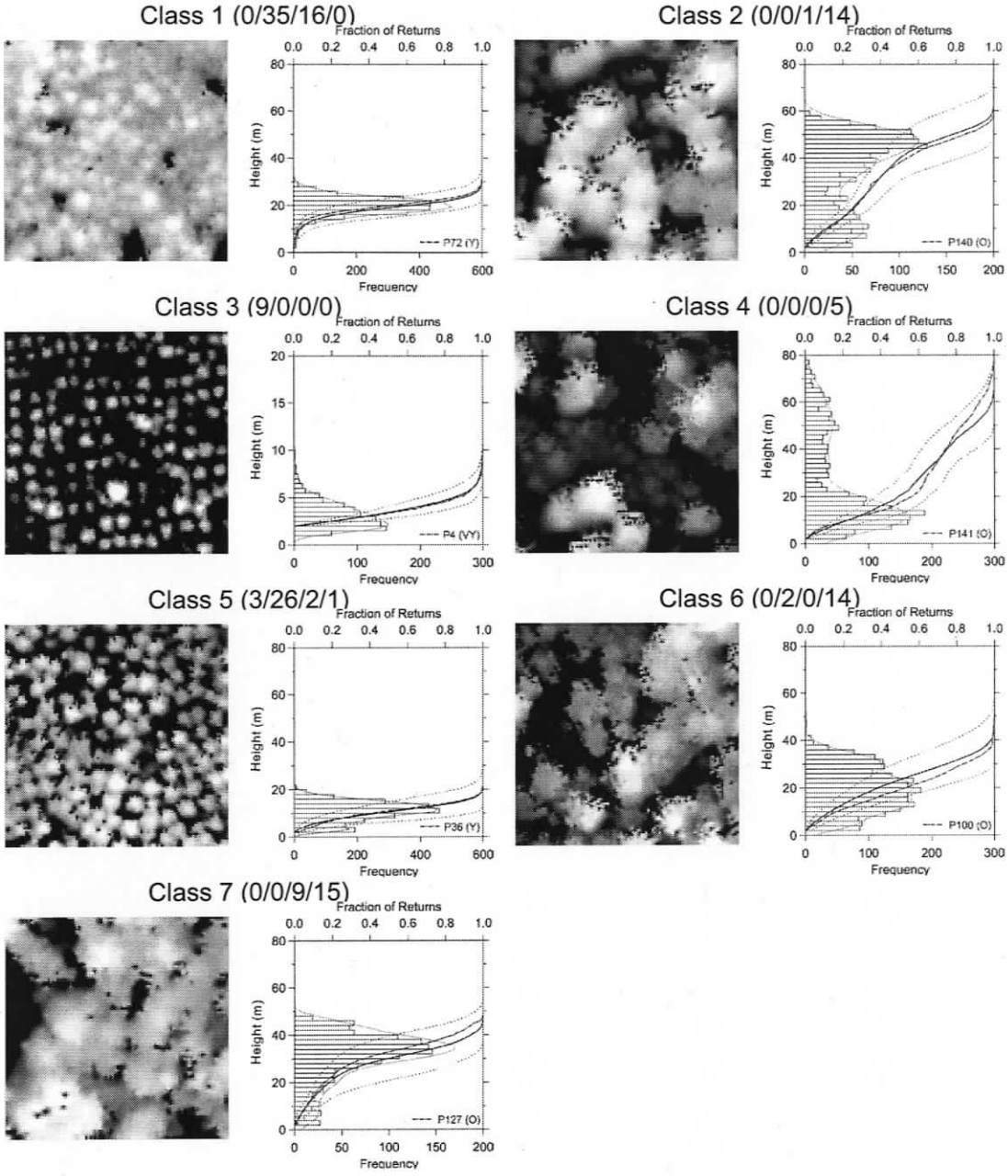

FIGURE 4.17. Illustrative examples of *k*-means classes derived from pooled attributes of vertical and horizontal canopy structure. Values in parentheses beside the arbitrarily assigned class ID represent the number of VY/Y/M/O sample units found in each cluster. Most of the class confusion tended to occur between adjacent age-classes. Two age-class Y sample units were placed into Class 6 because of their unusually high estimates of Λ_{Scale}. Broad age-class confusion associated with Class 5 was related to the presence of short, single-layered, late-successional (M and O) canopies, which had developed on highly unproductive sites.

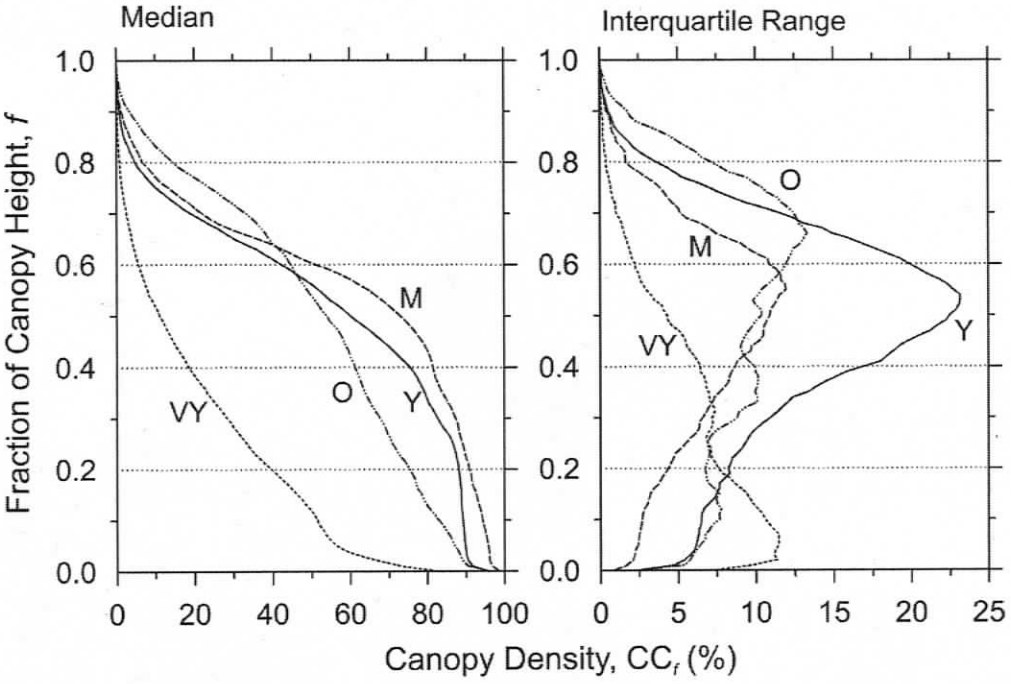

FIGURE 4.18. Median and interquartile ranges (IQR) of canopy density (CC_f) computed by age class for all relative canopy heights *f*. The vertical accumulation of CC_f with relative canopy depth (left) is closely related to the "hypsographs" presented by Lefsky et al. (1999: Fig. 1B) and Parker and Russ (2004: Fig. 3). Age-classes VY and O displayed a gradual accumulation of CC_f with depth, while age-classes Y and M exhibited a more rapid increase in CC_f to near maximum values by mid-canopy. Site-related differences in absolute stand age, productivity, species composition, and disturbance history may account for the large within-group (age-class) variances (IQR) of CC_f and their height dependence.

Measurements of CC_f varied markedly at the sample unit level, and the magnitude of this variation (estimated by the interquartile range—IQR) was also strongly age-class and height dependent (Fig. 4.18). Variation in CC_f was greatest in age-class O at $f > 0.7$; highest in age-class Y between $0.2 < f < 0.7$, and maximal in age-class VY at $f < 0.2$. Age-class M displayed moderate variability in CC_f at all values of *f*. CC_f varied increasingly towards the bottom of VY canopies, presumably in response to variations in crown shape and length. Vertical profiles of the variances associated with CC_f estimates were remarkably similar in shape to the canopy height profiles generally found for each of the four age classes (see, for example, Fig. 4.4). For example, CC_f variances associated

with age-classes Y and M were predominantly unimodal in height distribution with maximum peaks in IQR at $f = 0.54$ (± 23.2%) and $f = 0.55$ (± 12%), respectively; age-class O was multimodal with a global maximum in IQR at $f = 0.66$ (± 13.3%) and local maxima at $f = 0.38$ (± 10.2%) and $f = 0.12$ (± 7.8%); age-class VY was also multimodal with a maximum peak in IQR at $f = 0.07$ (± 11.5%) and local maximum at $f = 0.31$ (± 7.4%). We expect that site-related differences in absolute stand age, productivity, species composition, and disturbance history might account for the large within-group (age-class) variances of CC_f and their height dependence.

Median values of PGV were highest in age-class VY (81.1%), lowest in age-classes Y (49%) and M (45.1%), and moderately high in age-class O (53.8%) (Fig. 4.12). The general decline in median PGV from age-class VY to Y occurred as individual crowns quickly expanded in size to fill all available growing space. In contrast, PGV increased in magnitude from age-class M to O as continued height growth; crown expansion, differentiation, and branch reiteration (Ishii and McDowell, 2002; Ishii et al., 2007); and fine-scale gap creation and dynamics created more topographically elaborate crown and canopy surfaces (Franklin and Van Pelt, 2004; Parker and Russ, 2004). Age-classes Y and O both exhibited marked variability in PGV compared to YR and M. The large variance in PGV associated with age-class Y was a consequence of grouping sample units that were transitional in structure between open grown (high PGV) and closed canopy (low PGV). Had we have used a canopy height threshold ($Lh_{0.85} \geq 20$ m) to separate YR and Y similar to that of Lefsky et al. (1999), the median and variance (IQR) of PGV estimates for age-class Y would have been significantly lower (38.1% ± 3.7%). Thus, median PGV would be expected to reach minimum values at canopy closure and then increase steadily with stand age, thereafter. The large variance in PGV associated with age-class O reflected the heterogeneous nature of old-growth canopies in all spatial dimensions.

Median and IQR values of RI all increased monotonically with age class in response to the continued height growth and elaboration of crown and canopy surfaces: VY (2.1 m^2/m^2 ± 0.32 m^2/m^2); Y (3.8 m^2/m^2 ± 0.67 m^2/m^2); M (5.6 m^2/m^2 ± 0.93 m^2/m^2); O (8.2 m^2/m^2 ± 1.95 m^2/m^2) (Fig. 4.12). RI was strongly correlated with $Lh_{0.85}$ ($R^2 = 0.83$, $n = 152$). The maximum RI (14.3 m^2/m^2) recorded in this study was obtained from a

predominantly top-loaded, old-growth stand (P143) of moderate canopy height ($Lh_{0.85}$ = 51.9 m) and cover (CC_{LiDAR} = 81.5%). The wide range of RI measures that characterized age-class O, again, demonstrated the high structural variability of old-growth canopies compared to younger forests.

4.4. Discussion and Conclusions

4.4.1. LiDAR-derived measurements of forest canopy structure

LiDAR systems naturally measure the 3-D spatial arrangement of forest canopies (Lefsky et al., 2002; Parker et al., 2004), yet much of the focus in LiDAR remote sensing so far has been on the derivation of aspatial attributes of stand structure, such as tree height, volume, basal area, density, biomass, carbon, etc. (Lim et al., 2003; Nelson et al., 2005; Reutebuch et al., 2005; Evans et al., 2006). In this study, we demonstrated explicitly how discrete-return, small-footprint LiDAR could be used to capture fine-scale spatial properties of canopy structure within vertical and horizontal dimensions of a forest stand. Our statistical approach was necessarily a multivariate and partly multiscaled one, due to the inherent 3-D complexity of forest canopies. We used common statistical measures of location (Lh_q), dispersion (G), and shape (SK, KR, CHD, and J) extracted from the distribution of LiDAR canopy heights to describe vertical canopy structure. We also relied on lacunarity analysis and two derivative statistics ($\Lambda_{Integral}$ and Λ_{Scale}) to quantify the scale-dependent dispersion of forest biomass and canopy gaps within the horizontal domain. When used in combination, these two classes of canopy descriptors provided a comprehensive set of variables that facilitated (1) the separation of sample units and forest age classes in the original and reduced dimensions of feature space, and (2) the partition of n sample units into a smaller k number of statistically unique and relatively homogeneous structural groups.

Statistical measures of distributional shape or pattern associated with the vertical arrangement of LiDAR canopy heights can be formalized in many ways (Lovell et al., 2003; Kao et al., 2005; Coops et al., 2007; Weishampel et al., 2007). We chose several different metrics based on order statistics (G), quantiles (Lh_q), quantile-based moments

(*SK* and *KR*), and Shannon's diversity (CHD) and evenness (*J*) indices to characterize shape-related properties of the LiDAR canopy height distribution. Our motivation for selecting these different statistics was three-fold. First, Lh_q, *G*, *SK*, and *KR* were all considered to be robust estimators of distributional shape in the presence of non-normality and outliers. In the context of forests, non-normality and height extrema (outliers) can arise in canopy height distributions any time stands are composed of groups (cohorts) of trees of markedly different age, height, and shade-tolerance (Zenner, 2005a), or when even-aged stands have dominantly top or bottom loaded canopies (Oliver and Larson, 1996). Second, estimates of Lh_q would need to serve dual purposes (*i*) as an ecologically relevant measure of distributional location (i.e., average height of the dominant/codominant overstory trees), and (*ii*) as predictor variables in regression to model other attributes of stand structure (e.g., height, volume, basal area, biomass, etc.). Third, diversity-related indices such as CHD and *J* have a long history of use in ecological studies (Magurran, 2004; McElhinny et al., 2005).

We found that Lh_q was strongly correlated with several field-measured attributes of stand structure across a wide range of q values ($0.5 \leq q \leq 0.9$); however, correlations generally reached their maxima ($0.64 \leq R^2 \leq 0.99$) within a more restricted range of $0.74 \leq q \leq 0.92$ (mean = 0.85 ± 0.06 s.d.). Direct comparison of these optimal values of Lh_q with those reported in other studies was hampered by differences in stand structure, data processing, and LiDAR sensor and survey parameters (Magnussen and Boudewyn, 1998). Nevertheless, where similar height thresholds (≤2 m) were chosen to separate canopy and ground returns, estimates of Lh_q at $0.75 \leq q \leq 0.9$ consistently emerged as the strongest predictors of stand structure for a variety of forest types (Means et al., 2000; Næsset, 2002; Patenaude et al., 2004; Thomas et al., 2006; Skowronski et al., 2007). In this study, Lh_q at $0.5 \leq q \leq 0.9$ was always coincident (or nearly so) with the overstory modal height in single-layered canopies; however, in more vertically complex, multilayered (multimodal) canopies, it was a much narrower range of Lh_q at $0.8 \leq q \leq 0.9$ that was more closely associated with overstory modal heights (see Appendix 4A). This might help to explain why correlations between Lh_q and attributes of stand structure were maximal across a more restricted range of q, since it was the larger dominant-codominant

overstory trees captured by $Lh_{0.85 \pm 0.06\ s.d.}$ that contributed most to stand-level basal area and volume in our ground-reference plots.

Patenaude et al. (2004) also noted the strong height correspondence between $Lh_{0.8}$ and the mode of LiDAR height frequencies in single-layered canopies. Lim and Treitz (2004) applied a segmentation algorithm to separate overstory canopy returns from all other vegetation and ground returns, and found that correlations between aboveground biomass and Lh_q, although large at most values of q, were also maximal across a more restricted range of q. It is very likely that this narrower range of q reported by Lim and Treitz (2004: Table 4) also corresponded closely to the modal height of the overstory canopy. Given the apparent strong association between certain estimates of Lh_q and discrete vertical components of the canopy, we expect that no single estimate of Lh_q, alone, will accurately predict other size-related attributes of stand structure in forest canopies that are strongly multimodal in their height distributions (e.g., Classes 1, 5, 7 and 8, Fig. 4.13). Furthermore, in plantations that are under-stocked or where overstories have been partially disturbed, estimates of canopy cover (CC_{LiDAR}) or density (CC_f) are likely to improve the predictive strength of regression models based solely on Lh_q (Means et al., 2000; North et al., 2004). Here, for example, we found that CC_{LiDAR} and $CC_{f=0.04}$ were moderately to strongly correlated ($0.24 \leq R^2 \leq 0.63$) with residuals derived from fitted regression models of log-transformed y (volume, stem density, or quadratic mean diameter) on log-transformed x (Lh_q). Inclusion of either of these two cover metrics with Lh_q increased the adjusted R^2 for stand volume (0.95 to 0.96), quadratic mean diameter (0.82 to 0.91), and stand density (0.61 to 0.85). We therefore suggest that a complete specification of LiDAR-based regression models for structurally complex stands will include more than one estimate of Lh_q, CC_f (Lefsky et al., 1999; Means et al., 2000; Næsset et al., 2005; Maltamo et al., 2007), and perhaps other scale-invariant measures of distributional shape (van Aardt et al., 2006; Coops et al., 2007).

Location, scale, and shape parameters derived from fitted distribution functions (e.g., β, gamma, Johnson's S_B, Weibull, etc.) have been used in place of sample moments to describe crown and canopy height profiles (Yang et al., 1999; Godfree et al., 2003; Lovell et al., 2003; Jerez et al., 2005; Coops et al., 2007). Known drawbacks associated with this 'curve-fitting' approach relate to potentially large computational requirements

when distribution functions include several model parameters (Press et al., 1986), as well as the inability of many mathematical functions to adequately describe the complex vertical patterns inherent in late-successional forest canopies (Coops et al., 2007). Sample product moments have the desired quality of computational simplicity; however, the higher third and fourth moments (i.e., coefficients of skewness and kurtosis) can be ambiguous and unreliable in the presence of outliers (Hosking, 1992; Kim and White, 2004). Quantile-based estimators of *SK* and *KR* rely only on the quartiles and octiles, respectively, of a continuous distribution and therefore ignore sample points (outliers) in the far tails. Simple interpretations of *SK* and *KR* were difficult in the presence of strong asymmetry and multimodality, although like others (Wyszomirski, 1992) we did find that extremely small (negative) values of *KR* were often indicative of strong bimodality (e.g., Class 8, Fig. 4.13). Still, we found that *SK* and *KR* worked very well together to separate sample units, age classes, and *k*-means clusters. Evidence of this is shown, in part, by the strong similarity (low variability) of shapes of one-sample quantile curves found in each of the vertical *k*-means classes (Fig. 4.13). One possible drawback of these quantile-based estimators is that they may be too robust, and therefore insensitive to subtle, but important variations in the vertical arrangement of canopy structure. Therefore, other alternative robust moment estimators based on linear combinations of order statistics (Hosking, 1990; Elamir and Seheult, 2003) and quantiles (Mudholkar and Hutson, 1998) also need to be explored. Preliminary findings (G. Frazer, *unpublished data*) indicate that *L*-moments (Hosking, 1990) may substantially improve the characterization of canopy height profiles.

We applied Shannon's diversity index (H') as a measure of canopy height diversity (CHD): i.e., a measure of the uncertainty associated with predicting the height class of a randomly sampled LiDAR canopy return. H' is known to increase logarithmically with the number (richness) and evenness (equitability) of species (or height) classes (Magurran, 2004). We found CHD to be strongly nonlinearly correlated with $Lh_{0.85}$ ($\text{CHD} = -0.773 + 0.983 \times \ln(Lh_{0.85})$; $R^2 = 0.88$, $n = 152$); J, in turn, was highly correlated with CHD ($J = 0.635 + 0.256 \times \ln(\text{CHD})$; $R^2 = 0.76$, $n = 152$). Consequently, CHD and J imparted very little new information in the presence of $Lh_{0.85}$. Similar findings regarding the covariance and redundancy of CHD and canopy height have also

been noted by several others (Aber, 1979b; Parker and Brown, 2000; Godfree et al., 2003; Weishampel et al., 2007). Inclusion of CHD and J in the NMS ordinations also contributed to some distortion of the age-class (group) dispersions (Figs. 4.11 and 4.16). The most notable effect was the inflation of between-sample distances (variances) associated with short, young canopies ($Lh_{0.85} < 20$ m) and the compression of between-sample distances found among taller, older canopies ($Lh_{0.85} > 20$ m). The danger here of course is the false impression that young (VY and Y) and old canopies (M and O) are respectively far more and far less vertically diverse than they really are. Last, the loss of information and arbitrariness associated with the conversion of continuous LiDAR canopy heights to height-class frequencies further detracted from the usefulness of these two indices (Parker and Brown, 2000; Staudhammer and LeMay, 2001).

Few published examples currently exist where lacunarity analysis has been applied to continuous quantitative data (e.g., Plotnick et al., 1996; Frazer et al., 2005). Estimates of $\Lambda(r)$ are most often computed using frequency count data (i.e., number of pixels of a certain feature or spectral class) obtained from binary (Sun and Ranson, 1998; Butson and King, 2005) or gray-scale images (Du and Yeo, 2002). The major drawback of this latter approach, again, relates to the loss of textural information and arbitrariness of the selected number, location, and coding of class divisions (Dong, 2000). To avoid these shortcomings, we instead treated the canopy as a spatially contiguous surface of continuously varying height (mass) rather than the usual dichotomous array of gap (zeros) versus non-gap (ones) classes.

Two notable findings emerged from the use of lacunarity analysis in this study. First, log-transformed estimates of $\Lambda(r)$ computed at the finest possible spatial scale (r = 1 grid cell units = 0.5 m horizontal ground units in this study) were strongly linearly correlated with $CC_{f=0.2}$, and nonlinearly correlated with PGV. Similar findings derived from simulated forest canopies have been previously reported by Frazer et al. (2005); however, they had also noted that the relationship between log-transformed $\Lambda(r$ = 1 grid cell units) and canopy cover was clearly logarithmic rather than linear (Fig. 4.19). Others have also shown by way of the binomial theorem that $\Lambda(r$ = 1 grid cell units) is inversely related to pattern density (the ratio of occupied cells to total number of cells) in binary sets (Plotnick et al., 1993, 1996; Dale, 2000; Feagin, 2003). Therefore, we expect that the

linear relationship between log-transformed estimates of $\Lambda(r = 1$ grid cell units) and $CC_{f=0.2}$ observed in this study is more accurately defined as logarithmic (Fig. 4.19). Parameter differences between the two fitted functions derived for the simulated (Frazer et al., 2005) and real canopies (this study) indicated that the precise logarithmic relationship between these two variables may also be strongly data (scene) dependent.

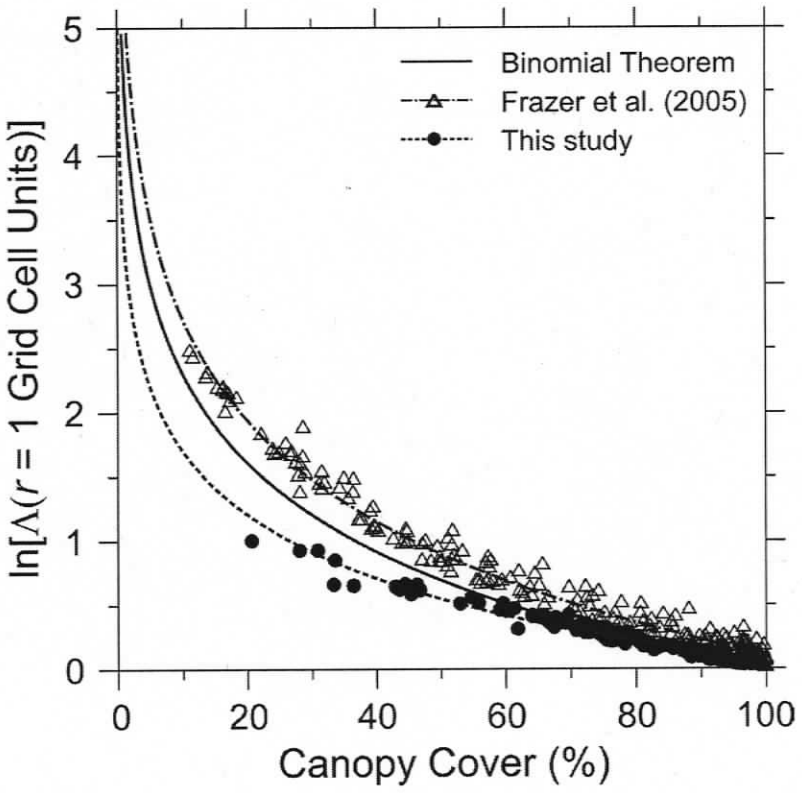

FIGURE 4.19. Scatterplot of log-transformed $\Lambda(r = 1$ in grid cell units) against canopy cover. The solid line shows the theoretical relationship between $\ln[\Lambda(r = 1)]$ and pattern density (ratio of occupied cells to total number of cells expressed as percentage) of a binary set. The other two broken lines represent 'best-fit' logarithmic models ($y = a + b \times \ln(x)$) constructed for real (circles; $R^2 = 0.96$, $n = 152$) and simulated (triangles; $R^2 = 0.98$, $n = 189$) CHMs.

Second, the pattern of decline in $\Lambda(r)$ with increasing spatial scale r was associated with the spatial arrangement of forest canopy structure at several distinct organizational scales: i.e., branch, crown, and neighbourhood scales. In double-log plots of $\Lambda(r)$ against r (e.g., Fig. 4.5), breaks in slope (points of inflection) marked the transition from one prominent scale of pattern to the next (Plotnick et al., 1996; Sun and Ranson, 1998; Dale, 2000; Butson and King, 2006). We believe that the dominant scale of pattern (Λ_{Scale}) identified in each of our sample plots was closely associated with branch, crown, or neighbourhood scales of canopy structure. Butson and King (2006) applied lacunarity analysis to high-spatial-resolution (54 cm) optical (binary) imagery collected over 50 m × 50 m field plots established in mature hardwood (*Acer saccharum*) and mixed (*Populus tremuloides*, *Picea mariana*, and *Abies balsamea*) forest stands in northern Ontario. They found in general that there were three prevalent scales of pattern in these stands: i.e., fine (2–5 m), intermediate (6–9 m), and coarse (8–14 m), and concluded that these scale classes corresponded directly to "components of crowns", individual crowns, and clusters of overlapping crowns, respectively.

We found that median, IQR, minimum, and maximum estimates of Λ_{Scale} also varied markedly with age class (Fig. 4.12): VY (2.9 m ± 0.46 m, 2.5–3.7 m); Y (3.5 m ± 0.46 m, 2.5–28.7 m); M (5.7 m ± 1.6 m, 4.1–18.3 m); O (9.1 m ± 3.1 m, 4.5–27.3 m). Cohen et al. (1990) and Parker et al. (2004) have reported dominate scales of pattern (determined by variography) of similar magnitude for young, mature, and old-growth *Pseudotsuga-Tsuga* forests of Washington and Oregon States, USA. We expect that median (± IQR) estimates of Λ_{Scale} were associated with the average size (diameter) and horizontal spacing of dominant-codominant tree crowns. Other estimates of Λ_{Scale} that occurred far outside the IQR may, however, indicate the dominance of spatial structures at scales smaller or larger than tree crowns (i.e., branch and neighbourhood scales, respectively). Unusually large values of Λ_{Scale} were far more common than exceptionally small ones, mainly because laser footprint size (90 cm) and post-spacing (50 cm) were too large to capture finer-scale branch structures in all but the oldest, largest, and most spatially complex forest crowns and canopies. Crown and neighbourhood scales of spatial aggregation were therefore found to be the most prevalent dominant scales of pattern in this study.

4.4.2. Structural differences among forest age classes

Our findings show that there were significant differences in vertical and horizontal patterns of canopy structure among the four age classes. However, several factors limited our ability to suggest that these differences were strictly age related. First, we made no attempt to control for site-related differences (i.e., soils, topographic position, and stand history) other than confining our sampling to the northern portion of SLW. In fact, we purposely sampled across a broad range of site and disturbance (human versus natural) types to try and capture as much stand structural variability as possible. Second, our sampling strategy, by necessity, was more opportunistic than random due to the patchy and discontinuous nature of the original LiDAR flight lines. Third, fragmentation of the original forest cover by logging and roads had left remnant stands (patches) subject to varying degrees of edge influence (i.e., altered resource and disturbance patterns). Although we tried to sample far away from stand edges, it was not always possible to find interior forest in some of the smaller patches. We therefore acknowledge that some portion of the structural variability noted among age classes may have been due to site-related differences rather than time—a well known drawback and criticism of space-for-time substitutions (Pickett, 1989; Spies and Franklin, 1991; Foster and Tilman, 2000). An additional source of sample bias in this study was related to the right-skewed distribution of absolute stand ages within age classes Y, M, and O. As a result, the mean ages of stands belonging to these three classes were all strongly biased toward the younger end of their age ranges. Much of this age bias arose naturally from the rarity of older Y (>50–80 yr.), M (>120–200 yr.), and O (>350 yr.) stands in SLW.

Though several attributes of canopy structure contributed to the statistical dissimilarity found among forest age classes, canopy height ($Lh_{0.85}$) emerged by far as the single best predictor of stand age class (Table 4.3). In fact, we found that a quadratic discriminant function based solely on $Lh_{0.85}$ was able to achieve an overall classification accuracy rate of 82%. We offer several explanations for the strong discriminatory power of $Lh_{0.85}$. First, inventory foresters rely on dominant overstory trees to determine stand age on the ground or by photo-interpretation (Spies and Franklin, 1991), and $Lh_{0.85}$ was highly correlated with the average height of these same dominant–codominant canopy trees (Fig. 4.6). Second, the three youngest age classes (VY, Y, and M) all fell within the

first two centuries of stand development—the period during which dominant *Pseudotsuga* accumulates most of its height growth and biomass (Acker et al., 2002; Franklin et al., 2002; Van Pelt and Nadkarni, 2004). Third, rapid height-growth, tallness, and longevity confer many competitive advantages in a closed canopy environment (e.g., access to light; avoidance of crown fires, browsing, crushing, and mechanical abrasion; enhanced seed dispersal, etc.). Therefore, the vertical dimension of a forest is likely to be an important spatial axis along which individual trees and stands develop and differentiate ecologically over time (King, 1990; Westoby et al., 2002; Petit and Hampe, 2006). Last, $Lh_{0.85}$ was strongly correlated with many other attributes of stand structure (i.e., crown size, stem height, basal area, density, volume, biomass, etc.), which also vary predictably with stand development and age (Spies and Franklin, 1991; Spies, 1998; Lefsky et al., 1999, 2005; Means et al., 1999, 2000). The utility of canopy height as a basic indicator of stand structural development has been recognized by several others in a variety of forest types (Aber, 1979b; Spies and Franklin, 1991; Brown and Parker, 1994; Lefsky et al., 1999; Parker and Russ, 2004).

The other dimension along which forest age classes differed significantly was associated with the size, scale, and arrangement of openings (holes, gaps, and valleys) in the upper canopy surface (Table 4.3). Various kinds of canopy gaps have been described in closed canopy forests (Parker, 1995; Lertzman et al., 1996; Connell et al., 1997; Lefsky et al., 1999); however, we only considered those that extended vertically downward from the top of the canopy to some height at or above the forest floor (Hubbell and Foster, 1986). Canopy gaps of this kind generally belong to one of three classes: (1) 'regeneration gaps' that result from incomplete or unsuccessful infilling (artificial or natural) of young trees during the stand establishment phase (MacIsaac et al., 2006); (2) 'developmental gaps' created by branch dieback, damage, or loss (Ishii and McDowell, 2002), or the death of one or more dominant canopy trees (Franklin et al., 1987; Spies et al., 1990; Lertzman et al., 1996); (3) 'edaphic gaps' formed by soils, substrates, topography, or other geomorphic features that limit tree growth (Lertzman et al., 1996). Casual observation suggested that all three classes of gaps were prevalent in this study, although we did not attempt to distinguish between them in our analyses.

We found the presence of canopy gaps (estimated by $\Lambda(r)$, PGV, and CC_{LiDAR}) to be a prominent feature of VY and O canopies, while age-classes Y and M generally displayed few gaps, as well as marked uniformity in crown cover (Fig. 4.12). Gaps in managed VY stands were closely associated with the free growing space that surrounded individual crowns (e.g., Classes 2, 3, and 6, Fig. 4.15). The added presence of regeneration and edaphic gaps, however, clearly contributed further horizontal heterogeneity to these otherwise uniformly spaced plantations (e.g., Classes 3 and 6, Fig. 4.15). Rapid height-growth, crown expansion, and self-thinning eliminated many of the larger canopy gaps in higher density Y and M stands (e.g., Class 1, Fig. 4.15). Although we did notice like others (Bradshaw and Spies, 1992; Roberts et al., 2004; Lutz and Halpern, 2006) that developmental gaps caused by storm damage (snow load) and pathogens (root rot) were common features in many of the younger (<60 yr.), even-aged *Pseudotsuga* stands. We also found, consistent with other studies (Song et al., 1997; Frazer et al., 2000; Parker et al., 2004; Van Pelt and Nadkarni, 2004), that age-class O exhibited substantial heterogeneity in the magnitude, scale, and arrangement of canopy gaps (e.g., Classes 4, 5, 8, and 9, Fig. 4.15). Several studies link the structural complexity of old-growth canopies to fine-scale disturbances operating late in stand development (Spies et al., 1990; Lertzman et al., 1996); however, recent findings suggest that horizontal diversification of forest canopies may begin much earlier in stand development in response to a variety of gap-forming processes (Franklin et al., 2002; Winter et al., 2002; Carey, 2003; Lutz and Halpern, 2006; MacIsaac et al., 2006).

4.4.3. Developmental aspects of *Pseudotsuga-Tsuga* canopies

None of the young forests (<60 yr.) sampled in this study originated naturally after wildfire, but were instead established as even-aged *Pseudotsuga* plantations subsequent to clear-cut harvesting. There is still considerable debate as to whether these modern young plantations will in the absence of wildfire or active stand management develop the level and breadth of structural complexity found in present-day, naturally regenerated, old-growth *Pseudotsuga-Tsuga* forests (Tappeiner et al., 1997; Winter et al., 2002; Carey, 2003). Our pooling of samples derived from plantations and natural forests, along with the potential site-related sample bias noted earlier, and wide recognition that

forests develop along multiple pathways (Spies, 2004; Zenner, 2005a) have further restricted our ability to view these sample units as a series of points along a continuum of stand structural development (i.e., as a chronosequence). An alternative and perhaps more realistic view of these samples may simply be as discrete vignettes or "snapshots of independent trajectories" (Chazdon et al., 2007: 275). Both interpretations are likely to hold true for certain samples in this dataset. Nevertheless, we still found that many structural features of young, mature, and old-growth stands documented in this study were generally consistent with the developmental patterns described by conceptualized, process-based models of even-aged stand development (Oliver and Larson, 1996; Spies, 1997; Franklin et al., 2002; Franklin and Van Pelt, 2004) and other canopy-specific research (Parker, 1995; Ishii and McDowell, 2002; Ishii et al., 2004a, b; Nadkarni et al., 2004; Parker and Russ, 2004; Van Pelt and Nadkarni, 2004).

Very young (VY) plantations, for example, were characterized by short, narrow, open-grown crowns (sensu Oliver and Larson, 1996: 215), with the majority of live needle-branch mass concentrated towards the lower half of their crowns (e.g., Class 3, Fig. 4.17). The spatial arrangement of crowns in the horizontal plane was noticeably uniform; however, canopy gaps and within-plot microsite variability contributed to coarser-scale patterns of spatial structure and substantial heterogeneity in the horizontal domain (e.g., Class 6, Fig. 4.15). The separation of individual tree crowns by unfilled (free) growing space was a dominant characteristic of VY stands (Yang et al., 2005; Schroeder et al., 2007). In statistical terms, estimates of $Lh_{0.85}$, CHD, J, Λ_{Scale}, and RI were low due to the short and narrow stature of VY crowns; the concentration of needle-branch mass towards the bottom half of the canopy was expressed as slight positive SK, near-zero KR, moderately high G, and a gradual increase in CC_f with relative canopy depth f; large values of $\Lambda(r = 0.5$ m) and PGV, and low CC_{LiDAR} reflected the large volume of unfilled growing space; large estimates and variances of $\Lambda(r)$ at all measurement scales r indicated significant scale-dependent spatial heterogeneity (patchiness) both within and between VY stands (Fig. 4.12).

Rapid height growth and crown expansion beyond age-class VY led to dramatic increases in canopy height and crown size; attainment of canopy closure; natural pruning of lower branch systems, and a concomitant rise in height-to-live-crown (e.g., see, in

sequential order: Classes 3, 5, and 1, Fig. 4.17). A shift and overall decline in *SK* from positive to negative values (Fig. 4.12) marked the transition from open-grown, bottom-loaded (VY) canopies to single-layer, top-loaded (Y and M) canopies. *KR* increased through to age-class M as biomass accumulation, self-thinning, and crown differentiation operated collectively to move crowns into upper and lower tails of a predominantly unimodal (single-layer) canopy height distribution. As dominant crowns expanded to fill all available growing space, CC_{LiDAR} reached maximum values; PGV, $\Lambda(r)$, and *G* declined to their lowest levels; CC_f increased rapidly from zero at the top of the canopy ($f = 1$) to near maximum values at $f = 0.5$ (Fig. 4.18). The small increase in CC_f at $f < 0.5$ indicated the rarity or absence of vegetation in the lower half of Y and M canopies. RI and Λ_{Scale} both continued to increase through to age-class O in response to the expanding height and roughness of the outer canopy surface. Canopy elaboration, although more subtle in these early- to mid-successional stands, was driven mainly by crown expansion and differentiation and not by the formation of crown- or stand-scale canopy gaps. Spatial homogeneity rather than heterogeneity appeared to be a distinguishing characteristic of age-class Y and several of the younger M stands.

The maturation phase (sensu Franklin et al., 2002) was not well represented in our study due to the rarity of age-class M (80–200 yr.) in SLW. As a result, the structural contrast between age-classes M and O was markedly more abrupt than what might have otherwise been expected (Spies et al., 1990; Spies and Franklin, 1991; Lertzman et al., 1996; Lefsky et al., 1999). This structural–developmental discontinuity was evidenced by a sharp rise (doubling) in the average within-group dissimilarity (distance) coefficient from 2.3 to 4.6 for age-classes M and O, respectively, as well as only minor overlap between their group dispersions (Fig. 4.16). Age-class O, though relatively young (>200–350 yr.) compared to old growth reported in other studies (e.g., Spies and Franklin, 1991; Lefsky et al., 1999; Parker et al., 2004), exhibited substantial heterogeneity in all attributes of vertical and horizontal canopy structure (Fig. 4.12). Key structural features were the presence of large overstory crowns and intercrown gaps; substantial variability in crown and gap sizes, and canopy surface heights; and a seemingly endless array of vertical and horizontal configurations (see Appendix 4A). Fine-scale canopy disturbances (e.g., pathogens, wind, insects, fire, etc.) and mortality operating at branch, crown, and

stand levels; establishment and recruitment of shade-tolerants (mainly *Tsuga* and *Thuja*) into intermediate and codominant canopy positions, and delayed adaptive reiteration by epicormic sprouting are considered to be the three main processes leading to elaboration of the outer canopy surface in these later stages of stand development (Ishii and McDowell, 2002; Franklin and Van Pelt, 2004; Ishii et al., 2007).

4.4.4. Structure-based classification of forest canopies

Stratification of the dataset by age class helped to highlight the general structural changes in forest canopies over time, but did little to show the true idiosyncratic nature of canopy structure. The wide dispersion of sample points in multivariate feature space, and overlap between adjacent age classes (Fig. 4.16) remind us of the importance of site and chance factors (i.e., stochastic processes influencing tree birth and death), as well as time in defining the rates, pathways, and endpoints of forest canopy development (Shugart, 1987; Swanson et al., 1988; Spies, 1997; Spies and Turner, 1999; White and Jentsch, 2001; Ishii et al., 2004b). Structure is regarded as a unifying variable by forest scientists and managers because of its direct link to timber production, ecosystem function, and biodiversity (Berg et al., 1996; O'Hara and Latham, 1996; O'Hara, 1998; Spies, 1998; Franklin et al., 2002). Here, we demonstrated how *k*-means partitioning, cluster validation by consensus, and NMS ordination could be integrated to separate sample units (and possibly landscapes) into an optimal number of homogeneous structural groups, based entirely on measurements of forest canopy structure derived from an airborne LiDAR.

The *k*-means algorithm searches iteratively to minimize the distance between sample points and their group centroids (i.e., the 'total error sum of squares' function). As such, *k*-means is well adept at optimizing within-group homogeneity (with respect to the variables analyzed), as well as finding discontinuities and outliers in multivariate datasets. Tessellations (cluster boundaries) tend toward an arbitrary and more even spatial distribution when sample points are randomly or uniformly arranged in feature space (Legendre and Legendre, 1998). Close inspection of the NMS ordinations of vertical (Fig. 4.11), horizontal (Fig. 4.14), and pooled vertical and horizontal variables (Fig. 4.16) indicated that *k*-means clusters formed primarily in response to the presence of

discontinuities and outliers within the distribution of sample points. We believe that certain discontinuities (including outliers) may have been naturally occurring and therefore ecologically relevant, while others were purely statistical artifacts imposed by incomplete or biased (nonrandom) sampling. Sharp breaks (bimodality) in age-class structure or the mixing of contrasting disturbance types (clearcut harvesting versus wildfire) are two instances that may induce natural divisions within these multivariate dispersions. Interpretation of discontinuities and outliers in these datasets is nevertheless difficult in the absence of a large random sample.

The use of quantitative stopping rules with *k*-means was necessary to determine an optimal value for *k* and the 'best' statistical partition of the dataset. The size, compactness, and placement of *k*-means clusters in NMS ordination space (Figs. 4.11, 4.14, and 4.16) confirmed that consensus among the three global stopping rules worked well to identify an optimal *k*. Minor overlap among *k*-means clusters in NMS biplots was also verification of the accuracy and efficiency with which NMS was able to reproject sample units in two-axis ordination space. We found through experimentation with principal components analysis that NMS, though more computationally intensive, was far better at capturing the original dissimilarity (Euclidean distances) among sample points in fewer dimensions. The optimal value of *k* was different for each of three datasets, because each set of canopy descriptors (vertical and/or horizontal) had its own unique way of separating sample units. A series of two-way contingency tables indicated that the majority of *k*-means clusters were associated with age-class O, and that vertical and horizontal patterns of canopy structure were not necessarily independent of one another (Table 4.5).

Cluster exemplars (samples found closest to their group centroid) selected from the three separate sets of *k*-means clusters provided a useful classification key to aid visual interpretation of the different classes of vertical and horizontal canopy structure found in the dataset. *k*-means partitioning identified nine separate classes of vertical canopy structure that differed primarily by maximum height and distributional shape (Fig. 4.13). Three of the nine 'vertical' classes were associated with early-successional stands, and characterized by short, unimodal canopy profiles; the remaining clusters were composed of late-successional canopies, and had the familiar tall, top-loaded to bottom

loaded, unimodal to multimodal profiles reported by others in similar *Pseudotsuga–Tsuga* forests (Easter and Spies, 1994; Lefsky et al., 1999; Van Pelt and Franklin, 2000; Parker et al., 2004). Nine 'horizontal' classes of canopy structure were also identified by *k*-means (Fig. 4.15). These clusters generally formed along multivariate gradients of crown cover and canopy surface texture, and class divisions appeared to be more arbitrary than for 'vertical' clusters. Partitioning of the complete set of structural variables by *k*-means produced fewer structural classes ($k = 7$), yet revealed the strong association between vertical and horizontal patterns of canopy structure (Fig. 4.17).

The methodology outlined in this study was based on a small number of sample plots ($n = 152$) positioned somewhat randomly along a few spatially discontinuous LiDAR flight lines. Although this sampling approach was reasonable for a proof-of-concept study, it did impose several constraints on our ability to analyze and interpret these data. Rather than relying on a random sample of points within the study area, our expectation is that these LiDAR-derived canopy metrics will be extracted on a cell-by-cell basis using a spatially contiguous grid of square cells (plots or quadrats) fitted over the entire LiDAR survey area (Appendix 4B). This kind of 'wall-to-wall' or 'complete-census' sampling will produce a spatially continuous surface model for each continuous random variable, and thus provide an opportunity to explore, analyze, and combine these multivariate surface data at a variety of spatial scales. We expect that the methods and metrics introduced in this study will provide an invaluable source of spatially continuous canopy structure data for variety of forest science applications, including (1) unbiased site selection for the installation of ground-reference plots (e.g., remote sensing, inventory, growth and yield, micrometeorology, habitat, fire, etc.); (2) habitat and fire modelling; (3) ecological research into the scale-dependent relationships between vegetation structure and terrain variables; vegetation structure and habitat; vegetation structure and ecosystem processes, and ultimately between biodiversity and ecosystem function. Further experimentation is required to eliminate or minimize redundancy between canopy descriptors (e.g., principal components analysis), optimize plot size for different forest types, and test other spatial (e.g., object-based and region-growing segmentation algorithms) and aspatial (e.g., cluster analysis, classification and regression

trees, logistic regression, etc.) statistical techniques for classifying forest canopy structure.

4.5. References

Aber, J.D., 1979a. A method for estimating foliage-height profiles in broad-leaved forests. Journal of Ecology 67, 35–40.

Aber, J.D., 1979b. Foliage-height profiles and succession in northern hardwood forests. Ecology 60, 18–23.

Acker, S.A., Halpern, C.B., Harmon, M.E., Dyrness, C.T., 2002. Trends in bole biomass accumulation, net primary production and tree mortality in *Pseudotsuga menziesii* forests of contrasting age. Tree Physiology 22, 213–217.

Acker, S.A., Sabin, T.E., Ganio, L.M., McKee, W.A., 1998. Development of old-growth structure and timber volume growth trends in maturing Douglas-fir stands. Forest Ecology and Management 104, 265–280.

Allain, C., Cloitre, M., 1991. Characterizing the lacunarity of random and deterministic fractal sets. Physical Review A 44, 3552–3558.

Avery, T.E., Burkhart, H.E., 2002. Forest measurements. McGraw-Hill, New York, NY.

Balanda, K.P., MacGillivray, H.L., 1988. Kurtosis: a critical review. The American Statistician 42, 111–119.

Bartemucci, P., Coates, K.D., Harper, K.A., Wright, E.F., 2002. Gap disturbances in northern old-growth forests of British Columbia, Canada. Journal of Vegetation Science 13, 685–696.

Berg, D.R., Brown, T.M., Blessing, B., 1996. Silvicultural systems design with emphasis on the forest canopy. Northwest Science 70 (Special Issue), 31–36.

Blair, J.B., Hofton, M.A., 1999. Modeling laser altimeter return waveforms over complex vegetation using high-resolution elevation data. Geophysical Research Letters 26, 2509–2512.

Bradshaw, G.A., Spies, T.A., 1992. Characterizing canopy gap structure in forests using wavelet analysis. Journal of Ecology 80, 205–215.

Brokaw, N.V.L., 1982. The definition of treefall gap and its effect on measures of forest dynamics. Biotropia 14, 158–160.

Brokaw, N.V.L., Lent, R.A., 1999. Vertical structure. In: Hunter, M.L. (Ed.), Maintaining Biodiversity in Forest Ecosystems. Cambridge University Press, New York, NY, pp. 373-399.

Brown, M.J., Parker, G.G., 1994. Canopy light transmittance in a chronosequence of mixed-species deciduous forests. Canadian Journal of Forest Research 24, 1696–1703.

Butson, C.R., King, D.J., 2006. Lacunarity analysis to determine optimum extents for sample-based spatial information extraction from high-resolution forest imagery. International Journal of Remote Sensing 27, 105–120.

Caliński, R.B., Harabasz, J., 1974. A dendrite method for cluster analysis. Communications in Statistics 3, 1–27.

Carey, A, B., 2003. Biocomplexity and restoration of biodiversity in temperate coniferous forests: inducing spatial heterogeneity with variable-density thinning. Forestry 76, 127–136.

Chapin, F.S., Matson, P.A., Mooney, H.A., 2002. Principles of terrestrial ecosystem ecology. Springer-Verlag, New York, NY.

Chazdon, R.L., Letcher, S.G., van Breugel, M., Martínez-Ramos, M., Bongers, F., Finegan, B., 2007. Rates of change in tree communities of secondary Neotropical forests following major disturbances. Philosophical Transactions of the Royal Society B 362, 273–289.

Chen, J., Bradshaw, G.A., 1999. Forest structure in space: a case study of an old-growth spruce-fir forest in Changbaishan Natural Reserve, PR China. Forest Ecology and Management 120, 219–233.

Chen, J., Saunders, S.C., Crow, T.R., Naiman, R.J., Brosofske, K.D., Mroz, G.D., Brookshire, B.L., Franklin, J.F., 1999. Microclimate in forest ecosystem and landscape ecology. BioScience 49, 288–297.

Chen, J., Song, B., Rudnicki, M., Moeur, M., Bible, K., North, M., Shaw, D.C., Franklin, J.F., Braun, D.M., 2004. Spatial relationship of biomass and species distribution in an old-growth *Pseudotsuga-tsuga* forest. Forest Science 50, 364–375.

Chen, J.M., Cihlar, J., 1996. Retrieving leaf area index of boreal conifer forests using Landsat TM images. Remote Sensing of Environment 55, 153–162.

Cheng, Q., 1997. Multifractal modeling and lacunarity analysis. Mathematical Geology 29, 919–932.

Clark, M.L., Clark, D.B., Roberts, D.A., 2004. Small-footprint lidar estimation of sub-canopy elevation and tree height in a tropical rainforest landscape. Remote Sensing of Environment 91, 68–89.

Cohen, W.B., Spies, T.A., Bradshaw, G.A., 1990. Semivariograms of digital imagery for analysis of conifer canopy structure. Remote Sensing of Environment 34, 167–178.

Connell, J.H., Lowman, M.D., Noble, I.R., 1997. Subcanopy gaps in temperate and tropical forests. Australian Journal of Ecology 22, 163–168.

Coops, N.C., Hilker, T., Wulder, M.A., St-Onge, B., Newnham, G., Siggins, A., Trofymow, J.A., 2007. Estimating canopy structure of Douglas-fir forest stands from discrete-return LiDAR. Trees 21, 295–310.

Curtis, R.O., Marshall, D.D., 2000. Why quadratic mean diameter? Western Journal of Applied Forestry 15, 137–139.

Dale, M.R.T., 2000. Lacunarity analysis of spatial pattern: A comparison. Landscape Ecology 15, 467–478.

Damgaard, C., Weiner, J., 2000. Describing inequality in plant size or fecundity. Ecology 81, 1139–1142.

David, H.A., 1968. Gini's mean difference rediscovered. Biometrika 55, 573–575.

Dial, R., Bloodworth, B., Lee, A., Boyne, P., Heys, J., 2004. The distribution of free space and its relation to canopy composition at six forest sites. Forest Science 50, 312–325.

Dong, P., 2000. Test of a new lacunarity estimation method for image texture analysis. International Journal of Remote Sensing 21, 3369–3373.

Du, G., Yeo, T.S., 2002. A novel lacunarity estimation method applied to SAR image segmentation. IEEE Transactions on Geoscience and Remote Sensing 40, 2687–2691.

Dubrasich, M.E., Hann, D.W., Tappeiner, J.C., 1997. Methods for evaluating crown area profiles of forest stands. Canadian Journal of Forest Research 27, 385–392.

Easter, M.J., Spies, T.A., 1994. Using hemispherical photography for estimating photosynthetic photon flux density under canopies and in gaps in Douglas-fir forests of the Pacific Northwest. Canadian Journal of Forest Research 24, 2050–2058.

Elamir, E.A.H., Seheult, A.H., 2003. Trimmed *L*-moments. Computational Statistics and Data Analysis 43, 299–314.

Evans, D.L., Roberts, S.D., Parker, R.C., 2006. LiDAR-A new tool for forest measurements? The Forestry Chronicle 82, 211–218.

Feagin, R.A., 2003. Relationship of second-order lacunarity, Hurst exponent, Brownian motion, and pattern organization. Physica A 328, 315–321.

Foster, B.L., Tilman, D., 2000. Dynamic and static views of succession: Testing the descriptive power of the chronosequence approach. Plant Ecology 146, 1–10.

Fournier, R.A., Mailly, D., Walter, J-M. N., Soudani, K., 2003. Indirect measurement of forest canopy structure from *in situ* optical sensors. In: Wulder, M.A., Franklin, S.E. (Eds.), Remote Sensing of Forest Environments: Concepts and Case Studies. Kluwer Academic Press, Norwell, MA, pp. 77–114.

Franklin, J.F., Spies, T.A., Van Pelt, R., Carey, A.B., Thornburgh, D.A., Berg, D.R., Lindenmayer, D.B., Harmon, M.E., Keeton, W.S., Shaw, D.C., Bible, K., Chen, J., 2002. Disturbances and structural development of natural forest ecosystems with silvicultural implications, using Douglas-fir forests as an example. Forest Ecology and Management 155, 399–423.

Franklin, J.F., Shugart, H.H., Harmon, M.E., 1987. Tree death as an ecological process: the causes, consequences, and variability of tree mortality. BioScience 37, 550–556.

Franklin, J.F., Van Pelt, R., 2004. Spatial aspects of structural complexity in old-growth forests. Journal of Forestry 102, 22–28.

Frazer, G.W., Trofymow, J.A., Lertzman, K.P., 2000. Canopy openness and leaf area in chronosequences of coastal temperate rainforests. Canadian Journal of Forest Research 30, 239–256.

Frazer, G.W., Wulder, M.A., Niemann, O., 2005. Simulation and quantification of the fine-scale spatial pattern and heterogeneity of forest canopy structure: A lacunarity-based method designed for analysis of continuous canopy heights. Forest Ecology and Management 214, 65–90.

Gaveau, D., Hill, R., 2003. Quantifying canopy height underestimation by laser pulse penetration in small-footprint airborne laser scanning data. Canadian Journal of Remote Sensing 29, 650–657.

Gobakken, T., Næsset, E., 2005. Weibull and percentile models for lidar-based estimation of basal area distribution. Scandinavian Journal of Forest Research 20, 490–502.

Godfree, R.C., Tinnin, R.O., Forbes, R.B., 2003. Relationships between dwarf mistletoe and the canopy structure of an old-growth lodgepole pine forest in central Oregon. Canadian Journal of Forest Research 33, 997–1009.

Gordon, A.D., 1999. Classification. Chapman & Hall/CRC, Boca Raton, FL.

Hann, D.W., 1999. An adjustable predictor of crown profile for stand-grown Douglas-fir trees. Forest Science 45, 217–225.

Harper, K.A., MacDonald, S.E., Burton, P.J., Chen, J., Brosofske, K.D., Saunders, S.C., Euskirchen, E.S., Roberts, D., Jaiteh, M.S., Esseen, P-A., 2005. Edge influence on forest structure and composition in fragmented landscapes. Conservation Biology 19, 768–782.

Hartigan, J.A., 1985. Statistical theory of clustering. Journal of Classification 2, 63–76.

Holmgren, J., Nilsson, M., Olsson, H., 2003. Simulating the effects of lidar scanning angle for estimation of mean tree height and canopy closure. Canadian Journal of Remote Sensing 29, 623–632.

Hosking, J.R.M., 1990. *L*-moments: analysis and estimation of distributions using linear combinations of order statistics. Journal of the Royal Statistical Society B 52, 105–124.

Hosking, J.R.M., 1992. Moments or *L* moments? An example comparing two measures of distributional shape. The American Statistician 46, 186–189.

Hubbell, S.F., Foster, R.B., 1986. Canopy gaps and the dynamics of a neotropical forest. In: M.J. Crawley (Ed.), Plant Ecology. Blackwell Science, Oxford, pp. 77–96.

Hyndman, R.J., Fan, F., 1996. Sample quantiles in statistical packages. The American Statistician 50, 361–365.

Ishii, H.T., Ford, E.D., Kennedy, M.C., 2007. Physiological and ecological implication of adaptive reiteration as a mechanism for crown maintenance and longevity. Tree Physiology 27, 455–462.

Ishii, H., McDowell, N., 2002. Age-related development of crown structure in coastal Douglas-fir trees. Forest Ecology and Management 169, 257–270.

Ishii, H., Reynolds, J.H., Ford, E.D., Shaw, D.C., 2000. Height growth and vertical development of an old-growth Pseudotsuga-Tsuga forest in southwestern Washington State, U.S.A. Canadian Journal of Forest Research 30, 17–24.

Ishii, H.T., Tanabe, S., Hiura, T. 2004a. Exploring the relationships among canopy structure, stand productivity, and biodiversity of temperate forest ecosystems. Forest Science 50, 342–355.

Ishii, H.T., Van Pelt, R., Parker, G.G., Nadkarni, N.M., 2004b. Age-related development of canopy structure and its ecological functions. In: Lowman, M.D., Rinker, H.B., (Eds.), Forest Canopies, Second Edition. Elsevier Academic Press, Burlington, MA, pp. 102–117.

Jennings, S.B., Brown, N.D., Sheil, S., 1999. Assessing forest canopies and understorey illumination: canopy closure, canopy cover and other measures. Forestry 72, 59–73.

Jerez, M., Dean, T.J., Cao, Q.V., Roberts, S.D., 2005. Describing leaf area distribution in loblolly pine trees with Johnson's S_B function. Forest Science 51, 93–101.

Kao, D.L., Kramer, M.G., Love, A.L., Dungan, J.L., Pang, A.T., 2005. Visualizing distributions from multi-return lidar data to understand forest structure. The Cartographic Journal 42, 35–47.

Kim, T-H., White, H., 2004. On more robust estimation of skewness and kurtosis. Finance Research Letters 1, 56–73.

King, D.A., 1990. The adaptive significance of tree height. The American Naturalist 135, 809–828.

Knox, R.G., Peet, R.K., Christensen, N.L., 1989. Population dynamics in loblolly pine stands: changes in skewness and size inequality. Ecology 70, 1153–166.

Koukoulas, S., Blackburn, G.A., 2004. Quantifying the spatial properties of forest canopy gaps using LiDAR imagery and GIS. International Journal of Remote Sensing 25, 3049–3071.

Krzanowski, W.J., Lai, Y.T., 1988. A criterion for determining the number of groups in a data set using sum-of-squares clustering. Biometrics 44, 23–34.

Latham, P.A., Zuuring, H.R., Coble, D.W., 1998. A method for quantifying vertical forest structure. Forest Ecology and Management 104, 157–170.

Lefsky, M.A., Cohen, W.B., Acker, S.A., Parker, G.G., Spies, T.A., Harding, D., 1999. Lidar remote sensing of the canopy structure and biophysical properties of Douglas-fir western hemlock forests. Remote Sensing of Environment 70, 339–361.

Lefsky, M.A., Cohen, W.B., Parker, G.G., Harding, D.J., 2002. LiDAR remote sensing for ecosystem studies. BioScience 52, 19–30.

Lefsky, M.A., Hudak, A.T., Cohen, W.B., Acker, S.A., 2005. Patterns of covariance between forest stand and canopy structure in the Pacific Northwest. Remote Sensing of Environment 95, 517–531.

Legendre, P., Legendre, L., 1998. Numerical ecology. Elsevier Science B.V., Amsterdam.

Lertzman, K.P., Fall, J.G., 1998. From forest stands to landscapes: spatial scales and the roles of disturbances. In: Peterson, D.L., Parker, V.T. (Eds.), Ecological Scale: Theory and Applications. Columbia University Press, New York, NY, pp. 339–367.

Lertzman, K.P., Sutherland, G.D., Inselberg, A., Saunders, S.C., 1996. Canopy gaps and the landscape mosaic in a coastal temperate rain forest. Ecology 77, 1254–1270.

Lewis, J.D., McKane, R.B., Tingey, D.T., Beedlow, P.A., 2000. Vertical gradients in photosynthetic light response within an old-growth Douglas-fir and western hemlock canopy. Tree Physiology 20, 447–456.

Lim, K.S., Treitz, P.M., 2004. Estimation of above ground forest biomass from airborne discrete return laser scanner data using canopy-based quantile estimators. Scandinavian Journal of Forest Research 19, 558–570.

Lim, K., Treitz, P., Wulder, M., St-Onge, B., Flood, M., 2003. LiDAR remote sensing of forest structure. Progress in Physical Geography 27, 88–106.

Lloyd, C.D., Atkinson, P.M., 2002. Deriving DSMs from LiDAR data with kriging. International Journal of Remote Sensing 23, 2519–2524.

Lovell, J.L., Jupp, D.L.B., Culvenor, D.S., Coops, N.C., 2003. Using airborne and ground-based ranging lidar to measure canopy structure in Australian forests. Canadian Journal of Remote Sensing 29, 606–622.

Lowman, M.D., Rinker, H.B., 2004. Forest canopies. Elsevier Academic Press, Burlington, MA.

Lutz, J.A., Halpern, C.B., 2006. Tree mortality during early forest development: a long-term study of rates, causes, and consequences. Ecological Monographs 76, 257–275.

MacArthur, R.H., MacArthur, J.W., 1961. On bird species diversity. Ecology 42, 594–598.

MacArthur, R.H., Horn, H.S., 1969. Foliage profile by vertical measurements. Ecology 50, 802–804.

MacIsaac, D.A., Comeau, P.G., MacDonald, S.E., 2006. Dynamics of regeneration gaps following harvest of aspen stands. Canadian Journal of Forest Research 36, 1818–1833.

Magnussen, S., Boudewyn, P., 1998. Derivations of stand heights from airborne laser scanner data with canopy-based quantile estimators. Canadian Journal of Forest Research 28, 1016–1031.

Magurran, A.E., 2004. Measuring biological diversity. Blackwell Publishing, Malden, MA.

Maltamo, M., Korhonen, K.T., Packalén, P., Mehtätalo, L., Suvanto, A., 2007. Testing the usability of truncated angle count sample plots as ground truth in airborne laser scanning-based forest inventories. Forestry 80, 73–81.

Maltamo, M., Packalén, P., Yu, X., Eerikäinen, K., Hyyppä, J., Pitkänen, J., 2005. Identifying and quantifying structural characteristics of heterogeneous boreal forests using laser scanner data. Forest Ecology and Management 216, 41–50.

McComb, W.C., Spies, T.A., Emmingham, W.H., 1993. Douglas-fir forests—managing for timber and mature forest habitat. Journal of Forestry 93, 31–42.

McCune, B., Grace, J.B., 2002. Analysis of ecological communities. MjM Software Design, Gleneden Beach, OR.

McCune, B., Mefford, M.J., 1999. PC-ORD. Multivariate analysis of ecological data, version 4. MjM Software Design, Gleneden Beach, OR.

McElhinny, C., Gibbons, P., Brack, C., Bauhus, J., 2005. Forest and woodland stand structural complexity: Its definition and measurement. Forest Ecology and Management 218, 1–24.

McGarigal, K., Cushman, S., Stafford, S., 2000. Multivariate statistics for wildlife and ecology research. Springer-Verlag Inc., New York, NY.

Means, J.E., Acker, S.A., Harding, D.J., Blair, J.B., Lefsky, M.A., Cohen, W.B., Harmon, M.E., McKee, W.A., 1999. Use of large-footprint scanning airborne lidar to estimate forest stand characteristics in the western Cascades of Oregon. Remote Sensing of Environment 67, 298–308.

Means, J.E., Acker, S.A., Fitt, B.J., Renslow, M., Emerson, L., Hendrix, C.J., 2000. Predicting forest stand characteristics with airborne scanning lidar. Photogrammetric Engineering & Remote Sensing 66, 1367–1371.

Milligan, G.W., Cooper, M.C., 1985. An examination of procedures for determining the number of clusters in a dataset. Psychometrika 50, 159–179.

Moors, J.J.A., 1988. A quantile alternative for kurtosis. The Statistician 37, 25–32.

Mudholkar, G.S., Hutson, A.D., 1998. *LQ*-moments: analogs of *L*-moments. Journal of Statistical Planning and Inference 137, 3024–3039.

Nadkarni, N.M., Parker, G.G., Rinker, H.B., Jarzen, D.M., 2004. The nature of forest canopies. In: Nadkarni, N.M., Rinker, H.B. (Eds.), Forest Canopies. Elsevier Academic Press, Burlington, MA, pp. 3–23.

Næsset, E., 2002. Predicting forest stand characteristics with airborne scanning laser using a practical two-stage procedure and field data. Remote Sensing of Environment 80, 88–99.

Næsset, E., Bollandsås, O.M., Gobakken, T., 2005. Comparing regression methods in estimation of biophysical properties of forest stands from two different inventories using laser scanner data. Remote Sensing of Environment 94, 541–553.

Nelson, R., Valenti, M.A., Short, A., Keller, C., 2005. A multiple resource inventory of Delaware using airborne laser data. BioScience 53, 981–992.

North, M., Chen, J., Oakley, B., Song, B., Rudnicki, M., Gray, A., Innes, J., 2004. Forest stand structure and pattern of old-growth western hemlock/Douglas-fir and mixed-conifer forests. Forest Science 50, 299–311.

Ogunjemiyo, S., Parker, G., Roberts, D., 2005. Reflections in bumpy terrain: implications of canopy surface variations for the radiation balance of vegetation. IEEE Geoscience and Remote Sensing Letters 2, 90–93.

O'Hara, K.L., 1998. Silvicultural for structural diversity: a new look at multiaged systems. Journal of Forestry 96, 4–10.

O'Hara, K.L., Latham, P.A., 1996. A structural classification for Inland Northwest forest vegetation. Western Journal of Applied Forestry 11, 97–102.

Oliver, C.D., 1981. Forest development in North America following major disturbances. Forest Ecology and Management 3, 153–168.

Oliver, C.D., Larson, B.C. 1996. Forest stand dynamics. John Wiley & Sons, New York, NY.

Ozanne, C.M.P., Anhuf, D., Boulter, S.L., Keller, M., Kitching, R.L., Korner, C., Meinzer, F.C., Mitchell, A.W., Nakashizuda, T., Silva Das, P.L., Stork, N.E., Wright, S.J., Yoshimura, M., 2003. Biodiversity meets the atmosphere: a global view of forest canopies. Science 301, 183–186.

Pacala, S.W., Deutschman, D.H., 1995. Details that matter: the spatial distribution of individual trees maintains ecosystem function. Oikos 74, 357–365.

Parker, G.G., 1995. Structure and microclimate of forest canopies. In: Lowman, M.D., Nadkarni, N.M. (Eds.) Forest Canopies. Academic Press, Orlando, FL, pp. 73–98.

Parker, G.G., Brown, M.J., 2000. Forest canopy stratification—Is it useful? The American Naturalist 155, 473–484.

Parker, G.G., Harmon, M.E., Lefsky, M.A., Chen, J., Van Pelt, R., Weiss, S.B., Thomas, S.C., Franklin, J.F., 2004. Three-dimensional structure of an old-growth *Pseudotsuga-tsuga* canopy and its implications for radiation balance, microclimate, and gas exchange. Ecosystems 7, 440–453.

Parker, G.G., Russ, M.E., 2004. The canopy surface and stand development: assessing forest canopy structure and complexity with near-surface altimetry. Forest Ecology and Management 189, 307–315.

Patenaude, G., Hill, R.A., Milne, R., Gaveau, D.L.A., Briggs, B.B.J., Dawson, T.P., 2004. Quantifying forest above ground carbon content using LiDAR remote sensing. Remote Sensing of Environment 93, 368–380.

Perry, D.A., 1998. The scientific basis of forestry. Annual Review of Ecology and Systematics 29, 435–66.

Petit, R.J., Hampe, A., 2006. Some evolutionary consequences of being a tree. Annual Review of Ecology and Systematics 37, 187–214.

Pickett, S.T.A., 1989. Space-for-time substitution as an alternative to long-term studies. In: Likens, G.E. (Ed.), Long-term studies in ecology: approaches and alternatives. Springer-Verlag, New York, NY, pp. 110–135.

Pickett, S.T.A., White, P.S., 1985. The ecology of natural disturbance and patch dynamics. Academic Press, Orlando, FL.

Plotnick, R.E., Gardner, R.H., Hargrove, W.W., Prestegaard, K., Perlmutter, M., 1996. Lacunarity analysis: a general technique for analysis of spatial pattern. Physical Reviews E 53, 5461–5468.

Plotnick, R.E., Gardner, R.H., O'Neill, R.V., 1993. Lacunarity indices as measures of landscape texture. Landscape Ecology 8, 201–211.

Pregitzer, K.S., Euskirchen, E.S., 2004. Carbon cycling and storage in world forests: biome patterns related to forest age. Global Change Biology 10, 2052–2077.

Press, W.H., Flannery, B.P., Teukolsky, S.A., Vetterling, W.T., 1986. Numerical recipes: the art of scientific computing. Cambridge University Press, Cambridge, UK.

Rautiainen, M., Stenberg, P., Nilson, T., 2005. Estimating canopy cover in Scots pine stands. Silva Fennica 39, 137–142.

Reutebuch, S.E., Andersen, H-E., McGaughey, R.J., 2005. Light detection and ranging (LIDAR): An emerging tool for multiple resource inventory. Journal of Forestry 103, 286–292.

Riaño, D., Meier, E., Allgöwer, B., Chuvieco, E., Ustin, S.L., 2003. Modeling airborne laser scanning data for the spatial generation of critical forest parameters in fire modeling. Remote Sensing of Environment 86, 177–186.

Roberts, D.A., Ustin, S.L., Ogunjemiyo, S., Greenberg, J., Dobrowski, S.Z., Chen, J., Hinckley, T.M., 2004. Spectral and structural measures of northwest forest vegetation at leaf to landscape scales. Ecosystems 7, 545–562.

Ryan, M.G., 2002. Canopy processes research. Tree Physiology 22, 1035–1043.

Saunders, S.C., Chen, J., Drummer, T.D., Gustafson, E.J., Brosofske, K.D., 2005. Identifying scales of pattern in ecological data: A comparison of lacunarity, spectral and wavelet analyses. Ecological Complexity 2, 87–105.

Schroeder, T.A., Cohen, W.B., Yang, Z., 2007. Patterns of forest regrowth following clearcutting in western Oregon as determined by a Landsat time-series. Forest Ecology and Management 243, 259–273.

Shugart, H.H., 1987. Dynamic ecosystem consequences of tree birth and death patterns. BioScience 37, 596–602.

Skowronski, N., Clark, K., Nelson, R., Hom, J., Patterson, M., 2007. Remotely sensed measurements of forest structure and fuel loads in Pinelands of New Jersey. Remote Sensing of Environment 108, 123–129.

Song, B., Chen, J., Desenker, P.V., Reed, D.D., Bradshaw, G.A., Franklin, J.F., 1997. Modeling canopy structure and heterogeneity across scales: from crowns to canopy. Forest Ecology and Management 96, 217–233.

Song, B., Chen, J., Silbernagel, J., 2004. Three-dimensional canopy structure of an old-growth Douglas-fir forest. Forest Ecology and Management 96, 217–229.

Spies, T.A., 1997. Forest stand structure, composition, and function. In: Kohm, K.A., Franklin, J.F. (Eds.), Creating a Forestry for the 21st Century: The Science of Ecosystem Management. Island Press, Washington, D.C., pp. 11–30.

Spies, T.A., 1998. Forest structure: A key to the ecosystems. In: Trofymow, J.A., MacKinnon, A. (Eds.), Structure, Process, and Diversity in Successional Forests of Coastal British Columbia. Northwest Science 72 (Special Issue No. 2), 34–39.

Spies, T.A., 2004. Ecological concepts and diversity of old-growth forests. Journal of Forestry 102, 14–20.

Spies, T.A., Franklin, J.F., 1991. The structure of natural young, mature, and old-growth Douglas-fir forests in Oregon and Washington. In: Ruggiero, L.F., Aubry, K.B., Carey, A.B., Huff, M.H. (Eds.), Wildlife and Vegetation of Unmanaged Douglas-fir Forests. U.S. Department of Agriculture, Forest Service, Pacific Northwest Research Station, Portland, Oregon. General Technical Report PNW-GTR-285, May 1991.

Spies, T.A., Franklin, J.F., Klopsch, M., 1990. Canopy gaps in Douglas-fir forests of the Cascade Mountains. Canadian Journal of Forest Research 20, 649–658.

Spies, T.A., Franklin, J.F., Thomas, T.B., 1988. Coarse woody debris in Douglas-fir forests of Western Oregon and Washington. Ecology 69, 1689–1702.

Spies, T.A., Turner, M.G., 1999. Dynamic forest mosaics. In: Hunter Jr., M.L. (Ed.), Maintaining Biodiversity in Forest Ecosystems. Cambridge University Press, New York, NY, pp. 95–160.

Staudhammer, C., LeMay, V., 2001. Introduction and evaluation of possible indices of stand structural diversity. Canadian Journal of Forest Research 31, 1105–1115.

Sun, G., Ranson, K.J., 1998. Radar modelling of forest spatial patterns. International Journal of Remote Sensing 19, 1769–1791.

Swanson, F.J., Kratz, T.K., Caine, N., Woodmansee, R.G., 1988. Landform effects on ecosystem patterns and processes. BioScience 38, 92–98.

Tabachnick, B.G., Fidell, L.S., 2001. Using multivariate statistics. Allyn and Bacon, Needham Heights, MA.

Tappeiner, J.C., Huffman, D., Marshall, D., Spies, T.A., Bailey, J.D., 1997. Density, ages, and growth rates in old-growth and young-growth forests in coastal Oregon. Canadian Journal of Forest Research 27, 638–648.

Thomas, V., Treitz, P., McCaughey, J.H., Morrison, I., 2006. Mapping stand-level forest biophysical variables for a mixedwood boreal forest using lidar: an examination of scanning density. Canadian Journal of Forest Research 36, 34–47.

Titus, K., Mosher, J.A., Williams, B.K., 1984. Chance-corrected classification for use in discriminant analysis: ecological applications. The American Midland Naturalist 111, 1–7.

Trofymow, J.A., Porter, G.L., Blackwell, B.A., Arksey, R., Marshall, V., Pollard, D., 1997. Chronosequences for research into the effects of converting coastal British Columbia old-growth to managed forests: an establishment report. Canadian Forest Service, Pacific Forestry Centre, Information Report BC-X-374, Victoria, BC.

Turner, D.P., Acker, S.A., Means, J.E., Garman, S.L., 2000. Assessing alternative algorithms for estimating leaf area of Douglas-fir trees and stands. Forest Ecology and Management 126, 61–76.

van Aardt, J.A.N., Wynne, R.H., Oderwald, R.G., 2006. Forest volume and biomass estimation using small-footprint lidar-distributional parameters on a per-segment basis. Forest Science 52, 636–649.

Van Pelt, R., Nadkarni, N.M., 2004. Development of canopy structure in Pseudotsuga menziesii forests of southern Washington Cascades. For. Science 50, 326–341.

Weishampel, J.F., Drake, J.B., Cooper, A., Blair, J.B., Hofton, M., 2007. Forest canopy recovery from 1938 hurricane and subsequent salvage damage measured with airborne LiDAR. Remote Sensing of Environment 109, 142–153.

West, D.C., Shugart, H.H., Botkin, D.B., 1981. Forest succession: concepts and applications. Springer-Verlag, New York, NY.

Westoby, M., Falster, D.S., Moles, A.T., Vesk, P.A., Wright, I.J., 2002. Plant ecological strategies: Some leading dimensions of variation between species. Annual Review of Ecology and Systematics 33, 125–159.

White, P.S., Jentsch, A., 2001. The search for generality in studies of disturbance and ecosystem dynamics. Progress in Botany 62, 399–450.

Williams, B.K., 1983. Some observations on the use of discriminant analysis in ecology. Ecology 64, 1283–1291.

Winchester, N.N., 2006. Ancient temperate rain forest research in British Columbia. Canadian Entomologist 138, 72–83.

Winter, L.E., Brubaker, L.B., Franklin, J.F., Miller, E.A., DeWitt, D.Q., 2002. Initiation of an old-growth Douglas-fir stand in the Pacific Northwest: a reconstruction from tree-ring records. Canadian Journal of Forest Research 32, 1039–1056.

Wishart, D., 2005. Number of clusters. In: Everitt, B.S., Howell, D.C. (Eds.), Encyclopedia of Statistics in Behavioral Science. John Wiley & Sons, Ltd., Chichester, U.K. pp. 1442–1446.

Wyszomirski, T., 1992. Detecting and displaying size bimodality: kurtosis, skewness, and bimodalizable distributions. Journal of Theoretical Biology 158, 109–128.

Yang, X., Witcosky, J.J., Miller, D.R., 1999. Vertical overstory canopy architecture of temperate deciduous hardwood forests in eastern United States. Forest Science 45, 349–358.

Yang, Z., Cohen, W.B., Harmon, M.E., 2005. Modeling early forest succession following clear-cutting in western Oregon. Canadian Journal of Forest Research 35, 1889–1900.

Yorath, C.J., Nasmith, H.W., 1995. The geology of Southern Vancouver Island. Orca Book Publishers, Victoria, BC.

Zar, J.H., 1999. Biostatistical analysis. Prentice Hall, Upper Saddle, NJ.

Zenner, E.K., 2005a. Development of tree size distributions in Douglas-fir forests under differing disturbance regimes. Ecological Applications 15, 701–714.

Zenner, E.K., 2005b. Investigating scale-dependent stand heterogeneity with structure-area-curves. Forest Ecology and Management 209, 87–100.

Zenner, E.K., Hibbs, D.E., 2000. A new method for modeling the heterogeneity of forest canopy structure. Forest Ecology and Management 129, 75–87.

Zimble, D.A., Evans, D.L., Carlson, G.C., Parker, R.C., Grado, S.C., Gerard, P.D., 2003. Characterizing vertical forest structure using small-footprint airborne LiDAR. Remote Sensing of Environment 87, 171–182.

Appendix 4A

Catalogue[4] of LiDAR canopy height models (CHM), height-frequency histograms, and one-sample quantile plots compiled for all 152 sample units used in this study.

[4] Sample units were sorted in ascending order by $Lh_{0.85}$; Letter in parentheses beside sample ID denotes age class: VY (<20 yr.); Y (>20-80 yr.); M (>80-200 yr.); O (>200 yr.); Plot-level inventory data for 16 ground-reference summarized in Table 4.2. Canopy heights increase from black to white.

P1 (VY)

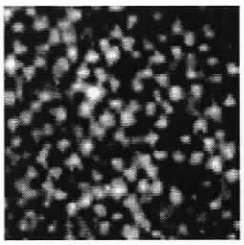

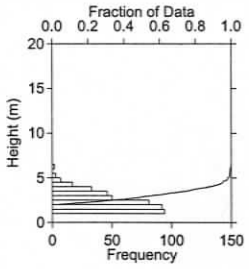

P2 (VY)

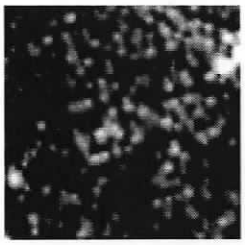

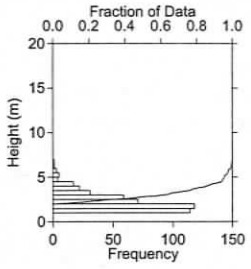

P3 (VY)

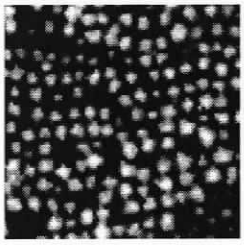

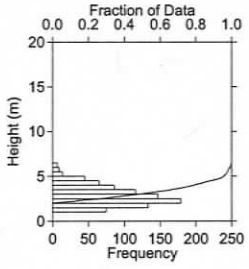

P4 (VY)

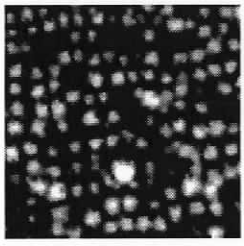

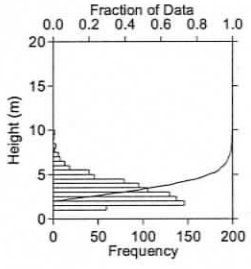

P5 (VY)

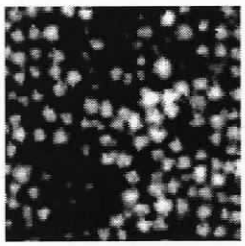

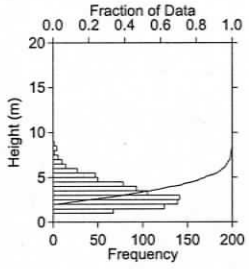

P6 (VY)

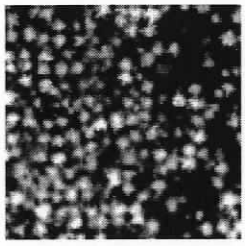

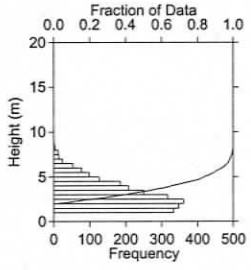

P7 (VY)

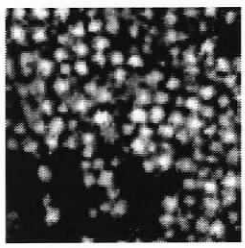

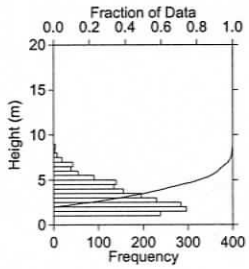

P8 (VY)

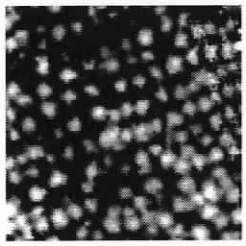

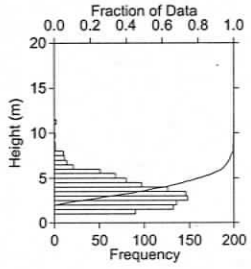

P9 (VY)

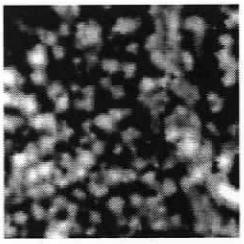

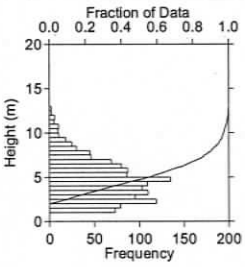

P10 (VY)

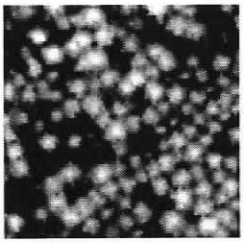

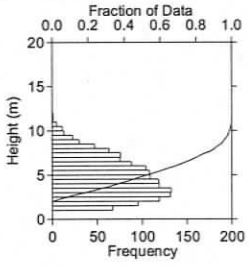

P11 (VY)

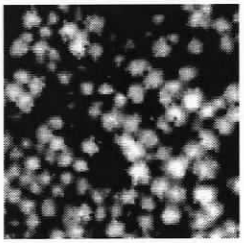

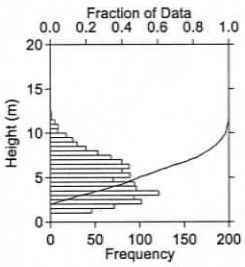

P12 (VY)

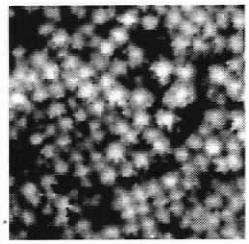

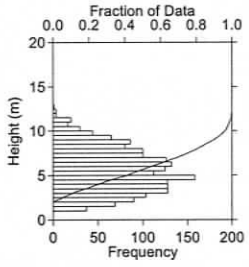

P13 (Y)

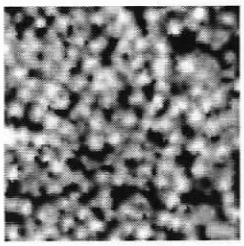

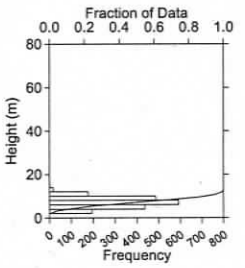

P14 (Y)

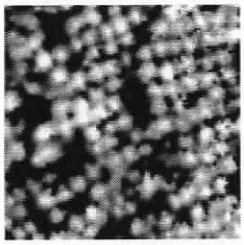

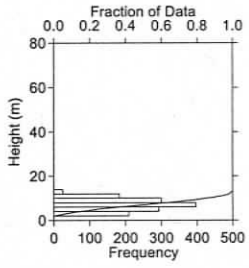

P15 (Y)

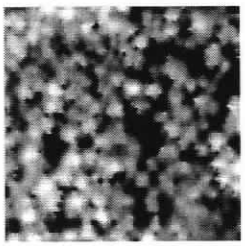

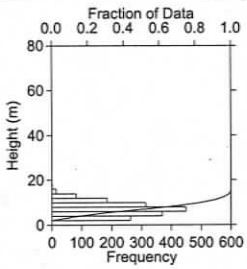

P16 (Y)

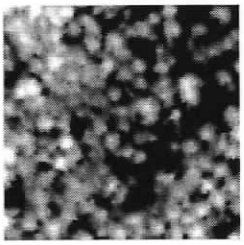

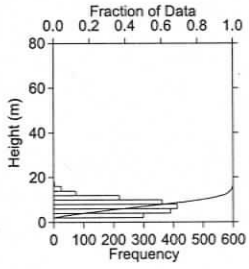

P17 (Y)

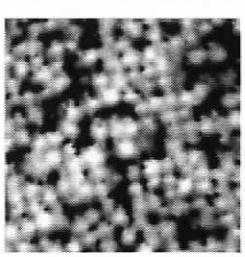

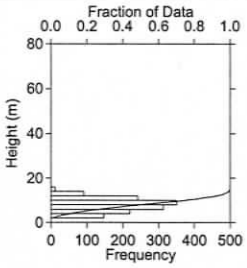

P18 (Y)

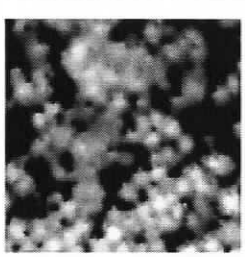

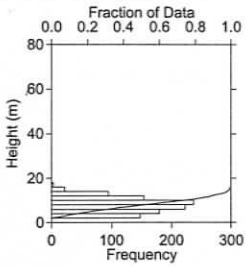

P19 (Y)

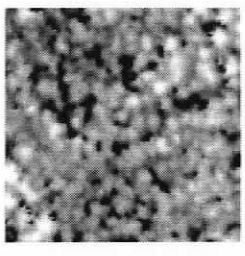

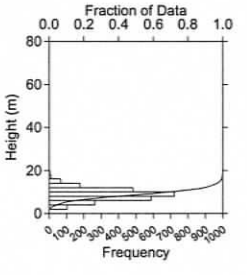

P20 (Y)

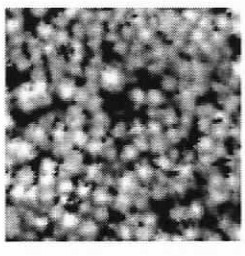

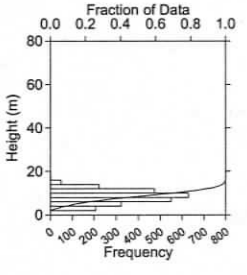

P21 (Y)

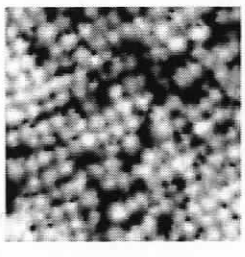

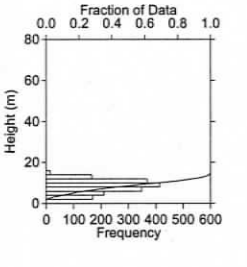

P22 (Y)

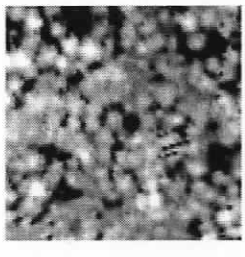

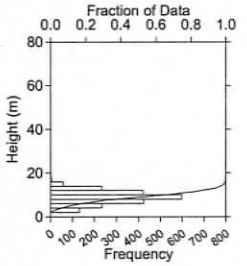

P23 (Y)

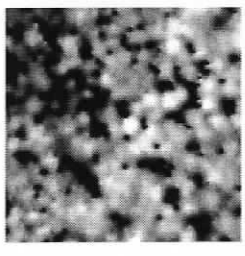

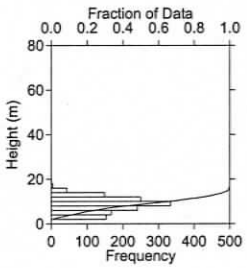

P24 (Y)

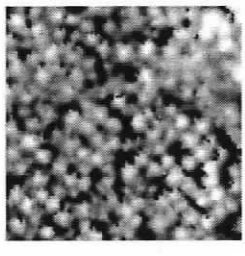

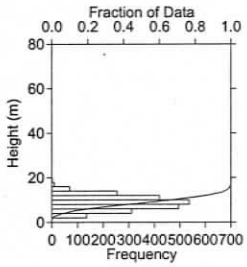

P25 (Y)

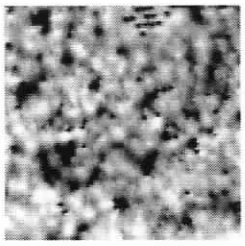

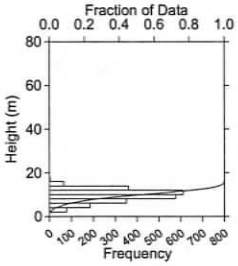

P26 (Y)

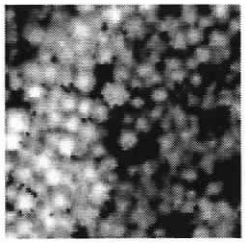

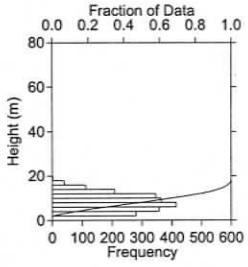

P27 (Y)

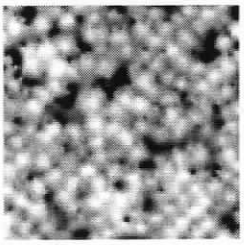

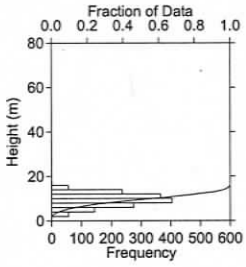

P28 (Y)

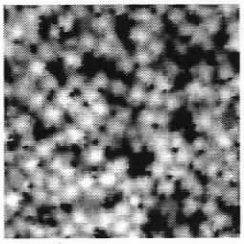

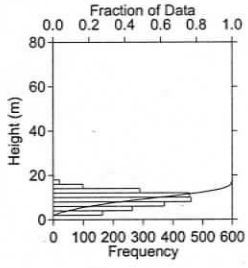

P29 (Y)

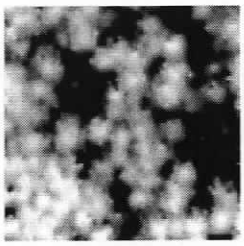

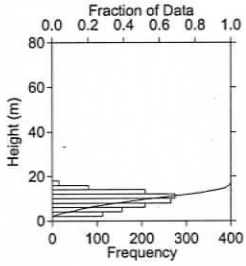

P30 (Y)

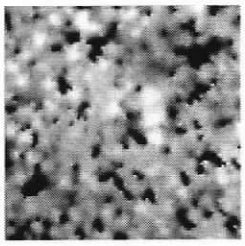

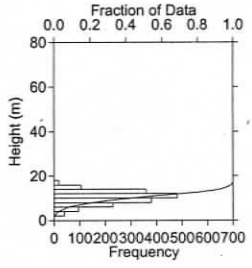

P31 (Y)

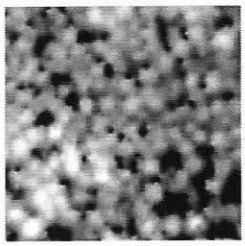

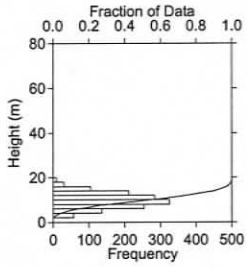

P32 (Y)

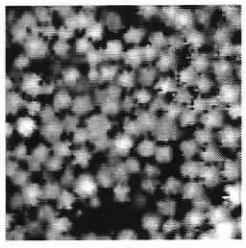

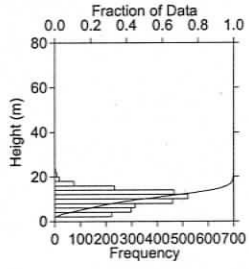

P33 (Y)

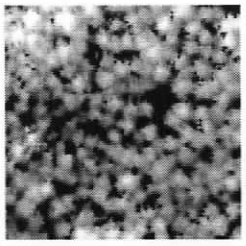

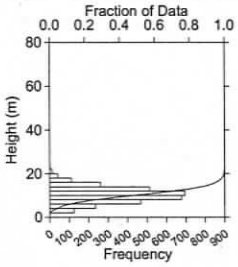

P34 (Y)

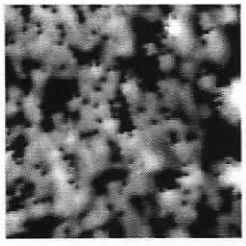

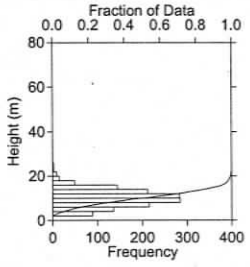

P35 (Y)

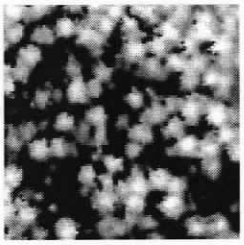

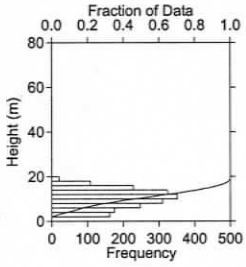

P36 (Y)

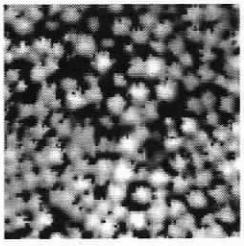

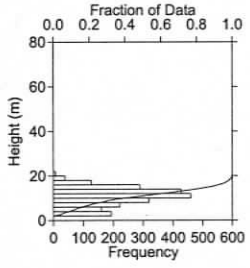

P37 (Y) (Ground Reference)

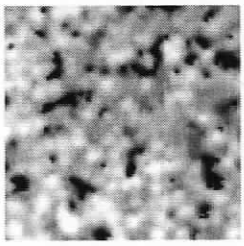

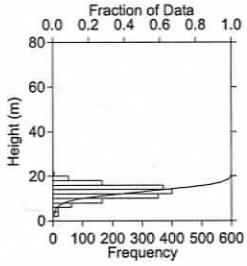

P38 (Y)

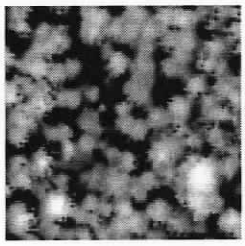

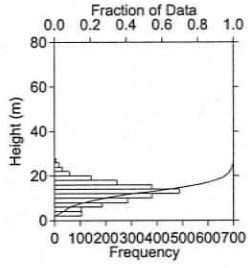

P39 (Y)

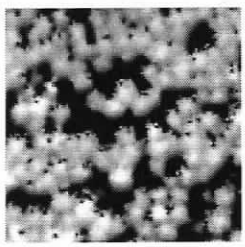

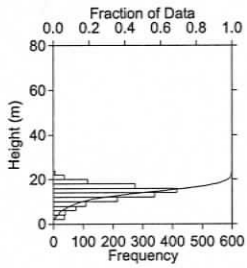

P40 (Y)

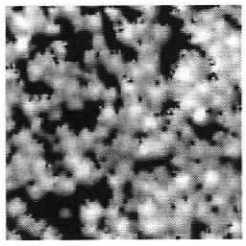

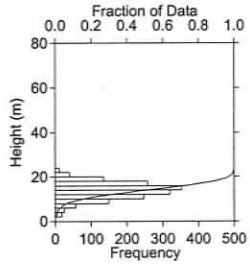

P41 (Y)

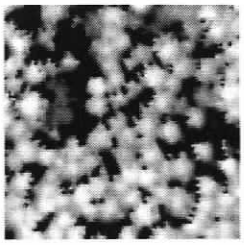

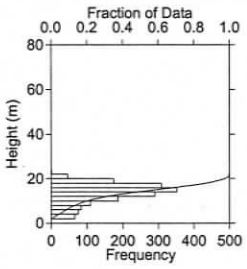

P42 (Y)

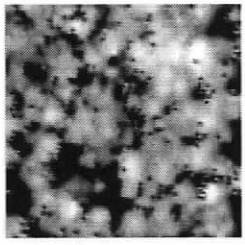

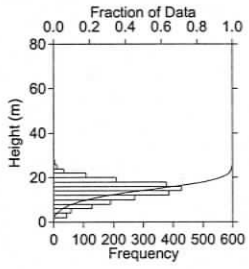

P43 (Y)

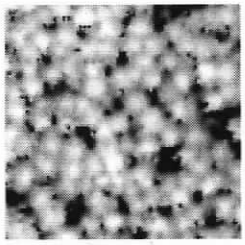

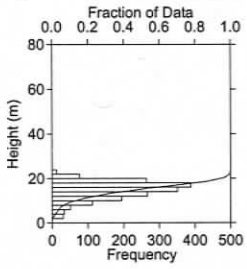

P44 (Y)

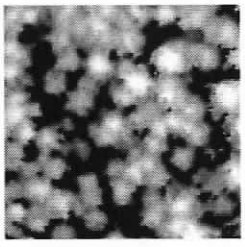

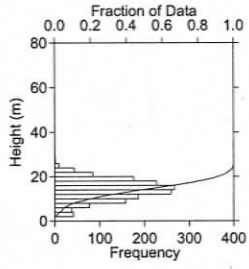

P45 (Y)

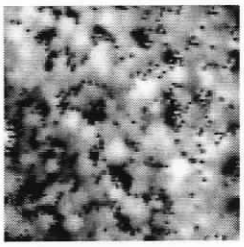

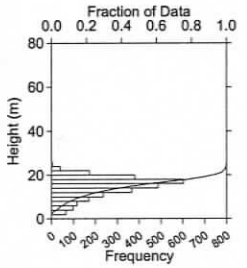

P46 (Y)

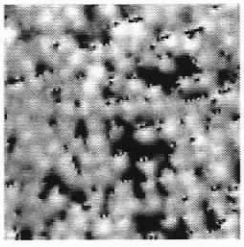

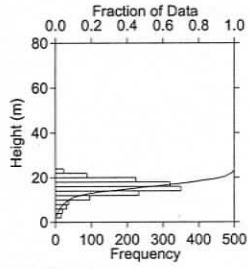

P47 (M)

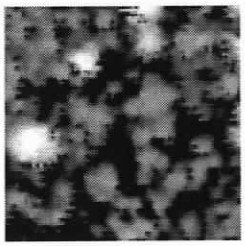

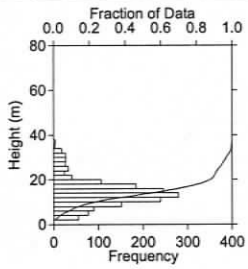

P48 (Y)

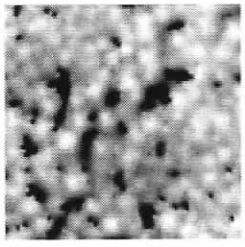

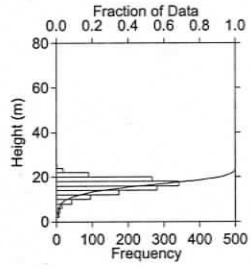

P49 (Y)

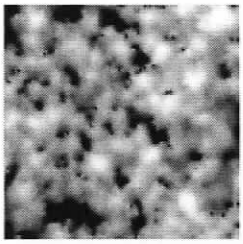

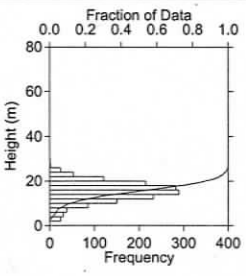

P50 (Y)

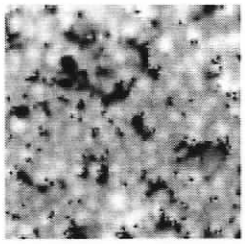

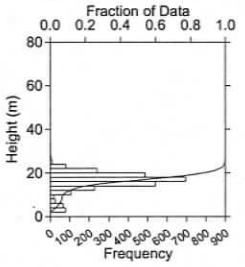

P51 (M) (Ground Reference)

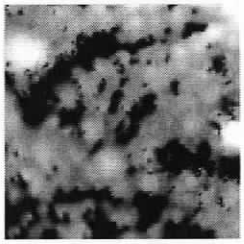

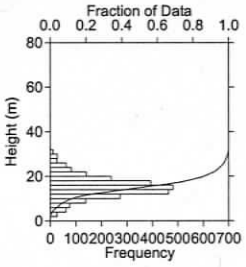

P52 (Y)

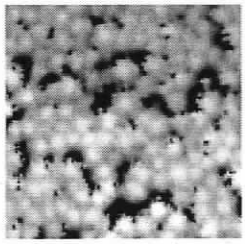

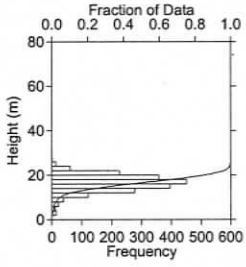

P53 (Y) (Ground Reference)

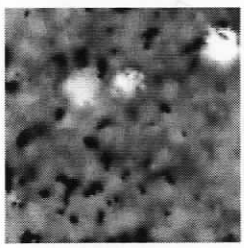

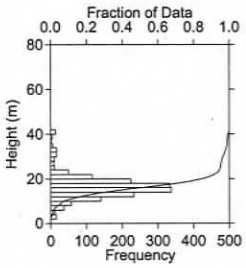

P54 (Y)

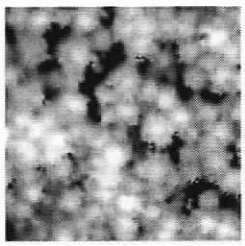

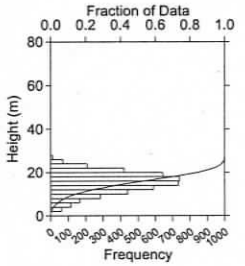

P55 (M)

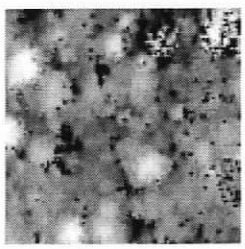

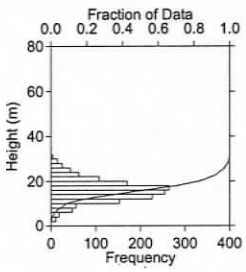

P56 (Y)

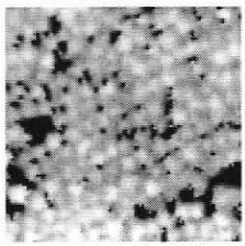

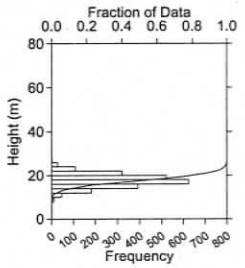

P57 (Y) (Ground Reference)

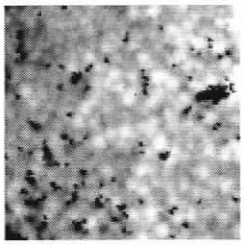

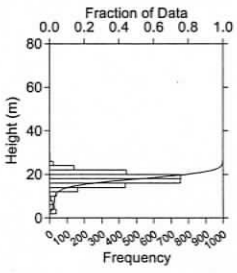

P58 (Y)

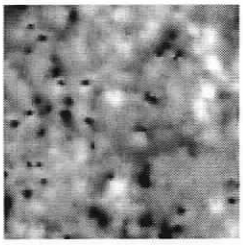

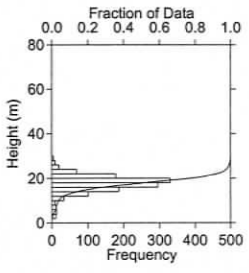

P59 (Y) (Ground Reference)

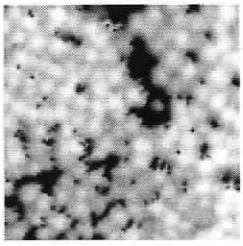

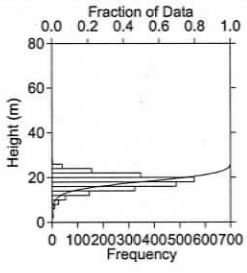

P60 (Y)

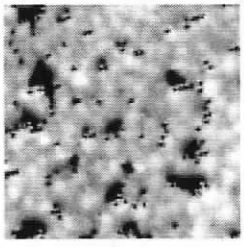

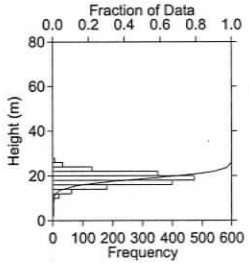

P61 (Y)

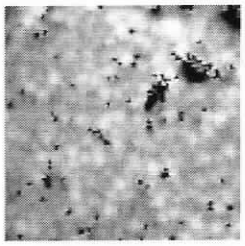

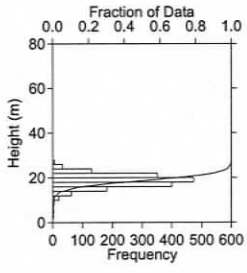

P62 (Y) (Ground Reference)

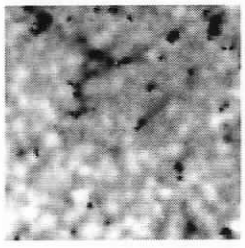

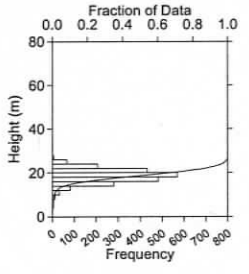

P63 (Y)

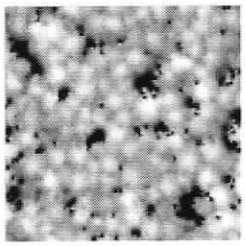

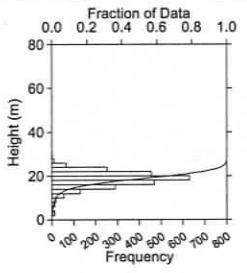

P64 (Y)

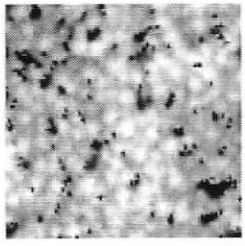

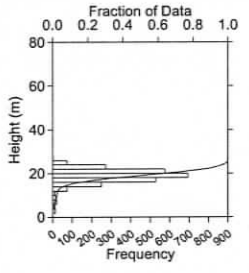

P65 (Y)

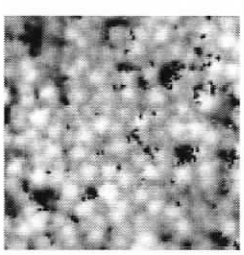

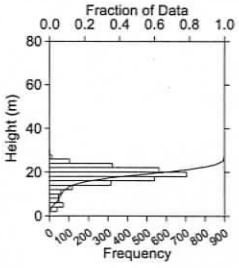

P66 (Y)

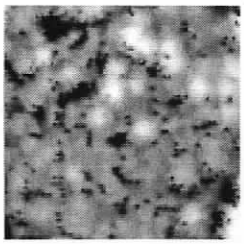

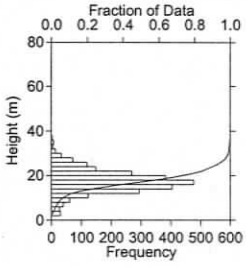

P67 (Y)

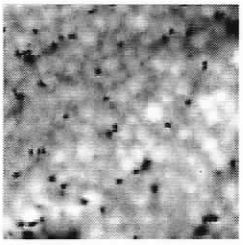

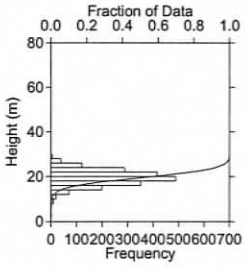

P68 (Y)

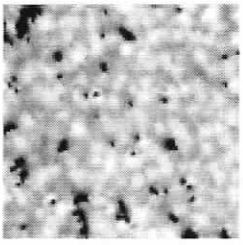

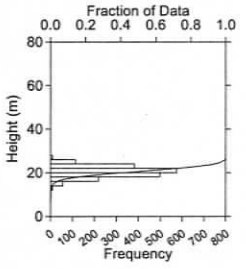

P69 (Y)

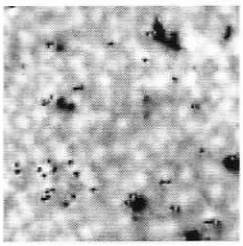

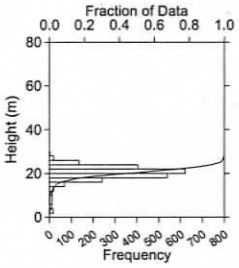

P70 (Y)

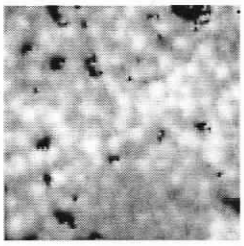

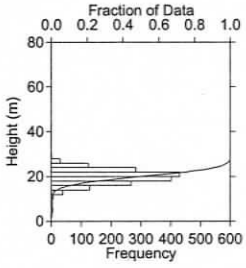

P71 (M)

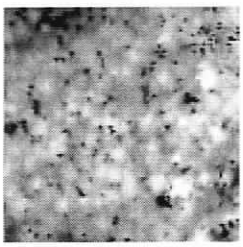

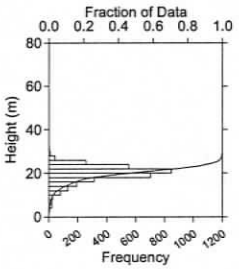

P72 (Y)

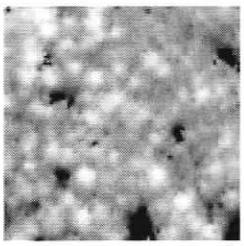

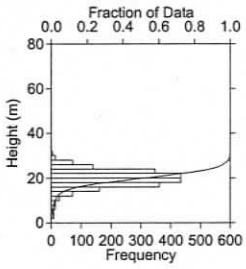

P73 (M)

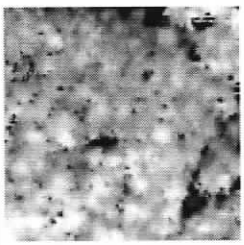

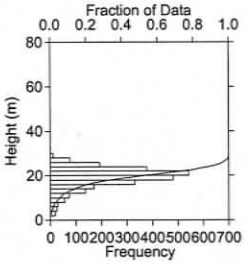

P74 (M)

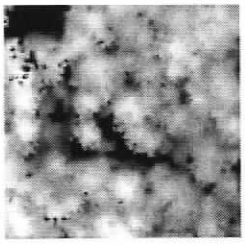

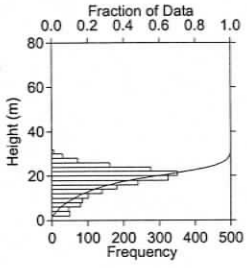

P75 (M)

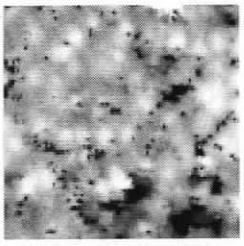

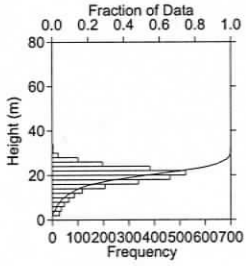

P76 (Y)

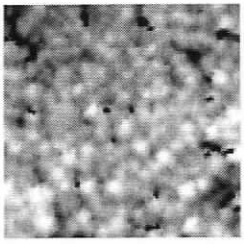

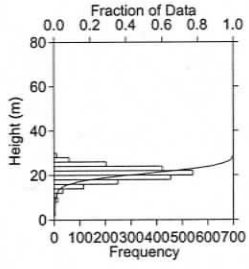

P77 (M) (Ground Reference)

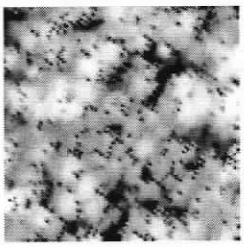

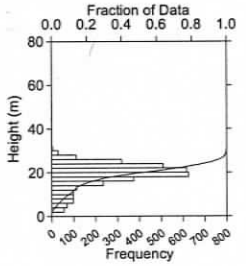

P78 (Y)

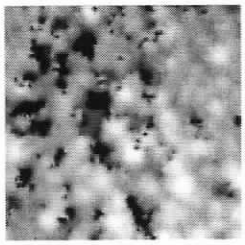

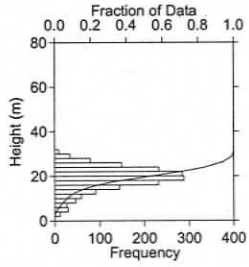

P79 (O) (Ground Reference)

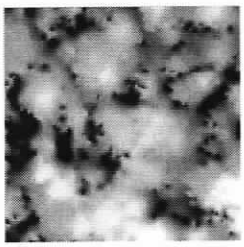

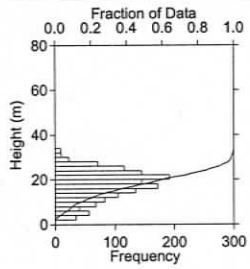

P80 (Y)

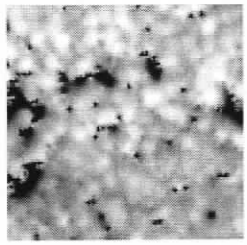

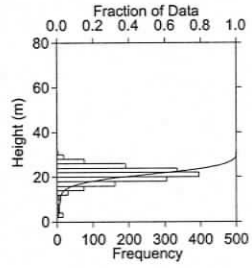

P81 (M)

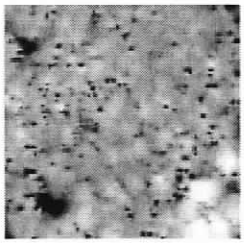

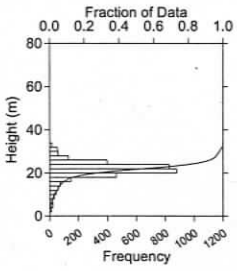

P82 (Y)

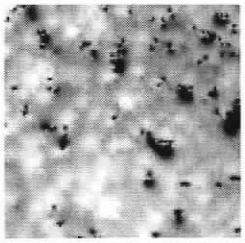

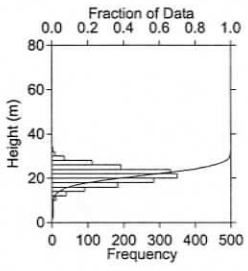

P83 (M)

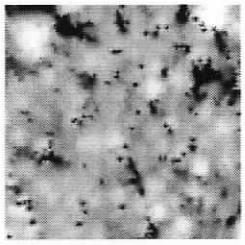

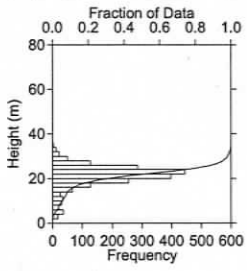

P84 (M) (Ground Reference)

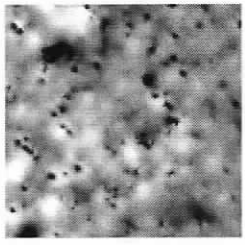

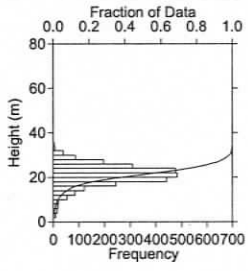

P85 (M)

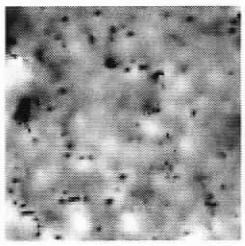

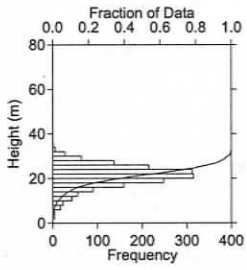

P86 (Y)

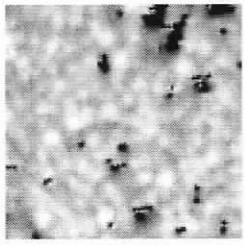

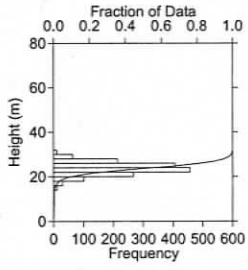

P87 (O) (Ground Reference)

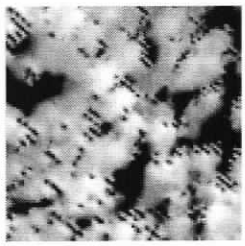

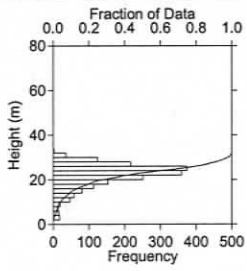

P88 (Y)

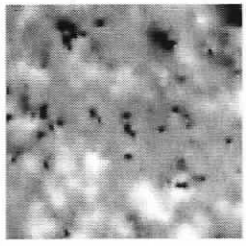

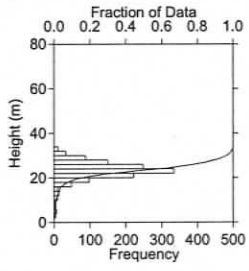

P89 (M)

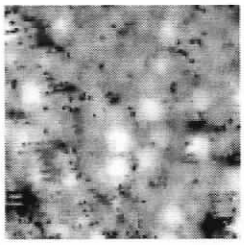

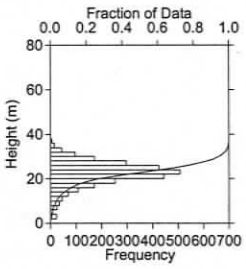

P90 (O)

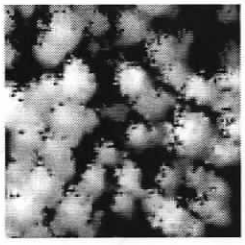

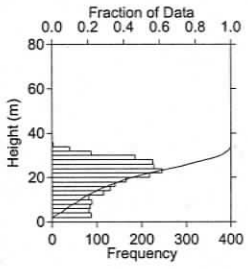

P91 (M)

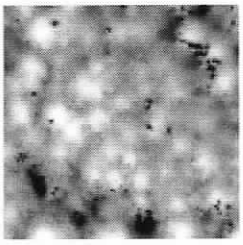

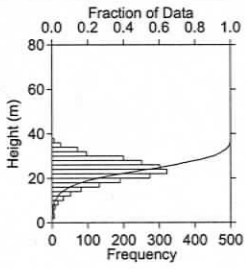

P92 (O)

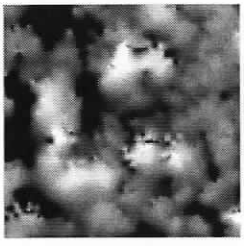

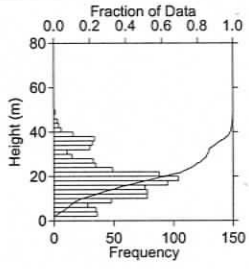

P93 (M)

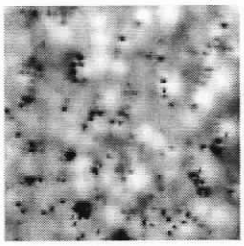

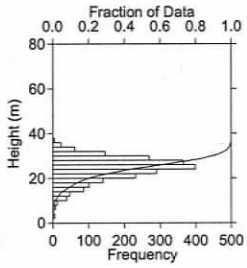

P94 (M)

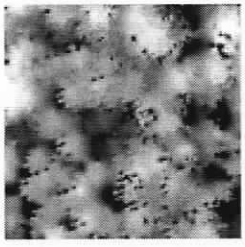

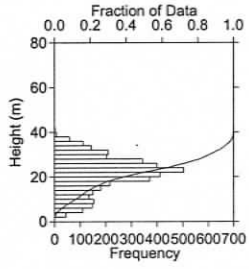

P95 (M)

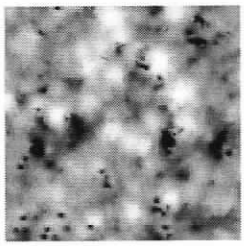

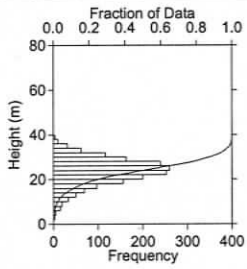

P96 (M) (Ground Reference)

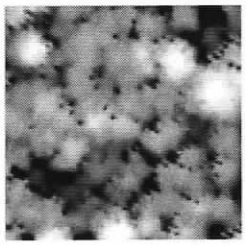

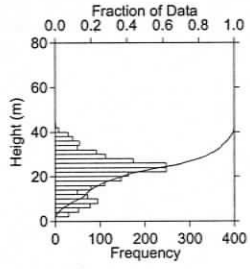

P97 (M) (Ground Reference)

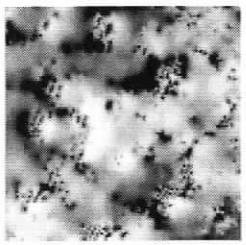

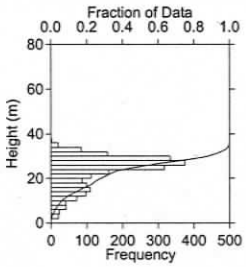

P98 (M)

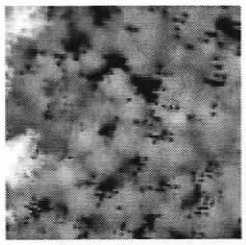

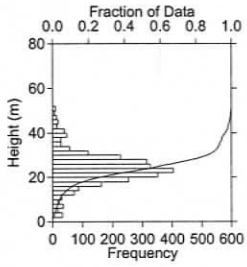

P99 (M)

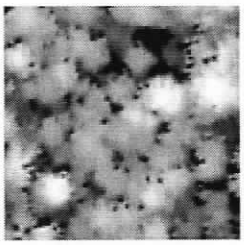

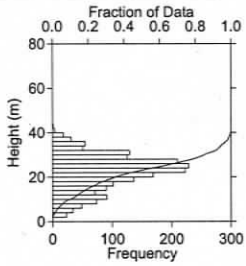

P100 (O)

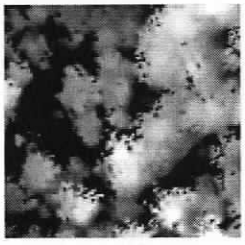

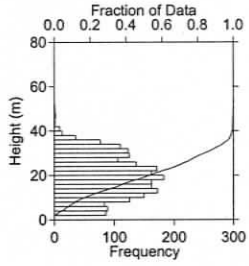

P101 (O)

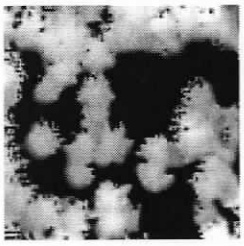

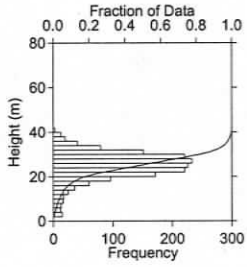

P102 (M)

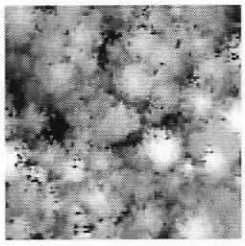

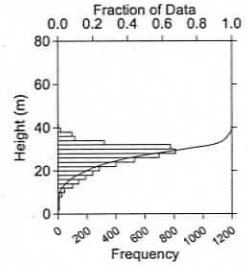

P103 (M)

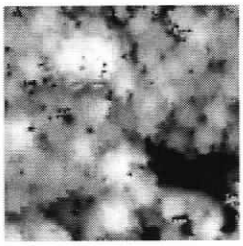

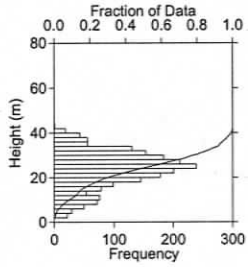

P104 (O)

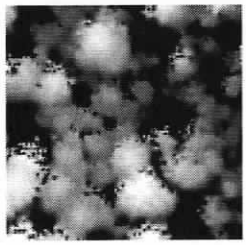

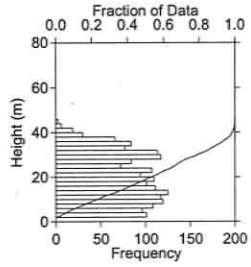

P105 (M)

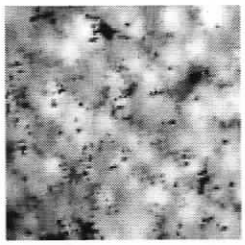

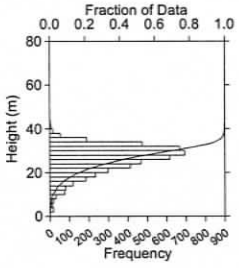

P106 (M)

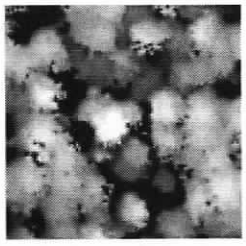

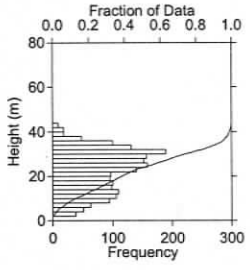

P107 (M)

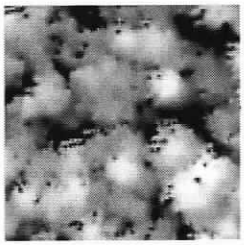

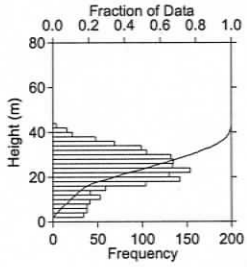

P108 (O)

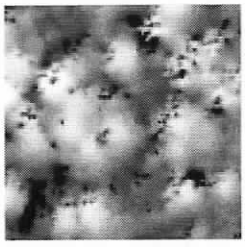

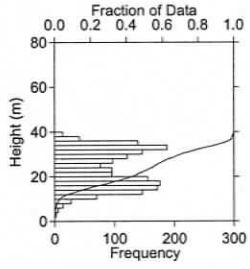

P109 (O)

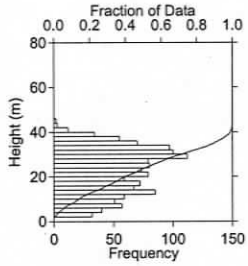

P110 (M)

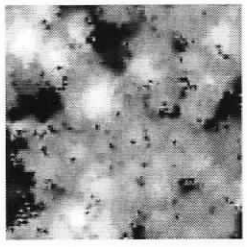

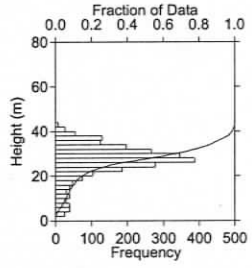

P111 (O)

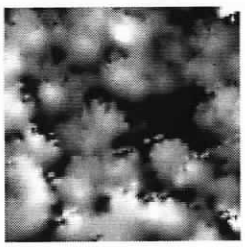

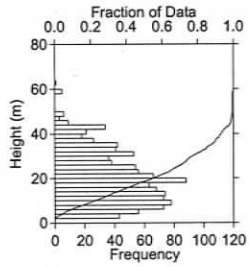

P112 (O) (Ground Reference)

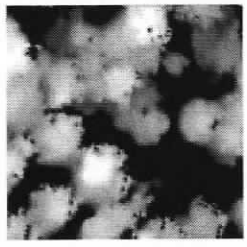

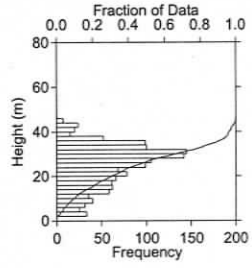

P113 (O)

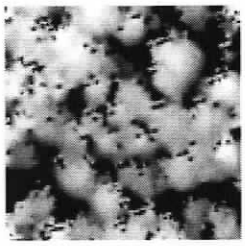

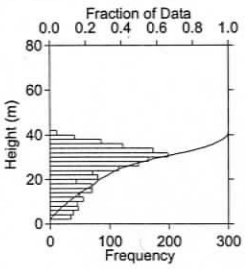

P114 (O)

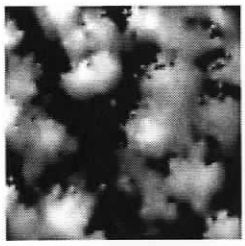

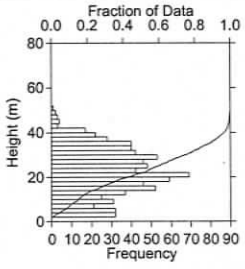

P115 (M)

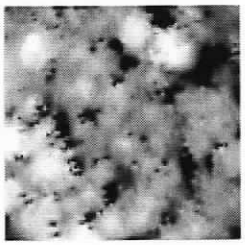

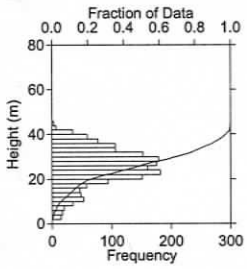

P116 (O)

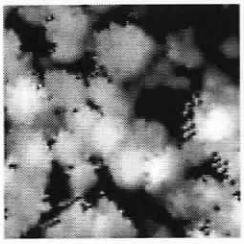

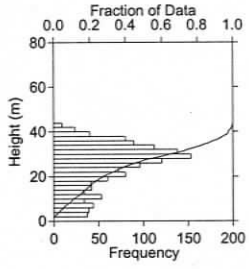

P117 (O) (Ground Reference)

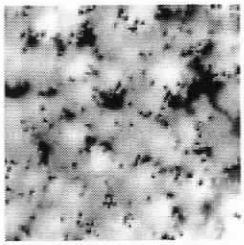

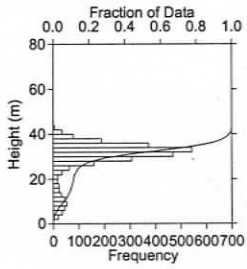

P118 (O)

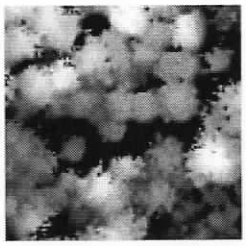

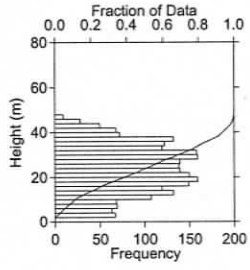

P119 (O)

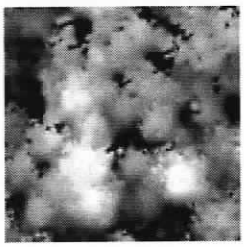

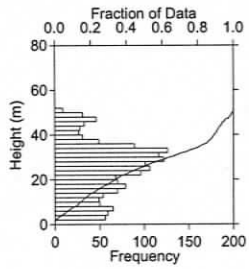

P120 (O)

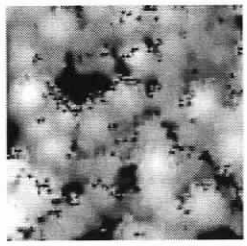

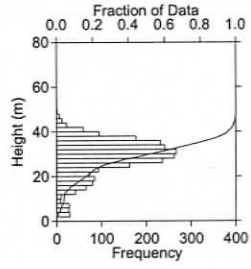

P121 (O) (Ground Reference)

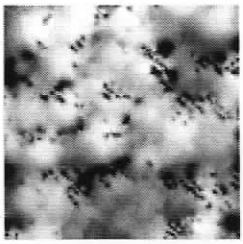

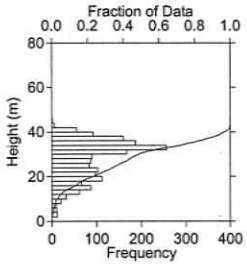

P122 (O)

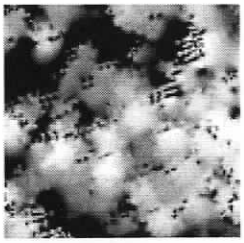

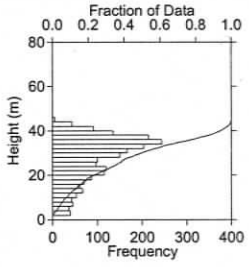

P123 (O)

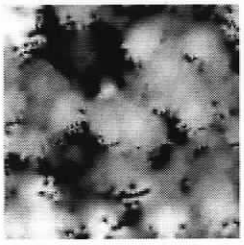

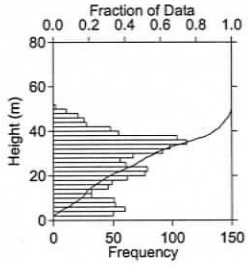

P124 (O)

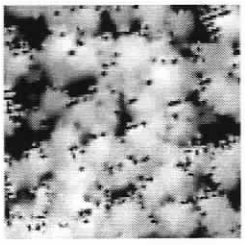

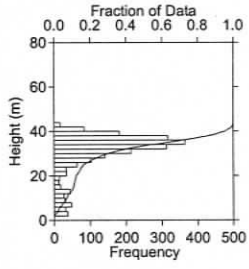

P125 (O)

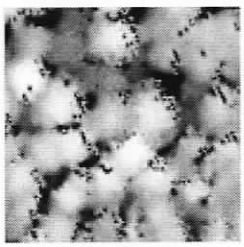

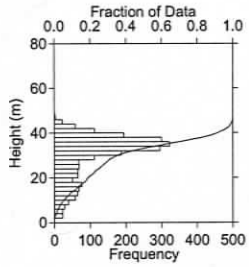

P126 (O)

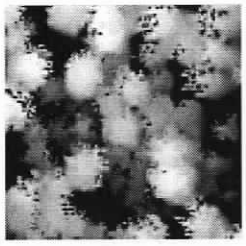

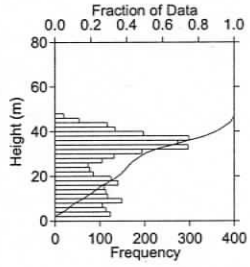

P127 (O)

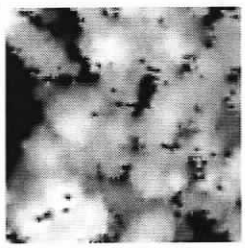

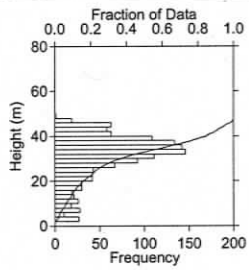

P128 (O)

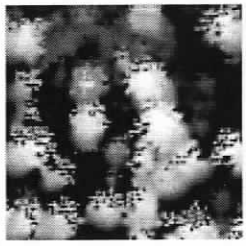

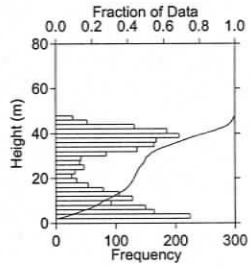

P129 (O)

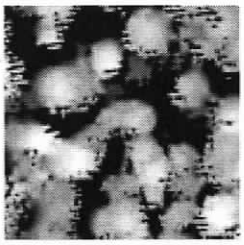

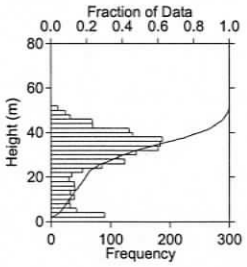

P130 (O)

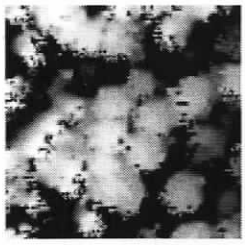

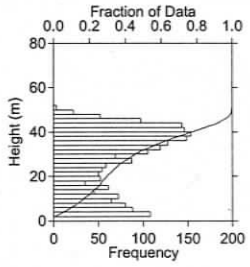

P131 (O)

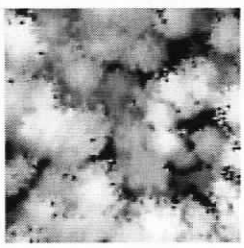

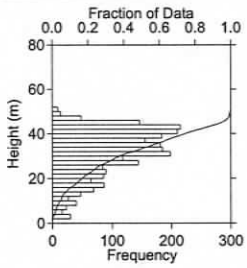

P132 (O)

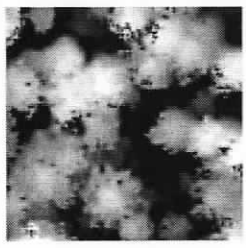

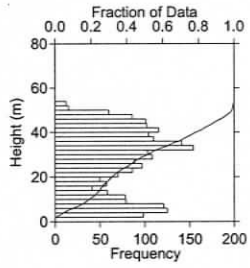

P133 (O)

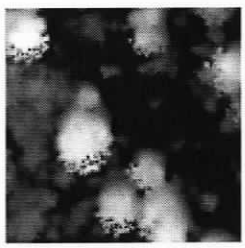

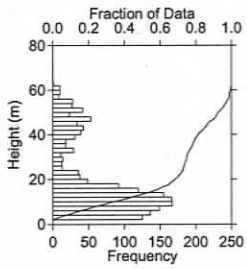

P134 (O)

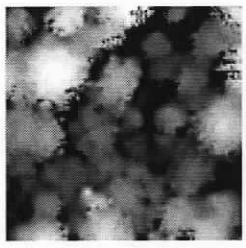

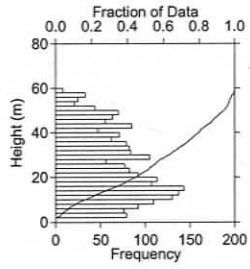

P135 (O) (Ground Reference)

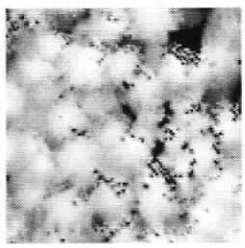

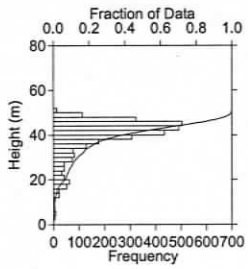

P136 (O)

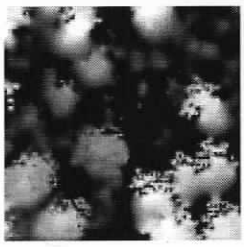

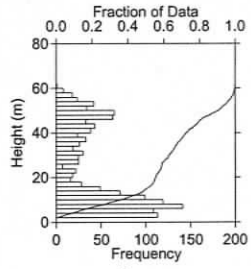

P137 (O)

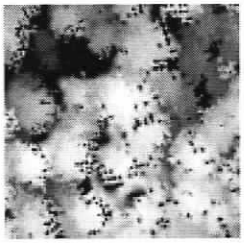

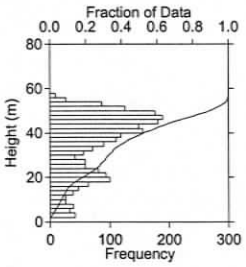

P138 (O)

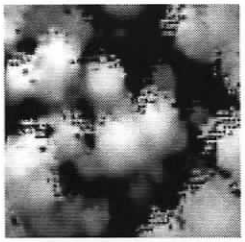

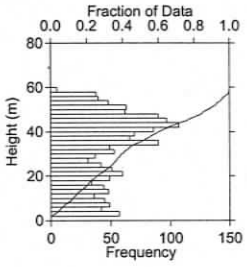

P139 (O)

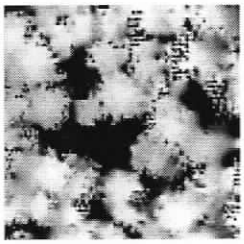

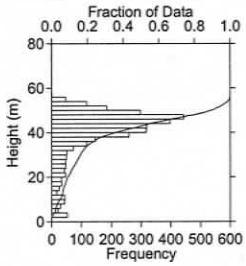

P140 (O)

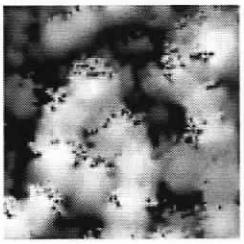

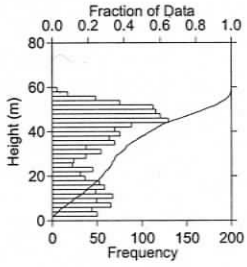

P141 (O)

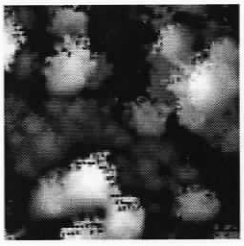

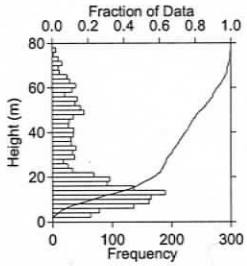

P142 (O)

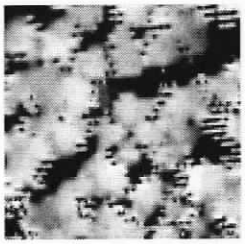

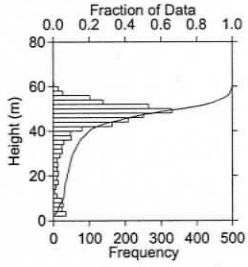

P143 (O)

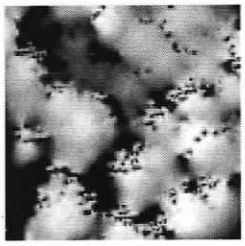

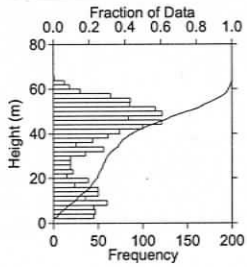

P144 (O)

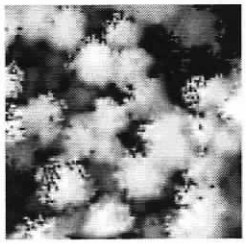

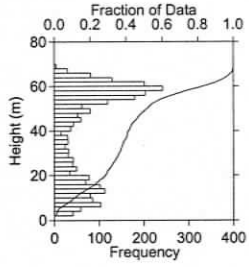

P145 (O)

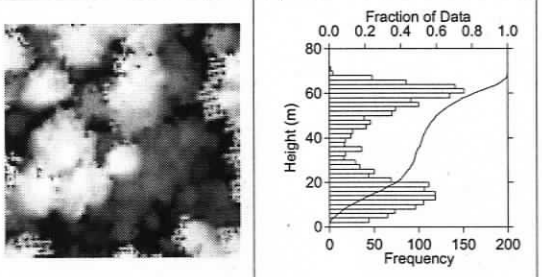

P146 (O)

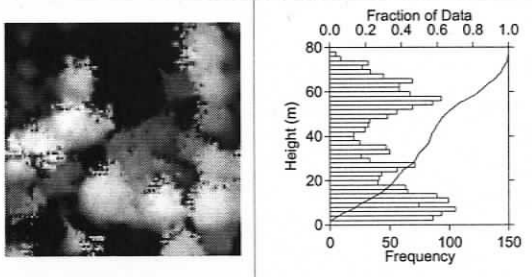

P147 (O)

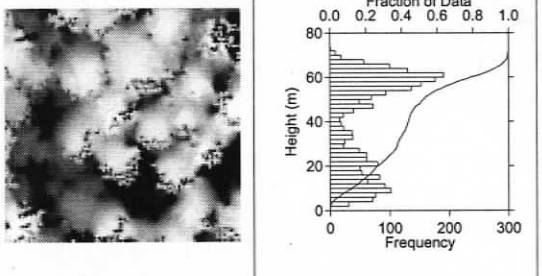

P148 (O)

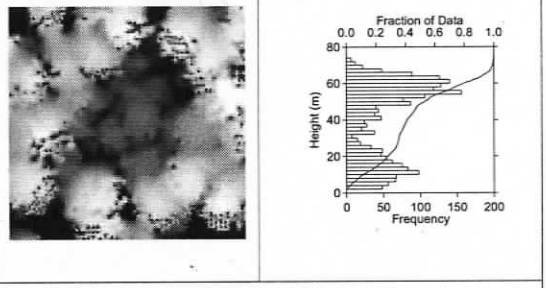

P149 (O)

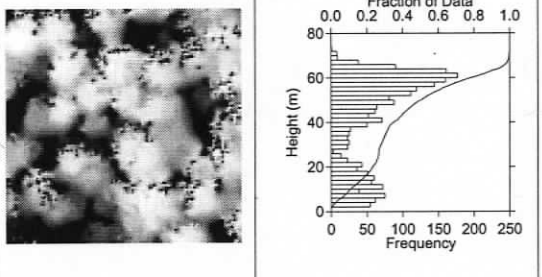

P150 (O)

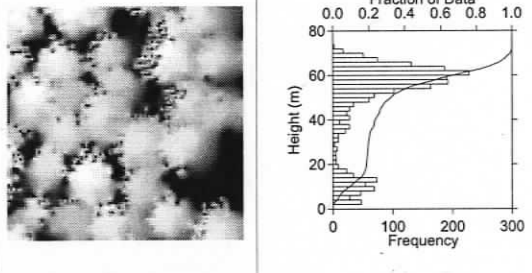

P151 (O)

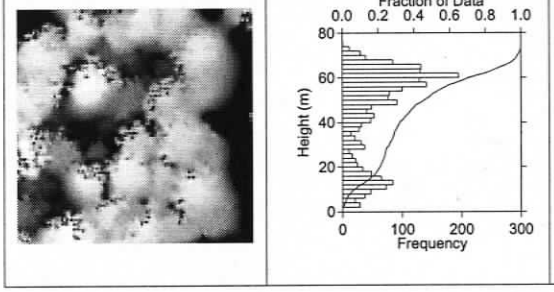

P152 (O)

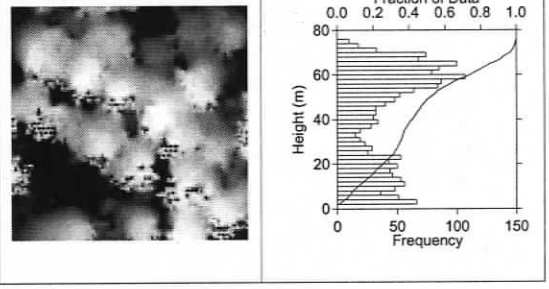

Appendix 4B

An example of k-means partitioning (k = 8) results for a spatially contiguous LiDAR dataset collected over Sooke Lake and Goldstream watersheds (13,986 hectares) during August 2006.

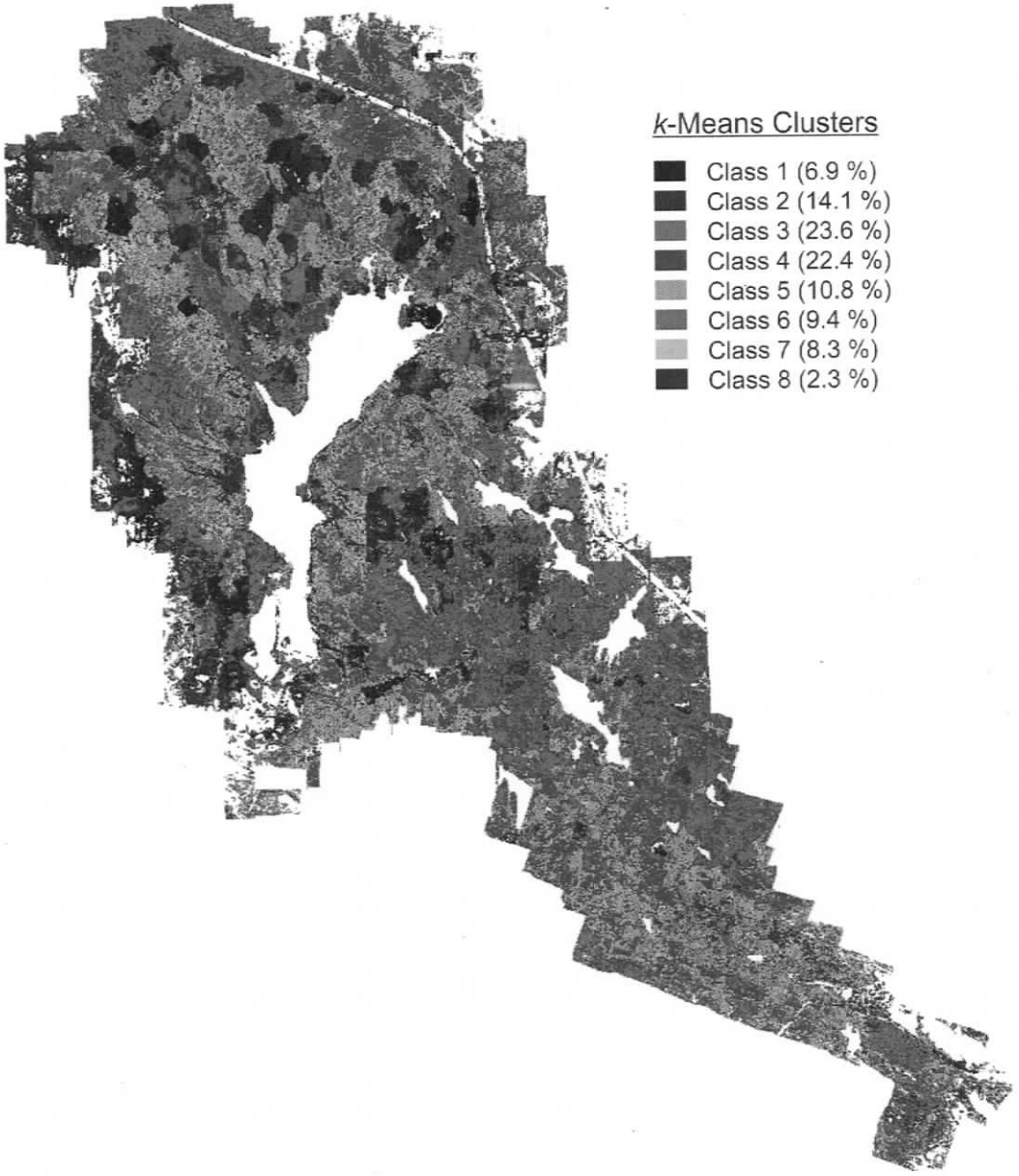

FIGURE 4B.1. Results of a non-hierarchical cluster analysis by *k*-means partitioning ($k = 8$). The dataset included six LiDAR-derived attributes of canopy structure extracted from 349,655 spatially contiguous grid cells (20 m) covering 13,986 hectares of Sooke Lake and Goldstream watersheds (see Fig. 4.1 for location, direction, and scale information). The attributes included in the analysis were $Lh_{0.85}$, rugosity (standard deviation of *Lh*); second (coefficient of variation, COV), third (skewness), and fourth (kurtosis) *L*-moments (see, Hosking, 1990), and the canopy gap fraction $[(100 - CC_{0.25})/100\%]$ computed for relative height $f = 0.25$. Canopy structural properties of each *k*-means class are summarized in Fig. 4B.2. Class 8 may represent very old stands occupied by fire refugia.

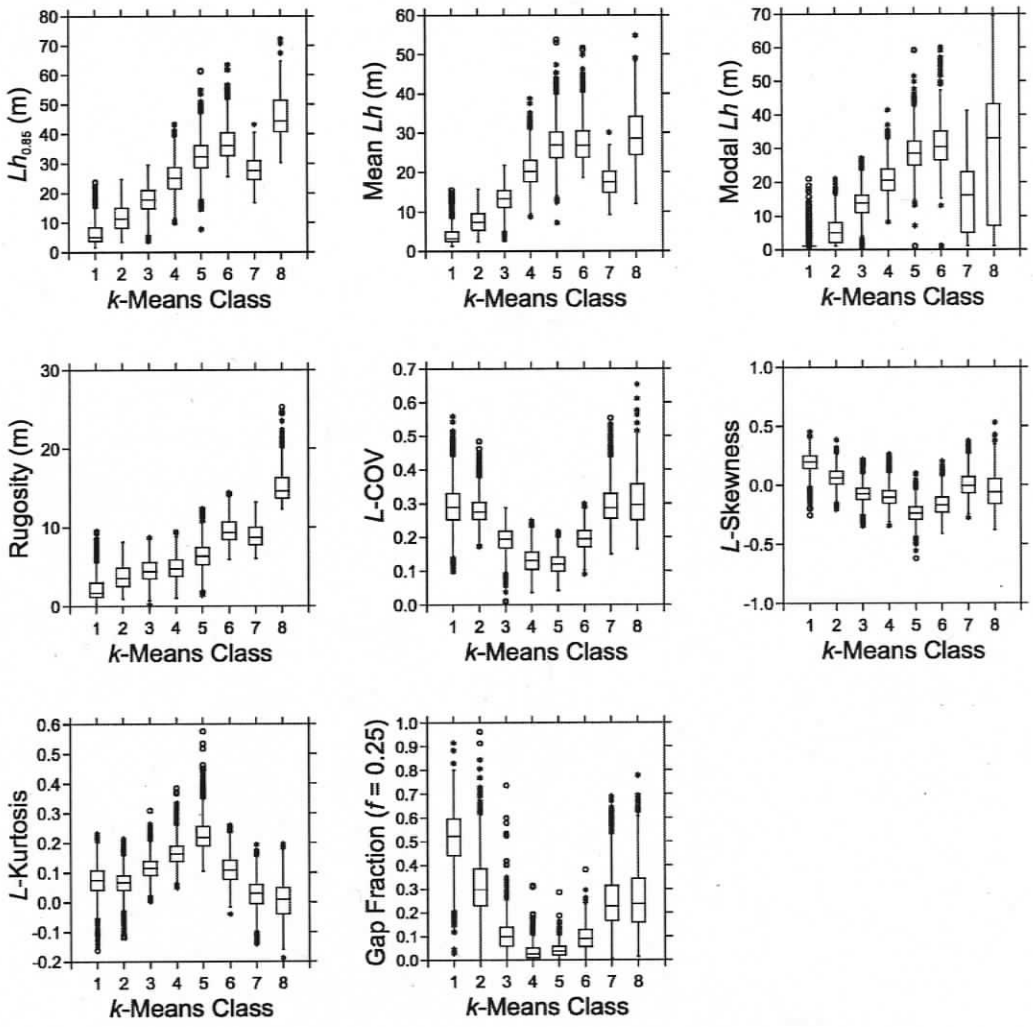

FIGURE 4B.2. k-means classes were assigned by order of ascending height ($Lh_{0.85}$). Close inspection of Class 7 showed that this cluster was contaminated by many sample plots (cells) found at the boundary between tall, old forests and very young, regenerating plantations. The value of k = 8 was assigned based on the optimal number (k = 7 to 9) determined for the smaller n = 152 dataset presented in this study. However, substantial within-cluster heterogeneity suggested that k = 8 was not the best partition for this dataset. Nevertheless, changes (trends) in all variables with increasing canopy height are consistent with the differences found among age classes (see Sections 4.4.2 and 4.4.3). For example, as canopy height increases from Class 1 to Class 5, kurtosis increases, while COV, skewness, and gap fraction decline as the canopy 'lifts', infills, and differentiates—the 'closure and expansion' phases (Nadkarni et al., 2004). The abrupt rise in COV, skewness, and gap fraction, as well as a decline in kurtosis and modal height between Classes 5 and 8 marked the onset of maturation (Franklin et al., 2002) and the development of marked spatial heterogeneity in vertical and horizontal patterns of canopy structure—the 'canopy elaboration' phase (Nadkarni et al., 2004).

CHAPTER 5

Conclusions and Future Directions

Forest structure is regarded as a unifying variable and key ecological indicator in conservation biology, ecosystem science, and sustainable forest management, because of its strong link to habitat, ecosystem function, and timber production. This dissertation research focused explicitly on the development of ecologically relevant remotely sensed measurements of angular, vertical, and horizontal patterns of forest canopy structure at fine spatial scales. Forest canopy structure is defined by the size, shape, number, and variety of all aboveground vegetational components, such as foliage, branches, and boles, and their spatial distribution in space and time. Fine-scale patterns of forest canopy structure play key roles in the regulation of forest microclimates, light interception, photosynthesis, and plant production; biosphere–atmosphere exchanges of energy, matter, and traces gases; nutrient and hydrological cycles; stand dynamics; and the provision of critical habitat for many species. Fine-scale patterns, processes, and dynamics naturally scale across larger aggregates of space and time, and therefore also contribute to regional and global scale ecological patterns, processes, and dynamics.

Hemispherical canopy photography provides a permanent 2-D record of the angular distribution of foliage, branches, boles, and gaps, and therefore allows considerable opportunity to quantify various aspects of fine-scale canopy structure and its influence on light capture, plant production, microclimate, and stand dynamics. The element-clumping index $\Omega(\theta)$ is a zenith-angle-dependent measure of spatial aggregation (clumping) integrated across three major levels of canopy organization (i.e., the clumping of foliage within branches, crowns, and stands). $\Omega(\theta)$ equals one when foliage (flat leaves or needle shoots) is randomly distributed at view (zenith) angle θ; it approaches zero when foliage is perfectly clumped, and will be greater than one when foliage is uniformly spaced. Stand age, species composition, site productivity, and disturbance history have a strong impact on the magnitude of $\Omega(\theta)$ and its pattern of change across the full range of zenith angles ($0 \leq \theta \leq 90°$). Foliage clumping alters the size-frequency and spatial

distributions of forest canopy gaps, and therefore strongly influences light capture and penetration into lower canopy layers.

Benoît Mandelbrot developed the concept of 'lacunarity' to describe the disparate gap (void) structures observed in different geometrical patterns that shared the same fractal dimension. Spatial pattern is inherently scale dependent, and lacunarity analysis was specifically designed to quantify and visualize the nature of this dependency across a broad range of measurement scales. Forest canopies also display unique, scale-dependent gap (empty space) or patch (filled space) structures within one or more spatial dimensions. In Chapter 2, lacunarity analysis was used to derive zenith-angle-dependent (local) estimates of $\Omega(\theta)$ from hemispherical canopy photographs, while numerical integration of $\Omega(\theta)$ across all zenith angles θ provided a global measure of Ω. Inclusion of lacunarity-derived estimates of $\Omega(\theta)$ into the Beer-Lambert equation improved optical estimates of LAI, but could not completely eliminate the negative effect of clumping. Four main explanations were given for this shortcoming: (1) element clumping is explicitly a 3-D spatial phenomenon, which cannot be fully characterized by 2-D angular data; (2) clumping eliminates the small canopy gaps needed to accurately predict $P(\theta)$; (3) hemispherical canopy photography lacks the spatial and spectral resolution needed to identify the finest canopy gaps; (4) $G(\theta)$ is also inherently scale dependent when $\Omega(\theta) < 1$ (i.e., $P(\theta)$ is strongly influenced by leaf, branch, and crown angles), and may therefore be poorly specified by Miller's theorem or at $\theta = 57.5°$.

Solutions to these methodological weaknesses are varied. For example, ground-based 3-D imaging lasers could provide full 3-D datasets for analysis (Danson et al., 2007; Omasa et al., 2007), but may be limited to short, low-density stands with sparsely vegetated understories (Van der Zande et al., 2006). Mounting these instruments on a stable platform (e.g., scaffold, tower, crane, etc.) with mobility in the vertical dimension may improve their effectiveness in tall canopies. Non-fisheye lens configurations, higher image resolutions (spatial and spectral), alternative sampling strategies (e.g., random sampling using a longer focal-length optical lens or range-finding laser at $\theta = 57.5°$), and more sophisticated inversion models may also help to improve in situ optical measurements of LAI. Nevertheless, optical-based estimates of $\Omega(\theta)$ should be considered a valuable complement to traditional measurements of canopy openness (CO),

since the same CO can be accompanied by an infinite variety of gap-size distributions and spatial arrangements (Fig. 2.1). Variation in the magnitude, scale, and angular pattern of foliage clumping is an important source of spatial heterogeneity that influences the location, timing, and rate of many key canopy processes and functions. Hemispherical photographs contain a rich variety of spatial information that has so far been underexploited. Future studies need to focus more closely on the development of statistical methods that can be used to characterize this richness (e.g., Walter and Grégoire, 1996; Melloh et al., 2003; Montes et al., 2007).

In Chapter 3, lacunarity analysis was extended from multiscale statistical descriptions of 1-D binary sets to 2-D quantitative fields of simulated canopy heights. A simulation approach provided strict control over geometrical and spatial properties of the canopy and its internal stand structure. It also allowed for rapid development of a well-documented dataset that covered a broad range of forest canopy structures (Appendix 3). Lacunarity analysis was used to quantify the spatial heterogeneity found in the horizontal distribution of canopy heights at nine discrete observation scales. Principal component analysis (PCA) reduced the high dimensionality of this dataset into two orthogonal, synthetic variables (PC1 and PC2). PC1 captured 89.3% of the total variance contained in the original dataset, and was strongly correlated ($R^2 = 0.84$) with the canopy gap fraction (or inversely, canopy cover). PC2 accounted for 9.1% of the total variance, and was associated with the scale-dependent pattern (uniform, random, or aggregated) found within the array of continuous canopy heights. Therefore, much of the information contained in these multiscale lacunarity statistics was inherently aspatial and related to the magnitude of the canopy gap fraction. The remaining information, in contrast, was dominantly spatial in nature and related to the scale-dependent arrangement of canopy heights.

Ordination is an effective statistical tool used for multivariate data reduction, visualization, and interpretation. Unconstrained, distance-preserving techniques like PCA maintain the Euclidean distances (dissimilarities) that occur among sample units in their original dimensions of multivariate space, while ordination graphs (2-D scatterplots or matrices) provide simple graphical summaries of these dissimilarity data. Here, ordination graphs showed how sample units varied along multivariate gradients of

canopy cover, texture, and spatial pattern, and may therefore provide a basis for assessing the natural variability of forest canopy structure, as well as the influence of silvicultural manipulations and other management prescriptions on forest patterns (Lundquist and Beatty, 1999). Euclidean or other metric distance-based estimates of dissimilarity (or proximity) computed among samples or groups of samples (e.g., stand age or structural classes) may also serve as useful quantitative measures of beta (stand) and gamma (landscape) levels of structural diversity (Anderson et al., 2006). Further work is needed to (1) recover meaningful quantitative spatial attributes from scale-dependent estimates of lacunarity; (2) identify optimal ordination and distance-based statistical techniques that would allow for the reliable assessment and comparison of canopy structure and its range of variability across the landscape; (3) understand how lacunarity-based estimates of spatial heterogeneity relate to other ecologically relevant patterns of forest composition, structure, and function.

In the final study (Chapter 4), a detailed methodology was presented that showed how airborne discrete-return LiDAR data could be used to characterize vertical and horizontal patterns of forest canopy structure at fine spatial scales. This methodology was demonstrated using a few discontinuous LiDAR flight lines located over young to old Douglas-fir/western hemlock forests located on southeastern Vancouver Island, British Columbia. Vertical canopy structure was characterized by statistical measures of location (85th percentile of LiDAR canopy height), scale (Gini coefficient), and shape (skewness, kurtosis, Shannon's diversity and evenness indices) derived from the distribution of LiDAR canopy heights sampled within a 50 × 50 m (0.25 ha) sample plot. Lacunarity analysis along with two other derivative statistics (dominant scale of pattern, and integral of the normalized lacunarity curve) were used to describe the spatial scale, texture, and pattern of canopy structure in the horizontal dimension. This multivariate dataset was further used to investigate the general structural characteristics and differences found among young to old Douglas-fir/western hemlock forest canopies, as well as to partition sample units into an optimal number of relatively homogeneous groups based solely on the vertical and horizontal arrangement of canopy structure.

Quantile-based estimates of distributional location (85th percentile of LiDAR canopy height, $Lh_{0.85}$) and shape (skewness, *SK*, and kurtosis, *KR*) were computed

because of their statistical robustness, computational simplicity, and widespread use in LiDAR-based predictive modelling of other stand-level forest inventory attributes (i.e., height, basal area, stem density, and volume). Shannon's diversity (H) and evenness (J) indices were also used to describe distributional shape; however, these attributes were highly correlated with $Lh_{0.85}$, and their computation required the arbitrary conversion of continuous canopy heights to frequency count data. Neither index is therefore recommended for use when direct measurements of canopy height are available. Quantile-based estimates of SK and KR provided reliable separation between sample units in reduced ordination space; however, further experimentation by G. Frazer (not presented in this dissertation) revealed high cell-to-cell variation in both these variables when applied to a regularized grid of spatially contiguous sample cells. L-moments, 'trimmed' L-moments, LQ-moments, and other alternative robust moment estimators should therefore be evaluated as alternatives to the quantile-based third and fourth moments implemented in this study.

Log-transformed quantiles (q) of LiDAR canopy height Lh_q were maximally linearly correlated ($0.64 \leq R^2 \leq 0.99$) with log-transformed field-measured attributes of stand structure (i.e., stand height, quadratic mean diameter, basal area, stem density, and volume) at values of q ranging from 0.74 to 0.92 (mean $q = 0.85 \pm 0.06$ s.d.). Estimates of Lh_q at $0.8 \leq q \leq 0.9$ appeared to be well correlated with the modal canopy height in single-layered (unimodal) canopies and the upper (overstory) modal height in multi-layered (multimodal) canopies (see Appendix 4A). LiDAR-based estimates of canopy cover (CC_{LiDAR}) were also strongly linearly correlated ($R^2 = 0.93$) with ground-based estimates of canopy cover measured indirectly with the LAI-2000 Plant Canopy Analyzer (CC_{PCA}). The inclusion of both Lh_q and CC_{LiDAR} (or CC_f) as independent variables in linear regression models significantly improved the prediction ($0.85 \leq R^2 \leq 0.96$) of field-measured attributes of quadratic mean diameter, basal area, stem density, and volume. Model specification is likely to be further improved by including estimates of Lh_q and CC_f computed at different values of q and f. Ordination techniques, such as PCA, may well facilitate the improved selection of an optimal set of predictor variables by identifying measures of Lh_q and CC_f that are weakly intercorrelated, yet capable of explaining most of the variance within the dataset.

Log-transformed estimates of the lacunarity statistic $\Lambda(r = 0.5$ m or 1 grid cell unit) were maximally negatively and nonlinearly correlated ($R^2 = 0.96$) with canopy cover (CC_f) at relative canopy height $f = 0.2$, and also positively and nonlinearly correlated with PGV ($R^2 = 0.88$). These two results were corroborated by similar findings derived from the analysis of simulated canopies (Chapter 3). Nonmetric multidimensional scaling (NMS) was far more computationally intensive than PCA; however, NMS was able to preserve as much or more of the original dissimilarity (Euclidean distance) found among sample units in fewer dimensions. NMS results supported earlier findings (Chapter 3) that most (75–85%) of the information contained in multiscale lacunarity statistics was inherently aspatial and related to the magnitude of the canopy gap fraction. The remaining variance (15–25%) associated with $\Lambda(r)$ was best explained by the scale-dependent spatial arrangement of canopy surface heights. Further work is needed to derive other relevant spatial metrics from standard and normalized double-log lacunarity plots of $\Lambda(r)$ versus r.

Discriminant analysis (DA) indicated that canopy height was the single best predictor of stand age class. For example, a quadratic discriminant function based solely on $Lh_{0.85}$ had an overall classification accuracy rate of 82%. This accuracy rate increased to 89% when $\Lambda(r = 0.5$ m) was added to the classification model. It was no surprise that $Lh_{0.85}$ was such a strong predictor of stand age class, since sustained height growth can occur over several centuries in relatively undisturbed Pacific Coast Douglas-fir/western hemlock forests of northwestern North America. Gap-filling (growth) and gap-making (mortality) processes are key features of all seral forests, especially those that are long-lived and subject to infrequent stand-replacing disturbances. Therefore, it was also clear that $\Lambda(r = 0.5$ m) would be an important discriminator of stand-age class. A maximum overall accuracy rate of 92% was achieved when the quadratic classification function included three of the best discriminating variables: i.e., $Lh_{0.85}$, $\Lambda(r = 0.5$ m), and KR. Most of the class confusion was associated with the mature age class (>80–200 yr.), largely because mature forests occupy a transitional (intermediate) structural stage between young and old growth, and the rates, pathways, and endpoints of stand development can be highly variable in this forest type.

The structural differences found among very young (VY), young (Y), mature (M), and old-growth (O) forest canopies sampled in this study were consistent with the developmental patterns predicted by generalized models of even-aged stand and canopy development for other Pacific Coast Douglas-fir/western hemlock forests of northwestern North America. VY (<20 yr.) stands were characterized by short, narrow, open-grown crowns, with the majority of live needle and branch mass concentrated towards the lower half of their crowns. Unfilled growing space, regeneration gaps, and microsite variability contributed to substantial spatial heterogeneity in the horizontal dimension. Rapid height growth and crown expansion beyond age-class VY led to marked increases in canopy height and crown size; attainment of canopy closure; natural pruning of lower branch systems, and a concomitant rise in height-to-live-crown. Biomass accumulation, self-thinning, and crown differentiation operated collectively throughout age-class Y (>20–80 yr.) to shift crowns into upper (dominant) and lower (suppressed) tails of a predominantly unimodal (single-layer) canopy height distribution. Spatial homogeneity rather than heterogeneity was the distinguishing feature of age-class Y and many of the younger age-class M (>80–200 yr.) forest canopies. Canopy elaboration during early- to mid-successional stands (age-classes Y and M) was driven by crown expansion and differentiation rather than by gap formation. Age-class O (>200 yr.) uniquely exhibited substantial heterogeneity in all attributes of vertical and horizontal canopy structure. Fine-scale canopy disturbances, establishment of shade-tolerant tree associates, and adaptive reiteration by epicormic branching were considered to be the three main processes leading to the elaboration of late-successional forest canopies.

Non-hierarchical clustering by *k*-mean partitioning facilitated the separation of sample units into a number of relatively homogeneous classes of vertical and/or horizontal canopy structure. Consensus among three global stopping rules worked well to determine an optimal value for *k* and the 'best' statistical partition of the dataset. Class exemplars, presented in the form of height frequencies (histograms), one-sample quantile plots, and 2-D canopy height models, served as a visual classification key for the different vertical and/or horizontal classes (Fig. 4.17). Samples found closest to their group centroids were selected as class exemplars. Alternatively, boxplots of canopy variables (*y*-axis) versus *k*-means classes (*x*-axis) also allowed for easy graphical

interpretation of individual structural groups (Fig. 4B.2). *k*-means clusters formed along multivariate gradients of canopy height, cover, and scale-dependent spatial pattern. The majority of these structural classes were associated with late-successional forest canopies, because these older, naturally regenerated, fire-initiated stands exhibited far more within- and between-stand spatial heterogeneity than any of the young, managed plantations. A much larger, random sample of points located throughout Sooke Lake watershed is needed to develop a more comprehensive and operational classification of forest canopy structure for this area.

Forest inventory measurements have traditionally focused almost exclusively on bole size and condition for timber production, and have ignored the finer-scale plant structures, patterns, and dynamics contributed by foliage and branches. Successful future management of forest stands and landscapes for multiple purposes, including biodiversity and ecosystem function, will require new forest measurements that complement traditional inventory data and allow for statistical analyses across a broad range of observation scales (crowns to landscapes). This dissertation research has demonstrated how ground-based (in situ) hemispherical optical instruments (i.e., fisheye photography and LAI-2000 Plant Canopy Analyzer) and airborne discrete-return LiDAR can be used to characterize various aspects of fine-scale canopy structure at the plot level. In situ optical measurements of fine-scale canopy structure complement standard inventory measures of bole diameter, height, and condition, and also provide important ground-reference or calibration data for passive (optical) and active (light and microwave) airborne and satellite sensors. Spatially continuous measurements of 3-D canopy structure obtained from airborne LiDAR allow plot-level attributes to be extended across the landscape (Fig. 4B.1). The ability to quantify canopy structure at fine to coarse spatial scales is essential, because the relationships between vegetation structure, ecosystem processes, and habitat are well known to be strongly space, time, and variable dependent (Saunders et al., 1998; Cushman and McGarigal, 2002; Tews et al., 2004).

The remote sensing-based methodologies presented in this dissertation can provide spatially continuous quantitative datasets of 3-D vegetation structure, which are required by forest scientists to model various aspects of forest ecosystems, such as material and energy exchanges with the atmosphere, stand dynamics, productivity,

growth and yield, species-habitat relationships, fuel loading and fire risk, basin hydrology, etc. These spatially explicit datasets also support vegetation resource inventories, ecosystem mapping, effectiveness monitoring, quantification of natural or historical variability concepts, and design of site-specific silvicultural systems and prescriptions. LiDAR systems also capture fine-scale terrain information, and when combined with onboard passive optical (multispectral and hyperspectral) instruments allow simultaneous measurements of fine-scale vegetation and terrain (topographic) features and their spectral characteristics. Topographic variables (e.g., elevation, slope, aspect, curvature, etc.) provide important information about site energy and moisture balance (Pierce et al., 2005), while spectral reflectance data supply floristic details related to community composition, nutrient and moisture status, productivity, and health (Roberts et al., 2004). Future research efforts need to further investigate the synergies between vegetation, terrain, and spectral variables (Franklin, 1995; Franklin, 2001), and the ways in which these comprehensive, remotely sensed datasets can help to improve our understanding of the complex scale-dependent relationships between forest ecosystem composition, structure, and function.

5.1. References

Anderson, M.J., Ellingsen, K.E., McArdle, B.H., 2006. Multivariate dispersion as a measure of beta diversity. Ecology Letters 9, 683–693.

Cushman, S.A., McGarigal, K., 2004. Patterns in the species–environment relationship depend on both scale and choice of response variables. Oikos 105, 117–124.

Danson, F.M., Hetherington, D., Morsdorf, F., Koetz, B., Allgöwer, B., 2007. Forest canopy gap fraction from terrestrial laser scanning. IEEE Geoscience and Remote Sensing Letters 4, 157–160.

Franklin, J., 1995. Predictive vegetation mapping: geographical modelling of biospatial patterns in relation to environmental gradients. Progress in Physical Geography 19, 474–499.

Franklin, S.E., 2001. Remote sensing for sustainable forest management. Lewis Publishers, Boca Raton, FL.

Lundquist, J.E., Beatty, J.S., 1999. A conceptual model for defining and assessing the condition of forest stands. Environmental Management 23, 519–525.

Melloh, R., Ballard, J., Hardy, J., Woodcock, C., Liu, J., Smith, J., Koenig, G., Davis, R., 2003. Spatial distribution of canopy gaps in lodgepole pine forests. 60th Eastern Snow Conference, Sherbrooke, Québec, 2003, pp. 111–123.

Montes, F., Rubio, A., Barbeito, I, Cañellas, I., 2007. Characterization of the spatial structure of the canopy in *Pinus silvestris* L. in Central Spain from hemispherical photographs. Forest Ecology and Management, in press.

Omasa, K., Hosoi, F., Konishi, A., 2007. 3D lidar imaging for detecting and understanding plant responses and canopy structure. Journal of Experimental Botany 58, 881–898.

Pierce, Jr., K.B., Lookingbill, T., Urban, D., 2005. A simple method for estimating potential relative radiation (PRR) for landscape-scale vegetation analysis. Landscape Ecology 20, 137–147.

Roberts, D.A., Ustin, S.L., Ogunjemiyo, S., Greenberg, J., Dobrowski, S.Z., Chen, J., Hinckley, T.M., 2004. Spectral and structural measures of northwest forest vegetation at leaf to landscape scales. Ecosystems 7, 545–562.

Saunders, S.C., Chen, J., Crow, T.R., Brosofske, K.D., 1998. Hierarchical relationships between landscape structure and temperature in a managed forest landscape. Landscape Ecology 13, 381–395.

Tews, J., Brose, U., Grimm, V., Tielbörger, K., Wichmann, M.C., Schwager, M., Jeltsch, F., 2004. Animal species diversity driven by habitat heterogeneity/diversity: the importance of keystone structures. Journal of Biogeography 31, 79–92.

Van der Zande, Hoet, W., Jonckheere, I., van Aardt, J., Coppin, P., 2006. Influence of measurement set-up of ground-based LiDAR for derivation of tree structure. Agricultural and Forest Meteorology 141, 147–160.

Walter, J-M.N., Grégoire, C., 1996. Spatial heterogeneity of a Scots pine canopy: an assessment by hemispherical photographs. Canadian Journal of Forest Research 26, 1610–1619.